

**EXPERIMENTAL AND THEORETICAL STUDIES OF PROTEIN TRANSPORT  
IN HOLLOW-FIBRE BIOREACTORS FOR MAMMALIAN CELL CULTURE**

by

**MAREK ŁABĘCKI**

M.Sc., Technical University of Szczecin, Poland, 1987

M.A.Sc., University of British Columbia, 1994

A THESIS SUBMITTED IN PARTIAL FULFILMENT OF  
THE REQUIREMENTS FOR THE DEGREE OF

DOCTOR OF PHILOSOPHY

in

THE FACULTY OF GRADUATE STUDIES

DEPARTMENT OF CHEMICAL AND BIOLOGICAL ENGINEERING

We accept this thesis as conforming  
to the required standard

THE UNIVERSITY OF BRITISH COLUMBIA

July 2001

© Marek Łabęcki, 2001

### Authorisation

In presenting this thesis in partial fulfilment of the requirements for an advanced degree at the University of British Columbia, I agree that the Library shall make it freely available for reference and study. I further agree that permission for extensive copying of this thesis for scholarly purposes may be granted by the head of my department or by his or her representatives. It is understood that copying or publication of this thesis for financial gain shall not be allowed without my written permission.

Department of Chemical and Biological Engineering  
The University of British Columbia  
Vancouver, Canada

Date ..... 27 July 2001 .....

## Abstract

Cultivation of mammalian cells in the extracapillary space (ECS) of hollow-fibre bioreactors (HFBRs) is increasingly used for the production of useful proteins such as monoclonal antibodies. One of the greatest challenges associated with the operation of HFBRs is the maintenance of a uniform cell growth environment. In particular, the distributions of growth-factor proteins can be highly heterogeneous, leading to poor performance or even failure of the culture. Another important aspect of HFBR operation is the harvesting of product proteins from the ECS. Considering the high costs of the product and media proteins, there is a strong motivation for carrying out studies that will provide a better understanding of protein behaviour in HFBRs.

The main focus of this thesis was the development of mathematical models describing different aspects of protein transport in HFBRs. The models were validated using protein concentration data collected during cell-free HFBR experiments. A one-dimensional Krogh cylinder model was employed to analyse hindered transmembrane transport relevant to the leakage of smaller proteins from the ECS. A two-dimensional porous medium model (PMM) was used to simulate open-shell operations such as harvesting. An advanced, three-dimensional PMM formulation permitted an extensive analysis of gravity-influenced free-convective ECS protein transport at different HFBR orientations.

The dynamics of protein leakage in HFBRs was found to depend on many factors, including initial protein placement, perfusion flow rate, and the addition of a nonleaking protein to the ECS. An open-shell ECS shunt was predicted to be a viable alternative to the traditional closed-shell HFBR configuration, while cocurrent harvesting was found more efficient than countercurrent harvesting. Most studies revealed that the protein transfer between the fibre bundle and the manifolds played a significant role in ECS protein redistribution. Numerous model simulations confirmed the occurrence of forced-convective downstream polarisation of ECS proteins under typical operating conditions. The

heterogeneity of protein distribution was greatly reduced by directing the perfusion flow upward, in which case strong free-convective flows mixed the contents of the ECS. These effects were most pronounced in cartridges oriented vertical-up, which might be a nonstandard but nonetheless promising configuration for use in future HFBR cell culture.

## Contents

Abstract	ii
Tables	vii
Figures	ix
Acknowledgements	xvii
Dedication	xviii
Chapter 1: INTRODUCTION	1
Chapter 2: BACKGROUND AND PREVIOUS WORK	6
2.1. Hollow-Fibre Mammalian Cell Culture	6
2.1.1. The Cells	6
2.1.1.1. Cell Types	6
2.1.1.2. Extracellular Matrix	7
2.1.1.3. Growth Requirements	8
2.1.2. The Membranes	12
2.1.2.1. Materials	12
2.1.2.2. Permeability Properties	14
2.1.2.3. Concentration Polarisation and Fouling	16
2.1.3. Bioreactor Operation	18
2.1.3.1. Conventional System Setup	18
2.1.3.2. Inoculation	19
2.1.3.3. Closed-Shell Operation	21
2.1.3.4. Product Harvesting	22
2.1.3.5. Alternative HFBR Systems	24
2.2. Previous Models of Protein Transport in HFBRs	29
2.2.1. Krogh Cylinder Models	30
2.2.2. Porous Medium Model	39
2.2.3. Essential Predictions	44
2.2.4. Motivation for Present Modelling Work	49
Chapter 3: ONE-DIMENSIONAL ANALYSIS OF HINDERED PROTEIN TRANSPORT THROUGH HOLLOW-FIBRE MEMBRANES	51
3.1. Motivation and Objectives	51
3.2. Model Development	52
3.2.1. Underlying Assumptions	52
3.2.2. Mathematical Formulation and Numerical Techniques	53
3.2.2.1. Pore Geometry and Hydrodynamics	53

3.2.2.2. ECS and ICS Hydrodynamics	58
3.2.2.3. Transmembrane Protein Transport	58
3.2.2.4. ECS and ICS Protein Transport	60
3.2.2.5. ECS Manifold Extension	63
3.2.3. Model Parameters	65
3.3. Experimental Procedures	69
3.3.1. Cartridge Pretreatment	69
3.3.2. Leakage Experiments	70
3.3.3. Protein Analysis	72
3.4. Results and Discussion	74
3.4.1. ICS Myoglobin	74
3.4.2. ECS Myoglobin and BSA	76
3.4.3. Potential Sources of Discrepancies in Best-Fit Results	84
3.4.3.1. ICS Protein Sink	84
3.4.3.2. Membrane Pore Plugging	85
3.4.3.3. Pore Size Distribution	86
3.4.3.4. Sensitivity to Transmission Parameters	88
3.4.3.5. Other Factors	89
3.5. Conclusions	90
Chapter 4: TWO-DIMENSIONAL ANALYSIS OF PROTEIN TRANSPORT IN OPEN-SHELL HOLLOW-FIBRE BIOREACTORS	93
4.1. Motivation and Objectives	93
4.2. Experimental Procedures	94
4.2.1. Inoculation Experiments	94
4.2.2. Protein Analysis	96
4.3. Model Simulations	97
4.4. Results and Discussion	100
4.4.1. Inoculation	100
4.4.2. Harvesting and ECS Shunt	114
4.5. Conclusions	116
Chapter 5: THREE-DIMENSIONAL ANALYSIS OF GRAVITY-INFLUENCED PROTEIN TRANSPORT IN CLOSED-SHELL HOLLOW-FIBRE BIOREACTORS	121
5.1. Motivation and Objectives	121
5.2. Model Development	122
5.2.1. Underlying Assumptions	122
5.2.2. Mathematical Formulation	123
5.2.2.1. Fluid Dynamics	123
5.2.2.2. ECS Protein Transport	131
5.2.2.3. Modelling of ECS Manifolds	134
5.2.3. Model Parameters	137
5.3. Numerical Techniques	140
5.3.1. Solution of the Pressure Equations	140
5.3.1.1. Iterative Solver	140

5.3.1.2. Direct Solver for the ECS Pressure Problem	143
5.3.2. Solution of the ECS Concentration Problem	145
5.3.3. Organisation of Numerical Input and Output	146
5.3.3.1. Input	146
5.3.3.2. Output	148
5.3.4. Computational System	152
5.3.5. Preliminary Simulations	152
5.3.5.1. Consistency with 2-D and 1-D Formulations	153
5.3.5.2. Sensitivity Analyses	155
5.4. Experimental Procedures	159
5.5. Results and Discussion	162
5.5.1. Experimental Observations and Model Validation	163
5.5.2. Model Predictions	173
5.5.2.1. Effect of HFBR Inclination Angle	173
5.5.2.2. Effect of ECS Manifolds	193
5.5.2.3. Effect of ICS Flow Rate	202
5.5.2.4. Effect of Initial ECS Protein Concentration	204
5.6. Conclusions	208
 Chapter 6: OVERALL CONCLUSIONS AND RECOMMENDATIONS	 211
6.1. Conclusions	211
6.2. Recommendations	216
 Nomenclature	 219
 References	 229
 Appendix A: ONE-DIMENSIONAL HYDRODYNAMIC SOLUTIONS FOR A TORTUOUS KROGH CYLINDER	 242
 Appendix B: HINDERED TRANSMEMBRANE PROTEIN TRANSPORT ANALYSIS INCLUDING PORE SIZE DISTRIBUTION	 244
 Appendix C: FORTRAN CODE OF THE MODIFIED GAUSS ELIMINATION ROUTINE	 248
 Appendix D: ADI METHOD AND UPWIND CONTROL SCHEME FOR THE SOLUTION OF THREE-DIMENSIONAL ECS CONCENTRATION PROBLEM	 251

## Tables

1. Examples of alternative HFBR systems	25
2. Boundary conditions for the PMM equations (28), (29), and (35)	43
3. Major parameters for the 1-D Krogh cylinder model of transmembrane protein transport in HFBRs	66
4. Summary of leakage experiments (note: experiment #1 was conducted by Yves Dudal)	71
5. Summary of the ICS results of the experimental and simulation leakage studies	74
6. Summary of HFBR inoculation experiments; $C_{in}$ , inlet protein concentration; $Q$ , inoculation flow rate; $t_{act}$ , actual experiment duration (i.e., time elapsed between the start and stoppage of inoculation flow)	95
7. Parameters used in the 2-D PMM simulations of open-shell HFBR operations	98
8. Summary of HFBR inoculation experiments; $C_{in}$ , inlet protein concentration; $Q$ , inoculation flow rate; $t_{act}$ , actual experiment duration (i.e., time elapsed between the start and stoppage of inoculation flow)	101
9. Boundary conditions for the ECS and ICS pressure equations (107) and (109)	132
10. Boundary and initial conditions for the ECS protein concentration equation (115)	133
11. Parameters for the three-dimensional HFBR model	138
12. Essential input parameters for the numerical code of the three-dimensional HFBR model (default or commonly used values are given in boldface)	147
13. Output files generated at each desired time; the ?? symbol in the file name denotes a two-digit code identifying the output time	149
14. Input parameters for the test of consistency between the 3-D and 2-D PMM codes ( $\hat{P}_L = P_L$ in the 2-D model)	153

15. Selected results of the numerical consistency test for the 3-D and 2-D PMMs; the overbars denote radially-averaged quantities;  $C_{AVE}$  is the final average ECS concentration (including the manifolds) 154
16. Effects of grid coarsening on steady-state results for  $\Psi = 90^\circ$ ,  $Q_L = 600$  mL/min,  $C_0 = 5$  g/L (other input parameters at their defaults, see table 12); original grid  $50 \times 10 \times 9$ , the changed values are underlined;  $C_{UpMan}$  and  $C_{DnMan}$  are the average concentrations in the upstream and downstream ECS manifold, respectively; the double overbar denotes a quantity averaged both radially and angularly 156
17. Summary of azoalbumin transport experiments for different cartridge orientations ( $Q_L = 850$  mL/min); the initial ECS concentrations in 6B-D, denoted with an asterisk, were determined from the ICS concentration data; the extent of protein leakage, i.e., the fraction of ECS protein that has leaked to the ICS over the experiment duration, was calculated based on the known ICS recycle volumes and the approximate total ECS volume of 100 mL 161
18. Model predictions of ECS heterogeneity index ( $HetIx$ ), ECS protein concentration in the fibre bundle ( $C_{Bundle}$ ), and average global magnitude of  $dC/dt$  ( $dCdtAve$ ) for different HFBR orientations at steady state; times needed to reach steady state ( $t_{StSt}$ ) are also given 174
19. Model-predicted effects of normal and double-size manifolds on the ECS protein heterogeneity index ( $HetIx$ ) and on the average protein concentration in the fibre bundle ( $C_{Bundle}$ ) at steady state for different cartridge orientations;  $C_0 = 5$  g/L,  $Q_L = 600$  mL/min; the listed values represent changes relative to the case of a hypothetical cartridge with no ECS manifolds 194
20. Average protein concentrations in the ECS fibre bundle ( $C_{Bundle}$ ), in the upstream manifold ( $C_{UpMan}$ ), and in the downstream manifold ( $C_{DnMan}$ ) for different cartridge orientations at steady state;  $C_0 = 5$  g/L,  $Q_L = 600$  mL/min, normal manifolds 195

## Figures

1. Longitudinal section through a typical hollow-fibre cartridge (not to scale). The terms *upstream* and *downstream* indicate axial position with respect to the bulk ICS flow. 3
  
2. Conventional HFBR system configuration (components not to scale): 1, HFBR cartridge; 2, oxygenator; 3, ICS recycle medium reservoir; 4, ICS sampling port; 5, ICS recycle pump; 6, ICS feed pump; 7, fresh ICS medium reservoir; 8, air cylinder; 9, waste gas outlet; 10, waste ICS medium reservoir; 11, fresh ECS medium reservoir; 12, harvest collector; 13, harvesting pump. 19
  
3. Example flow configurations in the inoculation procedure: *a*, countercurrent (standard); *b*, dead-end; *c*, cross-flow; *IP*, inoculation port. 20
  
4. Examples of HFBR harvesting configurations: *a*, cocurrent (standard); *b*, cross-flow; *c*, ECS fluid cycling through an expansion chamber (Acusyst); *H*, harvest outlet; *FM*, fresh medium intake; *EC*, expansion chamber; *PR*, pressure regulator. 23
  
5. Cross-sectional arrangement of Krogh cylinders in a hollow-fibre bundle (not to scale); partial overlapping compensates for the void space between the neighbouring cylinders (Łabęcki 1994);  $R_L$ , lumen radius;  $R_F$ , fibre outer radius;  $R_K$ , Krogh cylinder radius. Typically,  $R_L$  is of order  $10^{-4}$  m,  $R_F - R_L \approx 1.2 \times 10^{-6}$  m, and  $R_K \approx 1.5\text{-}2.0 \times 10^{-4}$  m. 31
  
6. Longitudinal section through the cylindrical domain of the two-dimensional porous medium model (Łabęcki 1994, Łabęcki et al. 1995, 1996); *REV*, representative elementary volume;  $z_m$ , axial length of the ECS manifold. 40
  
7. KCM predictions of radially-averaged BSA concentration distributions (solid lines) and axial velocities (dotted lines) in the ECS of a closed-shell HFBR (adapted from Koska et al. (1997));  $L_p = 6 \times 10^{-15}$  m,  $Q_L = 500$  mL/min (from left to right), average ECS protein concentration 10 g/L; *a*, cell-free ECS,  $k_s = 10^{-9}$  m<sup>2</sup>; *b*, cell-packed ECS,  $k_s = 5 \times 10^{-14}$  m<sup>2</sup>. The final profiles shown are practically identical to the steady-state ones. 45

8. KCM predictions of radially-averaged ECS protein (BSA) concentrations in a closed-shell HFBR at steady state for different ECS hydraulic permeabilities (adapted from Koska et al. (1997)); average ECS protein concentration 10 g/L,  $L_p = 6 \times 10^{-15}$  m,  $Q_L = 500$  mL/min; *a*,  $k_s = 10^{-9}$  m<sup>2</sup>; *b*,  $k_s = 5 \times 10^{-13}$  m<sup>2</sup>; *c*,  $k_s = 5 \times 10^{-14}$  m<sup>2</sup>; *d*,  $k_s = 5 \times 10^{-16}$  m<sup>2</sup>; *e*,  $k_s = 5 \times 10^{-17}$  m<sup>2</sup>. Times to reach steady state are given in parentheses. 46
  
9. Steady-state radially-averaged ECS protein (BSA) concentrations in a closed-shell HFBR at cell-free conditions (adapted from Taylor et al. (1994)); *a*, effect of the ICS flow rate,  $C_0 = 10$  g/L; *b*, effect of the average ECS protein concentration,  $Q_L = 570$  mL/min. Membrane hydraulic permeability  $L_p = 1.25 \times 10^{-13}$  m. 48
  
10. Experimental (symbols) versus KCM-predicted (solid lines) steady-state distributions of ECS transferrin at the average BSA concentrations of 20 g/L, 29 g/L, and 82 g/L (adapted from Patkar et al. (1995)); average transferrin concentration 0.02 g/L,  $Q_L = 600$  mL/min,  $L_p = 6 \times 10^{-15}$  m. 49
  
11. An equivalent representation of a tortuous pore within a differential element of the hollow-fibre membrane (adapted from Łabęcki et al. (1998)). 54
  
12. Illustration of the ECS concentration adjustment in the manifold extension to the tortuous Krogh cylinder model of HFBR protein transport (not to scale; adapted from Łabęcki et al. (1998)). Hatched areas are the regions of uniform concentration for different grid points: 1, point  $i = 1 + \text{NINT}(z_m / \Delta z)$  (edge of the upstream manifold) or  $i = N - \text{NINT}(z_m / \Delta z)$  (edge of the downstream manifold); 2, point  $i$  of the interior of the manifold length subdomain; 3, point  $i = 1$  (upstream end) or  $i = N$  (downstream end). 64
  
13. Setup of a hollow-fibre leakage experiment. 73
  
14. Changes of ICS myoglobin concentration with time in experiments with myoglobin loaded into the ECS (*a*) or ICS (*b*). Symbols – experimental data, solid lines – best-fit model predictions, dashed line – best-fit model prediction without the ECS manifold extension; *fast*,  $Q_L = 300$  mL/min; *slow*,  $Q_L = 10$  mL/min; *BSA*, BSA present in the ECS. The best-fit curves for experiments #6 and #7 are practically identical. 75
  
15. Model-predicted (smooth curves) and experimental (step lines) ECS myoglobin concentrations within the length of the downstream manifold: *a*, experiment #2 (myoglobin loaded into the ECS); *b*, experiment #3 (myoglobin loaded into the ICS). No BSA, ICS flow from left to right,  $Q_L = 300$  mL/min. 77

16. Model-predicted (smooth curves) and experimental (step lines) concentrations of ECS myoglobin and BSA in experiment #4 (myoglobin loaded into the ECS). ICS flow from left to right,  $Q_L = 300$  mL/min. 78
17. Model-predicted (smooth curves) and experimental (step lines) concentrations of ECS myoglobin and BSA in experiment #5 (myoglobin loaded into the ICS). ICS flow from left to right,  $Q_L = 300$  mL/min. 79
18. Model-predicted (smooth curves) and experimental (step lines) concentrations of ECS myoglobin at the completion of experiments #6 (upper panel) and #7 (lower panel). ICS flow from left to right,  $Q_L = 10$  mL/min. 80
19. Model predictions of the time-dependent changes in the fraction of total myoglobin present in the ECS fibre-free regions for the conditions of experiments #2-7; *ECS*, myoglobin loaded into the ECS; *ICS*, myoglobin loaded into the ICS; *fast*,  $Q_L = 300$  mL/min; *slow*,  $Q_L = 10$  mL/min. 81
20. Effect of ECS manifold extension on the best-fit membrane constant,  $k_m$ , and standard deviation (eq. 87),  $SD$ , for different leakage experiments. 83
21. Temporal changes in the ICS myoglobin concentration in experiment #1 (no BSA,  $Q_L = 300$  mL/min); symbols – experimental data; curves – best-fit model predictions. 85
22. Effect of pore plugging extension (eq. 88) on the best-fit membrane constant,  $k_m$ , and standard deviation (eq. 87),  $SD$ , for different leakage experiments. 87
23. Flow configurations in the open-shell processes investigated using the 2-D PMM: *a*, dead-end inoculation; *b*, cocurrent harvesting; *c*, countercurrent harvesting; *d*, countercurrent ECS shunt. 94
24. Diagram illustrating a typical scheme of cartridge sectioning into axial, radial, and angular segments (adapted from Łabęcki et al. (1996)). Dotted regions denote sections of the fibre bundle, blank regions are fibre-free sections. 96
25. Experimental versus model-simulated axial ECS protein concentration profiles at  $t = t_{eff}$  for experiments #2 (*a*) and #3 (*b*); step lines – radially- and angularly-averaged experimental data; smooth solid lines – radially-averaged 2-D PMM predictions; smooth dashed lines – 1-D KCM predictions. The angular standard deviation (ASD) bars signify the angular concentration variation in each axial segment. Shaded areas mark the positions of ECS manifolds. Adapted from Łabęcki et al. (1996). 103
26. PMM-predicted two-dimensional ECS protein concentration fields (g/L) at the end of experiments #2 (top) and #3 (bottom). The ECS concentration values have been scaled by a factor of  $m_{exp}/m_{eff}$ , equal to 0.752 for #2 and 1.019 for #3. Domain dimensions are not to scale. 104

27. Model-predicted radially-averaged transient concentration profiles for the conditions of experiment #3; solid lines – PMM, dashed lines – KCM. Shaded areas mark the positions of ECS manifolds. Adapted from Łabęcki et al. (1996). 105
28. Experimental (step lines) and PMM-predicted (smooth lines) axial ECS concentration profiles in the inside bore (solid lines) and the outside annulus (dashed lines) of the fibre bundle at  $t = t_{eff}$  for experiment #2. The PMM data have been averaged radially within each radial subsection. Shaded areas mark the positions of ECS manifolds. Adapted from Łabęcki et al. (1996). 107
29. Experimental versus model-simulated axial ECS protein concentration profiles at  $t = t_{eff}$ : *a*, experiment #5 (upward flow); *b*, experiment #6 (downward flow). Solid step lines – raw experimental data; dotted step lines – experimental data adjusted to account for protein present in the downstream manifold; smooth lines – radially-averaged 2-D PMM predictions. Shaded areas mark the positions of ECS manifolds. Adapted from Łabęcki et al. (1996). 108
30. PMM-predicted two-dimensional ECS protein concentration fields (g/L) at  $t = t_{eff}$  in experiment #5. The ECS concentration values have been scaled by a factor of  $m_{exp}/m_{eff} = 0.928$ . Domain dimensions are not to scale. 109
31. Experimental (step line) versus PMM-predicted (smooth curve) radial protein concentration variation at  $t = t_{eff}$  in experiment #6. The plots express the difference between the average concentrations in the inside bore and the outside annulus of the fibre bundle, relative to the concentrations averaged radially over the whole bundle radius. Shaded areas mark the positions of ECS manifolds. Adapted from Łabęcki et al. (1996). 112
32. Effect of flow direction on the axial progress of the protein front. Circles – experiment #5 (upward flow); squares - experiment #6 (upward flow); the PMM curves for both cases are indistinguishable. Shaded areas mark the positions of ECS manifolds. Adapted from Łabęcki et al. (1996). 113
33. Initial protein (BSA) distributions used in the PMM harvesting simulations; ICS flow rate  $Q_L = 200$  mL/min, average BSA concentration 10 g/L. 114
34. PMM predictions of the outlet protein (BSA) concentration (*a*) and the fraction of protein removed from the ECS (*b*) for different harvesting modes: *Co*, cocurrent flow; *Cn*, countercurrent flow; *U*, uniform initial protein distribution; *P*, steady-state (polarised) initial protein distribution. The outlet concentrations were averaged over the ECS manifold length. ICS flow rate  $Q_L = 200$  mL/min; ECS inlet flow rate 1 mL/min; average starting protein concentration 10 g/L. The ECS volume (not including manifolds) was 74.1 mL. 115

35. PMM predictions of radially-averaged ECS protein (BSA) distribution at steady state in the countercurrent shunt and closed-shell configurations. ICS flow rate  $Q_L = 200$  mL/min, ECS inlet flow 0.5 mL/min, average initial ECS protein concentration 10 g/L. 117
36. Diagram illustrating the arrangement of spatial parameters in a three-dimensional cylindrical domain and the elevation  $h$  of a point  $M(r, \theta, z)$  relative to the datum level (dimensions not to scale). 126
37. Longitudinal (left) and cross-sectional (right) slices through an ECS manifold and the contiguous fibre bundle (not to scale). Black dots signify the centres of representative control volumes involved in the manifold concentration adjustment schemes (see text). 135
38. Three-dimensional grid arrangement around an interior point  $(i, j, k)$  in a cylindrical domain. Upper diagram:  $z$ - $r$  projection, lower diagram:  $r$ - $\theta$  projection. The faces of the control volume are labelled as bottom and top ( $r$ -direction), west and east ( $\theta$ -direction), and south and north ( $z$ -direction). 141
39. Transformation of the coefficient matrix in the modified Gauss elimination procedure (see text). 144
40. Experimental (left) and model-simulated (right) transient distributions of ECS azoalbumin in a GFE-15 cartridge inclined at  $45^\circ$ . Conditions of experiment 4 (table 17),  $Q_L = 850$  mL/min,  $C_0 = 4.38$  g/L (assumed unchanged over the experiment duration). Black arrows indicate the direction of bulk ICS flow. The lumen space in the last photograph was emptied to increase contrast between the ICS and ECS. All panels have been resized for the convenience of arrangement in the layout and hence the cartridges are not shown to scale. 164
41. Experimental (left) and model-simulated (right) transient distributions of ECS azoalbumin in a horizontal GFE-15 hollow-fibre cartridge. Conditions of experiment 1 (table 17),  $Q_L = 850$  mL/min,  $C_0 = 6.16$  g/L (assumed unchanged over the experiment duration). The lumen space in the last photograph was emptied to increase contrast between the ICS and ECS. All panels have been resized for the convenience of arrangement in the layout and hence the cartridges are not shown to scale. 165
42. Experimental (left) and model-simulated (right) transient distributions of ECS azoalbumin in a GFE-15 cartridge inclined at  $135^\circ$ . Conditions of experiment 3 (table 17),  $Q_L = 850$  mL/min,  $C_0 = 4.71$  g/L (assumed unchanged over the experiment duration). Black arrows indicate the direction of bulk ICS flow. All panels have been resized for the convenience of arrangement in the layout and hence the cartridges are not shown to scale. 166

43. Experimental (top panels) and model-simulated (middle and bottom panels) transient distributions of ECS azoalbumin in a vertical GFE-15 cartridge with upward ICS flow (indicated by black arrows). Conditions of experiment 5 (table 17),  $Q_L = 850$  mL/min,  $C_0 = 4.09$  g/L (assumed unchanged over the experiment duration). The bottom panels show the predicted effect of a  $1^\circ$  deviation from the vertical orientation towards the right (i.e.,  $\Psi = 179^\circ$ ) for the same simulation conditions. All panels have been resized for the convenience of arrangement in the layout and hence the cartridges are not shown to scale. 167
44. Azoalbumin distributions in a GFE-15 cartridge for the experimental series 6A-D (table 17): *a*,  $\Psi = 0^\circ$ , at the end of 6A (6 h); *b*,  $\Psi = 90^\circ$ , at the end of 6B (20 h, considered to be steady state); *c*,  $\Psi = 45^\circ$ , at the end of 6C (26 h, considered to be steady state); *d*,  $\Psi = 135^\circ$ , 1 h of 6D; *e*,  $\Psi = 135^\circ$ , 2 h of 6D; *f*,  $\Psi = 135^\circ$ , 4 h of 6D. The final distribution for  $\Psi = 135^\circ$  (case 6D) is not shown because of significant protein depletion from the ECS due to leakage, but is qualitatively similar to the 4 h transient in panel *f*. Black arrows indicate the direction of bulk ICS flow. 168
45. Steady-state output parameters as functions of the HFBR inclination angle: *a*, global average magnitude of  $dC/dt$ ; *b*, ECS heterogeneity index (squares, left axis) and ECS fibre bundle concentration (circles, right axis). At  $\Psi = 170^\circ$ , no data point is plotted for  $dCdtAve$ , and the mean values from table 49 are plotted for  $HetIx$  and  $C_{Bundle}$ . 174
46. Temporal changes of  $dCdtMax$  for different HFBR orientations (all other parameters at their default values – see table 12). 177
47. Model-predicted steady-state protein concentrations (g/L; left panels) and ECS flow patterns (superficial velocities, right panels) at nonvertical orientations of HFBR cartridge:  $\Psi = 45^\circ$  (inclined-down),  $\Psi = 90^\circ$  (horizontal), and  $\Psi = 135^\circ$  (inclined-up). Shown are longitudinal sections in the vertical plane passing through cartridge centerline (not to scale). ICS flow is from left to right and the thick arrows indicate the direction of the gravity vector ( $g$ ). See also table 17 for more of the relevant steady-state data. 179
48. Model-predicted steady-state protein concentrations (g/L) and ECS superficial velocity vectors at the vertical and near-vertical orientations of HFBR cartridge (top inclined to the right). Left column:  $\Psi = 179^\circ$ , middle column:  $\Psi = 179.9^\circ$ , right column:  $\Psi = 180^\circ$ . The top two rows show longitudinal sections in the vertical plane passing through cartridge centerline (not to scale), with the upward arrows on the left-hand side marking the direction of ICS flow. The third and fourth rows of graphs show cross-sections at  $z = 0.5L$  (axial half-length) and at  $z = 0.9L$  (edge of the downstream ECS manifold), respectively, with the ICS flow coming out of the paper plane. See also table 17 for more of the relevant steady-state data. 180

49. Selected transients for  $\Psi = 135^\circ$ , plotted in the vertical section through the cartridge centreline. Left panels: ECS protein concentration contours (g/L), right panels: ECS superficial fluid velocity vectors. ICS flow from left to right,  $Q_L = 600$  mL/min,  $C_0 = 5$  g/L. 183
50. Selected transients predicted for  $\Psi = 170^\circ$ , plotted in the vertical section through the cartridge centreline. Left panels: ECS protein concentration contours (g/L), right panels: ECS superficial fluid velocity vectors. ICS flow left to right,  $Q_L = 600$  mL/min,  $C_0 = 5$  g/L. 184
51. Selected transients predicted for  $\Psi = 179^\circ$  (top of the cartridge inclined to the right). Upper panels: ECS protein concentration contours (g/L), lower panels: ECS superficial fluid velocity vectors. All plots are shown in the vertical section through the cartridge centreline (not to scale). The upward arrows on the left-hand side mark the direction of ICS flow.  $C_0 = 5$  g/L,  $Q_L = 600$  mL/min. 185
52. Model-predicted temporal changes of the ECS protein heterogeneity index for different orientations of HFBR cartridge; uniform initial concentration field,  $C_0 = 5$  g/L,  $Q_L = 600$  mL/min, other input parameters at their default values (see table 12). 193
53. Temporal changes of the average protein concentration in the ECS fibre bundle for cartridges with normal (solid lines) and double-size manifolds (dashed lines) at different HFBR orientations;  $C_0 = 5$  g/L,  $Q_L = 600$  mL/min. 196
54. Temporal changes of the average protein concentrations in the ECS fibre bundle and in the manifolds at different HFBR orientations (cartridge with normal-size manifolds);  $C_0 = 5$  g/L,  $Q_L = 600$  mL/min. Note that different concentration scales are used for  $\Psi \leq 90^\circ$  and for  $\Psi > 90^\circ$ . 197
55. Selected transients predicted for a hypothetical manifold-free cartridge at  $\Psi = 179^\circ$  (top inclined to the right). Upper panels: ECS protein concentration contours (g/L), lower panels: ECS superficial fluid velocity vectors. All plots are shown in the vertical section through the cartridge centreline (not to scale).  $C_0 = 5$  g/L,  $Q_L = 600$  mL/min (upward ICS flow). 199
56. Selected transients predicted for a hypothetical manifold-free cartridge at the vertical-upward orientation ( $\Psi = 180^\circ$ ). Upper panels: ECS protein concentration contours (g/L), lower panels: ECS superficial fluid velocity vectors. All plots are shown in the vertical section through the cartridge centreline (not to scale).  $C_0 = 5$  g/L,  $Q_L = 600$  mL/min;  $t = 32.9$  h marks the steady state for this case. 201

57. Periodic protein redistribution over one oscillation cycle (132 h) in the vertical section through the cartridge centreline at  $\Psi = 179^\circ$ . Upper panels – ECS concentration contours (g/L), lower panels – ECS velocity vectors. Thick arrows on the left mark the direction of ICS flow.  $Q_L = 200$  mL/min,  $C_0 = 5$  g/L. 203
58. Effects of ICS flow rate on the protein heterogeneity index ( $a$ ) and on the protein concentration in the fibre bundle ( $b$ ) at steady state for different HFBR orientations. No steady-state solutions were obtained at  $179^\circ$  and  $180^\circ$ ; error bars signify the oscillation amplitudes for the periodic solutions in these two cases. 205
59. Effects of the initial ECS protein concentration on the heterogeneity index ( $a$ ) and the concentration in the fibre bundle ( $b$ ) at steady state for different HFBR orientations ( $Q_L = 600$  mL/min). Error bars signify the oscillation amplitudes of a periodic solution obtained for  $180^\circ$  at  $C_0 = 20$  g/L. 207

## **Acknowledgements**

I feel deeply indebted to Dr. Bruce D. Bowen and Dr. James M. Piret for their continuous support and guidance over the duration of this project. Financial assistance in the form of a University Graduate Fellowship from the University of British Columbia is also acknowledged.

This work is dedicated to my Mother

## Chapter 1

### INTRODUCTION

Hollow-fibre membrane devices are widely employed in a variety of fields, e.g., in desalination and purification of water by reverse osmosis, blood purification by haemodialysis or haemofiltration, production of therapeutic and diagnostic proteins, separation of complex solute mixtures, etc. One of their most important applications is as biological reactor-separators, or hollow-fibre bioreactors (HFBRs), in which either enzymes or whole cells are immobilised and perfused with specially formulated media for the purpose of obtaining valuable biochemical products. The first uses of hollow-fibre membranes in this capacity were reported in the early 1970s (Rony 1971, Knazek et al. 1972). Over time, whole-cell immobilisation has generally become preferred to enzyme immobilisation, owing to the elimination of an expensive enzyme purification step, greater stability of intracellular enzymes, and the ability of whole cells to catalyse complete metabolic pathways (Webster and Shuler 1978). Furthermore, perfusion cell cultures have offered some important advantages over traditional suspension cultures, including protection of cells from shear stresses, higher cell densities, reduced medium requirements, and increased product concentrations (Piret and Cooney 1990a).

All of these attractive features, in addition to a large membrane surface area per unit reactor volume and the availability and ease of production of hollow-fibre membranes, can ultimately translate into high productivity and low cost of HFBR systems. Not surprisingly therefore, the ever increasing demand for various therapeutic and diagnostic proteins, such as erythropoietin (EPO), human growth hormone, blood coagulation factors, or monoclonal antibodies (MAbs) (Butler 1987), has stimulated considerable interest in their commercial production using hollow-fibre devices. Although recombinant DNA technology (Alberts et al. 1994, chapter 7) has offered the possibility of obtaining some of these products from genetically-modified bacterial, plant, insect, or yeast cells (which usually grow faster and

require less complex media), it has been found that most useful proteins can be obtained in a fully functional form only by using mammalian cells (Belfort 1989). The option of cultivating prokaryotic cells (e.g., *E. coli*) in hollow-fibre reactors has raised further concerns, including possible oxygen depletion due to very high specific (i.e., per cell) oxygen uptake rates (Piret and Cooney 1990a); production of endotoxins, which can cause product contamination (Butler 1987, p. 42); intracellular location of the product, which requires its extraction from the cell lysate (ibid.); or potential cell overgrowth leading to fibre damage (Inloes et al. 1983). Recently, production of monoclonal antibodies in HFBRs has been an increasingly viable alternative to the traditional way of obtaining MABs from ascites tumours in mice. Although the latter technology can be competitive with cell culture in terms of cost and product concentration, it also suffers from serious disadvantages, such as ethical issues, practical problems with handling large numbers of animals in large-scale production, high risk of product contamination by viruses and extraneous antibodies, and limitations in obtaining human antibodies from rodents (Birch et al. 1985, p. 1; Jackson et al. 1996). For all of the above reasons, there has been a rapid expansion of research in the field of mammalian cell HFBRs in recent decades.

Numerous HFBR designs have been proposed (Tharakan et al. 1988), but the most conventional option involves entrapment of mammalian cells in the extracapillary space (ECS), or shell side, of a cylindrical cartridge densely packed with hollow fibres which are fixed at both ends in an epoxy support (fig. 1). Recirculation flow of medium through the fibre lumina, or intracapillary space (ICS), allows exchange of oxygen as well as small nutrients and metabolites with the ECS, thus providing the cells with stable growth conditions. The ICS recycle flow is analogous to blood flow through capillaries embedded in tissue, and the whole configuration mimics to a certain extent an *in vivo* system. Oxygen is provided by aerating the ICS stream, usually with CO<sub>2</sub> added for buffering purposes, in an on-line oxygenator. The two annular, fibre-free regions at both ends of the cartridge are the ECS manifolds; they are used to introduce cells and fresh medium into the ECS and to harvest the product protein. The manifolds may also trap some of the cells and proteins, and hence complicate bioreactor operation. Since the ultrafiltration membranes normally retain most proteins in the ECS, it is possible to concentrate the useful product prior to harvesting,

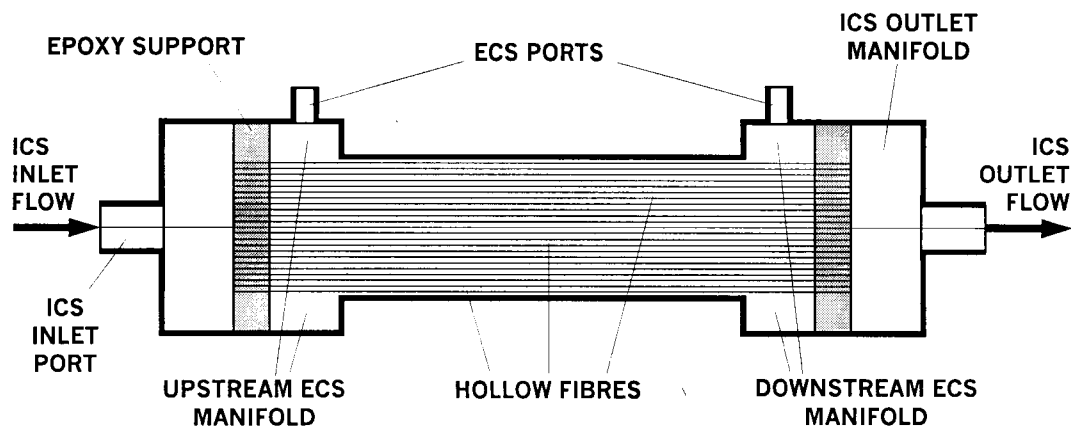


Fig. 1. Longitudinal section through a typical hollow-fibre cartridge (not to scale). The terms *upstream* and *downstream* indicate axial position with respect to the bulk ICS flow.

thereby reducing the expense of subsequent downstream purification. A typical setup of an HFBR cell culture system is discussed in more detail in section 2.1.3.1.

The two ECS ports of the HFBR cartridge shown in fig. 1 remain closed during most of the culture run, and the corresponding flow configuration is termed the closed-shell mode. In this case, the axial pressure gradient in the ICS, in the presence of the membranes, induces a secondary flow in the ECS, also referred to as Starling flow.<sup>1</sup> As a consequence, cells and proteins can be convectively carried to the downstream part of the ECS (Waterland et al. 1975; Piret and Cooney 1990b), which may lead to spatial heterogeneities in the growth environment and hence deterioration of the bioreactor performance. Flow configurations with at least one ECS port open are termed open-shell; the most important open-shell operations in HFBR cell culture being inoculation, or introduction of cell-containing medium into the ECS, and harvesting, or product collection from the ECS. Inoculation and harvesting are typically carried out countercurrently and cocurrently to the bulk ICS flow, respectively, with both ECS ports open, although other configurations are also used. More information on the biological and engineering foundations of HFBR cell culture will be provided in section 1 of chapter 2, with section 2.1.3 focusing specifically on the details of bioreactor operation and the different phases of the culture.

<sup>1</sup> The English physiologist Ernest H. Starling, 1866-1927, studied the analogous fluid exchange between body tissues and blood vessels (Starling 1896).

The promises and challenges of cell cultivation in HFBRs have encouraged a great deal of modelling work. Early HFBR models usually included the kinetics of low-molar-mass (low-MM)<sup>2</sup> substrate consumption and neglected convective transport in the membranes and in the ECS (Rony 1971, Waterland et al. 1974, Kim and Cooney 1976, Webster and Shuler 1978, Davis and Watson 1986, Piret and Cooney 1991, Jayaraman 1993). Many of the subsequent experimental (Waterland et al. 1975, Heifetz et al. 1989, Piret and Cooney 1990b) as well as theoretical studies (Kleinstreuer and Agarwal 1986, Schonberg and Belfort 1987, Salmon et al. 1988, Kelsey et al. 1990) recognised the importance of ECS convective transport in HFBR operation. More recent models developed in our research group additionally accounted for the effect of osmotic pressure due to protein rejection by the membranes, which was found to be one of the crucial factors influencing protein distribution in the ECS (Taylor et al. 1994, Patkar et al. 1995, Łabęcki et al. 1996, 1998, Koska et al. 1997).

Previous theoretical analyses of HFBR fluid flow and protein transport are presented in section 2.2, which is divided into two parts covering two distinct modelling approaches. Section 2.2.1 is concerned with Krogh cylinder models (KCMs), which are based on the assumption that the fluid flow and mass transfer phenomena in the HFBR can be analysed using a representative single fibre unit, the so-called Krogh cylinder.<sup>3</sup> Limitations of this assumption in the presence of transverse pressure or concentration gradients in the bioreactor stimulated the development of the porous medium model (PMM), which was part of this author's Master's project (Łabęcki 1994). The PMM domain was defined around the entire bundle of fibres, rather than a single fibre only, thus providing a more realistic description of the HFBR. The early work using this modelling approach is discussed in section 2.2.2.

The main objective of this thesis was to develop and validate experimentally a comprehensive mathematical model of protein transport in hollow-fibre membrane devices. Underlying this task was a strong belief that a good understanding of protein behaviour in

---

<sup>2</sup> The more precise term *molar mass* (MM) will be used throughout this thesis instead of the commonly encountered *molecular weight* (MW). The MM (or MW) for a macromolecular solute is normally expressed in kilodaltons (kDa), equivalent to kg/mol.

<sup>3</sup> The Danish physiologist August Krogh, 1874-1949, introduced a similar approximation in his studies of capillary blood flow in muscles (Krogh 1919). For his work in this field, Krogh won the 1920 Nobel prize in physiology/medicine.

the bioreactor – whether the proteins of interest are growth factors<sup>4</sup>, growth inhibitors, or useful products – is critical to the success and efficiency of the culture. The project has been divided into several parts, each addressing a different aspect of protein transport in the HFBR. Ultimately, these parts could be combined into a single “supermodel”, but such a task exceeds the scope of this thesis. A study of transmembrane protein leakage in closed-shell cartridges, using a one-dimensional KCM approach with an extension that accounts for the ECS manifolds, is described in chapter 3. The following chapter 4 discusses example open-shell processes that were simulated using a two-dimensional PMM.

In the presence of recirculation flow through the ICS of a closed-shell HFBR, forced convection normally dominates the ECS protein transport and causes downstream polarisation of the concentration field. The resulting ECS fluid density gradients may trigger natural-convective flows that can significantly contribute to protein redistribution. These phenomena were investigated using a three-dimensional PMM formulation that accounts for variable density and viscosity in the ECS as well as allowing a more advanced analysis of ECS manifold effects. Chapter 5 discusses the most important results of these studies. Overall conclusions and recommendations for future work on HFBRs are included in the closing chapter 6.

---

<sup>4</sup> In cell culture, growth factors are usually defined as highly specific proteins required for cell growth (Alberts et al. 1994, p. 893), although a broader definition used in physiology and medicine also includes vitamins and minerals (*Stedman's Medical Dictionary*, 27<sup>th</sup> ed., s.v. “growth factors”). In this thesis, the term *growth factors* or *growth-factor proteins* will normally be used in the former meaning.

## Chapter 2

### BACKGROUND AND PREVIOUS WORK

The objectives of this chapter are twofold. The first is to provide the fundamental background necessary to understand the various factors and challenges of hollow-fibre cell culture, emphasising the importance of proteins in the bioreactor operation. The second objective is to illustrate the evolution of the models of hydrodynamics and protein transport in HFBRs, leading to the research described in this thesis. The organisation of the chapter follows the same structure, with the biological and engineering background given in section 2.1, and the previous modelling work outlined in section 2.2.

#### 2.1. Hollow-Fibre Mammalian Cell Culture

##### 2.1.1. The Cells

###### 2.1.1.1. *Cell Types*

Mammalian cell lines<sup>5</sup> are typically derived from either epithelial or connective tissue (Butler 1987, p. 5). The first group includes, for example, the Chinese hamster ovary (CHO) cells, used extensively for the production of recombinant proteins; and HeLa (human cervical cancer cells), used mostly in research. The second group includes fibroblasts, isolated from the connective tissue proper, as well as cells obtained from blood or lymph fluids, such as lymphocytes. Important examples of fibroblast cell lines are the baby hamster kidney (BHK) cells, used for the production of clotting factors and veterinary vaccines; Vero cells (African green-monkey kidney cells), used for the production of polio vaccine; and a family of cell lines (e.g., MRC-5) derived from embryonic human lung and used for

---

<sup>5</sup> A cell line can be defined as a culture of cells propagated by periodic reseeding into a fresh vessel, or subculturing, which leads to the establishment of a uniform population with high growth capacity (Freshney 1994, p. 6).

the production of various human vaccines. A comprehensive summary of different animal cell lines can be found in chapter 1 of Butler and Dawson (1992). Non-modified epithelial and fibroblast cells are anchorage-dependent, i.e., they require a surface substratum for attachment and growth; while cells derived from the body fluids are anchorage-independent. Under standard culture conditions, many anchorage-dependent cells grow in adherent monolayers, which makes them suitable for cultivation in systems having large ratios of surface to volume, such as hollow fibres, provided a suitable membrane material has been selected or the fibres have been precoated to facilitate cell attachment (Griffiths 1986, 1990).

Since cells can only be propagated for a limited number of generations, it is usual for the cells used for protein production in bioreactors to be transformed into continuous cell lines (Freshney 1994, p. 12). This is achieved either by genetic modification or by deriving the cells from neoplastic (tumour) tissues. Compared with non-modified cells, transformed cells are immortal and tumourigenic, exhibit higher growth rates, have less complex medium requirements, and may partly or completely lose their anchorage-dependence (Butler 1987, p. 8; Freshney 1994, chapter 15). Genetic modification, whose purpose is to enhance the low protein yields of normal human cells, can be carried out using recombinant DNA technology, leading to recombinant cell lines; or by hybridisation, which gives rise to hybridomas (Cartwright 1994, p. 11). The first hybridoma cell line capable of continuous secretion of a single type of antibody to a specific antigen was produced by Köhler and Milstein (1975), who fused short-living B-lymphocytes (from mouse spleen), which produce the antibody, with myelomas, which are immortal tumour cells. This technique has since been improved to obtain more stable and more productive cell lines (Merten 1989, Kitano et al. 1989, McCullough and Spier 1990), and the cultivation of hybridomas for the production of monoclonal antibodies has become one of the leading HFBR applications.

#### 2.1.1.2. *Extracellular Matrix*

Many types of mammalian cells in culture, especially fibroblasts, synthesise and deposit some form of extracellular matrix (ECM). Transformation usually decreases ECM production by the cells and reduces their anchorage-dependence. The major constituents of ECM are collagens, forming insoluble protein fibrils; glycoproteins (e.g., fibronectin, laminin), containing a protein moiety with carbohydrates attached to it; and proteoglycans,

composed predominantly of a polysaccharide known as glycosaminoglycan, which is bound to a core protein (Barnes 1984). Owing to their net negative charge, the glycosaminoglycan molecules are able to bind cations as well as large amounts of solvation water and thus act as shock absorbers in connective tissues (Gartner and Hiatt 1997, p. 60).

Flow through several types of solid tissues, both *in vivo* and *in vitro*, was found to obey a linear relationship between the flow rate and the applied pressure gradient, and the tissue hydraulic permeabilities correlated with the glycosaminoglycan contents (Swabb et al. 1974). A comprehensive study by Levick (1987) demonstrated, however, that the ECM resistance to fluid flow arises from the combined effects of collagen fibrils, glycosaminoglycans, and the proteoglycan core proteins, and that none of the ECM components alone could account for the low hydraulic permeabilities of most tissues. A dramatic effect of ECM on convective flow in hollow-fibre bioreactors was observed by Ryll et al. (1990), who reported extreme difficulties in product removal from an ECS packed with BHK cells. Although high densities similar to those of solid tissues *in vivo* are often observed in hollow-fibre cultures (Knazek 1974; Freshney 1994, p. 363; Marx et al. 1994), problems with product recovery have not been encountered in the case of hybridomas or other cell lines which are not expected to produce ECM (Ryll et al. 1990). This is consistent with the observation that the drag effect of the cells, estimated from the Carman-Kozeny equation by treating the tissue as a porous bed in which the cells are impervious obstacles, contributes only negligibly to the interstitial hydraulic resistance measured in the presence of ECM (Levick 1987).

#### 2.1.1.3. *Growth Requirements*

##### *Oxygen, nutrients, and metabolites*

One of the most important factors affecting cell growth is the availability of nutrients and oxygen. The nutrients required in mammalian cell culture include carbohydrates, amino acids, lipids, fatty acids, vitamins, salts, and trace elements (Mather and Tsao 1990). Oxygen, glucose, and glutamine are of paramount importance because of their high demand by the cells. For both oxygen and glucose, the approximate range of uptake rate by mammalian cells has been reported to be  $0.053\text{-}0.59 \times 10^{-9}$  mmol/(cell·h) (Fleischaker and Sinskey 1981), while glutamine is utilised 3-4 times more slowly (Adamson et al. 1987,

Davis et al. 1991), but 5-10 times faster than any other consumed amino acid (Thomas 1990). There often exists a substrate level that is optimal for cell growth, which may be different from the optimal level for product generation. For example, several studies have found the optimum dissolved oxygen (DO) tension for hybridoma growth to be 50-60% of air saturation, with maximal MAb secretion occurring at a DO of 25% (Reuveny et al. 1985, Ryan et al. 1994).

Adequate oxygen delivery has raised particular concern owing to the constraints imposed by its low solubility in water (0.22 mmol/L at 37°C in equilibrium with atmospheric air) and potential toxicity at hyperbaric concentrations (Kilburn and Webb 1968). Unlike that of most other low-MM substrates, the supply of O<sub>2</sub> cannot therefore be enhanced by simply adjusting its concentration in the medium to a higher level. At the high cell densities typically encountered in HFBRs, oxygen depletion can easily become a problem if the system is not properly designed; for example, if the fibres are packed too sparsely, or if the ICS flow rate is too low. Indeed, several theoretical (Heifetz et al. 1989, Heath and Belfort 1987) as well as experimental (Piret et al. 1991) studies identified oxygen as the most important limiting substrate in hollow-fibre cultures. Other investigators also confirmed that glucose and glutamine should not become limiting as long as their concentrations are maintained at sufficiently high levels (Glacken et al. 1988, Schneider and Lavoix 1990, Handa-Corrigan et al. 1992).

The types of metabolic end-products and their potential inhibitory effect on mammalian cell growth depend strongly on the cell line, medium composition, and other culture conditions (Piret and Cooney 1990a). The most abundant metabolites are lactic acid, ammonium, and carbon dioxide, but the cells can also produce alanine, glutamic acid, or other amino acids (Thomas 1990). A sodium lactate concentration of 10 mmol/L was reported to inhibit the growth of Ehrlich ascites tumour cells by about 50%, and lactate buildup in the hollow-fibre culture of these cells became inhibitory to growth even before oxygen was limiting (Chresand et al. 1988). On the other hand, CRL-1606 hybridomas were virtually unaffected by lactate concentrations up to 40 mmol/L (Glacken et al. 1988). Nutrient depletion and metabolite accumulation did not impair growth or antibody production of the same hybridoma cell line in HFBRs (Piret et al. 1991).

Concern about diffusional limitations in the ECS of hollow-fibre bioreactors, due to insufficient rates of substrate delivery or metabolite removal, stimulated work on the feasibility of convective enhancement of these transport processes (Brotherton and Chau 1996). To that end, alternative HFBR designs were proposed, such as a dual-circuit system with two fibre bundles operated at different pressures (Wei and Russ 1977, Gullino and Knazek 1979), a cross-flow flat-bed reactor (Ku et al. 1981), or a radial-flow cartridge with a central feed distributor (Tharakan and Chau 1986a, 1986b) (see also section 2.1.3.5 below). ECS convective flow was also predicted to have a marked influence on the behaviour of low-MM solutes in an experimental bioreactor composed of two concentric hollow-fibre membranes (Salmon et al. 1988). A theoretical study by Pillarella and Zydney (1990) demonstrated that ECS convection could play a significant role in establishing the desired insulin response in a hollow-fibre bioartificial pancreas, where insulin-producing beta cells were cultured as monolayers on the surface of the fibres. In such devices, however, substrate consumption is relatively low because of the small cell numbers involved. In conventional closed-shell HFBR systems under standard operating conditions, the Peclet numbers for transmembrane and ECS transport of low-MM solutes can be estimated to be less than 0.01, which indicates a negligible role of convection (Piret and Cooney, 1990a, 1991).

#### *Serum supplementation*

Mammalian cells have traditionally been cultivated in media containing approximately 10% foetal bovine serum (FBS), a rich source of nutrients and growth-factor proteins such as albumin, transferrin, insulin, or interleukins (Jäger 1991). The benefits of using serum are numerous and include protection against pH fluctuations (buffering capacity), neutralisation of toxins such as heavy metals, protease inhibition, and protection against shear forces (Cartwright 1994, p. 43). Its drawbacks include undefined composition; lot-to-lot variation; high cost; potential cytotoxicity; risk of contamination by viruses, prions, or mycoplasma; and complication of downstream processing. A vast amount of research has been devoted to the formulation of serum-free or protein-free media (Maurer 1986, Brown 1987, Schneider and Lavoix 1990, Wyatt 1994), although the process of cell adaptation to such conditions may often be time-consuming. Several studies have reported

on the successful use of serum-free media in the production of monoclonal antibodies in HFBRs (von Wedel 1987, Schönherr and van Gelder 1988, Heifetz et al. 1989, Ryll et al. 1990, Davis et al. 1991, Dhainaut et al. 1991). Despite the confinement of many serum components to the ECS of the hollow-fibre reactor, supplementation of the ICS medium is often necessary to compensate for partial leakage of lower-MM growth factors through the membranes (Gramer and Poeschl 1998). Various aspects of serum-supplemented and serum-free animal cell culture have been discussed, for example, by Freshney (1994, p. 91), Jäger (1991), and Maurer (1986).

#### *pH and temperature*

The culture performance is very much dependent on the proper setting and control of pH and temperature. The optimal pH range for mammalian cells is approximately 7.0-7.4; pH values below 6.8 usually inhibit cell growth (Griffiths 1986), although they may increase specific antibody production (Miller et al. 1988, Handa-Corrigan et al. 1992). Some hybridoma cells have been able to adapt to elevated pH; for example, Sp2/0-derived mouse hybridomas were cultivated at pH 7.7, eventually reaching growth and antibody production rates similar to those at optimum (lower) pH levels (Miller et al. 1988). Variations in pH are expected to occur naturally in the culture as a result of cell metabolic activity, such as glucose consumption leading to the formation of lactic acid. In order to avoid accumulation of acidic metabolites, it has been recommended that glucose concentrations in the media be maintained at low levels (below 2 g/L) (Griffiths 1986).

Selection of a proper buffering system is another important factor in cell culture. For example, pH gradients existing in a hollow-fibre culture of hybridoma CRL-1606 cells were shown to decrease when the commonly used CO<sub>2</sub>-bicarbonate buffer was replaced by HEPES (*N*-2-hydroxyethylpiperazine-*N'*-2-ethane sulphonic acid) (Piret et al. 1991). The major strategies used to control pH in HFBRs are: adjustment of the amount of CO<sub>2</sub> delivered with the air through the oxygenator, addition of a base (NaHCO<sub>3</sub> or NaOH) to the culture medium, or variation of the medium supply rate (Andersen and Gruenberg 1987, Handa-Corrigan et al. 1992). However, the main challenge lies not in the regulation of pH level in the ICS medium, but in the minimisation of local pH gradients in the ECS, especially in the presence of mass transfer limitations that may arise at high cell densities.

The magnitude of these local gradients can be roughly estimated from the difference between the measured pH values of the ECS and ICS samples (Piret et al. 1991), but the actual pH distribution within the extracapillary space is much more difficult to determine.

The optimal cultivation temperature for most mammalian cells is 36-37°C (Freshney 1994, p. 101). It is especially important to avoid hyperthermic conditions, as temperatures in excess of approximately 2°C above optimal result in rapid cell death. While primary cell metabolism and growth are negatively affected by thermal variations, thermal shock (within reasonable limits) may enhance protein production (Wurm et al. 1986, Glacken et al. 1988, Kretzmer et al. 1998). In some cases, thermal degradation of the product proteins may be attenuated at lower temperatures, thus leading to improved product characteristics (Mather and Tsao 1990). The temperature, as well as the pH and medium composition, can also affect the stability of some nutrients. For example, glutamine has been known to undergo a relatively rapid (half-life of several days) chemical decomposition at 37°C (Ozturk and Palsson 1990). Minor temperature variations that may be caused by nonuniform heating or fluctuations within the control range should have a negligible effect on transport phenomena in the HFBR (2% changes in water viscosity and solute diffusivities and 0.04% changes in water density per 1 K of temperature change near 37°C).

### 2.1.2. The Membranes

#### 2.1.2.1. *Materials*

The membrane material and properties play an important role in HFBR operation and can have a significant effect on the protein behaviour in the bioreactor. The two most common membrane materials used in HFBRs are cellulose and its derivatives (Knazek 1974, Andersen and Gruenberg 1987, Tyo et al. 1988, Ryll et al. 1990, Lowrey et al. 1994, Jackson et al. 1996, Gramer and Poeschl 1998) and polysulphone (Knazek 1974, Ku et al. 1981, Altshuler et al. 1986, Tharakan and Chau 1986a, 1986b, Piret and Cooney 1990b). Membranes employed in hollow-fibre cell culture have also been made of poly(methylmethacrylate) (PMMA) (Lowrey et al. 1994), poly(vinyl chloride)-acrylic copolymer (Knazek 1974, Ku et al. 1981), and polyacrylonitrile (PAN) (Ku et al. 1981). HFBRs equipped with PMMA membranes were reported to support exceptionally high

growth of Vero cells and MAb production by hybridomas (Lowrey et al. 1994). Membranes used for cultivation of anchorage-dependent cells may require precoating with materials promoting adhesion, such as poly-D-lysine (Tharakan and Chau 1986a, Tyo et al. 1988).

Cellulose is a highly hydrophilic, mechanically strong material, used to manufacture fairly thin (5-10  $\mu\text{m}$ ) isotropic membranes (Schönherr and van Gelder 1988) having relatively small pores and low hydraulic permeabilities. In contrast to isotropic membranes, asymmetric (or anisotropic) membranes consist of a thin (1-2  $\mu\text{m}$ ) ultrafiltration skin and a thick (50-75  $\mu\text{m}$ ) spongy support layer. They are usually made of polysulphone or another hydrophobic polymer and have higher hydraulic permeabilities (Schönherr and van Gelder 1988, Radovich 1995). Cellulose-based membranes exhibit low affinity for protein adsorption and low cytotoxicity, which makes them suitable for applications such as mammalian cell culture or haemodialysis (Lysaght 1995).

Cuprophane, or regenerated cellulose, in its dry form possesses relatively high crystallinity ( $\sim 50\%$ ), but can become amorphous and swollen upon sorption of water (Filho and Bueno 1992). A manifestation of this morphological change is radial and axial expansion of Cuprophane fibres under wet conditions, usually by about 10% (Patkar et al. 1995). Since the fibres are fixed at both ends of the HFBR cartridge (see fig. 1), their elongation leads to the formation of local pockets and channels within the fibre bundle, which increases the ECS heterogeneity (Łabęcki et al. 1995). Cellulose acetate (CA) is obtained by acetylating (i.e., substituting H- with  $\text{CH}_3\text{CO}-$ ) approximately 80% of the hydroxyl groups in cellulose, while cellulose triacetate (CTA) is completely acetylated. Hemophane is another cellulose derivative, in which a fraction ( $< 1\%$ ) of the hydroxyl groups are replaced with  $(\text{CH}_3\text{CH}_2)_2\text{N}-\text{CH}_2\text{CH}_2-\text{O}-$  (diethylaminoethoxyl) (Radovich 1995). Compared with Cuprophane, the Hemophane, CA, and CTA membranes are less hydrophilic, and usually have slightly larger pores and higher permeabilities (Lysaght 1995).

#### 2.1.2.2. *Permeability Properties*

In a general sense, a coefficient of membrane permeability to solutes or water expresses proportionality between the transmembrane flux and the corresponding driving force. For example, the diffusive permeability, which has a unit of length/time, is defined as the ratio of diffusive solute flux and concentration difference across the membrane.

However, a fair amount of confusion appears to exist in the membrane literature as to a consistent definition of the hydraulic permeability,  $L_p$ . For example, Mulder (1991) once describes  $L_p$  as a negative ratio of the flux and pressure gradient (ibid, p. 12), which yields a unit of  $\text{length}^2 \cdot \text{time}^{-1} \cdot \text{pressure}^{-1}$ , while another time assigning to it a unit of  $\text{mass} \cdot \text{time}^{-1} \cdot \text{pressure}^{-1} \cdot \text{length}^{-2}$  (ibid, p. 354). More commonly,  $L_p$  is understood to be the proportionality coefficient between the fluid flux and pressure difference, which has a unit of  $\text{length} \cdot \text{time}^{-1} \cdot \text{pressure}^{-1}$  (Kedem and Katchalsky 1958, Kessler and Klein 1992). Unfortunately, none of the above definitions of  $L_p$  separates out the viscosity, thus lumping into one parameter properties of both the membrane and the fluid.<sup>6</sup> In this thesis, the membrane hydraulic permeability is more rigorously defined as

$$L_p = \frac{J_{TMF} \mu}{\Delta P_m} \quad (1)$$

where  $J_{TMF}$  is the transmembrane fluid flux,  $\mu$  is the fluid viscosity, and  $\Delta P_m$  is the effective transmembrane pressure difference, which includes both hydrostatic and osmotic contributions. According to the above equation, mentioned also by Zeman and Zydney (1996, p. 299),  $L_p$  is strictly a membrane property and has a unit of length. The approximate range of hydraulic permeabilities for hollow-fibre membranes of interest here is  $10^{-16}$  -  $10^{-12}$  m, the lower value marking roughly the boundary between reverse-osmosis and ultrafiltration membranes, and the higher between ultrafiltration and microporous membranes. Section 3.2.2.3 below will introduce other parameters used in this work to describe transmembrane transport of fluid and proteins.

Although microporous membranes have been used in hollow-fibre cell culture (Brown et al. 1985, Brotherton and Chau 1995, Kessler et al. 1997), the standard HFBR system employs ultrafiltration membranes, which are partly or completely impermeable to most proteins. A parameter frequently used to indicate the expected degree of solute rejection by ultrafiltration membranes is the so-called molar mass cutoff, conventionally referred to as the molecular weight cutoff (MWCO). It is generally accepted that the MWCO

---

<sup>6</sup> An unfortunate consequence of this practice is that the hydraulic permeability so defined varies with temperature – in the same way as does the fluid viscosity – which greatly complicates comparisons of  $L_p$  values quoted in different sources (since many authors do not specify the temperature).

is defined in a nominal sense as the critical molar mass (MM) of a solute that is 90% rejected by the membrane (Mulder 1991, 131; Kulkarni et al. 1992).<sup>7</sup> Unfortunately, the concept of MWCO can be misleading, especially when the solute in question is a protein. Firstly, the above definition does not specify the precise conditions of the solute rejection test. Secondly, it is the size of the molecules rather than their mass that determines the extent of rejection. Thirdly, MWCO values for most membranes are determined using rejection data for dextrans, whose molecules – random uncharged coils – differ in shape and properties from protein molecules – mostly globular polyelectrolytes (Zeman and Zydney 1996, p. 13). Indeed, leakage of proteins through membranes having a MWCO significantly lower than the protein MM has been observed. For instance, transferrin (MM = 77 kDa) passed through a 30-kDa cutoff membrane (Patkar et al. 1995), while immunoglobulin G (IgG, MM = 155 kDa) leaked through a 70-kDa cutoff membrane (Evans and Miller 1988).

The membrane MWCO (or pore size) can have a strong impact on the performance of a hollow-fibre cell culture. It has been observed that cell lines which grow poorly in cartridges with highly permeable (including microporous) membranes can grow well in modules with less-permeable membranes (MWCO  $\leq$  10 kDa) and vice versa (Kidwell et al. 1989). These contrasting results may be related to the differences in the type and size of positive and negative regulatory proteins secreted by the cells or supplied with the medium. Accumulation in the ECS of growth inhibitors such as transforming growth factor beta (TGF- $\beta$ , MM = 30 kDa) can lead to declines in cell growth and antibody production (Kidwell et al. 1989), while accumulation of autocrine growth factors can improve the culture performance. In the former case, the use of high-MWCO membranes may thus be preferred to maximise the leakage of growth inhibitors to the ICS; while in the latter case, low-MWCO membranes should be selected to retain the growth factors in the ECS. Improved IgG productivities in HFBRs with high-MWCO membranes were observed, for example, by Altshuler et al. (1986) and by Evans and Miller (1988).

---

<sup>7</sup> Conventionally, the nominal MWCO is used with reference to ultrafiltration membranes, while microporous membranes are characterised using the nominal pore size (NPS). The nominal, as opposed to absolute, rating indicates that only a certain percentage, rather than all, of the molecules with a given or larger size or MM will be retained by the membrane. The approximate NPS ranges for microporous and ultrafiltration membranes are 0.05-10  $\mu$ m and 1-100 nm, respectively (Zeman and Zydney 1996, p. 13).

The use of high-MWCO membranes may, unfortunately, lead to some negative side-effects. These include: (1) protein denaturation due to their oxidation at the air-liquid interface (especially in the oxygenator and in the ICS recycle reservoir, see section 2.1.3.1 below) (Łabęcki et al. 1998) or to the shearing action of the ICS pump (Meireles et al. 1991); (2) increased medium cost because of the dilution of serum or expensive protein additives in the ICS recycle volume, usually 1-2 orders of magnitude larger than the ECS volume; and (3) lower product concentrations because of its dilution in the ICS recycle volume. If a high-MWCO membrane is the preferred choice for a particular cell line, then the use of serum- or protein-free media may help alleviate some of these problems. The vast majority of hollow-fibre cartridges used for cell culture at the present time utilise ultrafiltration membranes having MWCOs of 10 or 30 kDa (Ryll et al. 1990, Handa-Corrigan et al. 1992, Lowrey et al. 1994, Jackson et al. 1996, Gramer and Poeschl 1998).

#### 2.1.2.3. *Concentration Polarisation and Fouling*

The phenomenon of membrane fouling and the formation of a concentration polarisation boundary layer are often of concern in ultrafiltration processes as they usually cause a decline of transmembrane fluid and solute fluxes. The extent of radial concentration polarisation on the lumen and shell sides of hollow-fibre membranes at the microscopic scale (not to be confused with the macroscopic downstream or downward polarisation phenomena mentioned earlier) can be assessed using the stagnant film theory (Blatt et al. 1970), modified for dialysis-type systems by Zydney (1993). Using this theory, it can be estimated that protein polarisation on low-permeability membranes in closed-shell HFBRs under typical operating conditions should be negligible (Łabęcki et al. 1998). However, the same conclusion may not be true in the presence of large transmembrane fluid fluxes, such as in some open-shell operations or in systems with highly permeable membranes. The stagnant film theory represents a fairly idealised picture of mass transfer in a hollow-fibre reactor; a more rigorous approach should include a two- or three-dimensional fluid flow and protein transport analysis for both the ICS and ECS as well as hindered protein transport through the membranes. An additional modelling challenge is associated with flow heterogeneities and hence fibre-to-fibre variations in mass transfer conditions which can be

expected to exist in real HFBR systems (Hammer et al. 1990, Laukemper-Ostendorf et al. 1998).

In cell culture HFBRs, two major factors may contribute to the fouling of the membranes: (1) pore blockage by cell debris, and (2) adsorption of proteins, often accompanied by their denaturation. The former factor is more likely to play a role at higher cell densities in the later stages of the culture and will not be considered here in further detail. Protein adsorption can take place on the surface of fully retentive membranes or on the pore walls of semipermeable membranes (Zeman and Zydney 1996, p. 409; Meireles et al. 1991). Substantial amounts of proteins and cell debris can accumulate in the spongy support matrix of asymmetric membranes. The extent of adsorption usually exhibits a maximum near the protein's isoelectric point. This can be explained by the fact that the globular protein molecule needs fewer sites for adsorption when its net charge is smaller; and that the repulsive interactions among the adsorbed molecules are lowest when the protein is electrically neutral (Lee and Ruckenstein 1988). In some cases, protein molecules can adsorb on a surface having the same-sign charge, namely by adopting an orientation in which the charge-carrying groups are away from the surface (Zeman and Zydney 1996, p. 410).

It has been noted by many investigators that the adsorption of proteins is more pronounced on more hydrophobic surfaces (Lee and Ruckenstein 1988). This is related to the energetically favourable displacement of water molecules from the hydrophobic surface to the bulk of the solution, where they can participate to a greater extent in hydrogen bonding and dipole interactions; as well as to the attractive van der Waals interactions between the membrane surface and the hydrophobic groups of the protein molecule (Norde 1986). About an order of magnitude larger amounts of bovine serum albumin (BSA) were found to adsorb on polysulphone and polyamide membranes, compared with less hydrophobic CA membranes (Matthiasson 1983), while another study reported no detectable adsorption of BSA and transferrin on hydrophilic regenerated-cellulose membranes (Patkar et al. 1995). The extent of adsorption can be very different on membranes differing in morphology (e.g., in surface roughness), even if they are made of the same polymer (Matthiasson 1983, Chen et al. 1995). Extensive theoretical studies of protein adsorption on

synthetic membranes were carried out, for example, by Zydney and coworkers (Mochizuki and Zydney 1993, Langsdorf and Zydney 1994).

Adsorption of proteins usually leads to a reduction of the membrane hydraulic and diffusive permeabilities, and hence to a decline in the magnitude of transmembrane fluxes and ECS Starling flow. A fourfold decrease in the  $L_p$  value of hollow-fibre polysulphone membranes as a result of BSA adsorption was observed by Patkar et al. (1995). An important consequence of protein adsorption in HFBR cell culture may be growth slowdown due to the depletion of growth factors from the ECS medium. This may be of particular concern for those proteins which are present at low concentrations. For example, more than 99% of the transferrin introduced into the ECS was found to adsorb to polysulphone hollow fibres within 2 h (Patkar et al. 1995). This problem could be partly overcome by adding to the ECS an excessive amount of a relatively inexpensive protein such as BSA, which competitively blocked the nonspecific adsorption sites (Brotherton and Chau 1995, Patkar et al. 1995).

### 2.1.3. Bioreactor Operation

#### 2.1.3.1. *Conventional System Setup*

The setup of a conventional HFBR cell culture system is shown schematically in fig. 2. The ICS medium is recirculated through the bioreactor cartridge 1, the oxygenator 2, and the medium reservoir 3, using the recycle pump 5. The oxygenator is normally placed downstream of the bioreactor to avoid air release in the cartridge and to allow air bubbles possibly carried by the recycle stream to be trapped in the reservoir 3. The sampling port 4 enables off-line monitoring of the pH, oxygen, nutrient, and metabolite levels in the recycle stream, although commercial systems are often equipped with probes and control units to maintain the setpoint levels of temperature, pH, and  $O_2$ . The ICS medium is periodically replenished using the feed pump 6, and the waste medium is collected in the reservoir 10. The ECS content is intermittently harvested from the downstream ECS port into the collector 12 using the harvesting pump 13, which simultaneously delivers through the other ECS port the fresh growth medium from reservoir 11. Typically, the HFBR cartridge is inclined at about  $45^\circ$  to the horizontal, with the ICS flow directed upward; such a

configuration is expected to reduce the undesirable effects of downstream protein polarisation and cell sedimentation (see also sections 5.5.1 and 5.5.2.1 for more details on the effect of inclination angle).

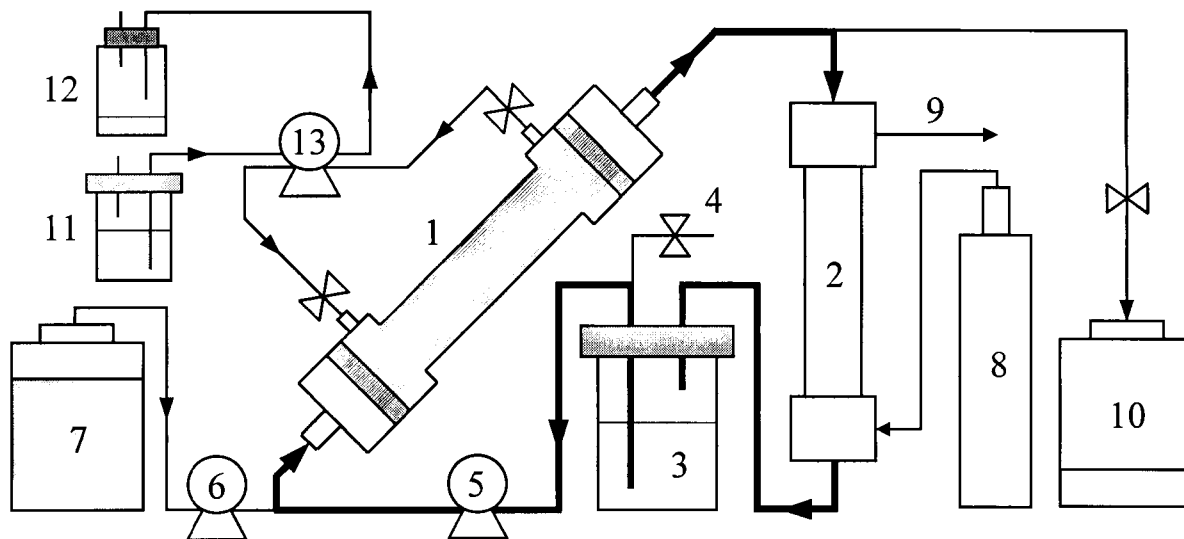


Fig. 2. Conventional HFBR system configuration (components not to scale):  
 1, HFBR cartridge; 2, oxygenator; 3, ICS recycle medium reservoir; 4, ICS sampling port;  
 5, ICS recycle pump; 6, ICS feed pump; 7, fresh ICS medium reservoir; 8, air cylinder;  
 9, waste gas outlet; 10, waste ICS medium reservoir; 11, fresh ECS medium reservoir;  
 12, harvest collector; 13, harvesting pump.

#### 2.1.3.2. Inoculation

After initial propagation in batch culture (e.g., in T-flasks, shake flasks, or spinners), the cells suspended in growth medium are introduced into the ECS of the bioreactor. This procedure is called inoculation and can be carried out in various flow configurations, examples of which are shown in fig. 3. In the standard, countercurrent arrangement (fig. 3a), the inoculum is introduced through the downstream ECS port, while the reactor is continuously perfused via a lumen recycle flow. The dead-end configuration (fig. 3b) can be used instead to increase the initial concentrations of cells and high-MM growth factors by filtering out some of the medium through the membranes. Cross-flow inoculation (fig. 3c) is similar to the dead-end mode, but has the advantage of uninterrupted oxygen delivery to the

ECS by the lumen-side perfusion flow. A sufficient number of cells must be present in the ECS at the end of inoculation; typically, cell concentrations greater than  $10^6$  cells/mL are required to effect a successful startup of the culture. It has been reported that a higher cell-number inoculum can shorten the time needed to reach the maximum level of antibody production (Evans and Miller 1988).

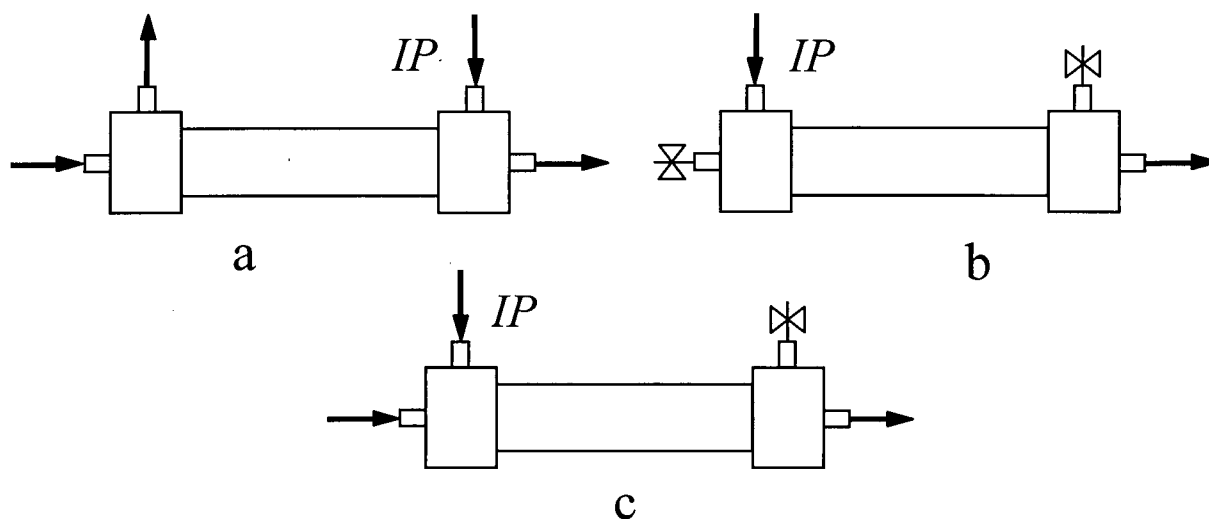


Fig. 3. Example flow configurations in the inoculation procedure: *a*, countercurrent (standard); *b*, dead-end; *c*, cross-flow; *IP*, inoculation port.

One of the major challenges of the inoculation procedure and of the initial stages of HFBR culture is to maximise spatial uniformity of cell growth in the ECS. This is not easy, considering that some of the cells usually settle by gravity to the bottom of the reactor and become trapped in the ECS manifolds, where they are susceptible to oxygen starvation. In order to remain viable, the cells must remain in close proximity to the oxygen source, i.e., to the hollow fibres, which excludes the possibility of their cultivation in fibre-free regions such as the manifolds. On the other hand, some of the inoculum may never leave the vicinity of the inoculation port, obstructed by the more densely packed regions of the fibre bundle (Sardonini and DiBiasio 1993). These problems can be partly alleviated by adjusting the inclination angle of the bioreactor or by periodically rotating the cartridge about its longitudinal axis. Nonetheless, system-specific optimisation of the inoculation procedure is

highly advisable to ensure efficient use of reactor space and hence increase the chance of successful startup of the culture.

#### 2.1.3.3. *Closed-Shell Operation*

##### *Cell growth*

After inoculation, a lag phase of several days usually occurs, during which the cells adapt to the new culture environment. Within the subsequent 2-4 weeks of exponential growth, the cells progressively fill up the ECS, until the cartridge walls restrain their further expansion. Over most of that period, the conditions in the ECS can still be regarded with good approximation as being essentially cell-free, i.e., the ECS hydrodynamic permeability and porosity are relatively unaffected by the presence of cells. The end of the exponential phase marks the onset of the stationary (or steady-state) period, in which the rates of growth and death are approximately equal (Butler 1987, p. 9; Pinton et al. 1994). The ECS cell densities at steady state can be as high as  $10^9$  cells/mL, which is equivalent to a bed of spheres having a diameter of 10  $\mu\text{m}$  each (i.e., the size of small mammalian cells) and packed to about 50% porosity. The hydraulic permeability of a cell-filled ECS can be 7-8 orders of magnitude lower than that at cell-free conditions (Koska et al. 1997), while the decrease in effective solute diffusivities can range from about 2-3 for small solutes like oxygen or glucose to more than 25 for proteins (Swabb et al. 1974). The stationary phase should theoretically continue indefinitely; in practice, an irreversible decline in overall cell viability is usually observed after 1-3 months of the culture. The shift to the death phase likely results from the excessive accumulation of dead cells, cell debris, and inhibitory factors (Kidwell et al. 1989), all of which are difficult to remove from the ECS in a steady and effective fashion.

##### *Starling flow and downstream polarisation*

The ICS flow rate,  $Q_L$ , is an important operating parameter which not only controls the rate of oxygen and nutrient delivery to the cells but also determines the magnitude of the ECS Starling flow in a closed-shell HFBR. The magnitude of Starling flow depends additionally on the membrane and ECS hydraulic permeabilities,  $L_p$  and  $k_S$ , which themselves are influenced by other factors, such as the cell density and the presence of ECM

( $k_s$ ), or the extent of membrane fouling ( $L_p$ ). It has been demonstrated that Starling flow can cause convective downstream polarisation of cells and proteins, leading to spatial heterogeneities in the ECS and thus compromising culture performance (Waterland et al. 1975, Piret and Cooney 1990b). The importance of convective transport of ECS cells and proteins in typical hollow-fibre modules (Piret and Cooney 1991, Łabęcki et al. 1998) under standard HFBR operating conditions can be estimated from an order-of-magnitude analysis. For a typical protein such as albumin, the axial ECS Peclet numbers are expected to be of the order of 10-1000, which indicates a negligible role of diffusion. For the cells, a comparison of the characteristic velocities associated with different modes of transport shows that convection and sedimentation should be 3-5 orders of magnitude more significant than Brownian diffusion, shear-induced diffusion, or inertial lift (Zeman and Zydney 1996, p. 415).

Convective polarisation of ECS proteins results in local elevations of osmotic pressure, fluid density, and fluid viscosity in the downstream part of the ECS. In the absence of free convection, the osmotic pressure increases locally until the total (i.e., hydrostatic minus osmotic) ECS pressure reaches the lumen-side pressure level. At this point, because of negligible transmembrane flow, the ECS fluid flow in the protein-rich region is practically shut down. Consequently, a stagnant zone develops downstream, and the effective axial length available to ECS convective flow decreases (Taylor et al. 1994). Under some conditions, fluid density gradients resulting from downstream polarisation can induce free-convective protein redistribution in the downward direction. For example, the combined effect of forced-convective downstream and free-convective downward polarisation of ECS proteins was observed in a horizontal HFBR (Piret and Cooney 1990b). See chapter 5 for an analysis and discussion of natural-convective phenomena in hollow-fibres cartridges.

#### 2.1.3.4. *Product Harvesting*

A well-designed harvesting strategy is important for an efficient and productive bioreactor operation, as it directly influences the ECS protein and cell distributions and determines the product concentration in the harvest. Unless significant quantities of the product are present in the lumen side as a result of leakage from the ECS, product recovery from the ICS recycle fluid is usually not undertaken. Examples of harvesting configurations

are shown in fig. 4. Most commonly, the product is collected from the ECS in a periodic (or batch) fashion, every 1-3 days, with closed-shell operation maintained between the harvest periods. The harvesting sequence is usually initiated at the beginning of the exponential phase of growth, i.e., long before the ECS becomes packed with cells. The downstream and downward convective polarisation phenomena can be used to help concentrate the product near the harvest port. To that end, measures such as a change in the HFBR cartridge orientation or a temporary increase in the ICS flow rate can be taken just before harvesting. Piret and Cooney (1990b) suggested also that the ICS flow direction might be alternated during the exponential phase of cell growth in order to homogenise the distributions of growth factors and cells in the ECS, while unidirectional flow and downward positioning of ECS ports should be maintained prior to harvesting or when steady-state production has been established. It should be noted that convective product polarisation may require considerably longer times in cell-packed HFBRs than it does in reactors operated at low cell densities (Koska et al. 1997).

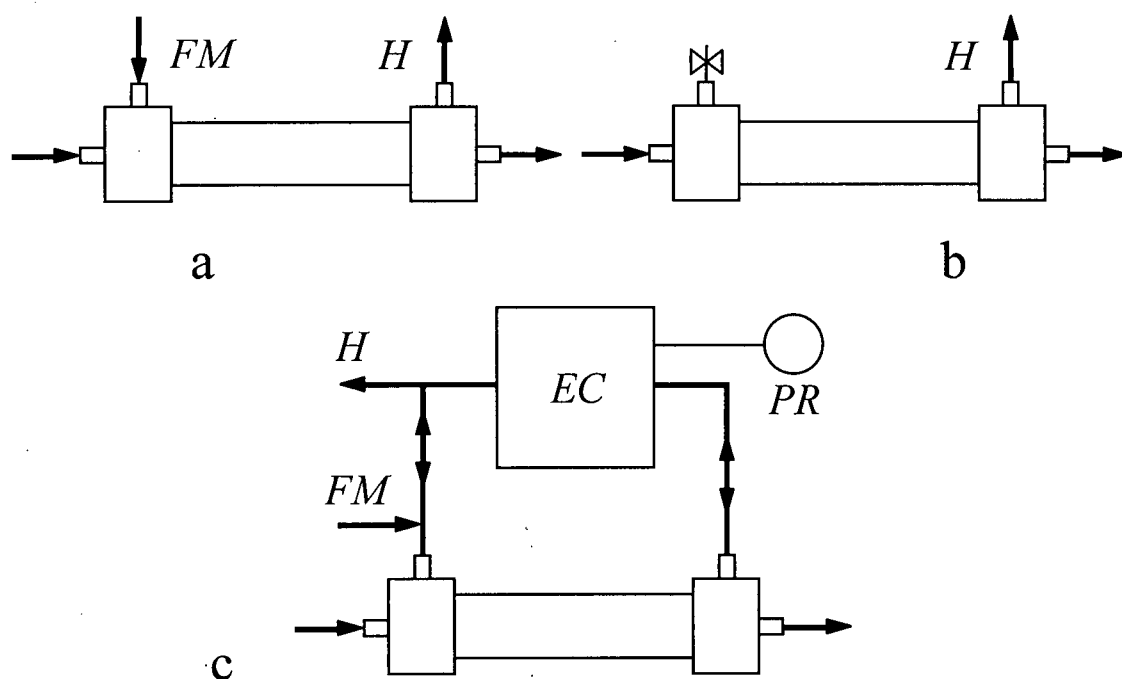


Fig. 4. Examples of HFBR harvesting configurations: *a*, cocurrent (standard); *b*, cross-flow; *c*, ECS fluid cycling through an expansion chamber (Acusyst); *H*, harvest outlet; *FM*, fresh medium intake; *EC*, expansion chamber; *PR*, pressure regulator.

The cocurrent flow configuration (fig. 4a) is a popular variant of batch harvesting, which takes most advantage of the downstream polarisation of the product and enables simultaneous replenishment of ECS medium. Owing to smaller pressure differences across the membrane and hence less short-circuiting of the harvesting flow through the fibre lumina, this configuration should yield a more complete product recovery than would the corresponding countercurrent process. Another option is the cross-flow mode (fig. 4b), although it is generally less practical because of potential medium degassing if a pump is used to withdraw the ECS fluid, or a decline in the ECS outlet flow with increasing cell density if the harvest is allowed to bleed out. If this configuration is used for harvesting, then the ECS medium can be replenished by using the cross-flow inoculation mode shown in fig. 3c. Some investigators (von Wedel 1987, Kessler et al. 1997) have pointed out the advantage of continuous harvesting in minimising product exposure to the degradative environment of the bioreactor (e.g., temperature, proteases, etc.). An example of continuous product harvesting and medium addition is a protocol developed by Cellex Biosciences (formerly Endotronics) and applied in their Acusyst system (Gramer and Keznoff 1998, Gramer et al. 1999). Here, the direction of medium flow between the ICS and the ECS is periodically changed by means of pressure regulators, and the excess ECS fluid is accommodated in an external expansion chamber, as illustrated in fig. 4c (see also the following section 2.1.3.5).

The efficiency of product recovery from the ECS is affected by a number of factors, such as the rate and configuration of harvesting flow, ECS cell density, degree of product polarisation, volume of harvest, and harvesting frequency (in batch protocols). Many of these operating parameters may require variation over time in order to accommodate the effects of variable cell density and changing growth conditions in the ECS. Variation of the ECS hydraulic permeability with time, ECS flow heterogeneities, complex influences of various polarisation phenomena, and a largely unknown product distribution prior to harvesting make the modelling of harvesting procedures a fairly challenging task.

#### 2.1.3.5. *Alternative HFBR Systems*

In the pursuit of higher bioreactor productivities and optimal conditions for cell growth, a number of operational modifications to the conventional HFBR system as well as

some alternative HFBR designs have been proposed (table 1). In spite of their ingenuity and potential for improved performance, each of these alternative systems also has its limitations. In many cases, for instance, the problem of cell maldistribution due to sedimentation has not been resolved. This difficulty could be addressed by fixing the cells within a collagen or agar gel matrix in the ECS (Chresand et al. 1988), but such a matrix could exclude much of the ECS volume otherwise available to the cells and also diminish harvesting efficiency because of its significant resistance to convective flow (Koska et al. 1997). Several alternative designs rely on the use of microporous membranes, thereby

Table 1. Examples of alternative HFBR systems

<b>Alternative configurations and operating modes</b>		
<b>System (reference)</b>	<b>Advantages</b>	<b>Disadvantages</b>
ICS flow cycling (Piret and Cooney 1990b, Patkar et al. 1995)	Improved homogeneity of cell and growth-factor distributions	Automated valve operation required for flow reversal and for product concentration prior to harvesting
Mass Culturing Technique by Bio-Response (Brown et al. 1985, von Wedel 1987)	Growth chamber rotation enabled uniform cell distribution; nonviable cells removed by cell drains; long-term productivity maintained	Depletion of growth factors leaking into the product removal loop; dilution of product as a result of using microporous membranes
ECS expansion chamber (Acusyst) by Cellex Biosciences (Andersen and Gruenberg 1987, Tyo et al. 1988, Gramer and Keznoff 1998)	Improved homogeneity of cell and growth-factor distributions; removal of dead cells and cell debris from the ECS	Cells subject to more shear than in closed-shell HFBRs; viable cells may be flushed out of ECS; product dilution in the ECS circuit volume; increased chance of membrane fouling due to high transmembrane fluxes; complex servomechanism
Countercurrent ECS flow circuit	Improved homogeneity of cell and growth-factor distributions; simple system	Viable cells may be flushed out if ECS flow rate too high; external ECS recycle volume should be small to avoid dilution of growth factors and products
Cells cultured in the ICS (Adema and Sinskey 1987, Nyberg et al. 1992)	Significant reduction of substrate and metabolite gradients; uniform cell growth	Dilution of growth factors and products in the recycle volume as a result of using microporous membranes; difficult removal of dead cell from inside the fibres

Table 1 – *continued*

<b>Alternative cartridge designs</b>		
System (reference)	Advantages	Disadvantages
Flat fiber-bed reactor (Ku et al. 1981)	Convection-enhanced nutrient delivery at low cell densities; independent oxygen delivery	Potential membrane fouling; limited possibility of product concentration; viable cells may be flushed out of ECS; cells on the downstream side may experience substrate limitations at cell-packed conditions
Radial-flow reactor with a central feed distributor (Tharakan and Chau 1986a, 1986b, 1987)	Convection-enhanced nutrient delivery at low cell densities; independent oxygen delivery	Potential membrane fouling; outermost cells away from the central distributor may experience substrate limitations at cell-packed conditions
Intercalated-spiral alternate-dead-ended reactor (Brotherton and Chau 1990, 1995)	Axially-uniform growth and high cell viability achieved; relatively easy to model, as axial flows are negligible	Membrane fouling due to protein gel deposit observed, therefore serum not recommended for this design; dilution of growth factors and product in the recycle volume as a result of using microporous membranes
Tecomouse by Integra Biosciences (Tzianabos and Smith 1995)	Uniform oxygenation; independent oxygen delivery	Little product concentration by downstream polarisation as a result of low flow rates
Tricentric reactor by Setec (Kessler et al. 1997)	Reduced downstream polarisation and growth-factor heterogeneities as a result of countercurrent flow	Dilution of growth factors and product in the recycle volume as a result of using microporous membranes

compromising some of the most attractive features of ultrafiltration hollow-fibre systems; viz., *in situ* product concentration and the confinement of expensive medium components to the relatively small volume of the ECS. It should be noted, nonetheless, that a meaningful comparison between the different HFBRs should ideally be based on a consistent study involving the use of the same cell line and similar culture conditions. Moreover, it is difficult to assess the commercial feasibility and competitiveness of the alternative systems without a detailed economic analysis including the costs of fabrication and downstream processing.

The simplest and most expedient improvements can be made to the systems that utilise the conventional HFBR cartridge shown in fig. 1. Examples of such modifications are given in the first part of table 1. The closed-shell HFBR with ICS flow cycling is closest to the conventional system described in section 2.1.3.1. The alternation of recirculation flow has been demonstrated both theoretically and experimentally to produce more homogeneous distributions of proteins and cells in the ECS (Piret and Cooney 1990b, Patkar et al. 1995). The next three examples are closed-shell configurations with cells grown in the ECS. The Mass Culturing Technique (MCT) system by Bio-Response (Brown et al. 1985, von Wedel 1987) enables continuous medium replenishment and antibody removal through microporous membranes in a cell exclusion loop, while a separate dialysis circuit with ultrafiltration membranes is used to exchange low-MM solutes with the ECS. Some of the nonviable cells are periodically removed from the MCT bioreactor by draining the cell growth chamber. In Cellex's Acusyst (Andersen and Gruenberg 1987, Tyo et al. 1988, Gramer and Keznoff 1998), the medium is cycled between the ICS and the ECS, passing through an external expansion chamber installed within the ECS loop (see also fig. 4c). Relatively high MAb productivity of this system can probably be attributed to enhanced ECS mixing as well as effective purging of dead cells, cell debris, and high-MM metabolites out of the reactor and into the expansion chamber. The countercurrent recirculation of ECS medium in an external shunt is another HFBR configuration that has shown promise in preliminary model simulations conducted in our research group, but still needs experimental verification and optimisation. Potential problems associated with the open-shell systems described above include cell damage by shear stresses and flushing of viable cells out of the ECS, both of which necessitate a careful selection of operating conditions. The dilution of the product in the external recycle volume may also increase the cost of downstream processing.

An example of an open-shell system with cells cultivated on the lumen side of the fibres is the bioartificial liver (BAL) device developed by Nyberg and colleagues (1992). Here, the hepatocytes are fixed inside the fibres using a collagen gel, and the medium passes in cross flow through the ECS. It should be noted, however, that the BAL differs from most other HFBR systems in that its main function is detoxification rather than biosynthesis. The

difficulty of dead cell removal from the fibre lumina or the product dilution in the recycle medium may limit the use of this HFBR configuration for production purposes.

The alternative HFBR designs listed in the second part of table 1 generally require fabrication of new cartridges, and their commercial availability is still limited. Some of them, such as the flat-bed system (Ku et al. 1981), the radial-flow reactor (Tharakan and Chau 1986a, 1986b, 1987), or the alternate-dead-ended HFBR (Brotherton and Chau 1990, 1995), utilise cross flow to minimise nutrient and metabolite gradients and thus can provide the cells with a more homogeneous growth environment. The radial-flow reactor employs a central feed distributor to deliver the dissolved nutrients to the ECS, while the spent medium is removed with the waste gas stream through the lumina of the hollow-fibres. Apart from a high likelihood of membrane fouling, the major concern about this system is possible maldistribution of convective flow under cell-packed conditions, leading to substrate limitations in the outer regions of the fibre bundle. In the alternate-dead-ended system, two intercalated-spiral microporous fibre layers are used to simulate the arterial and venous capillary networks. In this sense, the design is a modification of the dual-circuit concept described earlier (Wei and Russ 1977, Gullino and Knazek 1979). Although uniform pressure and substrate concentration profiles were shown to exist in this type of bioreactor, serious membrane fouling problems were also encountered due to protein denaturation.

In several designs (flat-bed, radial-flow, Tecnomouse, and Tricentric), oxygen – a substrate most likely to become limiting – is delivered to the cell chamber in a gas phase, separately from the liquid-phase nutrients, which enables a better control of its supply. The Tecnomouse system by Integra Biosciences (Tzianabos and Smith 1995) utilises exchangeable, flat cassettes, in which the hollow-fibre bundle is encompassed by a silicone membrane that facilitates uniform oxygenation of the culture. Setec's Tricentric bioreactor (Kessler et al. 1997) is operated in a countercurrent flow configuration, with cells grown in an annular space between two concentric fibres.

## 2.2. Previous Models of Protein Transport in HFBRs

Initial theoretical HFBR studies concentrated mainly on the modelling of the distribution and consumption of low-MM substrates, perceived as critical to cell growth and product generation (Rony 1971, Waterland et al. 1974, Kim and Cooney 1976, Webster and Shuler 1978, Piret and Cooney 1991). Since the dominant transport mode for low-MM solutes in the membranes and ECS is diffusion, the early models usually neglected Starling flow and convection in these two regions (Piret and Cooney 1991, Jayaraman 1993) or considered only a radial convective component on a microscale of a single fibre (Kleinstreuer and Agarwal 1986, Schonberg and Belfort 1987). A growing interest in understanding the role of fluid flow in HFBRs was stimulated by anticipation that convection might help alleviate potential problems of substrate limitation, metabolite inhibition, or growth heterogeneities. More recently, many investigators have realised that the distribution of proteins such as growth factors, growth inhibitors, or products in the hollow-fibre system can be as important to efficient bioreactor operation as is the transport of low-MM solutes.

In reactors equipped with highly permeable membranes, e.g., microporous or high-MWCO ultrafiltration membranes, most proteins can pass unhindered between the ECS and the ICS, and their distributions can be described using models similar to those developed for low-MM solutes. Owing to much lower diffusivities of the proteins, however, a meaningful model formulation should include ECS convection or at least its axial component, as has been appreciated by Salmon et al. (1988) and by Pillarella and Zydney (1990). The former study, unfortunately, is only of limited interest because of the unconventional geometry of the system. In the models of radial-flow HFBRs (Tharakan and Chau 1987, Brotherton and Chau 1990), axial ECS convection is typically negligible. These radial-flow designs are also considered unconventional and will not be considered here. None of the above models has included (often justifiably) the influence of osmotic pressure or gravity on protein distribution.

In conventional HFBRs equipped with semipermeable ultrafiltration membranes, the osmotic and convective phenomena usually play a significant role and, consequently, the modelling becomes more complex. Theoretical analyses relevant to this case will be covered

here in more detail. The models presented below have been classified as being either a Krogh cylinder formulation (section 2.2.1) or a porous medium formulation (section 2.2.2). They all neglect protein adsorption and the influence of density or viscosity gradients on convective flow. The closing section 2.2.3 will discuss some of the most important trends in HFBR protein transport predicted by the models.

### 2.2.1. Krogh Cylinder Models

Most previous models of hollow-fibre systems have been based on the Krogh cylinder approximation, which assumes that the fluid and solute behaviours in the vicinity of each fibre are the same. Accordingly, the fibre bundle in the bioreactor is divided into identical units called Krogh cylinders, each consisting of a single fibre surrounded by an annular fluid envelope. In the classical theory, the Krogh cylinders are assumed to be parallel and uniformly spaced, with no interfibre exchange of fluid or solutes. In a more general approach, Łabęcki et al. (1995) treated Krogh cylinders as one-dimensional (1-D) units that may not be straight or parallel, e.g., as a result of fibre expansion under wet conditions. The radius of a single Krogh cylinder understood in this more general sense can be calculated from the cartridge and fibre dimensions as

$$R_K = R_{HFBR} \sqrt{\frac{L}{n L_F}} \quad (2)$$

where  $R_{HFBR}$  is the radius of the HFBR cartridge,  $L$  is the ECS length,  $n$  is the number of fibres, and  $L_F$  is the permeable length of the wet fibre (Łabęcki et al. 1995, 1996). For Cuprophan fibres, Patkar et al. (1995) found  $L_F$  to be about 10% larger than  $L$ , but their model (see below) did not take into account the distinction between the two lengths. Other KCM formulations discussed in this section have also assumed  $L_F = L$ , in accordance with the classical KCM theory. Moreover, it should be noted that the Krogh cylinder concept outlined above does not consider the presence of the fibre-free manifolds, which can occupy as much as 25-30% of the ECS volume (Łabęcki 1994).

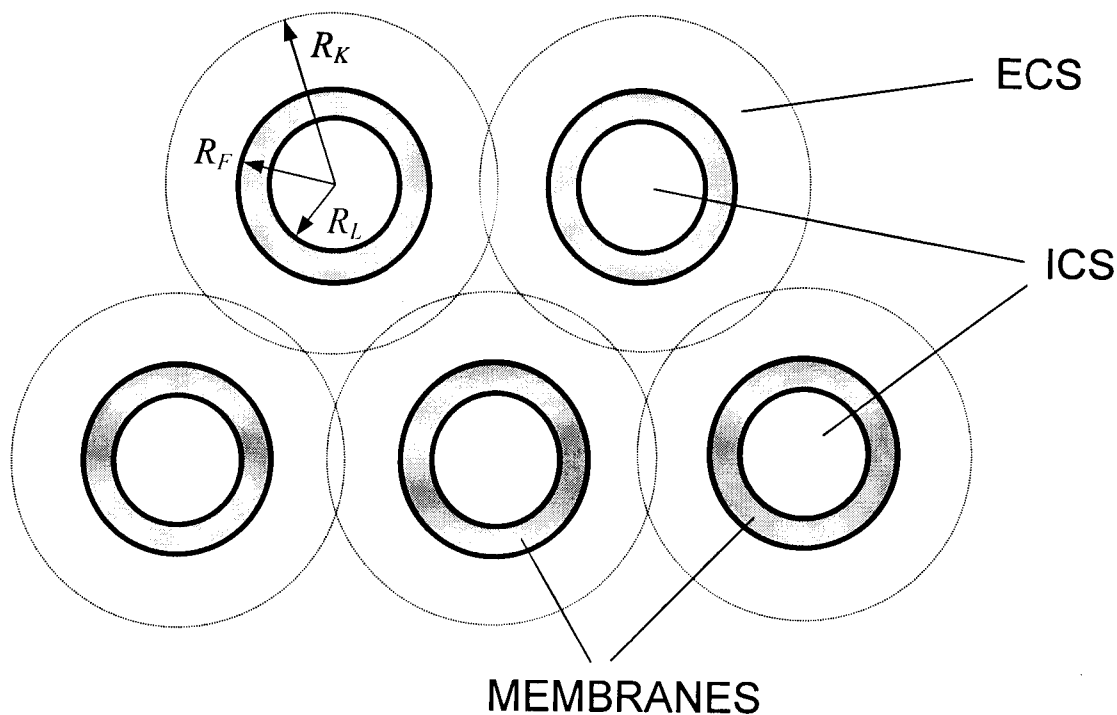


Fig. 5. Cross-sectional arrangement of Krogh cylinders in a hollow-fibre bundle (not to scale); partial overlapping compensates for the void space between the neighbouring cylinders (Łabęcki 1994);  $R_L$ , lumen radius;  $R_F$ , fibre outer radius;  $R_K$ , Krogh cylinder radius. Typically,  $R_L$  is of order  $10^{-4}$  m,  $R_F - R_L \approx 1.2 \times 10^{-6}$  m, and  $R_K \approx 1.5-2.0 \times 10^{-4}$  m.

If the fluid flow in the HFBR is assumed steady and independent of protein concentration, then the hydrodynamic analysis can be greatly simplified. Strictly speaking, however, such an assumption is justified only when highly permeable membranes are employed, the ECS protein concentrations are low, and the membrane permeability and cell density do not change significantly over the time periods of interest. This stipulation is satisfied to a sufficient degree in some hollow-fibre artificial organs such as the bioartificial pancreas (Chick et al. 1975) or liver support devices (Wolf et al. 1978). In these cases, the islets of Langerhans or the hepatocytes grown in the ECS are steadily exchanging smaller proteins or other biochemicals with the blood stream passing through the fibre lumina, while the high-MM plasma proteins are largely retained in the ICS by the membranes (Jaffrin et al. 1988, Catapano 1996). Pillarella and Zydney (1990) modelled the transport of insulin (MM = 5.2 kDa) in a closed-shell hollow-fibre system of this type by using the Krogh cylinder

approximation. The following convective-diffusion equation was solved to obtain the protein distributions in the lumen (ICS), membrane matrix, and shell (ECS):

$$\frac{\partial C}{\partial t} + u \frac{\partial C}{\partial z} + v \frac{\partial C}{\partial r} = \frac{D}{r} \frac{\partial}{\partial r} \left( r \frac{\partial C}{\partial r} \right) + \chi_{ins} \quad (3)$$

where  $C$  is the local insulin concentration;  $u$  and  $v$  are the axial and radial fluid velocities;  $D$  is the insulin diffusivity (assumed constant); and  $\chi_{ins}$ , the rate of insulin production, is a function of the local cell density, local glucose concentration, and time. Essentially cell-free conditions in the ECS were considered, and insulin was assumed to pass unhindered through the membrane. Osmotic effects, axial convection in the matrix, and axial diffusion in all three regions were neglected. Boundary conditions for eq. (3) include the symmetry of the radial concentration profile at  $r = 0$  and  $r = R_K$ , continuity of protein flux at the lumen-matrix ( $r = R_L$ ) and matrix-shell ( $r = R_F$ ) interfaces, radially uniform concentration at the lumen inlet, and no fluxes through the end boundaries of the shell. The initial condition at  $t = 0$  was the known, spatially uniform, protein concentration throughout the whole domain.

Since the fluid flow in the above approach was decoupled from the solute mass transfer, the fluid velocities in eq. (3) could be evaluated analytically using the hydrodynamic theory developed by Kelsey et al. (1990), which was based in part on an earlier analysis by Apelblat et al. (1974). This theory assumed laminar flow in all regions of the bioreactor, fully developed flow in the lumen, as well as negligible axial velocity gradients and inertial terms in the momentum equation. Many of these assumptions are justified by the low membrane permeabilities and low aspect ratios (both  $R_L / L_F$  and  $(R_K - R_F) / L_F$  are of order  $10^{-3}$ ), and hence very small radial Reynolds numbers ( $Re_r \approx 10^{-5} - 10^{-2}$ ), in typical HFBRs. Under these conditions, the continuity and Navier-Stokes equations for steady-state flow of a Newtonian, incompressible fluid in the ICS and the essentially cell-free ECS become

$$\frac{\partial u}{\partial z} + \frac{v}{r} + \frac{\partial v}{\partial r} = 0 \quad (4)$$

and

$$\frac{1}{r} \frac{\partial}{\partial r} \left( r \frac{\partial u}{\partial r} \right) = \frac{1}{\mu} \frac{dP}{dz} \quad (5)$$

where  $\mu$  is the fluid viscosity and  $P$  is the hydrostatic pressure, which is a function of  $z$  only. Combination of Darcy's law with fluid continuity for flow in the membrane matrix, together with the assumptions that the axial velocity in the membrane is negligible and that the pressure profile is continuous across the lumen-matrix and matrix-shell interfaces, leads to the following equation for the radial superficial velocity in the membrane:

$$v_m(z, r) = \frac{L_p R_L}{\mu r} [P_L(z) - P_S(z)]. \quad (6)$$

In order to derive the equations governing the ICS and ECS hydrodynamics, eq. (5) is integrated twice over  $r$ , with symmetry conditions ( $\partial u / \partial r = 0$  and  $v = 0$ ) applied at  $r = 0$  and  $r = R_K$  and no-slip conditions ( $u = 0$ ) at  $r = R_L$  and  $r = R_F$ , the result is then combined with eq. (4), and finally the obtained radial velocities  $v_L(z, R_L) = v_m(z, R_L)$  and  $v_S(z, R_F) = v_m(z, R_F)$  are substituted into eq. (6). In this manner, one arrives at the following set of coupled ordinary differential equations for the lumen and shell pressures:

$$\frac{d^2 P_L}{dz^2} = \frac{16 L_p}{R_L^3} [P_L(z) - P_S(z)] \quad (7)$$

and

$$\frac{d^2 P_S}{dz^2} = -\frac{16 L_p}{\gamma R_L^3} [P_L(z) - P_S(z)] \quad (8)$$

where

$$\gamma = \left[ 4 R_K^4 \ln(R_K / R_F) + 4 R_K^2 R_F^2 - 3 R_K^4 - R_F^4 \right] / R_L^4, \quad (9)$$

and  $R_L$ ,  $R_F$ , and  $R_K$  are the lumen radius, fibre outer radius, and Krogh cylinder radius, respectively. Upon applying the appropriate known-pressure, known-flow (known pressure-derivative), or no-flux (zero pressure-derivative) boundary conditions, analytical solutions to

eqs. (7) and (8) are easily obtained. For example, the expressions for the fluid velocities in a closed-shell HFBR with a specified centreline velocity at the lumen inlet,  $u_0$ , are as follows (Kelsey et al. 1990):

$$u_L(z, r) = u_0 \frac{1 - (r/R_L)^2}{1 + 1/\gamma} \left\{ \frac{\cosh[\lambda(z/L - 1/2)]}{\cosh(\lambda/2)} + \frac{1}{\gamma} \right\}, \quad (10)$$

$$u_S(z, r) = u_0 \frac{r^2 - R_F^2 - 2R_K^2 \ln(r/R_F)}{R_L^2(1 + \gamma)} \left\{ \frac{\cosh[\lambda(z/L - 1/2)]}{\cosh(\lambda/2)} - 1 \right\}, \quad (11)$$

$$v_L(z, r) = -u_0 r \left[ 2 - (r/R_L)^2 \right] \sqrt{\frac{L_p}{R_L^3(1 + 1/\gamma)}} \frac{\sinh[\lambda(z/L - 1/2)]}{\cosh(\lambda/2)}, \quad (12)$$

and

$$v_S(z, r) = -u_0 r \lambda \Omega(r) \sqrt{\frac{L_p}{R_L^3 \gamma (1 + \gamma)}} \frac{\sinh[\lambda(z/L - 1/2)]}{\cosh(\lambda/2)} \quad (13)$$

where

$$\lambda = 4L \sqrt{\frac{L_p(1 + 1/\gamma)}{R_L^3}} \quad (14)$$

and

$$\Omega(r) = \left[ 2R_K^2 - 2R_F^2 + r^2 - 3\frac{R_K^4}{r^2} + 2\frac{R_K^2 R_F^2}{r^2} + 4\frac{R_K^4}{r^2} \ln(R_K/R_F) - 4R_K^2 \ln(r/R_F) \right] / R_L^2. \quad (15)$$

In order to maintain consistency of the above formulation with the definition of  $R_K$  given by eq. (2), Łabęcki et al. (1995) proposed that the  $z$  co-ordinate in eqs. (7) and (8) be replaced by  $x = zL_F/L$ . In this manner, the flow path tortuosity due to fibre expansion under wet conditions could be taken into account. A general form of the hydrodynamic solutions for a tortuous Krogh cylinder was presented that could be used with any combination of open or closed lumen and ECS ports (see appendix A).

It should be noted that the Krogh cylinder approach assumes that the fluid in open-shell operations enters or exits the ECS axially at either end of the annular space. In reality, the inflow or outflow occurs radially through the outer circumference of the fibre bundle, over the length of the ECS manifold (see fig. 1). Therefore, the KCM formulations of the ECS boundary conditions for an open-shell reactor are rather crude approximations. Another frequently challenged boundary condition is the assumption of zero tangential velocity (no slip) at the inner and outer surfaces of the membrane. However, based on an empirical study performed by Beavers and Joseph (1967) and its supporting theory by Saffman (1971), the fractional increase in flow rate due to slip along the surface of a hollow-fibre membrane can be estimated to be of the order of  $\sqrt{L_p/R_L}$ , i.e., evidently negligible for hollow-fibre systems of any practical interest.

Taylor et al. (1994) developed a transport theory for proteins retained in an essentially cell-free ECS, taking into account the osmotic effects. Accordingly, the radial superficial velocity in the membrane was calculated as

$$v_m(z,r) = \frac{L_p R_L}{\mu r} [P_L(z) - P_S(z) + \Pi_S(z, R_F)] \quad (16)$$

with the osmotic pressure,  $\Pi_S$ , evaluated as a function of the local protein concentration using the formula derived by Vilker et al. (1981b):

$$\Pi_S(C_S) = \frac{R_g T}{M_p} \left[ \sqrt{(Z_p C_S)^2 + (2m_s M_p)^2} - 2m_s M_p + C_S + A_1 C_S^2 + A_2 C_S^3 \right] \quad (17)$$

where  $R_g$  is the gas constant,  $T$  is the absolute temperature,  $M_p$  is the molar mass of the protein,  $Z_p$  is the protein charge number (which depends on pH),  $m_s$  is the molar salt concentration, and the coefficients  $A_1$  and  $A_2$  are functions of  $Z_p$ . A simpler, virial form of  $\Pi_S(C_S)$  was also used in other studies (Patkar et al. 1995, Łabęcki et al. 1996, Koska et al. 1997). The time-dependent protein distribution in the ECS was described by Taylor et al. (1994) using

$$\frac{\partial C_s}{\partial t} = D \left[ \frac{\partial^2 C_s}{\partial z^2} + \frac{1}{r} \frac{\partial}{\partial r} \left( r \frac{\partial C_s}{\partial r} \right) \right] - u_s \frac{\partial C_s}{\partial z} - v_s \frac{\partial C_s}{\partial r} \quad (18)$$

which differs from eq. (3) by inclusion of the axial diffusive term and by neglect of sink/source term due, for instance, to protein uptake or production by the cells. The initial condition for eq. (18) was the known uniform concentration at  $t = 0$ , while the boundary conditions included zero concentration-derivatives at the solid and Krogh cylinder boundaries and a quasi-steady balance between protein diffusion and convection at the membrane surface. Unlike in the formulation of Kelsey et al. (1990), the axial pressure derivatives needed to calculate the local fluid velocities in the ECS were expressed in terms of the radially-averaged axial velocity in the lumen,  $\bar{u}_L$ . Substitution of these pressure-derivative terms into the differentiated form of eq. (16) and combination of the result with the fluid mass balance over a differential length of the ICS yielded the following ordinary differential equation for  $\bar{u}_L$ :

$$\frac{d^2 \bar{u}_L}{dz^2} - \frac{16L_p(1+1/\gamma)}{R_L^3} \bar{u}_L = -\frac{16L_p \bar{u}_{L0}}{R_L^3 \gamma} - \frac{2L_p}{\mu R_L} \frac{d\Pi_S [C_S(z, R_F)]}{dC_S} \frac{dC_S(z, R_F)}{dz} \quad (19)$$

where  $\bar{u}_{L0}$  is the average axial velocity at the lumen inlet or outlet. Because of the presence of the osmotic pressure derivative term, the above equation had to be solved numerically. The obtained axial distribution of  $\bar{u}_L$  was used to evaluate the local ECS velocities ( $u_s$  and  $v_s$ ) needed in eq. (18), which was also solved numerically. Because of the coupling between the HFBR hydrodynamics and ECS protein distribution, the solutions of equations (18) and (19) were iterated at each new time level until convergence was attained.

The same authors proposed a simple analysis of ECS protein distribution and HFBR hydrodynamics at steady state (Taylor et al. 1994). Accordingly, a critical initial protein concentration  $C_{S0}^{crit}$  was considered, above which the steady-state distribution of protein extends from  $z = 0$  to  $z = L$  and the ECS flow is effectively shut down over the whole length of the reactor because of osmotic effects. At initial concentrations below  $C_{S0}^{crit}$ , the ECS divides at  $z = z_s$  into two zones: a protein-free upstream region ( $z < z_s$ ) supporting Starling

flow, and a stagnant downstream region ( $z \geq z_s$ ) where all of the protein has accumulated. The ECS pressure in the upstream region is approximately constant and equal to

$$P_S^{up} = P_{L,out} + \frac{8\bar{\mu}u_{L0}}{R_L^2} \left( L - \frac{z_s}{2} \right) \quad (20)$$

where  $P_{L,out}$  is the absolute pressure at the lumen outlet. The local osmotic pressure  $\Pi_S(z)$  at  $z \geq z_s$  was found as a difference between  $P_S^{up}$  and the known ICS pressure  $P_L(z)$ , the latter assumed to vary linearly with  $z$ . The concentration distribution  $C_S(z)$  was then calculated implicitly from  $\Pi_S(z)$  using eq. (17), and the corresponding  $z_s$  value was determined from the overall protein mass balance by root-finding. Eventually,  $C_{S0}^{crit}$  was obtained as the average ECS concentration when  $z_s = 0$ .

In a subsequent study of closed-shell HFBRs by Patkar et al. (1995), radial gradients of velocities, pressures, and concentration were omitted, which simplified the two-dimensional (2-D) KCM of Taylor et al. (1994). This modification was justified by the good agreement of the 1-D model predictions both with the experimental ECS protein distribution data and with the radially-averaged predictions of the 2-D model. The radially-averaged concentrations of ECS proteins were calculated from

$$\frac{\partial \bar{C}_S}{\partial t} = D \frac{\partial^2 \bar{C}_S}{\partial z^2} - \frac{\partial}{\partial z} (\bar{u}_S \bar{C}_S) \quad (21)$$

where the radially-averaged axial velocity  $\bar{u}_S$  was linked through a local fluid mass balance (including the ICS inlet) to  $\bar{u}_L$ , and the latter was obtained as a solution of eq. (19) with  $C_S(z, R_F) = \bar{C}_S(z)$ . Since the flow distribution did not change significantly over each time increment, the hydrodynamic solution was lagged one step behind the solution of eq. (21). This measure greatly reduced the computational effort by avoiding an iterative procedure at each time level.

A KCM describing ECS protein transport in closed-shell HFBRs under conditions of high cell density was developed by Koska et al. (1997). The hydrodynamic analysis of such systems was similar to that presented by Apelblat et al. (1974) for protein-free reactors. By

using Darcy's law to describe fluid flow in the ECS and with other assumptions analogous to those made in the cell-free studies outlined above (Kelsey et al. 1990, Taylor et al. 1994, Patkar et al. 1995), the following equations for the lumen and shell pressures were derived:

$$\frac{d^2 P_L}{dz^2} = \frac{16L_p}{R_L^3} [P_L(z) - P_S(z, R_F) + \Pi_S(z, R_F)] \quad (22)$$

and

$$\frac{1}{r} \frac{\partial}{\partial r} \left( r \frac{\partial P_S}{\partial r} \right) + \frac{\partial^2 P_S}{\partial z^2} = 0. \quad (23)$$

Equation (22) is subject to known-pressure or known-flow-rate boundary conditions at the lumen inlet and outlet. Equation (23) is subject to no-flux boundary conditions at  $z = 0$ ,  $z = L$ , and  $r = R_K$ , and to the following condition expressing the fluid flux balance at  $r = R_F$ :

$$\frac{\partial P_S}{\partial r} = - \frac{L_p R_L}{k_s R_F} [P_L(z) - P_S(z, R_F) + \Pi_S(z, R_F)] \quad (24)$$

where  $k_s$  is the constant and isotropic ECS Darcy permeability of a cell-packed ECS. Koska et al. (1997) discussed different possible ways of estimating  $k_s$ , which could be (1) treated as a measurable system parameter, (2) approximated by the hydraulic permeability of tissues *in vivo* (Swabb et al. 1974), or (3) calculated using the Carman-Kozeny theory for a packed bed of spheres (Carman 1937).

For this model, the time-dependent protein distribution in a cell-packed ECS was governed by the equation

$$\frac{\partial C_S}{\partial t} = DK_d \left[ \frac{\partial^2 C_S}{\partial z^2} + \frac{1}{r} \frac{\partial}{\partial r} \left( r \frac{\partial C_S}{\partial r} \right) \right] - K_c \left[ \frac{u_s}{\varepsilon} \frac{\partial C_S}{\partial z} - \frac{v_s}{\varepsilon} \frac{\partial C_S}{\partial r} \right] \quad (25)$$

where  $C_S = C_S(z, r)$  is the interstitial ECS protein concentration (i.e., mass of protein per unit volume of ECS fluid),  $K_d$  and  $K_c$  are the diffusive and convective hindrance factors, respectively, and  $\varepsilon$  is the porosity of the cell mass in the ECS (Koska et al. 1997). For the

sake of comparison, simpler forms of eqs. (23) and (25) were also considered in which radial gradients were neglected, i.e.,

$$\frac{d^2 \bar{P}_s}{dz^2} = -\frac{2R_L L_p}{(R_K^2 - R_F^2)k_s} \left[ P_L(z) - \bar{P}_s(z) + \bar{\Pi}_s(z) \right] \quad (26)$$

and

$$\frac{\partial \bar{C}_s}{\partial t} = DK_d \frac{\partial^2 \bar{C}_s}{\partial z^2} - K_c \left( \frac{\bar{u}_s}{\varepsilon} \frac{\partial \bar{C}_s}{\partial z} \right) \quad (27)$$

where the overbars denote radially-averaged quantities. In both the 1-D and 2-D formulations, numerical methods were employed to solve the coupled hydrodynamic and protein transport problems.

### 2.2.2. Porous Medium Model

A porous medium approach to the analysis of transport phenomena in hollow-fibre bioreactors was proposed and extensively used by this author (Łabęcki 1994, Łabęcki et al. 1995, 1996). In this model, the intra- and extracapillary spaces of the fibre bundle are treated as two interpenetrating porous media with uniformly distributed sinks and sources of fluid. Both the fluid and the membranes are assumed to be incompressible, and axial pressure gradients in the membranes are neglected. Consequently, fluid that disappears from one subspace (ECS or ICS) appears instantly at the same position in the other subspace (ICS or ECS, respectively). Unlike in the various KCM formulations, the spatial domain of the porous medium model (PMM) corresponds to the dimensions of the whole fibre bundle in the reactor (fig. 6). Thus, this approach makes it possible to account for interfibre flows and macroscopic radial and angular concentration gradients which are normally present during open-shell operations, but may also arise in closed-shell HFBRs as a result of gravitational influences (Piret and Cooney 1990b) or radial pressure variations in the lumen manifolds (Park and Chang 1986). The flow properties and protein concentrations in the PMM are averaged over a representative elementary volume (REV), which is small enough to be treated in a differential sense, but must also contain a sufficient number of fibres to ensure

that it has the properties of a continuum (Bear 1972, p. 19). The PMM should be distinguished from the KCM formulations that treat the ECS of the Krogh cylinder as a porous medium (Brotherton and Chau 1996, Koska et al. 1997, Apelblat et al. 1974).

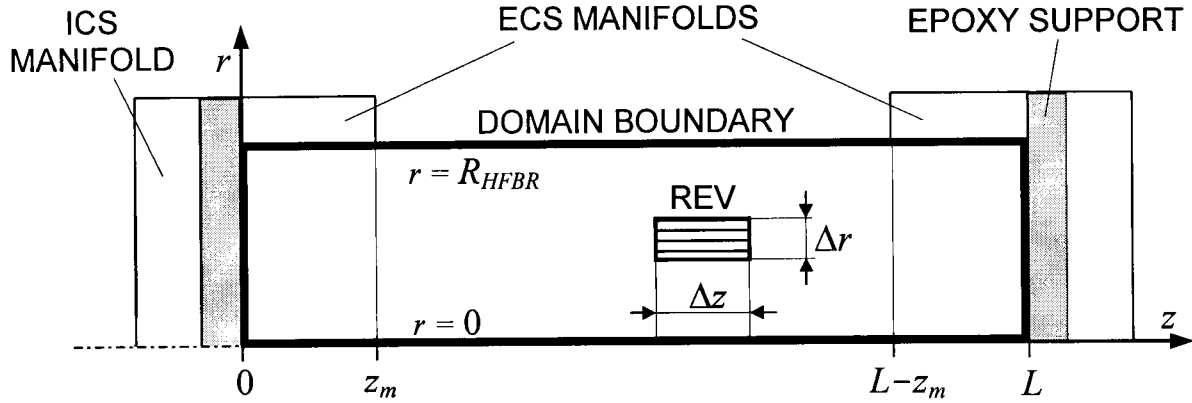


Fig. 6. Longitudinal section through the cylindrical domain of the two-dimensional porous medium model (Łabęcki 1994, Łabęcki et al. 1995, 1996); *REV*, representative elementary volume;  $z_m$ , axial length of the ECS manifold.

In the original PMM formulation (Łabęcki 1994, Łabęcki et al. 1995, 1996), two-dimensional cylindrical co-ordinates were used, gravity effects were neglected, and the proteins were confined to the ECS. Application of the Darcy and steady-state continuity laws to the lumen and shell spaces yielded the following equations governing the hydrodynamics:

$$-k_{s,r} \frac{1}{r} \frac{\partial}{\partial r} \left( r \frac{\partial P_s}{\partial r} \right) - k_{s,z} \frac{\partial^2 P_s}{\partial z^2} = A_v L_p (P_L - P_s + \Pi_s) \quad (28)$$

and

$$k_{L,z} \frac{\partial^2 P_L}{\partial z^2} = A_v L_p (P_L - P_s + \Pi_s) \quad (29)$$

where  $P_L = P_L(z, r)$  and  $P_S = P_S(z, r)$  are the ICS and ECS hydrostatic pressures; and  $\Pi_S$  is the ECS osmotic pressure, evaluated as a function of local protein concentration. In consistency with the way  $L_p$  was determined (see eq. (1)), the membrane surface area per unit volume of the reactor was based on the luminal fibre radius, i.e.,

$$A_V = \frac{2 n R_L L_F}{R_{HFBR}^2 L} \quad (30)$$

where  $n$  is the number of fibres. Owing to the lack of interfibre connectivity within the lumen space, the radial component of the ICS Darcy permeability,  $k_{L,r}$ , was assumed to be zero. The axial permeability components,  $k_{L,z}$  and  $k_{S,z}$ , could be determined experimentally or estimated theoretically using simple models. For instance, in the absence of cells, a 1-D Krogh cylinder analysis that accounts for wet fibre expansion yields

$$k_{L,z} = \frac{n R_L^4 L}{8 R_{HFBR}^2 L_F} \quad (31)$$

and

$$k_{S,z} = \frac{R_{HFBR}^2 L^3}{4 n L_F^3} \left( -\ln \varphi - \frac{3}{2} + 2\varphi - \frac{1}{2}\varphi^2 \right) \quad (32)$$

where  $\varphi = n R_F^2 L_F / (R_{HFBR}^2 L)$  is the fraction of the reactor volume occupied by the fibres. The ECS radial permeability,  $k_{S,r}$ , for a cell-free reactor was estimated from Happel's (1959) model of flow perpendicular to an assemblage of parallel cylinders, i.e.,

$$k_{S,r} = \frac{R_{HFBR}^2 L^3}{4 n L_F^3} \left( -\ln \varphi + \frac{\varphi^2 - 1}{\varphi^2 + 1} \right). \quad (33)$$

At sufficiently high cell densities, the ECS permeability may become essentially isotropic and should therefore be modelled in a different manner. For example, Łabecki (1994) used the Carman-Kozeny equation (Carman 1937),

$$k^* = \frac{\varepsilon^{\bullet 3}}{5 [A_V^* (1 - \varepsilon^{\bullet})]^2} \quad (34)$$

where  $k^*$  is the hydraulic permeability of the cell-packed ECS,  $A_v^*$  is its surface-area-to-volume ratio, and  $\varepsilon^*$  is its porosity. Both  $A_v^*$  and  $\varepsilon^*$  can be readily estimated by assuming that the cells are rigid spheres of known diameter (10-15  $\mu\text{m}$  for mammalian cells).

In the absence of protein sinks and sources, the protein distribution within the ECS was governed by the transient convective-diffusion equation:

$$\varepsilon_s \frac{\partial C_s}{\partial t} = \frac{\partial}{\partial z} \left( D_z \frac{\partial C_s}{\partial z} - u_s C_s \right) + \frac{1}{r} \frac{\partial}{\partial r} \left( r D_r \frac{\partial C_s}{\partial r} - r v_s C_s \right) \quad (35)$$

where  $\varepsilon_s$  is the effective ECS porosity, which equals  $1-\phi$  in the absence of cells, and  $C_s$  is the interstitial protein concentration in the ECS. The superficial shell velocities  $u_s$  and  $v_s$ , as well as the lumen velocity  $u_L$ , were obtained from the calculated ECS and ICS pressure fields and the respective hydraulic permeabilities by using Darcy's law. For cell-packed conditions, the ECS porosity  $\varepsilon_s$  in eq. (35) was replaced by  $\varepsilon^*(1-\phi)$  to account for volume exclusion due to the presence of both fibres and cells.  $D_z$  and  $D_r$ , the components of the effective protein diffusivity in a cell-free ECS, were modelled as

$$D_z = D \varepsilon_s (L/L_F)^2 \quad (36)$$

and

$$D_r = D \varepsilon_s / (2 - \varepsilon_s) \quad (37)$$

where  $D$  is the diffusivity in an unobstructed fluid. The ECS protein diffusivity at cell-packed conditions was assumed isotropic and was calculated from an equation valid for solute transport through a bed of spheres (Neale and Nader 1973), modified by the  $(1-\phi)$  factor, i.e.,

$$D^* = 2D (1-\phi) \varepsilon^* / (3 - \varepsilon^*). \quad (38)$$

The coupled fluid flow equations (28) and (29) and protein transport equation (35) were solved numerically, with the hydrodynamic solution lagged one time step behind the concentration solution.

The initial condition for eq. (35) was the known (e.g., uniform or downstream-polarised) concentration distribution at  $t = 0$ . The general boundary conditions for the pressure equations (28) and (29) and the concentration equation (35) are summarised in table 2. In the simulations of open-shell operations, Łabęcki (1994) assumed for simplicity that fixed-pressure conditions prevailed over the ECS inflow and outflow boundaries, i.e., at  $r = R_{HFBR}$  and  $0 \leq z \leq z_m$  or  $L - z_m \leq z \leq L$  (see fig. 6). Note that it is very difficult to determine the ECS inlet or outlet velocity distribution, and it is usually only the flow rate, or the average velocity, that is known in laboratory practice. In that case, rather than assuming an arbitrary flow profile such as a constant velocity, it may be more accurate to specify a constant pressure at the boundary and then adjust its value iteratively until the desired total flow rate is obtained. Such a procedure was adopted in the open-shell HFBR studies described in chapter 4 of this thesis.

Table 2. Boundary conditions for the PMM equations (28), (29), and (35)

Boundary (location)	Condition	Comment
$z = 0$ or $z = L$ (ICS inlet or outlet)	Known $P_L(r)$ or $u_L(r)$	$u_L = dP_L/dz = 0$ if ICS port closed
$z = 0$ or $z = L$ (epoxy surface at either end of ECS)	$\partial P_S / \partial z = 0$ $\partial C_S / \partial z = 0$	No fluid or protein flux through impermeable boundary
$r = 0$ (ECS centreline)	$\partial P_S / \partial r = 0$ $\partial C_S / \partial r = 0$	Axial symmetry
$r = R_{HFBR}$ and $z_m < z < L - z_m$ (cartridge wall between ECS manifolds)	$\partial P_S / \partial r = 0$ $\partial C_S / \partial r = 0$	No fluid or protein flux through impermeable boundary
$r = R_{HFBR}$ and $0 \leq z \leq z_m$ or $L - z_m \leq z \leq L$ (ECS fibre bundle boundary within the manifold length)	1) $\partial P_S / \partial r = 0$ , $\partial C_S / \partial r = 0$ 2) Known $P_S(z, R_{HFBR})$ or $v_S(z, R_{HFBR})$ , known $C_S(z, R_{HFBR})$ 3) $\partial C_S / \partial r = 0$	1) No fluid or protein flux if ECS port closed 2) Open ECS inlet or outlet port; $P_S$ and $C_S$ usually assumed constant over $z$ 3) Only convective protein flux at ECS outlet

It can be shown that, in the absence of radial gradients and with the axial hydraulic permeabilities calculated from equations (30) and (31), the 1-D PMM becomes identical to the radially-averaged 1-D KCM. Note, however, a fundamental difference between the 2-D formulations of these two models. Whereas the radial dimension in the KCM is considered only on the microscale of a single fibre, the PMM accommodates the dimensions of the whole fibre bundle. The third spatial dimension can easily be added to the above PMM formulation (see chapter 5), and it is also possible to extend the model domain by including the adjacent fibre-free manifolds, although the hydrodynamics in these regions will likely be governed by the Navier-Stokes equations rather than by Darcy's law.

### 2.2.3. Essential Predictions

This section briefly discusses some of the trends in ECS protein distribution predicted by the KCM and PMM formulations introduced above. Such a presentation will be helpful in understanding the results of the more advanced modelling studies described in the subsequent parts of this thesis. The most distinct trend apparent in closed-shell as well as some open-shell HFBR operations is the axial polarisation of ECS proteins towards the downstream end of the reactor (see also section 2.1.3.3) (Patkar et al. 1995, Łabęcki et al. 1996, Koska et al. 1997). In addition to the axial protein redistribution, similar convective polarisation in the transverse direction was predicted by the 2-D PMM simulations to occur in the presence of significant radial pressure gradients in the entrance or exit lumen manifolds (Łabęcki 1994). Figure 7 illustrates the KCM-predicted temporal evolution of the axial polarisation process at cell-free (fig. 7a) and cell-packed (fig. 7b) conditions in the ECS (Koska et al. 1997). These two cases were simulated by assuming different input values for the ECS hydraulic permeability. The investigated protein (BSA) was completely retained in the ECS, and its initial distribution was uniform. The 2-D KCM formulation based on equations (22), (23) and (25), and the 1-D formulation based on the use of radially-averaged quantities and equations (26) and (27), yielded virtually identical results.

As seen in fig. 7, the ECS becomes divided into a protein-free and a protein-rich region after a sufficiently long time of closed-shell operation. The boundary between these two regions continues to shift downstream until steady state is reached. At the same time,

parallel changes in the distribution of axial ECS flow occur, manifesting themselves through an upstream shift of the axial velocity maximum and a temporal decline in the magnitude of Starling flow. The downstream protein buildup continues until the sum of the ECS hydrostatic and osmotic pressures in the protein-rich zone locally balances the hydrostatic pressure on the lumen side (since natural-convective effects are not considered), which causes an effective shutdown of transmembrane and ECS flows in the downstream part of the reactor. Consequently, the boundary of the high-concentration zone coincides at steady state with the position at which the velocity profile drops to zero. In the absence of osmotic effects, all of the protein would accumulate to an extremely high concentration within a very thin layer at the downstream end of the ECS, such that the resulting axial concentration gradient at steady state is sufficiently large for the diffusive flux to locally balance the convective flux (Taylor et al. 1994). The implausibility of such a distribution confirms the importance of including the osmotic pressure terms in the model equations.

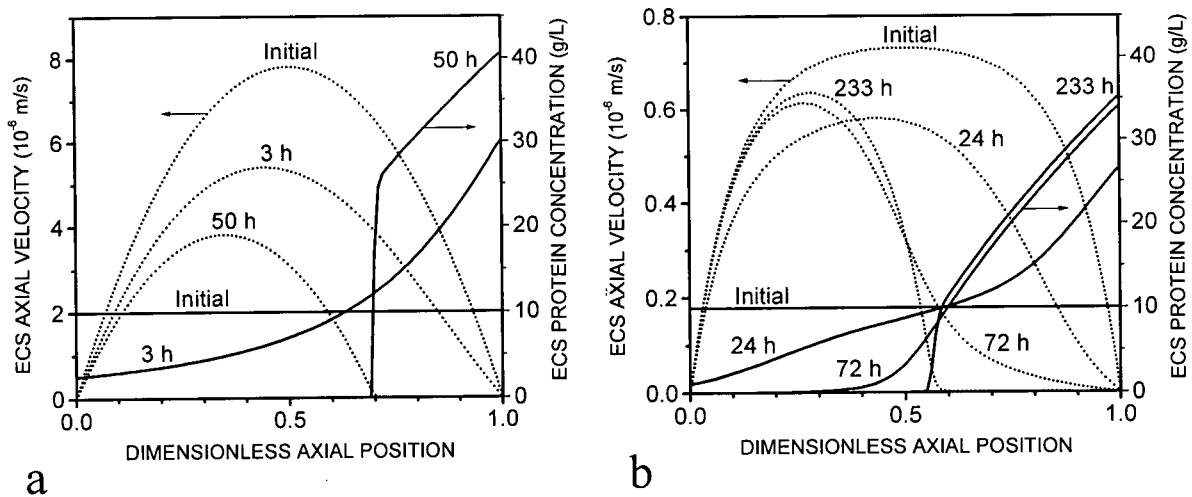


Fig. 7. KCM predictions of radially-averaged BSA concentration distributions (solid lines) and axial velocities (dotted lines) in the ECS of a closed-shell HFBR (adapted from Koska et al. (1997));  $L_p = 6 \times 10^{-15} \text{ m}$ ,  $Q_L = 500 \text{ mL/min}$  (from left to right), average ECS protein concentration  $10 \text{ g/L}$ ; a, cell-free ECS,  $k_s = 10^{-9} \text{ m}^2$ ; b, cell-packed ECS,  $k_s = 5 \times 10^{-14} \text{ m}^2$ .

The final profiles shown are practically identical to the steady-state ones.

For both values of the ECS permeability, the transient ECS concentration and velocity profiles shown in fig. 7 are qualitatively similar. Since the axial pressure drop in the ECS is higher under cell-packed conditions, the ECS hydrostatic pressure at the downstream end is lower, and hence the osmotic contribution required to offset the lumen pressure is smaller. Consequently, the steady-state protein concentrations are also lower and the polarised region extends over a larger portion of the ECS. Significantly longer times are necessary to produce an extent of downstream polarisation comparable to that in a cell-free ECS, which is a consequence of decreased Starling flow at low  $k_s$  values. This is also evident in fig. 8, which plots the KCM-predicted steady-state protein concentration profiles for different ECS hydraulic permeabilities. Note that the extent of protein polarisation over the typical one- or two-day period between harvests can be significantly diminished at low  $k_s$  values, which results in lower concentrations of the product harvested from a cell-packed ECS (Koska et al. 1997). An additional complication arising from the increased resistance to ECS convective flow at high cell densities is that most of the harvested fluid may actually be drawn from the luminal space in the vicinity of the ECS outlet port, thus leaving much of the product inside the reactor. Such effects have indeed been predicted by 2-D PMM simulations (Łabęcki 1994). One must keep it in mind, however, that the results discussed above were generated by assuming a uniform initial ECS protein distribution, no significant protein production during the polarisation process, and a homogeneous distribution of cell mass in the ECS, all of which were only approximations.

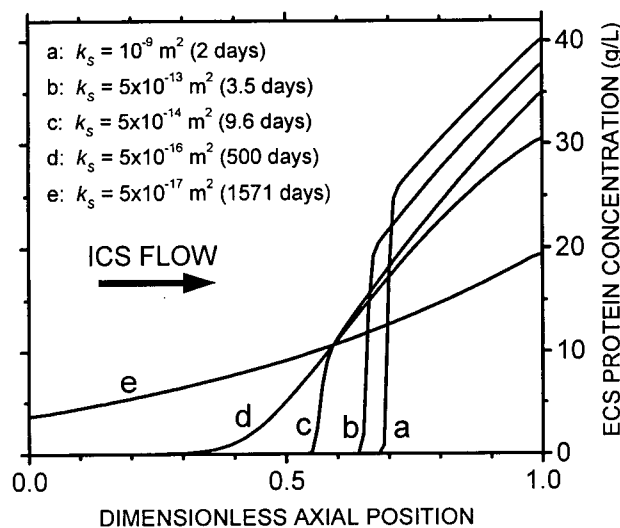


Fig. 8. KCM predictions of radially-averaged ECS protein (BSA) concentrations in a closed-shell HFBR at steady state for different ECS hydraulic permeabilities (adapted from Koska et al. (1997));  $L_p = 6 \times 10^{-15} \text{ m}$ ,  $Q_L = 500 \text{ mL/min}$ ; a,  $k_s = 10^{-9} \text{ m}^2$ ; b,  $k_s = 5 \times 10^{-13} \text{ m}^2$ ; c,  $k_s = 5 \times 10^{-14} \text{ m}^2$ ; d,  $k_s = 5 \times 10^{-16} \text{ m}^2$ ; e,  $k_s = 5 \times 10^{-17} \text{ m}^2$ ; average ECS protein concentration 10 g/L. Times to reach steady state are given in parentheses.

At sufficiently low ECS cell densities, the magnitude of Starling flow in closed-shell HFBRs will be limited by the hydraulic resistance of the membrane rather than by that of the ECS. Consequently, the axial polarisation of ECS proteins under such conditions will be more pronounced in reactors equipped with more permeable membranes. Taylor et al. (1994) found that the time needed to reach steady state in cell-free HFBRs with an initially uniform protein distribution in the ECS was, approximately, inversely proportional to  $L_p$ . The same investigators concluded that  $L_p$  variation over several orders of magnitude had little influence on the steady-state distribution, except for a decrease in the slope of the axial concentration profile in the narrow region between the protein-rich and protein-free zones.

The ECS protein distribution in a given reactor geometry depends also on the ICS flow rate ( $Q_L$ ) and on the protein loading, or the initial protein concentration in the ECS ( $C_0$ ). The predicted effects of these two factors for a closed-shell HFBR at essentially cell-free conditions are shown in fig. 9, which was adapted from the KCM study by Taylor et al. (1994). For their reactor geometry, the ICS flow rates of 57, 228, 570, and 1140 mL/min, used to generate the profiles in fig. 9a, correspond to lumen inlet Reynolds numbers of 1.6, 6, 16, and 32, respectively. At lower  $Q_L$ , the role of convection in the establishment of concentration profiles in the ECS is diminished, and hence the steady-state protein distributions are more uniform. This is due to the fact that a lower axial pressure drop in the ICS requires a smaller axial osmotic pressure gradient to compensate for it. The opposite effect is observed at higher flow rates, viz., the concentration profiles within the polarisation zone are steeper. Similarly, at higher protein contents in the ECS (fig. 9b), more homogeneous distributions exist at steady state, because the osmotic pressure gradient in the downstream region cannot exceed its maximum value determined by the flow conditions in the lumen. Using the simple steady-state model mentioned in section 2.2.1, the critical  $C_0$  value above which the protein extended over the whole length of the reactor and the ECS velocities were everywhere zero was estimated to be 45.1 g/L for the conditions of fig. 9b (Taylor et al. 1994). In the various cases discussed above, the time needed to reach steady state was generally found to be shorter if the steady-state distribution was closer to the initial one, i.e., more uniform. On the other hand, however, steady state was established sooner when  $Q_L$  was increased.

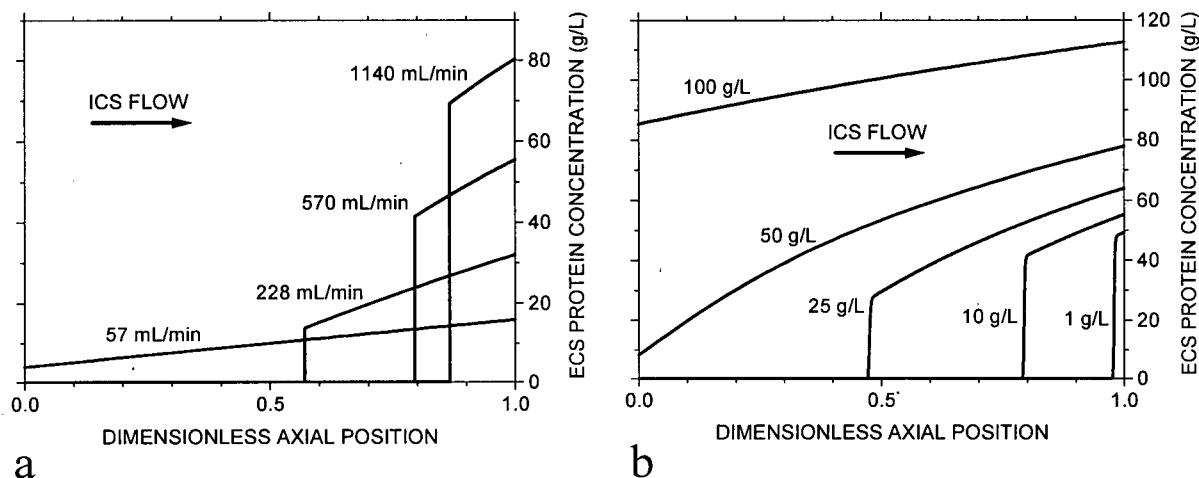


Fig. 9. Steady-state radially-averaged ECS protein (BSA) concentrations in a closed-shell HFBR at cell-free conditions (adapted from Taylor et al. (1994)): *a*, effect of the ICS flow rate,  $C_0 = 10$  g/L; *b*, effect of the average ECS protein concentration,  $Q_L = 570$  mL/min. Membrane hydraulic permeability  $L_p = 1.25 \times 10^{-13}$  m.

Patkar et al. (1995) concluded from their studies that a one-dimensional KCM (eq. 21) was sufficient to reproduce the protein concentration profiles existing in closed-shell HFBRs. Their theoretical predictions were verified experimentally using a system containing two proteins, BSA and transferrin, both of which were retained in the ECS. The average transferrin concentrations used in these experiments were more than an order of magnitude lower than the BSA concentrations, which is a fairly typical ratio of these two proteins in most mammalian cell culture media (Freshney 1994, p. 92). The steady-state distributions of transferrin for different BSA contents in the ECS (fig. 10) were found to bear a close resemblance to the distributions of BSA itself (cf. fig. 9*b*; note that different reactor geometries were used in the two studies). This can be explained by the fact that osmotic pressure had practically the same effect on the distribution of either protein, since the osmotic contribution of transferrin was negligible. A practical implication of this observation is that more uniform distributions of growth factors in the HFBR might be obtained by loading the ECS with a sufficient quantity of a relatively inexpensive non-leaking protein like BSA (Patkar et al. 1995).

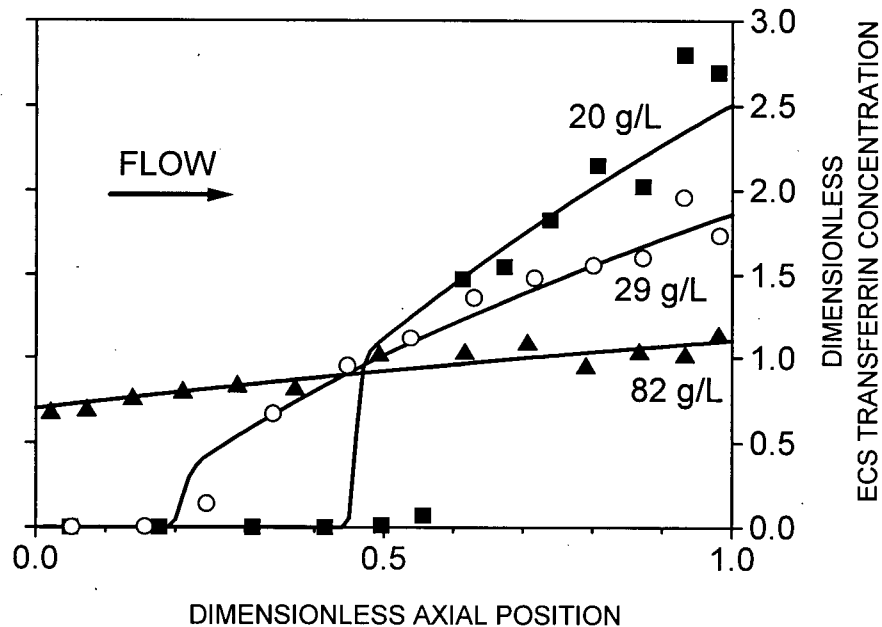


Fig. 10. Experimental (symbols) versus KCM-predicted (solid lines) steady-state distributions of ECS transferrin at the average BSA concentrations of 20 g/L, 29 g/L, and 82 g/L (adapted from Patkar et al. (1995)); average transferrin concentration 0.02 g/L,  $Q_L = 600$  mL/min,  $L_p = 6 \times 10^{-15}$  m.

#### 2.2.4. Motivation for Present Modelling Work

The above examples of model-predicted protein behaviour in HFBRs were mostly based on the results of one-dimensional analyses and emphasised the axial redistribution of proteins in the ECS. The process of downstream protein polarisation has been extensively investigated for a variety of conditions, including different ICS flow rates, ECS hydraulic permeabilities, ECS protein loadings, and membrane permeabilities (Łabęcki 1994, Taylor et al. 1994, Patkar et al. 1995, Koska et al. 1997). The predicted 1-D protein distributions have been successfully verified experimentally (Patkar et al. 1995), although a certain amount of data manipulation was necessary to account for protein entrapment within the ECS manifolds, which were not included in any of the models developed so far. Since the inclusion of the fibre-free ECS regions is an important part of a realistic HFBR description, the models developed within the present project included a more detailed analysis of the manifold effects (see sections 3.2.2.5, 4.2.3, 5.2.2.3, and 5.5.2.2).

Except for a relatively simple KCM study of insulin transport in a hollow-fibre bioartificial pancreas (Pillarella and Zydney 1990), no other models have considered protein leakage through the membranes. Chapter 3 below will present a more advanced approach to this problem, taking into account hindered protein transport through the molecular-size pores of the membrane, as well as the presence of ECS manifolds and the interdependence between the hydrodynamics and mass transfer in the HFBR. This is a pioneering work in this area, since the previous studies of hindered transmembrane solute transport rarely extended beyond theoretical analyses and did not consider membranes shaped as hollow fibres (Deen 1987).

Similarly, there have thus far been no experimental and only little theoretical studies (Łabęcki 1994) of protein transport in open-shell hollow-fibre cartridges. Investigation of open-shell HFBR operations was also a part of the present project and will be discussed in chapter 4 below. Finally, all of the previous analyses have ignored the influence of gravity and the effects of variable fluid density and viscosity on protein transport, thus limiting the application of the results to idealised systems such as vertical cartridges with downward ICS flow. This restriction has now been eliminated through a comprehensive analysis of ECS protein redistribution using a 3-D PMM, which will be presented in chapter 5 of this thesis. This new PMM predicts that free convection can be a powerful mechanism for homogenising the contents of the ECS, a phenomenon that had not previously been explained theoretically.

## Chapter 3

### ONE-DIMENSIONAL ANALYSIS OF HINDERED PROTEIN TRANSPORT THROUGH HOLLOW-FIBRE MEMBRANES

#### 3.1. Motivation and Objectives

Hindered transmembrane protein transport is of importance in many applications of hollow-fibre systems, such as extracorporeal blood purification (including haemodialysis, haemofiltration, and plasmapheresis), separation of protein mixtures in downstream processing, or cultivation of cells for the purpose of tissue engineering or MAb production. In particular, the productivity of cell culture HFBRs can be affected by the membrane properties through a complex combination of growth-factor, growth-inhibitor, and product leakage phenomena (Jackson et al. 1996). In spite of the strong motivation for studies in this area, the only related investigations reported thus far have been limited to systems where the proteins, similarly to low-MM solutes, pass unhindered through the membranes (Klein et al. 1977, Pillarella and Zydney 1990, Todisco et al. 1995). The objective of this study was to develop and verify experimentally a 1-D Krogh cylinder model that extends the earlier analyses of protein transport in closed-shell HFBRs (Taylor et al. 1994, Patkar et al. 1995) by taking into account hindered protein transport in the membrane pores, fibre expansion under wet conditions, the effect of a secondary protein in the ECS, and the influence of ECS manifolds. Although the details of membrane morphology or pore size distribution likely play a role in transmembrane protein transport, it was not a purpose of this work to characterise the hollow-fibre membranes at the microscopic level. Instead, a simpler modelling approach has been adopted, making use of an existing theory that relates the relevant transmission parameters to the ratio of the effective protein and pore radii (Deen 1987). The study described in this chapter has become the subject of a recent publication (Łabęcki et al. 1998).

## 3.2. Model Development

### 3.2.1. Underlying Assumptions

The model proposed here is based on the tortuous Krogh cylinder approximation (Łabęcki et al. 1995; see also section 2.2.1 and appendix A). Thus, the usual KCM limitations apply, viz., the theory is most applicable to hollow-fibre systems in which interfibre transverse pressure and concentration gradients are negligible. In addition to the primary protein, which is transferred through the membrane and redistributed on both the lumen and shell sides, the presence of a nonleaking secondary protein in the ECS is also considered. A detailed list of model assumptions is given below.

- (1) The fluid is incompressible and Newtonian. Gravitational effects are neglected.
- (2) Because of the very small aspect ratio of the Krogh cylinder (see section 2.2.1), radial variations of pressure and concentration in the ICS and ECS are negligible, i.e., fluid flow and protein transport in these two regions are essentially one-dimensional in the axial direction. The flow in either region is fully developed and quasi-steady.
- (3) Axial flow in the membranes is neglected. The membranes are incompressible and their structure is uniform over the membrane thickness. Extension of the theory to asymmetric membranes (see section 2.1.2.1 above) is relatively straightforward, if the hydraulic resistance of the supporting matrix is neglected.
- (4) The pores of the membrane are treated as “tortuous cylinders”, i.e., tortuous channels having a circular cross-section in the direction normal to the pore axis. Fluid flow in the pores is fully developed. All pores have the same effective radius,  $r_{p,eff}$ , which is constant over the pore length. Note that a consequence of assuming a constant pore cross-section for a hollow-fibre membrane is that the outer surface porosity,  $\varepsilon(R_F)$ , is smaller than the inner surface porosity,  $\varepsilon(R_L)$ , the two being related through  $R_L \varepsilon(R_L) = R_F \varepsilon(R_F)$ . An extension which assumes a log-normal distribution of pore radii is presented in appendix B.
- (5) The proteins present in the HFBR system are myoglobin and, in some cases, bovine serum albumin (BSA). Myoglobin is the primary leaking protein, its molar mass ( $M_M = 16.9$  kDa) being close to the molecular weight cutoff (MWCO  $\approx 18$  kDa) of the

membranes used in this study. BSA is a secondary, nonleaking protein which may be present in the ECS.

- (6) Any electrostatic interactions involving protein molecules are neglected. For myoglobin, this is justified by its electroneutrality under the conditions of the present study (fluid buffered at  $\text{pH} = 7.1\text{-}7.2$ , myoglobin isoelectric point  $\text{pI}_M = 7.0$ ). Protein adsorption is also neglected, based on the results of myoglobin tests mentioned in section 3.2.3 and of BSA studies performed by Patkar et al. (1995). Protein presence in the membranes is assumed negligible because of the very small volume of the membrane pores (see section 3.2.2.4). The membrane hydraulic permeability,  $L_p$ , fibre dimensions, and other properties of the proteins and membranes are constant. These assumptions notwithstanding, a simple extension to the model has been developed to consider the possibility of concentration-dependent pore plugging by protein molecules.
- (7) Radial concentration polarisation of either protein on the membrane surface is neglected. This assumption has been justified by the results of numerical tests conducted here on the basis of the stagnant film theory (Blatt et al. 1970), extended for dialysis-type systems by Zydney (1993). According to these results, the local ECS and ICS protein concentrations at the membrane surface were always within either 0.03 g/L or 1% of the concentration in the bulk of the ECS or ICS liquid.
- (8) The ECS manifold fluid is stagnant. At each time instant and over the whole axial length of each manifold, instantaneous equilibration of protein concentration occurs locally between the manifold and the adjacent portion of the fibre bundle (this is valid for both proteins). In addition, a small potting region that adjoins each ECS manifold is involved in instantaneous protein exchange with the terminal control volume at each end of the ECS. See section 3.2.2.5 for more information on the manifold concentration adjustment scheme used here.

### 3.2.2. Mathematical Formulation and Numerical Techniques

#### 3.2.2.1. *Pore Geometry and Hydrodynamics*

To properly account for the local changes in void fraction and pore curvature with radial position  $r$  (measured from the fibre axis), a differential annular membrane element

having length  $\Delta x$  and thickness  $dr$  is considered (fig. 11).<sup>8</sup> At this point, it will be convenient to introduce, without any loss of generality, the concept of an equivalent straight pore which has the same length and volume as the tortuous pore. The length of the pore within the differential element is

$$dh_p = \tau dr, \quad (39)$$

where  $\tau$  is the pore tortuosity. For a straight pore,  $\tau$  is a constant independent of  $r$  and equal to the ratio of pore length to membrane thickness. Simple geometric considerations show that

$$r_p = \tau r_{p,eff} \quad (40)$$

and

$$A_p = \tau A_{p,eff}, \quad (41)$$

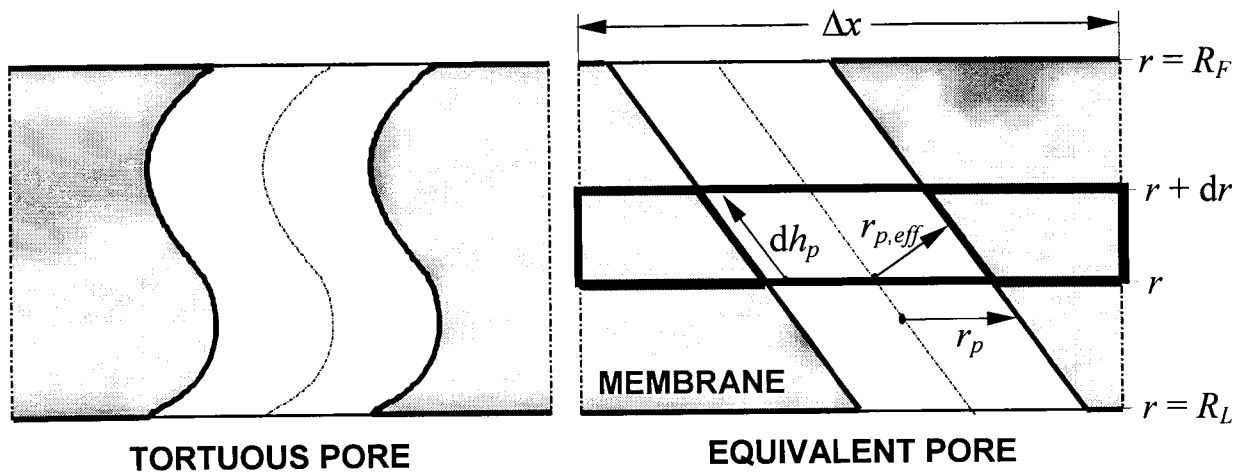


Fig. 11. An equivalent representation of a tortuous pore within a differential element of the hollow-fibre membrane (adapted from Łabęcki et al. (1998)).

<sup>8</sup>  $x \in \langle 0, L_F \rangle$ , the co-ordinate along the axis of the tortuous fibre, should be distinguished from  $z \in \langle 0, L \rangle$ , the co-ordinate along the axis of the HFBR cartridge.

where  $A_{p,eff} = N_{el} \pi r_{p,eff}^2$  is the pore area in the direction normal to the pore axis,  $A_p = N_{el} \pi r_{p,eff} r_p$  is the pore area measured in the  $x$ -direction (area of an ellipse with major half-axis  $r_p$  and minor half-axis  $r_{p,eff}$ ), and  $N_{el}$  is the number of pores within the membrane element under consideration. The ratio of  $A_p$  to the area of the membrane element at  $r$  defines the local cross-sectional porosity in the  $x$ -direction,  $\varepsilon(r)$ , such that

$$A_p = 2 \pi r \Delta x \varepsilon(r) \quad (42)$$

or, since  $A_p$  does not change with  $r$ ,

$$A_p = 2 \pi R_L \Delta x \varepsilon(R_L). \quad (43)$$

The volume of the membrane element is

$$dV(r) = 2 \pi r \Delta x dr, \quad (44)$$

while the pore volume within the element is

$$dV_p(r) = A_{p,eff} dh_p. \quad (45)$$

The ratio of these two differential volumes defines the local volumetric porosity, i.e.,

$$\varepsilon_v(r) = \frac{dV_p(r)}{dV(r)}, \quad (46)$$

which can be integrated over the membrane thickness to give the mean volumetric porosity,

$$\bar{\varepsilon}_v = \frac{2 R_L}{R_L + R_F} \varepsilon(R_L). \quad (47)$$

Combination of equations (39), (41), (42), and (44-46) yields

$$\varepsilon_v(r) = \varepsilon(r). \quad (48)$$

Equation (48) states that the local volumetric porosity should always be equal to the local cross-sectional porosity in the  $x$ -direction. This result is different from the relationship used, for example, by Sakai and co-workers (1987), who assumed that the volumetric porosity was a product of surface porosity and pore tortuosity. The reason for this difference is the

distinction made here between  $A_{p,eff}$  and  $A_p$ . Note also that, as expected, the mean volumetric porosity,  $\overline{\varepsilon_v}$ , lies between  $\varepsilon(R_L)$  and  $\varepsilon(R_F)$ .

To find a relationship between the effective pore radius,  $r_{p,eff}$ , and other membrane parameters, let us consider the transmembrane fluid flux, or superficial velocity, at  $r = R_L$ :

$$J_{TMF}(R_L) = \frac{L_p}{\mu} (P_L - P_S - \Delta\Pi_{eff}), \quad (49)$$

where  $P_L = P_L(x)$  and  $P_S = P_S(x)$  are the ICS and ECS hydrostatic pressures, respectively,  $\mu$  is the fluid viscosity and  $L_p$  is the membrane hydraulic permeability based on the membrane area at  $r = R_L$ . The effective osmotic pressure difference,  $\Delta\Pi_{eff}$ , can be expressed as

$$\Delta\Pi_{eff} = \sum_i \sigma_{re,i} (\Pi_{L,i} - \Pi_{S,i}), \quad (50)$$

where the summation is taken over all osmotically active species in the system,  $\Pi_{L,i}$  and  $\Pi_{S,i}$  are the ICS and ECS osmotic pressures, respectively, and  $\sigma_{re,i}$  is the Staverman osmotic reflection coefficient for the  $i$ th species (Staverman 1951). For a binary-protein system with one protein able to leak through the membrane (myoglobin) and one completely retained in the ECS (BSA), eq. (50) takes the form

$$\Delta\Pi_{eff} = \sigma_{re,M} (\Pi_{L,M} - \Pi_{S,M}) - \Pi_{S,A}, \quad (51)$$

where the subscripts  $M$  and  $A$  refer to myoglobin and albumin, respectively. The osmotic pressure for each protein is evaluated as a function of its local concentration in phosphate-buffered saline (PBS) as a reference fluid, using the relationship (Patkar et al. 1995)

$$\Pi(C) = \frac{R_g T}{M} (C + A_{\Pi 2} C^2 + A_{\Pi 3} C^3), \quad (52)$$

where  $R_g$  is the gas constant,  $T$  is the temperature,  $M$  is the protein molar mass, and  $A_{\Pi 2}$  and  $A_{\Pi 3}$  are the virial coefficients (see section 3.2.3).

If the Hagen-Poiseuille equation is used to describe pore hydrodynamics, then the transmembrane fluid flux can also be expressed as

$$J_{TMF}(R_L) = \frac{N_p \pi r_{p,eff}^4}{8 \mu} \cdot \frac{(P_L - P_S - \Delta\Pi_{eff})}{\tau (R_F - R_L)}, \quad (53)$$

where  $N_p$  is the number of pores per unit area of the membrane (at  $r = R_L$ ) and the second fraction on the right-hand side represents the linearised transmembrane pressure gradient,  $\tau (R_F - R_L)$  being the length of the pore. Combining eqs. (49) and (53) and noting that

$$\varepsilon(R_L) = N_p \pi r_{p,eff}^2 \tau \quad (54)$$

yields eventually the relationship

$$r_{p,eff} = \sqrt{8 L_p (R_F - R_L) k_m}, \quad (55)$$

where

$$k_m = \tau^2 / \varepsilon(R_L) \quad (56)$$

is the membrane constant, a parameter which plays a significant role in the subsequent analysis.

It is easy to show that the local fluid flux at any radial position  $r$  within the pore can be found from  $J_{TMF}(R_L)$  using

$$J_{TMF}(r) = \frac{R_L}{r} J_{TMF}(R_L) \quad (57)$$

and that the interstitial velocity inside the pore is related to  $J_{TMF}(r)$  through

$$v_p(h_p) = J_{TMF}(r) \frac{\tau}{\varepsilon_V(r)}, \quad (58)$$

which, upon making use of eq. (48), becomes

$$v_p(h_p) = J_{TMF}(r) \frac{\tau}{\varepsilon(r)}. \quad (59)$$

The results expressed in eqs. (57) and (59) will become useful when considering the convective solute transfer across the membrane (section 3.2.2.3 below).

### 3.2.2.2. ECS and ICS Hydrodynamics

The equations governing the ICS and ECS hydrodynamics are derived from the steady-state fluid balances for the representative hollow fibre, which lead to

$$\frac{d^2 P_L}{dx^2} = \frac{16 L_p}{R_L^3} (P_L - P_S - \Delta\Pi_{eff}) \quad (60)$$

and

$$\frac{d^2 P_S}{dx^2} = -\frac{16 L_p}{\gamma R_L^3} (P_L - P_S - \Delta\Pi_{eff}), \quad (61)$$

where  $x$  is the co-ordinate along the axis of the tortuous fibre. The ECS to ICS hydraulic permeability ratio,  $\gamma$ , can be determined experimentally or calculated from eq. (9) (section 2.2.1). In the closed-shell operational mode, equation (60) is subject to known-pressure or known-flow-rate (pressure-derivative) boundary conditions, whereas equation (61) is subject to no-flow (or zero pressure-derivative) boundary conditions at  $x = 0$  and  $x = L_F$ . Both equations (60) and (61) were discretised using a second-order finite difference method and the resulting set of linear algebraic equations was solved using a block tridiagonal matrix algorithm (Anderson et al. 1984). Since the osmotic pressure term,  $\Delta\Pi_{eff}$ , depends on the solute concentration, the pressure equations are coupled not only with each other but also with the ICS and ECS protein transport equations (see section 3.2.2.4 below).

### 3.2.2.3. Transmembrane Protein Transport

The approach presented in this section is based on an earlier theory (Anderson and Quinn 1974, Deen 1987), modified here for a hollow-fibre membrane having tortuous pores. The leaking protein molecules are approximated as rigid spheres and the solvent is treated as a continuum. The steady-state myoglobin mass balance equation for a differential membrane element (fig. 11) is in this case

$$\frac{\partial [A_p J_M(x, r)]}{\partial r} = 0, \quad (62)$$

where  $J_M(x, r)$  is the transmembrane myoglobin flux from the ICS to the ECS, evaluated per unit cross-sectional area of the pores. The protein flux along the pore axis,  $J_M(x, h_p)$ , is related to  $J_M(x, r)$  by

$$J_M(x, h_p) = \tau J_M(x, r) \quad (63)$$

and can be calculated as a sum of the diffusive and convective components, i.e.,

$$J_M(x, h_p) = -K_d D_M \frac{\partial C_M(x, h_p)}{\partial h_p} + K_c v_p(x, h_p) C_M(x, h_p), \quad (64)$$

where  $D_M$  is the unhindered protein diffusion coefficient,  $K_d$  and  $K_c$  are the diffusive and convective hindrance factors, respectively,  $v_p(x, h_p)$  is the interstitial velocity, and  $C_M(x, h_p) = C_M(x, r)$  is the pore protein concentration at a position  $x$  from the ICS inlet and a distance  $r$  from the fibre axis. Making use of eqs. (42) and (43) and substituting eqs. (63) and (64) along with eqs. (39), (57), and (59) into eq. (62) gives

$$J_M(x, r) = -\frac{K_d D_M}{\tau^2} \frac{\partial C_M(x, r)}{\partial r} + K_c \frac{J_{TMF}(x, R_L)}{\varepsilon(R_L)} C_M(x, r) \quad (65)$$

and, hence,

$$\frac{\partial}{\partial r} \left[ \frac{K_d D_M}{\tau^2} \frac{\partial C_M(x, r)}{\partial r} - K_c \frac{J_{TMF}(x, R_L)}{\varepsilon(R_L)} C_M(x, r) \right] = 0. \quad (66)$$

The boundary conditions for eq. (66) are

$$C_M(x, R_L) = \Phi C_{LM}(x) \quad (67a)$$

and

$$C_M(x, R_F) = \Phi C_{SM}(x), \quad (67b)$$

where  $C_{LM}(x)$  and  $C_{SM}(x)$  are the local concentrations of myoglobin in the ICS and ECS, respectively, and  $\Phi$  is the equilibrium partition coefficient (due to partial exclusion of protein molecules near the pore wall). Equation (66), subject to conditions (67), is readily solved for  $C_M(x, r)$  and  $\partial C_M(x, r)/\partial r$ , which are then substituted into eq. (65) to yield

$$J_M(x) = \frac{K_c J_{TMF}(x, R_L) \Phi}{\varepsilon(R_L)} \left[ C_{LM}(x) + \frac{C_{LM}(x) - C_{SM}(x)}{\exp[Pe_m(x) \cdot (R_F/R_L - 1)] - 1} \right]. \quad (68)$$

As can be seen, the transmembrane protein flux is independent of radial position in the membrane, although it varies with  $x$ . The pore Peclet number,  $Pe_m(x)$ , in eq. (68) is given by

$$Pe_m(x) = \frac{K_c J_{TMF}(x, R_L) R_L k_m}{K_d D_M}, \quad (69)$$

with  $k_m = \tau^2/\varepsilon(R_L)$  as defined by eq. (56). In the limiting cases of  $Pe_m \rightarrow \infty$  (dominant convection from ICS to ECS),  $Pe_m \rightarrow -\infty$  (dominant convection from ECS to ICS), and  $Pe_m \rightarrow 0$  (dominant diffusion), the bracketed expression in eq. (68) can be simplified to  $C_{LM}$ ,  $C_{SM}$ , and  $(C_{LM} - C_{SM})/[Pe_m(R_F/R_L - 1)]$ , respectively.

#### 3.2.2.4. ECS and ICS Protein Transport

The time-dependent distribution of the nonleaking protein (BSA) in the ECS is governed by the following convective-diffusive equation (Patkar et al. 1995):

$$\frac{\partial C_{S,A}}{\partial t} = D_A \frac{\partial^2 C_{S,A}}{\partial x^2} - \frac{\partial (u_S C_{S,A})}{\partial x}, \quad (70)$$

where  $C_{S,A}$  is the radially-averaged BSA concentration and  $D_A$  is the BSA diffusion coefficient (the functional dependence on  $x$  of  $C_{S,A}$  and  $u_S$  in eq. (70) is omitted). The ECS fluid velocity in the direction of the fibre axis,  $u_S$ , is calculated at each time step from the ECS axial pressure distribution, i.e.,

$$u_S = - \frac{\gamma R_L^4}{8\mu(R_K^2 - R_F^2)} \frac{dP_S}{dx}. \quad (71)$$

In the closed-shell operating mode, the boundary conditions for eq. (70) are no-flux (or zero concentration-derivative) conditions at  $x = 0$  and  $x = L_F$ . The initial condition is the known, uniform, concentration distribution at  $t = 0$ . Equation (70) was solved using the Crank-

Nicolson method (Anderson et al. 1984) with the power-law scheme (Patankar 1980, p. 90) to control the degree of upwinding as a function of the local Peclet number.

For the protein leaking through the membrane (myoglobin), a mass balance over a control volume in the ECS leads to (the functional dependence of  $C_{S,M}$ ,  $C_{L,M}$ ,  $J_M$ ,  $J_V$ , and  $Pe_m$  on  $x$  in the following equations has been omitted for clarity)

$$\frac{\partial C_{S,M}}{\partial t} = D_M \frac{\partial^2 C_{S,M}}{\partial x^2} - \frac{\partial (u_S C_{S,M})}{\partial x} + \frac{2 R_F \varepsilon (R_F)}{R_K^2 - R_F^2} J_M (R_F), \quad (72)$$

which, upon making use of  $R_F \varepsilon (R_F) = R_L \varepsilon (R_L)$  and substituting for  $J_M (R_F) = J_M$  from eq. (68), becomes

$$\begin{aligned} \frac{\partial C_{S,M}}{\partial t} = D_M \frac{\partial^2 C_{S,M}}{\partial x^2} - \frac{\partial (u_S C_{S,M})}{\partial x} + \\ + \frac{2 R_L K_c J_{TMF} (R_L) \Phi}{R_K^2 - R_F^2} \left[ C_{L,M} + \frac{C_{L,M} - C_{S,M}}{\exp [Pe_m (R_F / R_L - 1)] - 1} \right] \end{aligned} \quad (73)$$

The initial and boundary conditions as well as the solution method for the above equation are analogous to those applied to eq. (70).

Similarly, a mass balance for the leaking solute in the ICS incorporating eq. (68) yields

$$\frac{\partial C_{L,M}}{\partial t} = D_M \frac{\partial^2 C_{L,M}}{\partial x^2} - \frac{\partial (u_L C_{L,M})}{\partial x} - \frac{2 K_c J_{TMF} (R_L) \Phi}{R_L} \left[ C_{L,M} + \frac{C_{L,M} - C_{S,M}}{\exp [Pe_m (R_F / R_L - 1)] - 1} \right], \quad (74)$$

where the ICS fluid velocity,  $u_L$ , is calculated at each time step as

$$u_L = - \frac{R_L^2}{8 \mu} \frac{dP_L}{dx}. \quad (75)$$

The initial condition for eq. (74) is the known concentration at  $t = 0$ ,  $C_{L,M}(0)$ . The boundary condition at  $x = 0$  is specified as the known inlet concentration,  $C_{L,in,M}(t)$ , assumed here equal to the concentration in the well-mixed external volume,  $V_{EXT}$ , consisting of the ICS recycle fluid reservoir, the connecting tubing and the ICS manifolds at both ends of the cartridge.

$C_{L,M}(t)$  was updated at each time step using the recently calculated concentration at the fibre outlet,  $C_{L,out,M}(t - \Delta t)$ , the known  $V_{EXT}$  and the known ICS flow rate,  $Q_L$ . Since for all  $Q_L$  values of practical interest convection dominates protein transport in the ICS, the finite difference equivalent of eq. (74) has a fully upwind form, which corresponds to the limit of ICS Peclet number approaching infinity. Consequently,  $C_{L,out,M}(t)$  is obtained as part of the solution of eq. (74), without the need to specify the boundary condition at  $x = L_F$ .

For the solutions of eqs. (70), (73), and (74) to be numerically stable, the distance travelled by a fluid element within the chosen time step,  $\Delta t$ , should not exceed the axial grid increment,  $\Delta x$ . At a typical ICS flow rate of 300 mL/min and with 200 axial grid points, this stipulation is readily satisfied for a closed ECS (eqs. (70) and (73)). However, the stability of eq. (74) for the same conditions would require that  $\Delta t$  be smaller than about 0.07 s. Such a small time step would significantly extend the numerical solution time, considering that it can take weeks for a closed-shell hollow-fibre system with transmembrane protein leakage to reach steady state. However, if a sufficiently large  $\Delta t$  is used (e.g.,  $\Delta t = 300$  s), then the ICS concentration at each time step can be treated as constant throughout the entire recycle volume and equal to  $C_{L,M}(t)$ . In such a case, the change in  $C_{L,M}(t)$  can be calculated from the mass of protein that has leaked through the membrane during the interval  $\Delta t$  by integrating  $J_M(x)$  over the fibre length for all fibres, i.e.,

$$C_{L,M}(t) = \frac{C_{L,M}(t - \Delta t)V_{REC}(t - \Delta t) - 2\pi R_L \varepsilon(R_L) n \Delta t \int_0^{L_F} J_M(x) dx - C_{exp,j} V_{exp,j}}{V_{REC}(t)}, \quad (76)$$

where the recycle volume,  $V_{REC}(t)$ , is the sum of the ICS volume,  $V_L$ , and the external mixing volume,  $V_{EXT}(t)$ ; while  $C_{exp,j}$  and  $V_{exp,j}$  are the concentration and volume, respectively, of an ICS sample taken within the time interval between  $t - \Delta t$  and  $t$ . Note that the recycle volume is rendered a function of time to allow for its decrease due to sampling, i.e.,  $V_{REC}(t - \Delta t) = V_{REC}(t) + V_{exp,j}$ , where  $j$  is the sample index. If  $V_{exp,j} = 0$ , i.e., in the absence of sampling between  $t - \Delta t$  and  $t$ , eq. (76) simplifies to

$$C_{L,M}(t) = C_{L,M}(t - \Delta t) - \frac{2\pi R_L \varepsilon(R_L) n \Delta t}{V_{REC}(t)} \int_0^{L_F} J_M(x) dx. \quad (77)$$

Numerical solution of eq. (74) at various ICS flow rates, and sufficiently small  $\Delta t$  values, showed that  $C_{L,M}$  remained relatively constant over the length of the fibre, viz., within 1% of  $C_{L,in,M}$ . Thus, a satisfactory degree of solution accuracy could generally be obtained by using eqs. (76) and (77) rather than invoking the more time-consuming solution of eq. (74). Also, since the total (i.e., integrated over the fibre length) transmembrane myoglobin flux never varied by more than 0.3% between two consecutive time steps, the  $J_M$  values were lagged behind the ECS and ICS myoglobin concentration solutions. This simplified the numerical procedure by eliminating the need for extra iteration at each time step.

In the above analysis, it has been assumed that the transfer of myoglobin through the membrane is always quasi-steady, i.e., in essence, that the membrane pores have a negligible capacity for myoglobin. This assumption can be justified for the present system by the fact that the membranes occupy less than 7% of the total cartridge volume, their volumetric porosity (eq. (48)) is less than 100%, and the myoglobin partition coefficient is much less than 1 ( $\Phi \approx 0.02-0.03$ , see section 3.4). Indeed, model simulations indicated that less than 0.3% of the total myoglobin was retained in the membrane pores at any given time.

#### 3.2.2.5. ECS Manifold Extension

The ECS manifolds are annularly-shaped fibre-free regions which encompass the fibre bundle at each end and serve essentially as circumferential flow distributors for the ECS ports (see fig. 1). Since these regions may constitute (as in the cartridges used in this study) about 25-30% of the total ECS volume, they can absorb significant quantities of proteins, especially in the presence of downstream polarisation after extended periods of closed-shell operation (Piret and Cooney 1990b, Patkar et al. 1995). The influence of ECS manifolds has been included in the current model by means of a simple concentration adjustment scheme explained below and illustrated in fig. 12.

The fibre-free volume at each end of the ECS is divided into two parts: (i) the ECS manifold proper together with the adjacent port and tubing until the clamping point – these spaces are combined into one annular volume referred to as the manifold region; and (ii) the



As a consequence of these assumptions, the ECS solute concentrations calculated at each time step from eqs. (70) and (73) need to be appropriately adjusted. Performing a solute mass balance over a control volume around an axial grid point  $i$  at time  $t$  leads to

$$C_{S,ad}(i, t) = C_S(i, t) \frac{1}{1 + a_m a_{edg} + a_{pot}} + C_{S,ad}(i, t - \Delta t) \frac{1}{1 + (a_m a_{edg} + a_{pot})^{-1}}, \quad (78)$$

where  $C_{S,ad}$  is the adjusted local ECS concentration for either protein,  $C_S$  is its local ECS concentration prior to adjustment, and the constants  $a_m$ ,  $a_{edg}$ , and  $a_{pot}$  are calculated as

$$a_m = \frac{L}{L_F} \frac{V_{ff}}{z_m n \pi (R_K^2 - R_F^2)}; \quad (79)$$

$$a_{edg} = \begin{cases} \frac{z_m}{\Delta z} - \text{NINT} \left( \frac{z_m}{\Delta z} \right) + \frac{1}{2}, & \text{at } i = \text{NINT} \left( \frac{z_m}{\Delta z} \right) + 1, \quad i = N - \text{NINT} \left( \frac{z_m}{\Delta z} \right); \\ 1, & \text{at any other } i; \end{cases} \quad (80)$$

and

$$a_{pot} = \begin{cases} \frac{2V_{pot}}{n \pi \Delta z (R_K^2 - R_F^2)}, & \text{at } i=1, \quad i=N; \\ 0, & \text{at any other } i. \end{cases} \quad (81)$$

In the above equations,  $z_m$  is the axial length of the manifold,  $\Delta z$  is an axial grid increment along the cartridge axis,  $N$  is the total number of axial grid points,  $V_m$  is the volume of the manifold region,  $V_{pot}$  is the volume of the potting region, and NINT is a function returning the nearest integer value of its argument. Note that  $V_m$  and  $V_{pot}$  may be different for the upstream and downstream parts of the cartridge (see the following section on the model parameters).

### 3.2.3. Model Parameters

Values of the major model parameters are listed in table 3. Most of them are known from previous studies (Łabęcki 1994, Patkar et al. 1995) using the same Gambro GFE-15 hollow-fibre cartridges (Gambro Dialysatoren, Hechingen, Germany). The ECS to ICS

Table 3. Major parameters for the 1-D Krogh cylinder model of transmembrane protein transport in HFBRs

$R_L$	$1.09 \times 10^{-4}$ m
$R_F$	$1.24 \times 10^{-4}$ m
$R_{HFBR}$	0.01575 m
$R_m$	0.0206 m
$L$	0.215 m
$L_F$	0.238 m
$z_m$	0.021 m
$V_{pot}$	1.65 mL (upper limit)
$n$	8128
$L_p$	$7 \times 10^{-15}$ m
$\gamma$	1.795 (experimental)
$T$	4°C (277 K)
$\mu$	$1.567 \times 10^{-3}$ Pa·s (water, 4°C)
$r_M$	1.75 nm
$M_M$	16.9 kg mol <sup>-1</sup>
$M_A$	69 kg mol <sup>-1</sup>
$D_M$	$6.8 \times 10^{-11}$ m <sup>2</sup> s <sup>-1</sup> (4°C)
$D_A$	$4.2 \times 10^{-11}$ m <sup>2</sup> s <sup>-1</sup> (4°C)
$A_{\Pi 2,A}$	$1.0473 \times 10^{-2}$ g <sup>-1</sup> L
$A_{\Pi 3,A}$	$1.7374 \times 10^{-5}$ g <sup>-2</sup> L <sup>2</sup>
$N$	201

hydraulic permeability ratio in eq. (61),  $\gamma$ , was here determined experimentally by measuring the ECS and ICS flow rates and their corresponding pressure drops in the closed-lumen and closed-shell flow configurations, respectively. Although the value of  $\gamma$  obtained in this manner is almost 5 times higher than that resulting from eq. (9) (the main reason for the difference likely being ECS flow channelling due to fibre maldistribution), this fact subsequently turned out to have little impact on the simulation results. Since the above-mentioned measurements yielded a different ICS hydraulic permeability than that used before (Łabęcki 1994, Patkar et al. 1995), the wet lumen radius,  $R_L$ , was changed from the old value of  $1.15 \times 10^{-4}$  m to  $1.09 \times 10^{-4}$  m in order to preserve the validity of Hagen-Poiseuille equation for the ICS. The new  $R_L$  value is almost identical to that specified by the

manufacturer ( $1.10 \times 10^{-4}$  m). An extensive series of flow and pressure measurements in the dead-end filtration mode was also performed to determine how the membrane hydraulic permeability,  $L_p$ , was affected by prolonged exposure of the fibres to ICS recycle flows and to myoglobin solutions. As a result of these measurements, an  $L_p$  value of  $7 \times 10^{-15}$  m was determined, which was constant within experimental error over a period of six weeks and did not change after two weeks of contact with myoglobin solution. These tests also indicated that there was no adsorption of myoglobin to the hollow-fibre membranes used in this study.

The ICS recycle volume in eqs. (76) and (77),  $V_{REC}$ , measured at the end of each leakage experiment, ranged between 145.0 mL and 236.2 mL. The  $V_m$  and  $V_{pot}$  values needed in eqs. (79) and (81) were estimated individually for each experiment and ranged from 13.2 mL to 15.4 mL and from 0 mL to 1.65 mL, respectively. The variation in  $V_m$  was caused by slight differences in the positioning of the clamp closing the ECS port, while the exact  $V_{pot}$  value depended on the fraction of the potting region filled with air.

The fluid viscosity was assumed equal to that of water and was calculated as a function of temperature based on available literature data (Weast 1975, F-49). The protein diffusivities were obtained by extrapolation of the values reported for myoglobin (Balakrishnan et al. 1993) and BSA (van den Berg and Smolders 1989) to the experimental temperature of 4°C using the Stokes-Einstein equation, which implies that  $D\mu/T$  should be constant for a given solute. The effective myoglobin radius,  $r_M$ , was taken as the middle value of the three half-axis lengths (1.25 nm, 1.75 nm, and 2.25 nm) found from X-ray diffraction data by Colton and co-workers (1971). The virial coefficients  $A_{\Pi 2,A}$  and  $A_{\Pi 3,A}$  in the relationship between the osmotic pressure and BSA concentration were based on the values determined earlier by fitting eq. (52) to available experimental data (Patkar et al. 1995). Because of the lack of such data for myoglobin, and since only relatively dilute myoglobin solutions were used in this study, the virial coefficients for this protein were assumed to be zero.

There still remain five unknown parameters in the present model: the membrane constant,  $k_m$ , and four transmission parameters for the leaking protein, i.e., the partition coefficient,  $\Phi$ , the osmotic reflection coefficient,  $\sigma_{re}$ , and the diffusive and convective hindrance factors,  $K_d$  and  $K_c$ . Since a model with so many adjustable parameters would be of

limited use, available theory was utilised here to relate  $k_m$ ,  $\Phi$ ,  $\sigma_{re}$ ,  $K_d$ , and  $K_c$  to the effective pore radius,  $r_{p,eff}$ , thus reducing the number of unknown parameters to one. The partition coefficient was calculated using the following equation obtained by several authors (Renkin 1954, Colton et al. 1971):

$$\Phi = (1 - \lambda)^2, \quad (82)$$

where  $\lambda$  is the ratio of the effective protein and pore radii. The osmotic reflection coefficient, originally defined by Staverman (1951), was calculated using the relationship

$$\sigma_{re} = (1 - \Phi)^2, \quad (83)$$

valid for spherical solutes in cylindrical pores with inert walls (Anderson and Malone 1974). The hindrance factors were evaluated from the following expressions derived for closely fitting spheres translating along the pore centre-line (Bungay and Brenner 1973):

$$K_d = \frac{6\pi}{K_t} \quad (84)$$

and

$$K_c = \frac{(2 - \Phi)K_s}{2K_t}, \quad (85)$$

where  $K_t$  and  $K_s$  are defined by

$$\begin{bmatrix} K_t \\ K_s \end{bmatrix} = \frac{9}{4} \pi^2 \sqrt{2} (1 - \lambda)^{-5/2} \left( 1 + \sum_{n=1}^2 \begin{bmatrix} a_n \\ b_n \end{bmatrix} (1 - \lambda)^n \right) + \sum_{n=0}^4 \begin{bmatrix} a_{n+3} \\ b_{n+3} \end{bmatrix} \lambda^n \quad (86)$$

and the coefficients in eq. (86) are:  $a_1 = -73/60$ ,  $a_2 = 77293/50400$ ,  $a_3 = -22.5083$ ,  $a_4 = -5.6117$ ,  $a_5 = -0.3363$ ,  $a_6 = -1.216$ ,  $a_7 = 1.647$ ,  $b_1 = 7/60$ ,  $b_2 = -2227/50400$ ,  $b_3 = 4.018$ ,  $b_4 = -3.9788$ ,  $b_5 = -1.9215$ ,  $b_6 = 4.392$ , and  $b_7 = 5.006$ .

The transmission parameters for the model simulations were thus determined as follows:

- 1) assume a value for  $k_m$ ;
- 2) calculate  $r_{p,eff}$  from eq. (55);

3) calculate  $\lambda = r_M / r_{p,eff}$ ; and

4) evaluate  $\Phi$ ,  $\sigma_{re}$ ,  $K_d$ , and  $K_c$  as functions of  $\lambda$  from eqs. (82)-(85), respectively.

In the simulations of the leakage experiments (see the following section), the solution procedure initiated by the above input was repeated for different  $k_m$  values until the best-fit membrane constant was found. The best-fit  $k_m$  was determined as the value which minimised the standard deviation,  $SD$ , of the predicted versus experimental transient ICS myoglobin concentration data, i.e.,

$$SD = \sqrt{\frac{\sum_{j=1}^{N_{exp}} [C_{exp,j} - C_{L,M}(t)]^2}{N_{exp} - 1}}, \quad (87)$$

where  $j$  is the index of an ICS sample taken at time  $t$ ,  $C_{exp,j}$  is its concentration,  $C_{L,M}(t)$  is the model-predicted ICS concentration at time  $t$ , and  $N_{exp}$  is the total number of ICS samples in a given experiment. For comparison, two-parameter fitting of the experimental data was also carried out in which a second adjustable parameter, usually  $K_d$ , was used in addition to  $k_m$ .

### 3.3. Experimental Procedures

#### 3.3.1. Cartridge Pretreatment

A series of Gambro GFE-15 dialysis cartridges (Gambro Dialysatoren, Hechingen, Germany) equipped with Cuprophan (regenerated-cellulose) hollow-fibre membranes (MWCO  $\approx$  18 kDa) were employed in this study. Prior to each experiment, a fresh cartridge was subjected to a rinsing pretreatment procedure in order to cleanse and deaerate the fibres, allowing them to assume their equilibrium dimensions under wet conditions. A lack of reproducible results during preliminary experimental work with these cartridges indicated that insufficient rinsing could have a significant influence on transmembrane protein leakage, most likely due to the disturbing effect of residual air or other contaminants that were not completely removed from the cartridge. Consequently, after a series of trials, an enhanced pretreatment protocol was finally established that allowed removal of the potential contaminants from the membrane pores by both diffusion and convection, without their

being recycled back into the cartridge. The rinsing solution, prepared from ten parts of distilled water and one part of double-filtered PBS, was pumped through the cartridge using peristaltic pumps (Cole-Parmer, Barrington, Illinois). In order to provide effective air removal during the pretreatment, the cartridge was inclined at 45° to horizontal and the flow was directed upwards.

The pretreatment protocol consisted of the following steps:

- 1) ICS rinsing in the single-pass closed-shell flow configuration at 30 mL/min, until about 500 mL of effluent was collected from the ICS outlet;
- 2) membrane rinsing (from ICS to ECS) in the single-pass dead-end filtration mode at 5 mL/min for 20-24 h, followed by 15 mL/min for 2 h;
- 3) recirculation of about 2 L of rinsing solution through the ECS in the closed-lumen flow configuration at 300-400 mL/min for 30 min, with energetic shaking and tapping of the cartridge to dislodge air bubbles and thus maximise the wetting of fibres; and
- 4) equilibration for at least 20 h with all ports closed, i.e., in the absence of flow.

All of the above steps were carried out at room temperature (20-23°C). After the last step, the liquid was drained out of the intra- and extracapillary spaces and the cartridge was ready for a leakage experiment. The effectiveness of the established pretreatment procedure was subsequently confirmed by the markedly improved consistency of the protein leakage behaviour.

### 3.3.2. Leakage Experiments

Solutions of horse heart myoglobin (Sigma, St. Louis, Missouri) in PBS were used in all the experiments described below. To inhibit microbial growth, sodium azide (Baker, Phillipsburg, New Jersey) was added and the experiments were conducted in a cold room at 4°C (277 K). The initial studies revealed that the myoglobin solutions tended to become cloudy when recirculated through the ICS at 50-300 mL/min, resulting in up to 50% protein loss within 24 h. This was likely caused by myoglobin denaturation due to oxidation at the air-liquid interface (Harrington et al. 1991). A series of supplementary experiments demonstrated that this problem could be virtually eliminated by the addition of a surface-active compound, which would preferentially adsorb at the air-liquid interface. Serodex

NNP 10 (Servo Delden, Netherlands), containing polyoxyethelene nonyl-phenol (POENP, MM = 660 Da) (Enyart 1967), was selected from several surfactants tested. The so-called base solution was prepared by dissolving 0.2 mass%  $\text{NaN}_3$  and 0.004 vol% POENP in PBS. Because of their small size, the POENP molecules were assumed to distribute uniformly throughout the hollow-fibre cartridge, such that the local levels of POENP never exceeded its critical micelle concentration of 0.006 vol% (Becher 1961).

The conditions of the leakage experiments carried out here are summarised in table 4. The myoglobin solution was initially placed either in the ECS (#1, #2, #5, #6 and #7) or in the ICS (#3 and #4). In experiments #4, #5 and #7, BSA was additionally loaded into the ECS. In each experiment, the base solution containing either myoglobin (#1, #2 and #6), BSA (#4), both of these proteins (#5 and #7), or neither of them (#3) was first recirculated at 120-420 mL/min through the ECS of a pretreated cartridge using a peristaltic pump (Cole-Parmer). The cartridge was tilted and tapped to ensure removal of air from the ECS. After about 30-40 min, the protein concentration in the ECS was assumed to be uniform and a sample of ECS fluid was taken (except in #3). The pump was then stopped and both ECS ports were clamped. Afterwards, the cartridge was positioned vertically and an upward flow through the ICS was started, using the base solution with (#3 and #4) or without myoglobin

Table 4. Summary of leakage experiments (note: experiment #1 was conducted by Yves Dudal)

#	Flow rate (mL/min)	Duration	Initial ECS myoglobin concentration (g/L)	Initial ICS myoglobin concentration (g/L)	Initial ECS BSA concentration (g/L)
1	300	863.0 h (36.0 days)	2.93	< 0.01	0
2	300	195.5 h (8.1 days)	2.62	0.01	0
3	300	185.2 h (7.7 days)	0	1.23	0
4	300	190.5 h (7.9 days)	0	1.25	15.8
5	300	185.2 h (7.7 days)	2.79	< 0.01	16.5
6	10	191.8 h (8.0 days)	2.72	0.03	0
7	10	191.8 h (8.0 days)	2.75	0.03	16.7

(#1, #2, #5, #6 and #7). This flow was maintained at about 300 mL/min until no more air bubbles were seen in the effluent, i.e., for 30-45 min. At that point, the ICS flow direction was reversed and the flow rate was appropriately adjusted, which signified the formal onset of the experiment ( $t = 0$ ). To account for the amount of myoglobin transferred from the ECS to the ICS prior to  $t = 0$  (table 4), the initial ECS concentration was recalculated as  $C_{S,M}(0) - C_{L,M}(0)V_{REC}(0)/V_{ECS}$ . The vertical orientation of the cartridge and the downward flow direction were chosen in order to minimise free-convective protein transport (see also chapter 5).

The experimental setup is shown in fig. 13. ICS samples of 1.0-2.5 mL volume were periodically taken from the recycle flask through the sampling port with a syringe. The recycle flask was raised and maintained above the cartridge level in order to avoid problems with fluid degassing and partial fibre blockage by air bubbles, particularly in the low-flow-rate experiments (#6 and #7). Because of the dark-red colour of myoglobin, its redistribution within the ECS as well as between the ECS and ICS could be traced over time by visual observations through the transparent walls of the cartridge and of the ICS recycle flask. At the end of each experiment, the ICS fluid was collected in the recycle flask by pumping air at about 300 mL/min through the fibre lumina, the last ICS sample was taken, and the final recycle fluid volume was measured. After detaching the ICS tubing, the cartridge was transferred, without changing its vertical orientation, to a container filled with liquid nitrogen (except in experiment #1), in which it remained immersed for about 20 min. The frozen cartridge was stored at  $-20^{\circ}\text{C}$  until further analysis.

### 3.3.3. Protein Analysis

The HFBR cartridges were frozen in liquid nitrogen at the end of each experiment in order to fix the final protein distributions (Piret and Cooney 1990b). Each frozen cartridge was sectioned into about 10 disc-shaped pieces, whose axial dimensions were measured. The ECS manifold segments were additionally cut at  $r = R_{HFBR}$  to isolate the fibre-free annulus. The ECS ports and the “potting regions” (see fig. 12) were also cut off and retained for analysis. The lumen manifolds and epoxy potting were removed from both ends of the

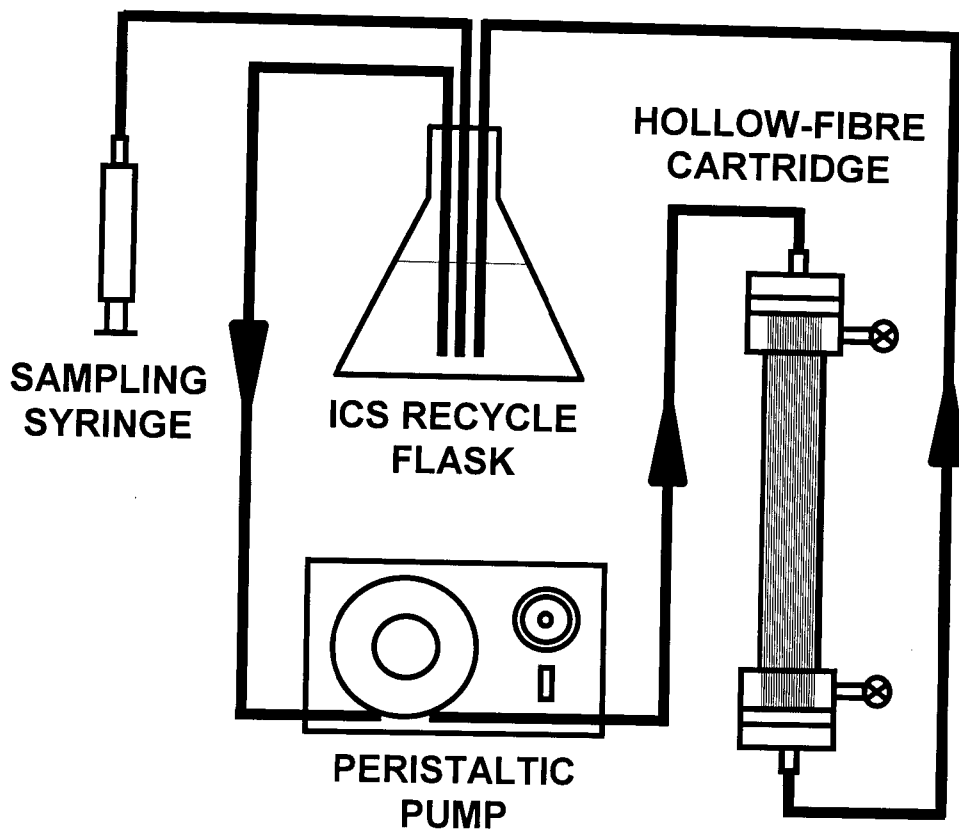


Fig. 13. Setup of a hollow-fibre leakage experiment.

cartridge and discarded. All of the collected pieces were thawed and the extracted fluid samples were centrifuged to separate the dust particles produced during cartridge sawing. The ECS and ICS fluid volumes within each axial segment were calculated from the known dimensions of the segment and of the fibres.

The protein contents in the samples were analysed using a Spectronic 601 spectrophotometer (Milton Roy, Rochester, New York). The ICS and ECS myoglobin concentrations were found by absorbance measurements at 405 nm. For the BSA-containing samples, the total (myoglobin and BSA) ECS protein concentrations were determined using the Bio-Rad protein assay (Bio-Rad, Hercules, California) and absorbance measurements at 595 nm. The BSA concentration was then calculated as the difference between the total ECS protein and the ECS myoglobin concentrations.

### 3.4. Results and Discussion

#### 3.4.1. ICS Myoglobin

The major results of the leakage experiments and their best-fit model simulations are summarised in table 5. The best-fit  $k_m$  and the corresponding  $r_{p,eff}$ ,  $K_d$ ,  $K_c$ ,  $\Phi$ , and  $\sigma_{re}$  values for each experiment were found as outlined in section 3.2.3 above. The mass balance for each protein was determined as the ratio of the amount of protein recovered from both the ECS and ICS at the end of the experiment as well as from ICS samples, to the amount of protein initially introduced to the cartridge. The leakage fraction was calculated as the net change in ECS myoglobin content over the experiment duration, relative to the total amount of myoglobin in the system at  $t = 0$ , with positive values indicating leakage from the ECS to the ICS. The choice of the more accurate eq. (74) or the approximate eqs. (76) and (77) for determining the ICS myoglobin concentration had no significant impact on the simulation results, even for the low-flow-rate experiments #6 and #7.

Figure 14 shows the temporal variations of ICS myoglobin concentration for the short-term experiments (#2-7), with the myoglobin initially loaded into the ECS (fig. 14a) or into the ICS (fig. 14b). Generally, a very good fit was obtained for each of these experiments. The long-term experiment #1, in which both the mass balance and the agreement between predicted and measured data were poorer (see table 5), will be discussed

Table 5. Summary of the ICS results of the experimental and simulation leakage studies

#	Myoglobin mass balance	BSA mass balance	Myoglobin leakage fraction		Best fit parameters					
			Exp.	Model	$k_m$	$r_{p,eff}$ (nm)	$K_d$	$K_c$	$\Phi$	$\sigma_{re}$
1	71 %	-	+34 %	+26 %	4.53	1.95	0.0023	1.13	0.011	0.98
2	90 %	-	+27 %	+26 %	4.86	2.02	0.0046	1.17	0.018	0.96
3	86 %	-	-50 %	-50 %	5.41	2.13	0.0099	1.23	0.032	0.94
4	97 %	79 %	-27 %	-26 %	5.05	2.06	0.0062	1.19	0.023	0.96
5	99 %	96 %	+52 %	+52 %	5.20	2.09	0.0077	1.21	0.026	0.95
6	101 %	-	+54 %	+58 %	5.14	2.08	0.0071	1.20	0.025	0.95
7	99 %	108 %	+55 %	+57 %	5.14	2.08	0.0071	1.20	0.025	0.95

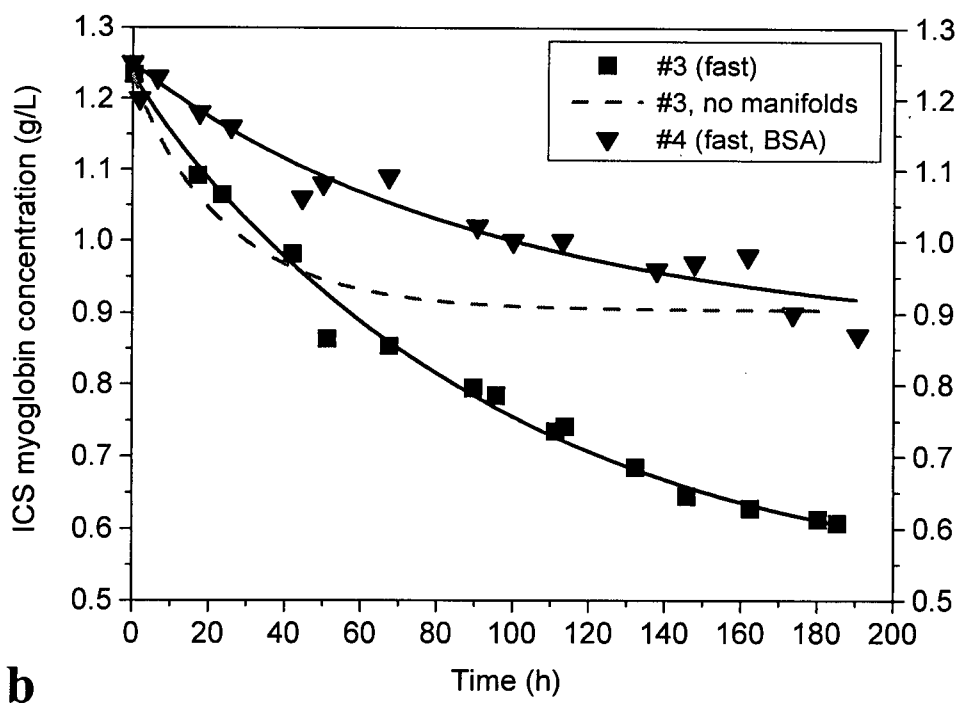
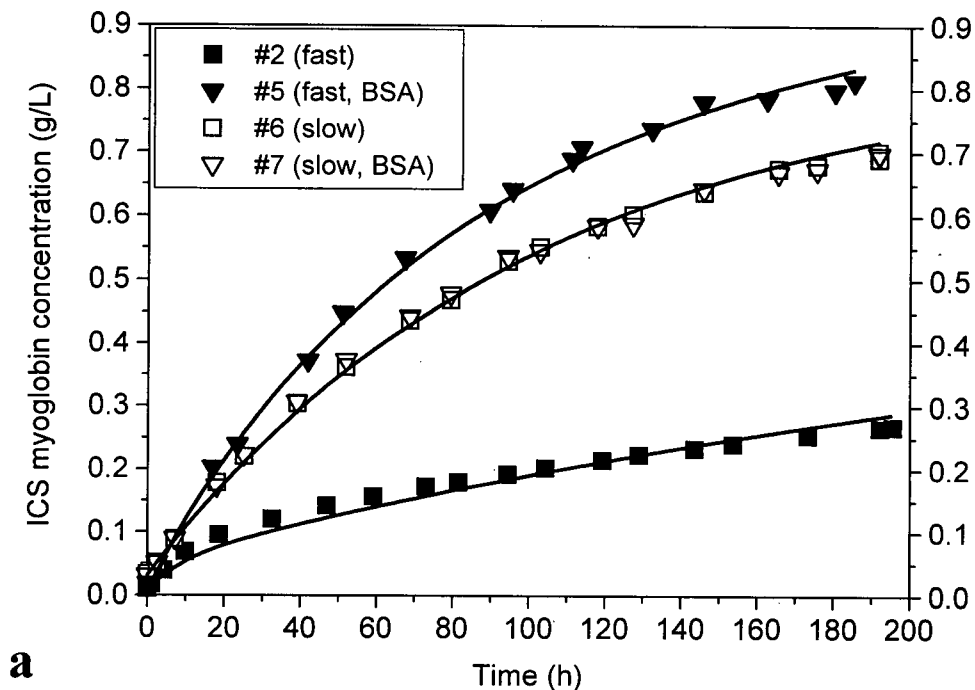


Fig. 14. Changes of ICS myoglobin concentration with time in experiments with myoglobin loaded into the ECS (a) or ICS (b). Symbols – experimental data, solid lines – best-fit model predictions, dashed line – best-fit model prediction without the ECS manifold extension; *fast*,  $Q_L = 300$  mL/min; *slow*,  $Q_L = 10$  mL/min; *BSA*, BSA present in the ECS. The best-fit curves for experiments #6 and #7 are practically identical.

in more detail in section 3.4.3 below. Despite some scatter in the best-fit parameters for different experiments (table 5), the trends and relative positions of the model curves plotted in fig. 14 remain unchanged if the same  $k_m$  value (5.14, the average from the short-term experiments #2-6) is used in all simulations. The issue of the  $k_m$  scatter will be addressed in more depth in section 3.4.3 below.

One striking aspect of the ICS results presented here is the strong influence of BSA on myoglobin leakage in the high-flow-rate experiments (#2 vs. #5 and #3 vs. #4). The presence of BSA caused a substantial elevation of the final level of myoglobin in the ICS by either increasing (#5) or decreasing (#4) the rate of its transmembrane passage (fig. 14). On the other hand, no effect of BSA on the ICS myoglobin profiles was seen in the low-flow-rate experiments (#6 vs. #7). Another interesting result is a significant increase in the net rate of myoglobin leakage as a consequence of ICS flow reduction in the absence of BSA (#2 vs. #6, fig. 14a and table 5). Although a decrease in transmembrane fluid fluxes in experiments #6 and #7 might be expected to reduce the rate of myoglobin transfer from the ECS to the ICS, quite the opposite effect was observed (fig. 14a). The relatively fast increase in the ICS myoglobin concentration in these two experiments, despite lower magnitudes of pressure difference across the membrane, suggests that diffusion was the dominant mechanism of transmembrane protein transport in this case. On the other hand, convective enhancement of myoglobin transfer from the downstream-concentrated region of the ECS over to the lumen side might have been responsible for the faster leakage observed in the high-flow-rate experiment #5, relative to #6 and #7.

#### 3.4.2. ECS Myoglobin and BSA

To gain a better understanding of the ICS results presented in the previous section, it is helpful to consider the corresponding final protein distributions in the ECS (figs. 15-18).<sup>9</sup> Figures 15-18 plot the model-predicted ECS concentration data as smooth lines and the experimental data as step lines, the axial dimension of each step corresponding to the length of one segment obtained by cartridge sectioning. As seen in figs. 15-17, the ECS Starling

---

<sup>9</sup> Note that the ECS data were not fitted; i.e., the model-predicted ECS protein distribution at the end of each experiment was part of the solution obtained by fitting the ICS data only.

flow in the high-flow-rate experiments was sufficiently strong to cause downstream protein polarisation. Starting from a uniform ECS concentration field, the downstream protein buildup zone would usually become distinct after about 10-20 h, as in the case of myoglobin in experiments #2 and #5 (figs. 15a and 17a, respectively) or BSA in experiments #4 and #5 (figs. 16b and 17b, respectively). If myoglobin was initially absent from the ECS, as in experiments #3 and #4 (figs. 15b and 16a, resp.), the high-concentration myoglobin zone did not appear until a sufficient amount of the protein had passed from the ICS to the ECS, which took about 20-50 h. In contrast to the ECS myoglobin and BSA profiles presented in figs. 15-17, the distributions of both proteins in experiments #6 and #7 were relatively uniform over the whole length of the ECS (fig. 18). For instance, the ECS BSA concentration in #7 (not shown) did not differ by more than 8% from its average value. The reduction of the ICS flow rate from 300 mL/min to 10 mL/min greatly diminished downstream protein polarisation in the ECS. The osmotic effects associated with the

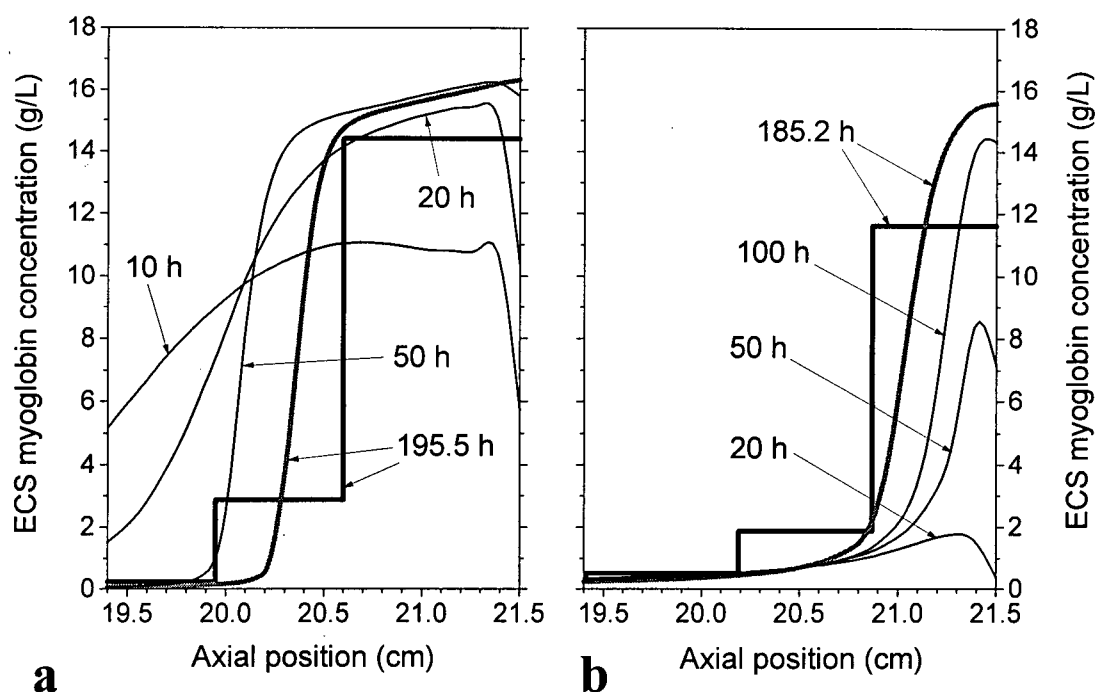


Fig. 15. Model-predicted (smooth curves) and experimental (step lines) ECS myoglobin concentrations within the length of the downstream manifold: *a*, experiment #2 (myoglobin loaded into the ECS); *b*, experiment #3 (myoglobin loaded into the ICS). No BSA, ICS flow from left to right,  $Q_L = 300$  mL/min.

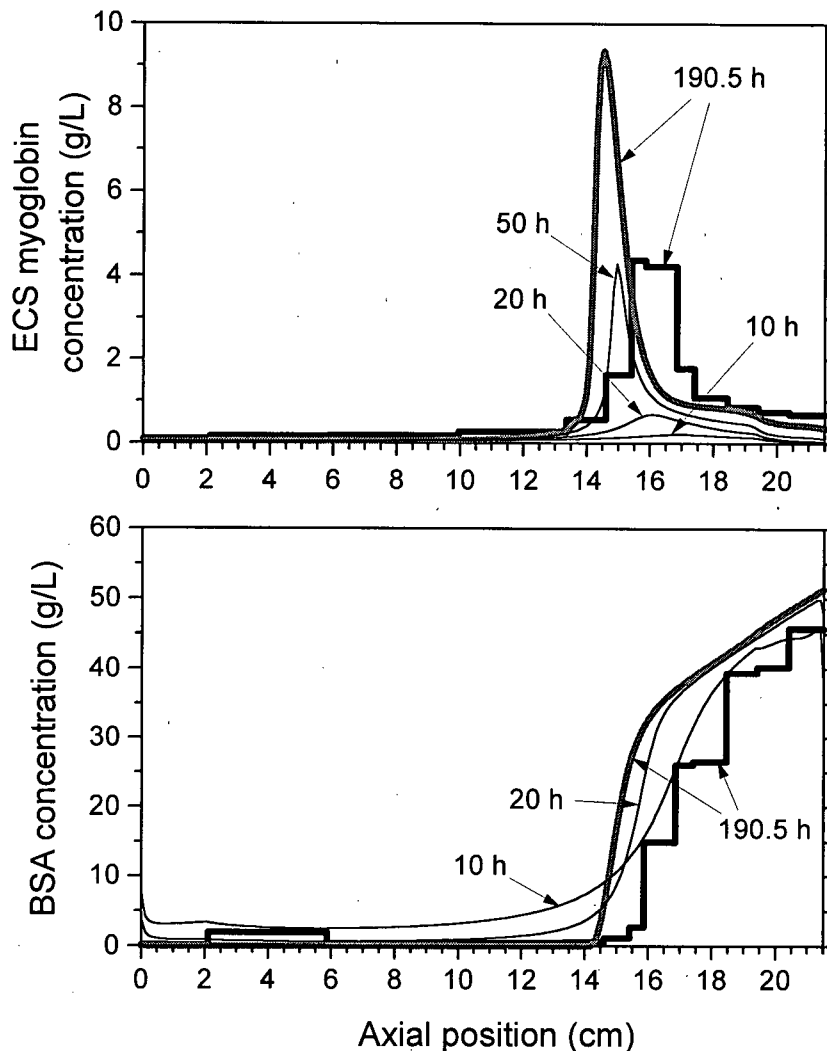


Fig. 16. Model-predicted (smooth curves) and experimental (step lines) concentrations of ECS myoglobin and BSA in experiment #4 (myoglobin loaded into the ECS). ICS flow from left to right,  $Q_L = 300$  mL/min.

presence of BSA in experiment #7 (fig. 18b) caused a further decrease in the ECS convective flow, to the point of virtually eliminating the downstream polarisation phenomenon.

When the total protein concentration, and hence the osmotic pressure, in the downstream-polarised zone reached a sufficiently high level, as in the high-flow-rate experiments #2-5, the fluid flow within the zone practically ceased (Taylor et al. 1994). This phenomenon was particularly noticeable in experiments #4 and #5 (figs. 16 and 17,

respectively), where the BSA polarisation region extended approximately 5 cm from the downstream end of the ECS. In both of these experiments, a distinct maximum of myoglobin concentration developed near the boundary of the BSA zone as the myoglobin continuously passing from the ICS to the ECS was being convectively swept downstream. The local maximum in experiment #5 became noticeable only after a sufficient amount of myoglobin had transferred from its initial downstream polarisation zone to the ICS and then

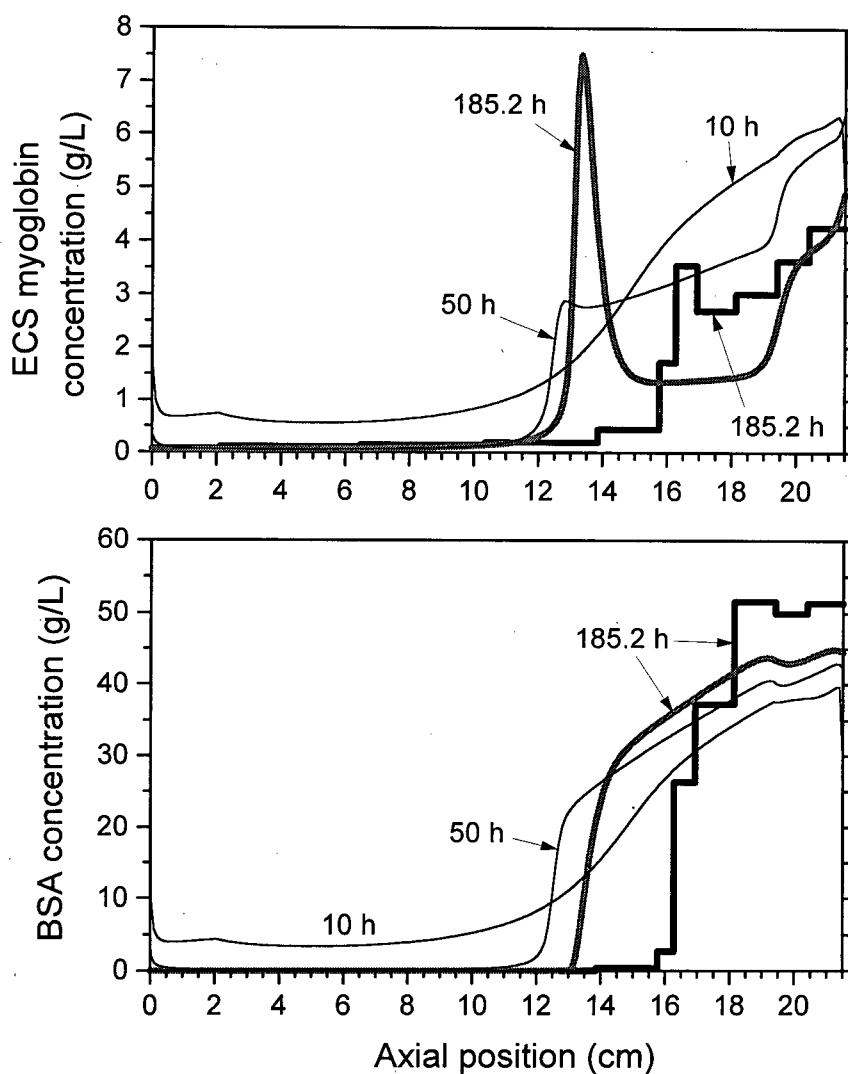


Fig. 17. Model-predicted (smooth curves) and experimental (step lines) concentrations of ECS myoglobin and BSA in experiment #5 (myoglobin loaded into the ICS). ICS flow from left to right,  $Q_L = 300$  mL/min.

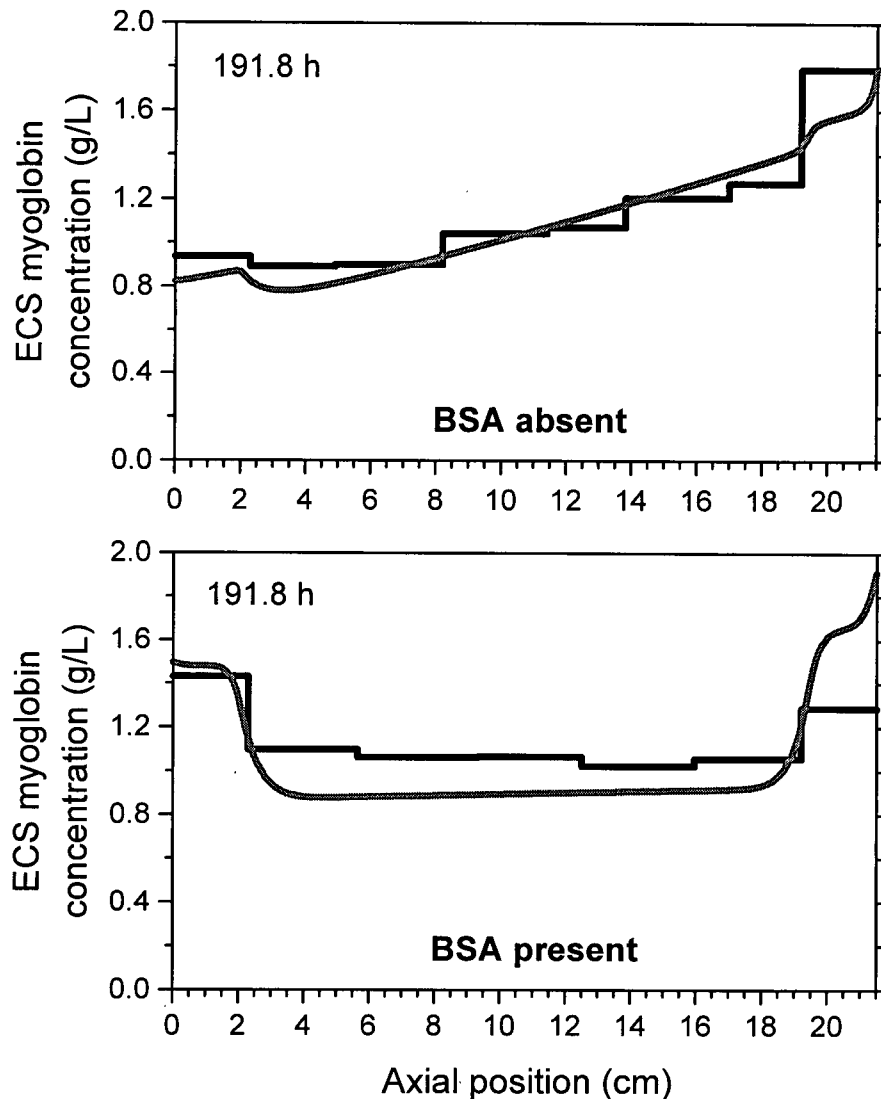


Fig. 18. Model-predicted (smooth curves) and experimental (step lines) concentrations of ECS myoglobin at the completion of experiments #6 (upper panel) and #7 (lower panel). ICS flow from left to right,  $Q_L = 10$  mL/min.

back to the ECS, which took about 50-60 h. In experiment #4, since all of the myoglobin was initially present in the ICS, the whole process required less time, and the ECS concentration maximum appeared after only about 20 h.

After about 30 h from the onset of the high-flow-rate experiments without BSA (#2 and #3), practically all of the ECS myoglobin was already polarised within the length of the downstream manifold, i.e., between 19.4 cm and 21.5 cm of the ECS length (fig. 15). In fact,

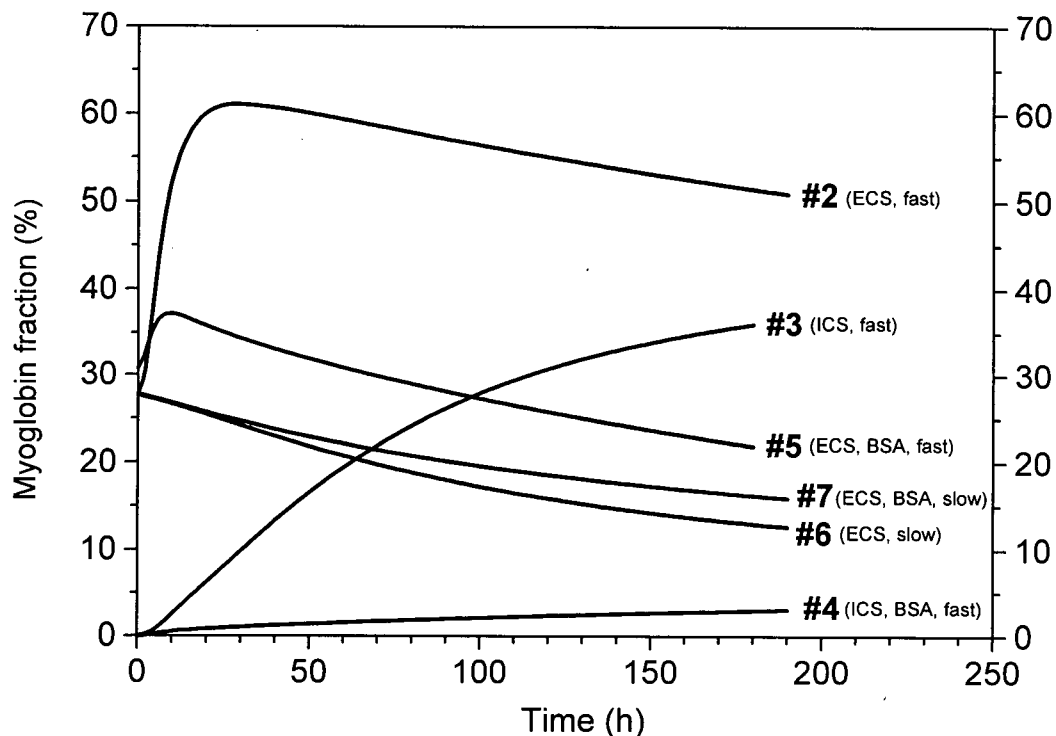


Fig. 19. Model predictions of the time-dependent changes in the fraction of total myoglobin present in the ECS fibre-free regions for the conditions of experiments #2-7; *ECS*, myoglobin loaded into the ECS; *ICS*, myoglobin loaded into the ICS; *fast*,  $Q_L = 300$  mL/min; *slow*,  $Q_L = 10$  mL/min.

most of the polarised myoglobin was present in the manifold and potting regions (see fig. 12), the total volume of which was about twice the volume of the adjacent portion of the ECS. The entrapment of myoglobin in these fibre-free regions effectively reduced its concentration in the ECS fibre bundle, which in turn affected the rate of myoglobin transfer across the membrane. Indeed, some degree of correlation appears to exist between the transient levels of ICS myoglobin or the rate of its leakage on the one hand (fig. 14) and the fraction of myoglobin trapped in the fibre-free regions of the ECS on the other (fig. 19).<sup>10</sup> For example, the average fraction of myoglobin present in the fibre-free regions was predicted to be about 20% for the conditions of the low-flow-rate experiment #6, versus about 55% for its high-flow-rate counterpart #2 (fig. 19). This is fairly consistent with the

<sup>10</sup> As was the case for the data plotted in fig. 14, the relative positions and shapes of the curves in fig. 19 are unchanged if the same  $k_m$  value (5.14) is used in the simulations for all experiments.

ratio of the ECS-to-ICS myoglobin transfer rates for these two experiments, which – as can be seen from fig. 14 – is about 2.5. In both low-flow-rate experiments (#6 and #7), the amounts of myoglobin contained within the ECS manifolds were very similar (fig. 19) and, hence, the corresponding ICS myoglobin concentration profiles were almost identical (fig. 14). A slight anomaly in this trend, however, can be noticed in the relative positions of the curves pertaining to the high-flow-rate experiment #5 and its low-flow-rate counterpart #7, in both of which BSA was present. As was mentioned above, this may perhaps be attributed to the convective enhancement of transmembrane myoglobin fluxes in the downstream part of the ECS in experiment #5.

Inclusion of the ECS fibre-free regions in the model considerably improved the quality of the ICS myoglobin concentration predictions. This was reflected both in the reduced values of the best-fit  $SD$  as defined by eq. 87 and in the less scattered best-fit  $k_m$  values for different experiments (fig. 20). The most dramatic effect of the manifold extension is visible in the results obtained by fitting the data of experiment #3. When the ECS fibre-free regions were neglected in the model, the obtained best-fit profile of ICS myoglobin concentration vs. time levelled off at about 0.9 g/L (fig. 14b, dashed line). The extended model version, on the other hand, correctly predicted that the ICS concentration is close to 0.6 g/L after 180 h and that the trend of its further changes with time is declining.

The major influence of BSA on the ICS myoglobin profiles in different experiments (fig. 14) is clearly associated with the above-described effects of the ECS manifolds. For example, since the ECS myoglobin concentration maxima in experiments #4 and #5 were located at the boundary of the BSA zone and upstream of the manifold region, the quantities of myoglobin trapped in the downstream manifold were significantly less than those in the corresponding experiments without BSA (i.e., #3 and #2, resp.). Consequently, the presence of BSA caused an increase in the net amount of myoglobin transferred through the membranes from the ECS to the ICS (#5 vs. #2) and a decrease in the net amount transferred from the ICS to the ECS (#4 vs. #3). The extremely low level of myoglobin present in the fibre-free regions throughout the duration of experiment #4 (fig. 19) also suggests that, with proper optimisation of the relevant operating procedures, addition of a nonleaking protein such as BSA to the ECS could provide a means of reducing the depletion of low-concentration growth factors from the ECS of cell culture HFBRs.

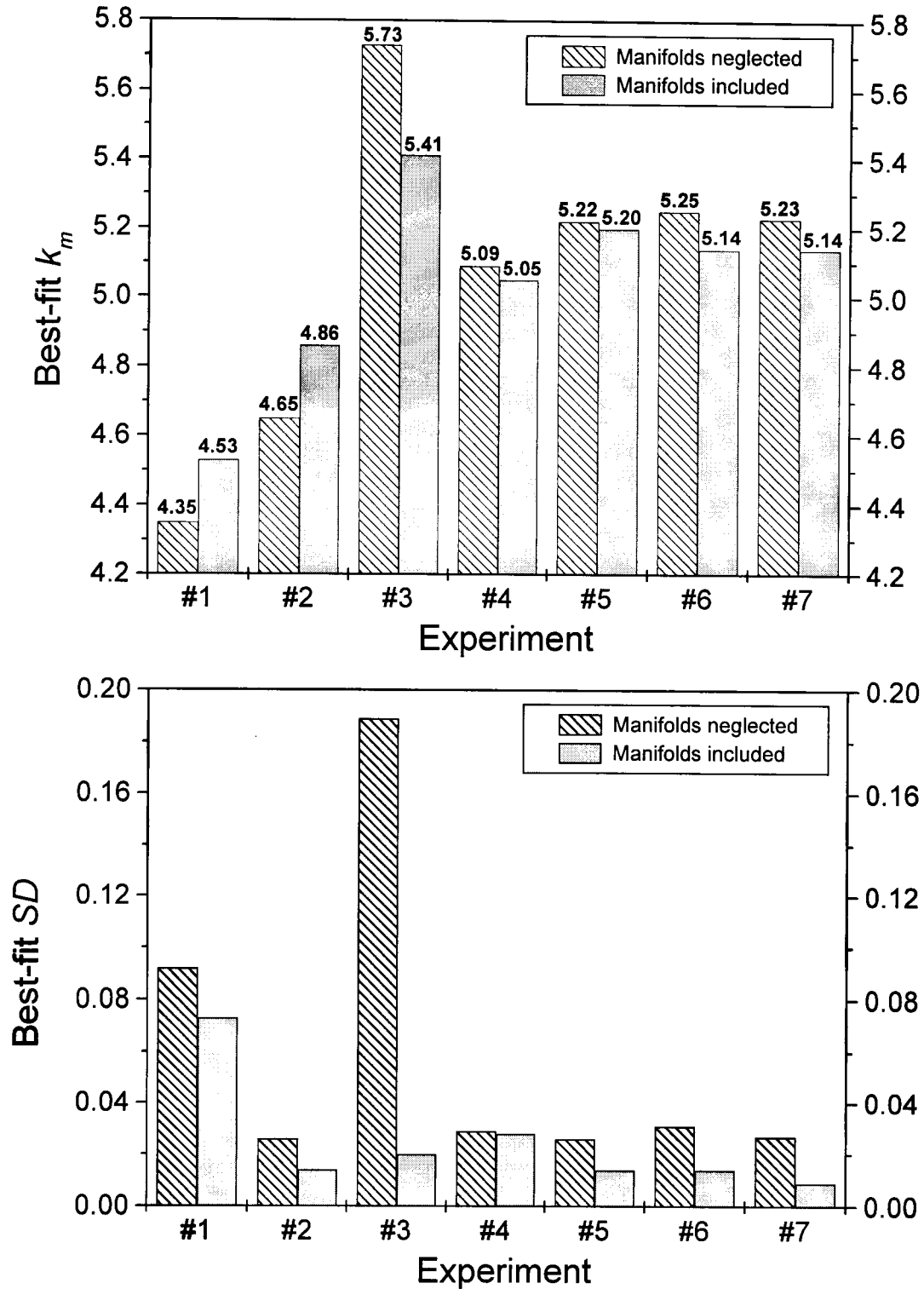


Fig. 20. Effect of ECS manifold extension on the best-fit membrane constant,  $k_m$ , and standard deviation (eq. 87),  $SD$ , for different leakage experiments.

### 3.4.3. Potential Sources of Discrepancies in Best-Fit Results

As was illustrated in fig. 20, the use of the ECS manifold extension to the leakage model reduced the scatter of the best-fit membrane constants and improved the overall fit of the experimental data. Nonetheless, the trend in the scatter remained relatively unchanged. Namely, the most extreme  $k_m$  values were obtained for the high-flow-rate experiments without BSA, the highest values for myoglobin loaded into the ICS (#3) and the lowest for myoglobin loaded into the ECS (#1 and #2). This section will discuss the results of various analyses employed here to explore the potential sources of these discrepancies. The discussion will illustrate the effects of selected hypothetical factors on the scatter of the best-fit  $k_m$  values and on the fit quality for different experiments.

#### 3.4.3.1. *ICS Protein Sink*

Denaturation or adsorption of myoglobin in the ICS recycle loop might explain the low fit quality in experiment #1 ( $SD = 0.073$ ) and the unusually high value of the best-fit membrane constant in experiment #3 ( $k_m = 5.41$ ). The same mechanism could also be responsible for a poorer myoglobin mass balance in each of these experiments (see table 5). To test the hypothesis of a protein sink existing in the ICS recycle loop, additional model simulations were performed in which a certain fraction of myoglobin was allowed at each time step to effectively disappear from the ICS. According to these predictions, if all of the myoglobin losses in experiment #3 (14%) had been due to an ICS sink, then the best-fit  $k_m$  would be reduced to 5.17, and  $SD$  would increase from 0.020 to 0.034. The results of similar simulations for experiment #1 are plotted in fig. 21. Assuming that all of the unrecovered myoglobin in this experiment (29%) had been lost to an ICS sink, the best-fit  $SD$  would be reduced from 0.073 to 0.033, and  $k_m$  increased from 4.53 to 4.75. Despite considerable improvement, the fit quality is still not as good as for the other experiments, and its qualitative value is diminished by the prediction of eventual concentration decline with time, which was not observed experimentally (fig. 21). These results clearly suggest that an ICS sink cannot be the sole explanation of the encountered discrepancies.

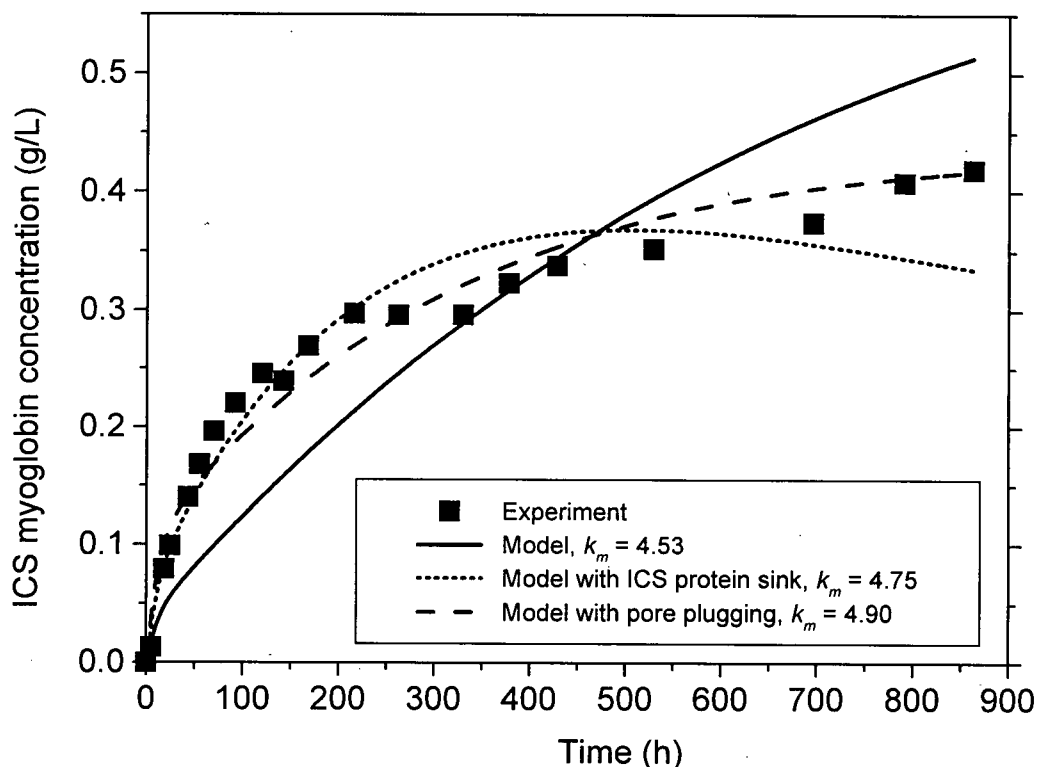


Fig. 21. Temporal changes in the ICS myoglobin concentration in experiment #1 (no BSA,  $Q_L = 300$  mL/min); symbols – experimental data; curves – best-fit model predictions.

#### 3.4.3.2. Membrane Pore Plugging

Since the average myoglobin radius (1.75 nm) is only slightly smaller than the effective membrane pore radius (see table 5), it seems likely that some of the myoglobin molecules might block passage through the pores even in the absence of significant interactions with the membrane material. Although preliminary studies conducted here did not indicate any detectable fouling of the Cuprophane membranes upon prolonged contact with myoglobin solutions, transmembrane transport might have increased the probability of myoglobin entrapment in the membrane pores or adsorption to the pore walls. In order to explore this issue theoretically, an extension to the model was developed by assuming that the membrane pores could be either reversibly or irreversibly plugged by myoglobin molecules. The probability of pore plugging,  $Pf(x)$ , was assumed to be a function of the maximum local concentration,  $C_{max}(x)$ , defined as the higher of the ECS and ICS myoglobin concentrations at position  $x$ . The consequence of this approach was a local decrease in the

effective surface porosity of the membrane by the factor of  $Pf(x)$  and, hence, a proportional reduction of the transmembrane myoglobin and fluid fluxes. The difference between the reversible and irreversible mechanisms was that  $C_{max}(x)$  in the latter was not allowed to decrease with time. Simulations using both plugging mechanisms yielded almost identical results.

A number of analytical forms for  $Pf(x)$  as a function of  $C_{max}(x)$  were tested in the fitting of the ICS myoglobin concentrations. The best agreement between the model predictions and the experimental data was obtained using a simplified Langmuir-type adsorption equation,

$$Pf(x) = \frac{C_{max}(x)/C_{crit}}{1 + C_{max}(x)/C_{crit}}, \quad (88)$$

with the fitted parameter  $C_{crit} = 50$  g/L. Equation (88) implies, for example, that the amount of myoglobin passing from the ECS to the ICS near the downstream end of the fibre at the final stage of experiment #2 would be reduced by approximately 25% ( $C_{max} \approx 15$  g/L). The dramatic effect of potential pore plugging is evident for the data of experiment #1 (fig. 21), where the consequence of employing eq. (88) was a reduction in the best fit  $SD$  value from 0.073 to 0.023 and a corresponding increase in  $k_m$  from 4.53 to 4.90 (fig. 22). By using the same form of  $Pf(x)$  in the simulations of experiment #2, the best-fit membrane constant was elevated from 4.86 to 5.12 and  $SD$  was reduced from 0.014 to 0.006. The best-fit  $k_m$  and  $SD$  values for the other experiments were less influenced by pore plugging. A functional dependence of  $Pf(x)$  on the local pore Peclet number (eq. (69)) was also considered but did not yield any further improvement of the fit.

#### 3.4.3.3. Pore Size Distribution

Although the distribution of pore sizes can influence membrane properties, its determination is difficult and the information yielded by most experimental methods uncertain (Baltus 1997). Several investigators have suggested that the log-normal function should yield a reasonable theoretical approximation of the pore size distribution in many membranes (Michaels 1980, Mochizuki and Zydney 1993, Zydney et al. 1994). Using the

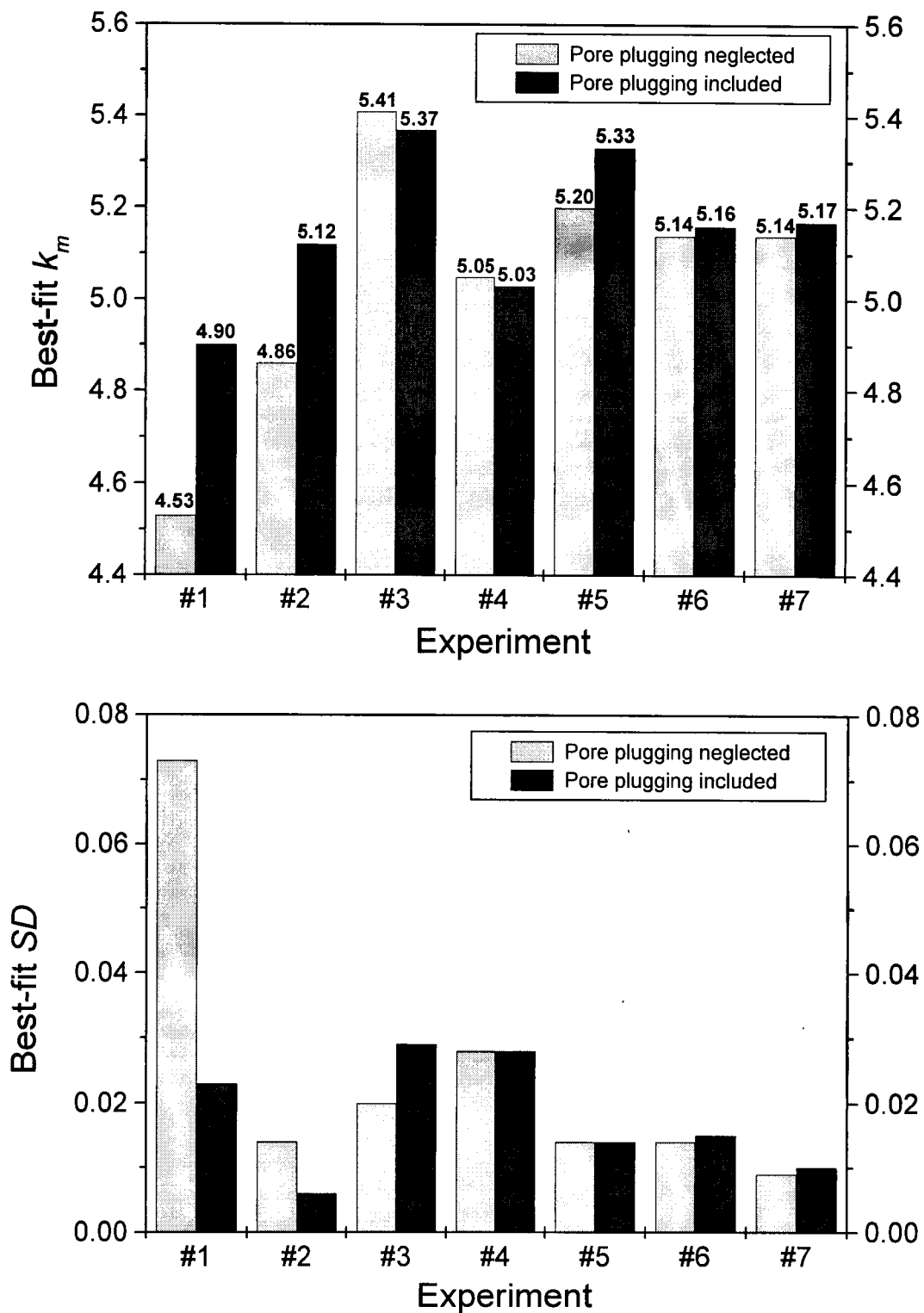


Fig. 22. Effect of pore plugging extension (eq. 88) on the best-fit membrane constant,  $k_m$ , and standard deviation (eq. 87),  $SD$ , for different leakage experiments.

algorithm outlined in appendix B and a distribution function in the form of eq. (B4), model simulations of experiments #2 and #3 were performed, both with and without the pore plugging assumption. In this case, compared with the procedure used so far, a parameter of the distribution function,  $\sigma_0^2$ , was fitted in addition to  $k_m$ . The purpose of these studies was to determine if there existed, for any  $k_m$  between 4.6 and 5.4, a best-fit value of  $\sigma_0^2$  which would be common for these two, as well as all other, experiments.<sup>11</sup>

The major effect of including the pore size distribution was an increase in  $K_d$  and, hence, in the diffusive flux through the membrane. It should be noted that the same effect could be produced by an increase in  $k_m$ . Since all the membrane constants in the range investigated here were below the previously determined best-fit value of 5.41 for experiment #3, a broader distribution of pore sizes, or larger  $\sigma_0^2$ , was needed to compensate for the decline in the predicted transmembrane myoglobin flux due to a smaller  $k_m$ . Therefore, an optimal, non-zero  $\sigma_0^2$  value was readily found for experiment #3. For the same reason, a non-zero best-fit  $\sigma_0^2$  value for experiment #2 could only be found at  $k_m$  lower than its previously determined best-fit value of 4.86 (or 5.12 with pore plugging), whereas the optimal distribution of pore sizes at higher  $k_m$  was always homoporous (i.e.,  $\sigma_0^2 = 0$ ). In conclusion, no best-fit  $\sigma_0^2$  value even approximately common for the two experiments was found at any  $k_m$  investigated, regardless of the pore plugging assumption. Either different  $k_m$  values at  $\sigma_0^2 = 0$  or different  $\sigma_0^2$  values at a fixed membrane constant were needed to explain the experimental results in a consistent fashion.

#### 3.4.3.4. Sensitivity to Transmission Parameters

Additional model simulations of experiments #2-7 were carried out to examine another potential source of discrepancy between the predicted and measured results, namely the approximate character of the analytical expressions for  $K_d$ ,  $K_c$ ,  $\Phi$ , and  $\sigma_{re}$  (eqs. (82)-(85)). It is clear from table 5 that  $K_c$  and  $\sigma_{re}$  did not change significantly from one

---

<sup>11</sup> Note that the existence of such a common  $\sigma_0^2$  value for experiments #2 and #3 would also imply its existence for all other experiments whose  $k_m$  fell between the  $k_m$  values for #2 and #3. This might not necessarily include experiment #1, which was not the main focus of this analysis owing to extra interferences related to its long duration.

experiment to another and that the major effect on myoglobin leakage was produced by  $K_d$  and  $\Phi$  (which appears to confirm the dominant role of diffusive transport in this process). Accordingly, the diffusive hindrance factor was selected as a second model parameter fitted independently of  $k_m$  (rather than calculated from eqs. (84) and (86)). Since the transmembrane diffusive flux is proportional to  $K_d \cdot \Phi$ , additional fitting of the partition coefficient was redundant. Assuming no pore plugging, no ICS protein sink, and no pore size distribution, the results of two-parameter fitting using both  $K_d$  and  $k_m$  were qualitatively similar to those obtained by fitting  $k_m$  alone. Over the investigated range of  $K_d$  from  $10^{-4}$  to 1, the best-fit membrane constants were consistently lowest for experiment #2 and highest for experiment #3. The difference in  $k_m$  between these two experiments was smallest (3.71 vs. 3.75) at  $K_d = 1$ , i.e., at no diffusive hindrance. However, the standard deviation of the fit was in that case extremely sensitive to  $k_m$  and higher than the *SD* values listed in table 5. For example, changing the membrane constants for experiments #2 and #3 from their respective best-fit values of 3.71 and 3.75 at  $K_d = 1$  to an average value of  $k_m = 3.73$  caused unacceptably large increases in *SD* from 0.021 to 0.086 (#2) and from 0.025 to 0.072 (#3). Thus, the use of an extra adjustable parameter in the simulations provided no clear advantage from the point of view of the fit quality.

#### 3.4.3.5. Other Factors

Although the assumptions of membrane pore plugging and shear-related protein losses in the ICS could partly explain the scatter of the best-fit membrane constants, there remains some uncertainty as to the source of these discrepancies. The difference in  $k_m$  for experiments #2 and #3 was particularly intriguing, since these two cases differed, in essence, only by the initial placement of myoglobin. When both of these experiments were duplicated, a significant difference between their best-fit  $k_m$  values was again obtained. Since numerous random and otherwise unaccounted-for factors, such as the cartridge-to-cartridge variation (e.g., in the fibre packing or in the distribution of pore sizes), analytical errors, and other phenomena (e.g., the presence of air bubbles), might have interfered with the experimental results, various sensitivity analyses were performed here to determine the potential influences of selected factors on the best-fit  $k_m$  values. The investigated factors were the initial myoglobin concentration, temperature, possible dimerisation of the

myoglobin, the final measured ICS recycle volume, the effective protein capacity of the ECS fibre-free regions, and a potential delay in the protein exchange between ECS manifolds and the fibre bundle.

Simulations showed that a hypothetical 5% underestimation of the initial myoglobin concentration in experiments #3 and #2 would have changed their respective best-fit membrane constants from 5.41 to 5.32 and from 4.86 to 4.88, without compromising the quality of the fit. Temperature elevation by 2 K produced a 7% increase in the protein diffusivity (mostly through a change in fluid viscosity at a constant  $D\mu/T$ , see also section 3.2.3), which then translated into lower best-fit  $k_m$  values for all experiments. The assumption of 100% myoglobin dimerisation, implemented through the increased effective radius and molar mass of the protein ( $r_M = 2.25$  nm,  $M_M = 33.8$  kDa), yielded higher best-fit membrane constants but did not reduce their scatter (e.g.,  $k_m$  was 8.30 and 9.46 for #2 and #3, resp.). A potential systematic error in the final measured ICS recycle volume (e.g., as a result of insufficient cartridge draining) could not explain the observed discrepancies either, since the best-fit  $k_m$  was found to increase with  $V_{REC}$  to a similar degree for both #2 and #3. A tenfold increase in  $V_m$ , imposed to simulate a hypothetical variation in the capacity of the ECS fibre-free regions for protein (e.g., as a result of natural convection), reduced the best-fit  $k_m$  for experiment #3 from 5.41 to 5.22, but the corresponding fit quality deteriorated significantly ( $SD$  increased from 0.020 to 0.044). An assumption that the protein exchange between the ECS manifolds and the fibre bundle was not instantaneous and that its rate depended on the direction (into or out of the manifold) did not change considerably the predicted ICS myoglobin concentrations, because the leakage process was limited primarily by the membrane resistance. In conclusion, the factors discussed in this section did not appear to have had a significant bearing on the scatter in the best-fit parameters for different experiments.

### 3.5. Conclusions

In spite of its many idealisations, the model developed in this study provided a fairly good quantitative description of ICS, ECS, and transmembrane protein transport in closed-shell HFBR cartridges. A set of transmission parameters defined by earlier investigators

(e.g., Deen 1987) was used here to describe the hindered transport of myoglobin as the leaking protein in the pores of the membrane. The present mathematical formulation related these transmission parameters to one another, thus reducing the number of adjustable model parameters to one, the membrane constant ( $k_m$ ), defined as the ratio of the square of pore tortuosity to the luminal surface porosity of the membrane. Estimates for  $k_m$  were obtained by forcing the model predictions to fit the transient ICS myoglobin concentration data collected from a series of hollow-fibre leakage experiments.

The process of myoglobin redistribution on both sides of the membrane was sensitive to a number of factors, including the membrane pretreatment procedure, the ICS flow rate, involvement of ECS manifolds, presence of a nonleaking protein (BSA) in the ECS, presence of a surfactant, and the duration of the experiment. At an ICS flow rate of 300 mL/min, significant downstream polarisation of ECS proteins was observed and the transmembrane myoglobin transfer was markedly influenced by the presence of ECS manifolds and by the distribution of BSA. In this case, the leakage process was a combination of space- and time-dependent convective and diffusive transport. In contrast, the ECS protein distributions at the ICS flow rate of 10 mL/min were very uniform, and the primary mechanism of transmembrane protein transfer was diffusion. When the downstream polarisation of myoglobin was diminished, either by the addition of BSA (in experiments #4, #5, and #7) or by the reduction of ICS flow (in experiments #6 and #7), the ECS-to-ICS protein passage was accelerated and the observed myoglobin concentrations in the ICS were higher (fig. 14).

A model extension which takes into account the fibre-free regions of the ECS considerably improved the quality of the fit between the theoretical and experimental results, although the scatter in the best-fit parameters could not be completely eliminated. This scatter was clearly related to the extent of convective polarisation of ECS myoglobin, since the most extreme  $k_m$  values were obtained when the myoglobin was concentrated within the region of the downstream manifold. In this case, depending on the initial myoglobin placement, the best-fit  $k_m$  was either lowest (ECS, experiments #1 and #2) or highest (ICS, experiment #3). Conversely, when the extent of downstream polarisation and the amount of myoglobin trapped in the downstream fibre-free region were significantly diminished due to a 30-fold reduction of ICS flow (i.e., experiments #6 and #7), the resulting best-fit

membrane constants were very close to their average value of all experiments (i.e.,  $k_m \approx 5.14$ ). This seems to indicate that an overly simplistic treatment by the present model – even including the manifold extension – of the complex role of the ECS manifolds was a likely cause of the  $k_m$  variation obtained in the fitting of the data from different experiments.

In addition, the higher  $k_m$  value for experiment #3 could be partly attributed to the error in the initial myoglobin concentration, the distribution of pore sizes in the membranes, or the existence of an ICS myoglobin sink due to adsorption or denaturation. The last effect might also play a role in the long-term experiment #1. Adsorption-like pore plugging by myoglobin molecules could very well explain the low  $k_m$  values for experiments #1 and #2. Model simulations including concentration-dependent pore plugging also produced a more consistent set of the membrane constants (4.90-5.37 vs. 4.53-5.41) without compromising the fit quality. However, no advantage was found in fitting two, rather than one, independent model parameters.

The obtained best-fit  $k_m$  values were used together with available theoretical formulae to yield estimates for the membrane transmission parameters. The osmotic reflection coefficient and the convective hindrance factor were relatively constant over the  $k_m$  range of interest here and equalled roughly 0.95 and 1.2, respectively. The values of the partition coefficient fell between 0.02 and 0.03, while the corresponding range of  $K_d$  values was 0.005-0.01 (based on  $4.86 \leq k_m \leq 5.41$  for experiments #2-7, see table 5). The effective pore radius ( $r_{p,eff}$ ) was estimated to be  $2.08 \pm 0.03$  nm (mean  $\pm$  standard deviation), which is only slightly larger than the average molecular radius of myoglobin (1.75 nm). No evidence was found that the actual distribution of pore sizes played a significant role in the membrane transport investigated here, which seems to agree with the indications of other authors that regenerated-cellulose membranes have fairly narrow pore size distributions (Broek et al. 1995).

## Chapter 4

### TWO-DIMENSIONAL ANALYSIS OF PROTEIN TRANSPORT IN OPEN-SHELL HOLLOW-FIBRE BIOREACTORS

#### 4.1. Motivation and Objectives

The main objectives of this part of the project were to validate experimentally the 2-D porous medium model (PMM) developed earlier (Łabęcki 1994) and to use the validated model for the prediction of protein redistribution during selected open-shell HFBR operations. As was mentioned in section 2.2.2, the spatial domain of the PMM corresponds to the dimensions of the entire bundle of hollow fibres, with the boundary conditions specified over the actual inflow and outflow areas of the ICS and ECS manifolds. The PMM allows therefore a more realistic description of HFBR fluid and mass transport phenomena than was possible using the Krogh cylinder formulations.

Three types of open-shell processes were investigated, the most attention being given to the study of dead-end inoculation. Here, a series of dead-end inoculation experiments were carried out, and the measured 2-D and 3-D ECS protein concentration data were compared with the predictions of both the 2-D PMM and the 1-D KCM (Łabęcki et al. 1996). The major goals of this study were to verify experimentally the validity of the PMM, to compare the results of the PMM and KCM simulations, and to gain a better understanding of the mechanisms governing the redistribution of proteins introduced into the ECS with the inoculum.

The other two processes were analysed only briefly, with no corresponding experimental work involved. For cocurrent and countercurrent harvesting, the 2-D PMM was used to predict the product removal efficiencies under essentially cell-free conditions in the ECS. Then, the feasibility of an alternative to closed-shell HFBR operation, a countercurrent ECS shunt, was tested using the model. Such a configuration might enable direct control of the magnitude of ECS convective flow and of the extent of downstream

polarisation of proteins and cells, thereby offering a potential benefit of sustaining more homogeneous growth conditions in the bioreactor. Schematics of the flow configurations pertaining to the different open-shell cases investigated here are presented in fig. 23.

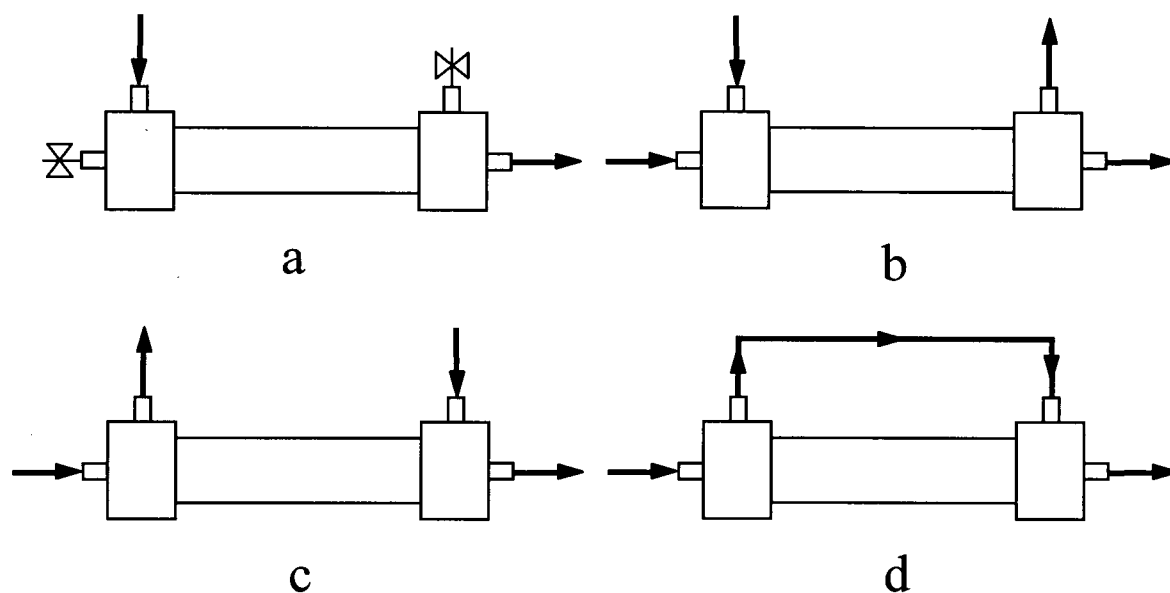


Fig. 23. Flow configurations in the open-shell processes investigated using the 2-D PMM: *a*, dead-end inoculation; *b*, cocurrent harvesting; *c*, countercurrent harvesting; *d*, countercurrent ECS shunt.

## 4.2. Experimental Procedures

### 4.2.1. Inoculation Experiments

A total of six dead-end inoculation experiments were performed using Gambro GFE-15 dialysers (Gambro Dialysatoren, Hechingen, Germany). This is the same type of hollow-fibre device as was used in the leakage study described in the previous chapter (section 3.3.1). The operating conditions for each experimental case are listed in table 6. The cartridges were oriented vertically in order to preserve, to the best extent possible, the axial symmetry of the fluid flow and protein concentration fields. Pretreatment of the hollow-fibre membranes was accomplished by employing the rinsing protocol described in section 3.3.1. All experiments were carried out at room temperature (20°C).

Table 6. Summary of HFBR inoculation experiments;  $C_{in}$ , inlet protein concentration;  $Q_{in}$ , inoculation flow rate;  $t_{act}$ , actual experiment duration (i.e., time elapsed between the start and stoppage of inoculation flow)

#	$C_{in}$ (g/L)	$Q_{in}$ (mL/min)	$t_{act}$ (min)	Flow direction
1	2.02	3.09	110	upward
2	12.15	3.00	22	upward
3	2.02	0.78	110	upward
4	12.15	3.18	22	upward
5	2.32	3.04	120	upward
6	2.22	3.08	120	downward

Azoalbumin (Sigma, St. Louis, Missouri), a BSA derivative containing azo groups, was selected for the experiments. Owing to its deep red colour, azoalbumin is an ideal model protein which can be easily traced visually as well as assayed using spectrophotometry. Because of the scarcity of azoalbumin data in the literature, the essential properties of the protein, such as its molar mass, diffusivity, and osmotic pressure, were assumed to be the same as for BSA. It was further assumed that the behaviour of protein solutions in PBS was similar to that of the corresponding water solutions. Since the membrane MWCO (~18 kDa) was lower than the molar mass of albumin (~69 kDa), the protein was not expected to leak through the membrane to the lumen side.

The dead-end flow configuration (fig. 23a) was used in all inoculation experiments. The azoalbumin solution was pumped at a constant flow rate into the ECS through one of its ports using a Watson-Marlow peristaltic pump (Falmouth, Cornwall, England). Since both the distal ECS port and the proximal lumen port<sup>12</sup> were closed, all of the inoculation flow had to pass through the membranes. The effluent leaving the cartridge through the ICS outlet port was collected in a graduated cylinder and analysed for protein at the end of each experiment. Small but measurable quantities of azoalbumin found in the lumen effluent might have gotten there via a leak between the potting and the wall at the lower end of the cartridge. After the desired time ( $t_{act}$ ) had elapsed, the inoculation flow was stopped and the

<sup>12</sup> The terms *proximal* and *distal* refer here to the positions relative to the inlet port; i.e., the proximal ICS port and the ECS inlet port are located at one end of the cartridge, while both distal ports are at the opposite end.

inlet tubing was clamped near the ECS port. The proximal lumen port was then opened and all of the ICS fluid was withdrawn into a separate graduated vessel and analysed for azoalbumin. The luminal space was emptied in order to prevent fibre rupture and possible cartridge cracking due to fluid volume expansion during the subsequent freezing procedure.

#### 4.2.2. Protein Analysis

The freeze-and-thaw technique developed by Piret and Cooney (1990b) was used to determine the final protein concentrations in all inoculation experiments (see also section 3.3.3 above). The cartridges were frozen by immersion in liquid nitrogen for approximately 20 min. In spite of the volumetric expansion of the ECS fluid during the procedure, no visual changes were noticed in the azoalbumin distribution, e.g., in the position of the protein front. Each frozen cartridge with its fixed protein distribution was cut into axial, radial, as well as angular sections, as illustrated in fig. 24. The lumen manifolds and epoxy potting were removed from both ends of the cartridge and discarded. The ECS ports together with the clamped pieces of tubing were sawed off and retained for subsequent analysis. The remainder of the cartridge was cut into axial segments with lengths varying from 1.05 cm to 3 cm. Each axial segment was cut at the radial position  $r = 0.85$  cm ( $\approx \frac{1}{2} R_{HFBR}$ ) to separate

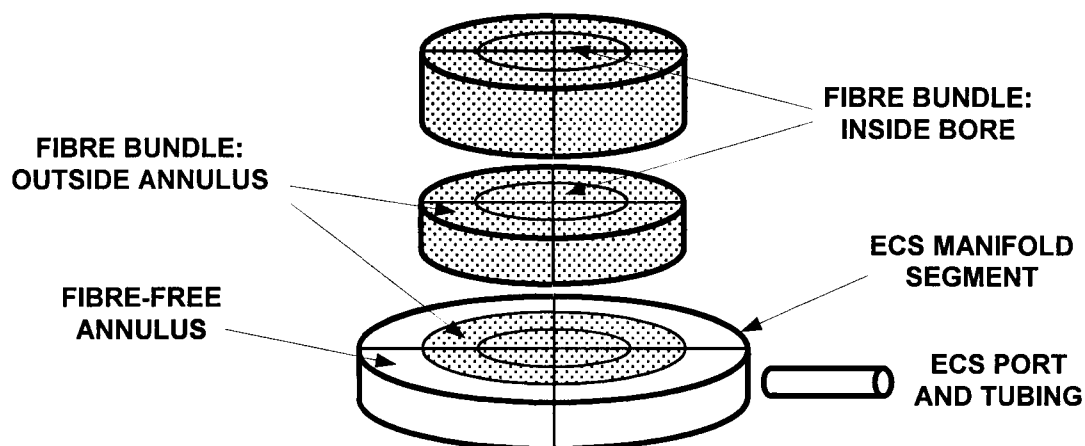


Fig. 24. Diagram illustrating a typical scheme of cartridge sectioning into axial, radial, and angular segments (adapted from Łabęcki et al. (1996)). Dotted regions denote sections of the fibre bundle, blank regions are fibre-free sections.

the outside annulus from the inside bore of the fibre bundle. In addition, the fibre-free portion of each ECS manifold segment was isolated by cutting the latter at  $r = R_{HFBR}$ . Finally, the radial subsections of cartridges in experiments #1-4 were cut into quarters, which provided data on the angular concentration variation. Thus, a total of up to eight sections of the hollow-fibre bundle were obtained within each axial segment, plus up to four fibre-free sections in the case of the ECS manifold segments.

The extent of cartridge penetration by azoalbumin could be easily estimated from the presence and distribution of colour over the cartridge cross-section. The azoalbumin detection threshold by visual estimation was found comparable to that of the spectrophotometric assays, i.e., approximately 0.005 g/L. Thanks to visual inspection, the number of samples could be reduced by eliminating all of the apparent protein-free segments at the stage of cartridge sectioning. For example, since the protein could be seen to have reached only about two-thirds of the ECS length in experiments #2-4, the cutting and analysis of the remaining one-third of the cartridge were in those cases redundant (which was also confirmed by spectrophotometric measurements).

Most of the thawed fibrous sections were squeezed to mix the sample and extract enough fluid for analysis. All extracted samples of azoalbumin solution were centrifuged to separate the plastic and fibrous dust particles produced during cartridge sawing. The samples were then diluted to a level corresponding to the linear range of optical density as a function of concentration, i.e., below approximately 2 g/L. A spectrophotometric analyser (Molecular Devices Model V<sup>max</sup>, Menlo Park, California) was used to measure the sample absorbance at 450 nm and hence determine the corresponding azoalbumin concentration. The method was also used to find the concentration of the inoculation solution,  $C_{in}$ , and the amount of protein lost to the lumen side,  $m_L$ , in each experiment. All standards and most samples were assayed in triplicate, except for the inoculation samples, which were analysed in sextuplicate.

### 4.3. Model Simulations

At each time step, the pressure equations (28) and (29) were solved together with the ECS protein transport equation (35), subject to the conditions listed in table 2 (section 2.2.2). The ICS and ECS hydraulic permeabilities were calculated from eqs. (30), (31), and

(33), while the osmotic pressure was evaluated locally as a function of protein concentration using the virial equation (52). The axial and radial components of the ECS protein diffusivity were calculated from eqs. (36) and (37), respectively. A list of the essential model parameters and their values is given in table 7. Note that the values of  $R_L$  and  $L_p$  were based on older data and hence are different from those used in the KCM leakage simulations (chapter 3, table 3).

Table 7. Parameters used in the 2-D PMM simulations of open-shell HFBR operations

$n$	8128
$R_L$	$1.15 \times 10^{-4}$ m
$R_F$	$1.24 \times 10^{-4}$ m
$R_{HFBR}$	0.01575 m
$L$	0.215 m
$L_F$	0.238 m
$z_m$	0.021 m
$\varepsilon_S$	0.4423
$L_p$	$6.2 \times 10^{-15}$ m
$k_{L,z}$	$6.47 \times 10^{-10}$ m <sup>2</sup>
$k_{S,z}$	$3.02 \times 10^{-10}$ m <sup>2</sup>
$k_{S,r}$	$2.01 \times 10^{-10}$ m <sup>2</sup>
$T$	20°C
$M_A$	69 kg mole <sup>-1</sup>
$A_{\Pi 2,A}$	$10.473 \times 10^{-3}$ L g <sup>-1</sup>
$A_{\Pi 3,A}$	$17.374 \times 10^{-6}$ L <sup>2</sup> g <sup>-2</sup>
$\mu$ (20°C)	$1.002 \times 10^{-3}$ Pa s
$D_A$ (20°C)	$7.0 \times 10^{-11}$ m <sup>2</sup> s <sup>-1</sup>

The boundary conditions for the pressure equations (28) and (29) can be specified as a known distribution at a given boundary of either pressure or velocity (or pressure derivative). In the latter case, unfortunately, the experimentally measurable quantity is usually not the local velocity but the flow rate, or the velocity averaged over the inlet or outlet area. Consequently, a condition imposed most conveniently at an open ECS port is

still a fixed pressure, normally also assumed constant over the boundary. Numerical simulations of the fixed-flow-rate experimental conditions were carried out accordingly by first guessing and then iteratively correcting a boundary pressure value until the set-point flow rate was obtained within the prescribed accuracy of 0.006 mL/min ( $10^{-10}$  m<sup>3</sup>/s). Every 1-5 time steps, re-adjustment of this pressure level was usually necessary in order to compensate for a temporal drift in the ECS flow rate due to the osmotic influences of the changing ECS concentration field.<sup>13</sup>

For the protein transport equation, the ECS inlet condition was a known concentration value, assumed uniform over the inlet area. In the inoculation and harvesting studies, this boundary value was fixed (and equal to zero in the latter case). In the countercurrent ECS shunt study (fig. 23*d*), the external shunt volume was assumed very small compared with the ECS volume and therefore negligible, thus implying that there was no delay in the protein transfer between the outlet and inlet ECS ports via the shunt. Consequently, the inlet concentration was always set equal to the average outlet concentration, and hence varied with time as the latter did. In all relevant cases, the boundary condition at the ECS outlet was imposed by forcing the radial concentration derivative to zero (see table 2).

Equations (28), (29) and (35) were discretised by integration over the representative elementary volume (REV), as recommended by Patankar (1980). The discretisation mesh was composed of 500-900 axial and 18 radial, equally-spaced grid points. The local transport conditions were taken into account by means of Patankar's (1980) power law scheme, which includes the effect of local Peclet number on solute flux. The resulting set of finite-difference equations was solved according to the following algorithm:

- (1) set the initial concentration field;
- (2) calculate the corresponding osmotic pressure distribution;
- (3) set the pressure boundary conditions and solve eqs. (28) and (29) iteratively using the line over-relaxation method (Anderson et al. 1984); the convergence criterion, defined as the largest local magnitude of the difference between the latest and previous pressure

---

<sup>13</sup> In the simulations of some cocurrent and countercurrent cases, this pressure correction scheme converged extremely slowly, virtually to the point of stalling. Whenever this occurred, the ECS flow rate drift due to osmotic effects was neglected and the ECS boundary pressure was maintained at the last determined level. The changes in the ECS protein distribution resulting from this approximation were found to be negligible.

- values at a given position, was set to a level that ensured a satisfactory mass balance of the fluid (usually  $10^{-6}$  Pa for both  $P_S$  and  $P_L$ );
- (4) from the ECS pressure field, calculate the ECS fluid velocities using Darcy's law (Bear 1972, p. 120); use a staggered grid with the velocity points placed halfway between the pressure points;
  - (5) calculate the inlet and outlet ECS flow rates; if necessary, adjust the boundary pressure and repeat steps (3-5) until the desired flow rate results;
  - (6) increment time by  $\Delta t$ ;
  - (7) set the concentration boundary conditions and calculate the new concentration field using the Alternating Direction Implicit (ADI) method (Anderson et al. 1984, p. 139); select a sufficiently small time step ( $\Delta t$ ) to ensure that the cumulative protein imbalance does not exceed a pre-determined tolerance level (0.1%);<sup>14</sup>
  - (8) repeat steps (2-7) until steady state, a specified time limit, or a maximum number of iterations is reached; steady state was assumed to exist when the maximum absolute value of the local concentration change with time was less than  $10^{-5}$  g/(L·s).

#### 4.4. Results and Discussion

##### 4.4.1. Inoculation

The amount of protein recovered from the fibre bundle in each inoculation experiment was found to be different from the amount apparently introduced into the cartridge over the actual experiment duration ( $m_{app} = Q_{in} \cdot C_{in} \cdot t_{act}$ ). This discrepancy was due to (1) unrecovered protein losses, (2) partial protein leakage to the lumen side, as well as (3) protein penetration into the ECS manifolds and adjacent tubing. Since none of these three effects were included in the 2-D PMM formulation employed here, a certain amount of data manipulation was necessary to allow meaningful comparisons between the results of experiments and simulations. To account for the time lag associated with the presence of a fibre-free region at the inlet, it was assumed that the effective duration of experiment,  $t_{eff}$ ,

---

<sup>14</sup> Note that a numerically-originated mass imbalance can arise when some of the unknowns in the finite-difference equations are taken from the previous time instant and the solution for the present time level is not iterated until convergence. This is the case in the standard ADI formulation, which makes this method inherently non-conservative.

was shorter than  $t_{act}$  by the time needed for the inlet solution at a flow rate  $Q_{in}$  and concentration  $C_{in}$  to fill the upstream manifold and part of the inlet tubing, whose combined volumes totalled 13.1 mL. The  $t_{eff}$  values calculated in this manner are listed in table 8. The amount of protein introduced into the cartridge over the effective time of the experiment could then be found as  $m_{eff} = Q_{in} \cdot C_{in} \cdot t_{eff}$ . If there were no protein losses, then  $m_{eff}$  should be equal to the amount of protein assayed in the fibre bundle and in the downstream manifold and tubing,  $m_{exp}$ . The recovered losses,  $m_L$ , include protein that had leaked to the lumen effluent during inoculation as well as protein withdrawn with the ICS fluid at the end of experiment. The effective fractional recovery of protein,  $f_{eff}$ , was calculated as  $(m_{exp} + m_L)/m_{eff}$ . In order to normalise the model-simulated ECS protein content to its experimental level, all local concentration values generated by the simulations were multiplied by a scaling factor of  $m_{exp}/m_{eff}$ . Thereby, it was assumed that the contribution to protein losses of each point of the ECS domain was proportional to the local concentration.

Table 8. Summary of protein recovery data in the inoculation experiments

Cartridge #	$t_{eff}$ (min)	$m_{eff}$ (g)	$m_{exp}$ (g)	$m_L$ (g)	$f_{eff}$	$N_V$
1	105.8	0.661	0.535	0.008	0.82	4.41
2	17.6	0.642	0.483	0.003	0.76	0.72
3	32.8	0.147	0.150	0.003	1.04	0.97
4	17.9	0.691	0.551	0.007	0.81	0.77
5	115.7	0.817	0.758	0.016	0.95	4.75
6	115.7	0.793	0.681	0.071	0.95	4.82

The number of fluid volumes displaced from the ECS over the effective time of the experiment, listed in the last column of table 8, was calculated as  $N_V = Q_{in} \cdot t_{eff}/V_{ECS}$ , where  $V_{ECS} = 74.1$  mL is the volume of the ECS excluding the manifolds. For convenience, the experiments in which  $N_V$  was less than 1 (i.e., #2-4) will be referred to as the low- $N_V$  group, and the remaining experiments (#1, #5, and #6) as the high- $N_V$  group. The main difference

between these two groups is that the protein reached the downstream manifold in the cartridges of the high- $N_V$  group but did not in the low- $N_V$  group. The former case required therefore additional normalising effort to account for the manifold-trapped protein. Unlike its upstream counterpart, the downstream manifold in the flow configuration shown in fig. 23a is a dead-end volume accessible to the protein only through the fibre bundle. For the purpose of comparing the experimental and predicted data, it was therefore assumed that the protein present in that region would otherwise (i.e., in the absence of the downstream manifold and tubing) have been recovered from the adjacent sections of the fibre bundle. Accordingly, adjustments were made to the experimental protein concentrations in the fibrous sections located within the axial length between  $L - z_m$  and  $L$  in the high- $N_V$  group cartridges, yielding higher apparent concentrations than the actual concentrations found for those sections from protein assays.

Figure 25 compares the experimental and model-simulated axial concentration profiles at  $t = t_{eff}$  for two cartridges of the low- $N_V$  group, #2 and #3. The third experiment of this group (#4) essentially duplicated the results for cartridge #2 (fig. 25a). The corresponding two-dimensional concentration distributions predicted by the PMM for the final instants of experiments #2 and #3 are plotted in fig. 26. To obtain the profiles shown in fig. 25, the 2-D PMM data were averaged radially, while the 3-D experimental data were averaged both radially and angularly. Each step in the experimental profiles (fig. 25) corresponds to one axial segment of the cartridge, with the angular standard deviation (ASD) bars quantifying the angular concentration variation within the segment, according to the following formula:

$$ASD_i = \sqrt{\frac{1}{m} \sum_{j=1}^m (\bar{C}_{ij} - \bar{C}_i)^2}, \quad (89)$$

where  $m = 4$  is the number of angular sections per segment,  $\bar{C}_{ij}$  is the radially-averaged concentration of angular section  $j$  in segment  $i$ , and  $\bar{C}_i$  is the average concentration in segment  $i$ . Since no correlation was found between the angular concentration variation and position, the angular effects were concluded to be of random nature, most likely due to nonuniform fibre packing.

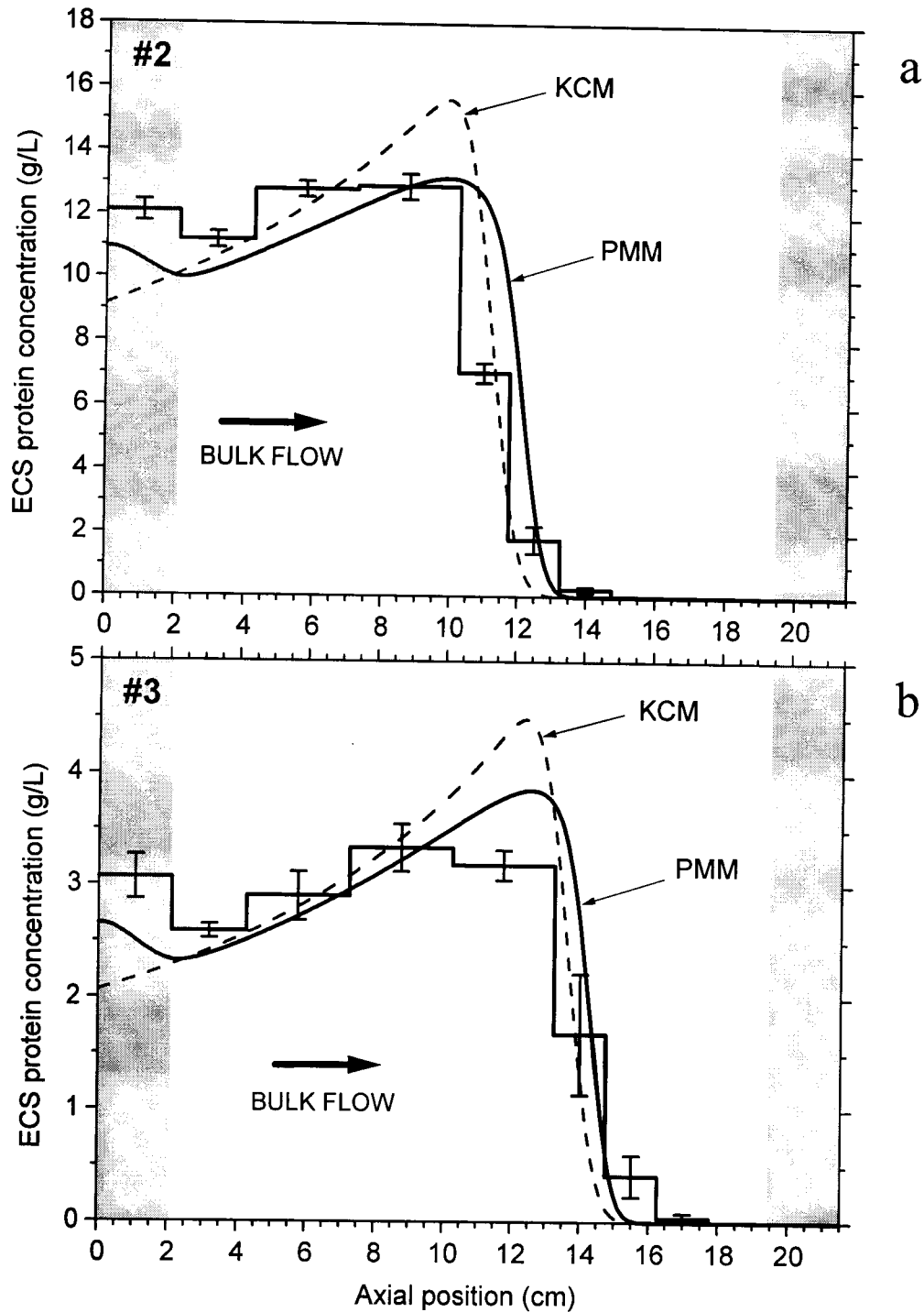


Fig. 25. Experimental versus model-simulated axial ECS protein concentration profiles at  $t = t_{eff}$  for experiments #2 (a) and #3 (b); step lines – radially- and angularly-averaged experimental data; smooth solid lines – radially-averaged 2-D PMM predictions; smooth dashed lines – 1-D KCM predictions. The angular standard deviation (ASD) bars signify the angular concentration variation in each axial segment. Shaded areas mark the positions of ECS manifolds. Adapted from Łabęcki et al. (1996).

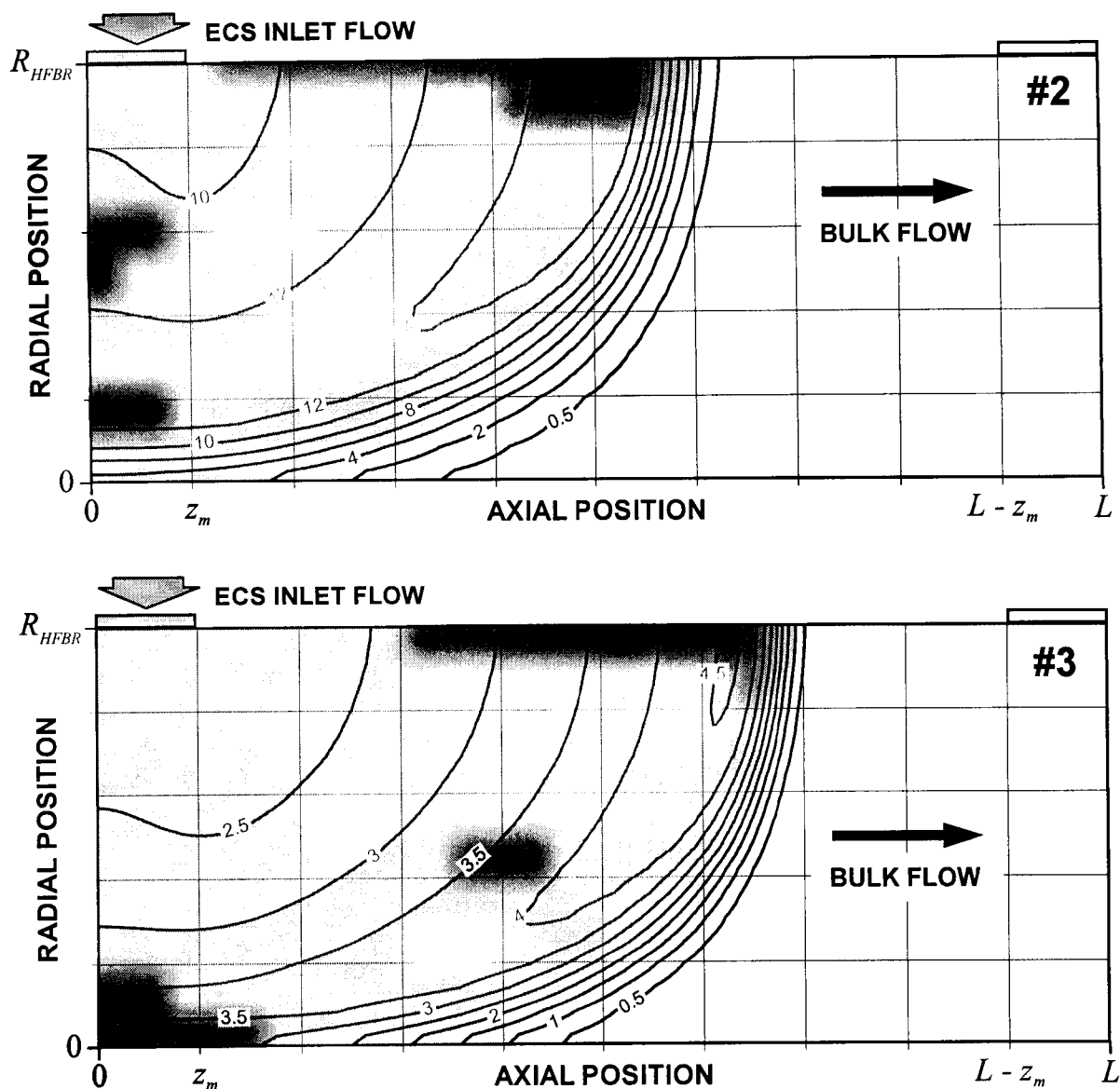


Fig. 26. PMM-predicted two-dimensional ECS protein concentration fields (g/L) at the end of experiments #2 (top) and #3 (bottom). The ECS concentration values have been scaled by a factor of  $m_{exp}/m_{eff}$ , equal to 0.752 for #2 and 1.019 for #3. Domain dimensions are not to scale.

The experimental profiles in fig. 25 (step lines) display two concentration maxima, both of which have been predicted by the PMM (smooth solid lines). The major maximum, located near the protein front, is a result of protein filtering due to transmembrane fluid transfer. Because the incoming ECS fluid gradually passes to the lumen side, the magnitude

of ECS flow decreases with axial position. Consequently, the protein front slows in its downstream movement, and the protein brought from the inlet zone begins to accumulate near the front boundary. The slowdown of axial protein movement leading to the formation of the concentration maximum can also be clearly seen in fig. 27, which plots the model-predicted concentration transients for experiment #3.

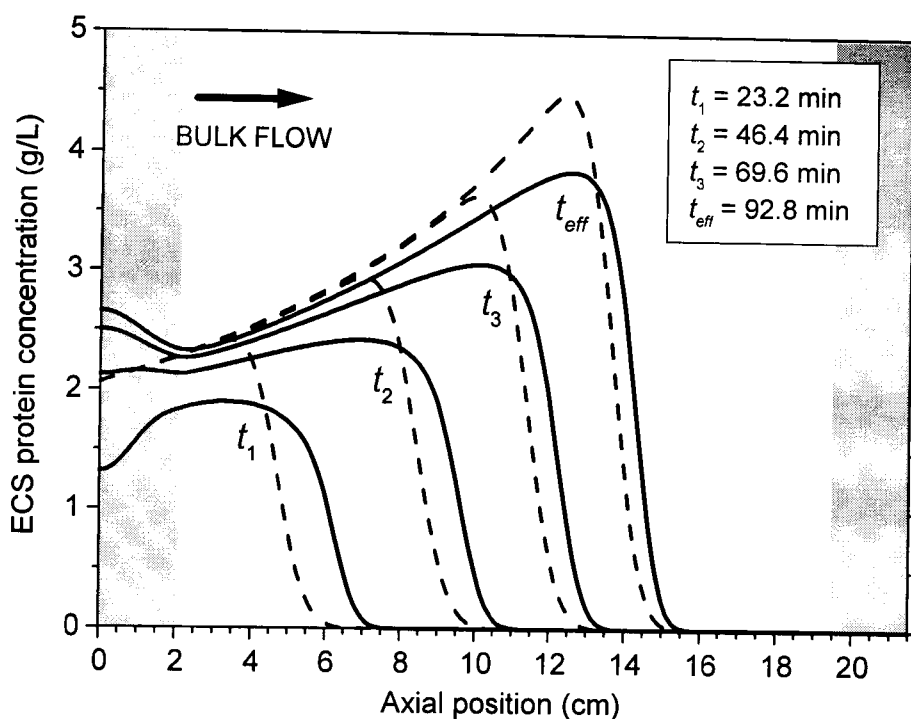


Fig. 27. Model-predicted radially-averaged transient concentration profiles for the conditions of experiment #3; solid lines – PMM, dashed lines – KCM. Shaded areas mark the positions of ECS manifolds. Adapted from Łabęcki et al. (1996).

The second concentration peak is located in the first axial segment at the upstream end of the cartridge (fig. 25). This maximum results from at least two combined effects: a decline in the ECS radial flow towards the cartridge symmetry line ( $r = 0$ ); and a distribution of the inlet (radial) fluid velocity, which increases with axial position from  $z = 0$  to  $z = z_m$  by as much as an order of magnitude. The latter effect is a consequence of using a fixed-pressure condition along the inlet ECS boundary – the fluid simply seeks the shortest route

from the upstream ECS manifold to the ICS outlet. As the transient PMM curves in fig. 27 illustrate, the upstream maximum did not arise until about 45 min ( $\frac{1}{2} t_{eff}$ ) of inoculation. Initially, only one broad concentration peak was present near the edge of the inlet manifold, i.e., in the region of highest inlet velocities. When the average protein concentration in the vicinity of ECS entrance increased sufficiently high above the inlet concentration, the same region became the site of a local concentration minimum (fig. 27). Over the time scale considered, neither axial or radial convective flow was able to effectively transport downstream protein accumulated near the upstream end of the ECS (fig. 26), which led to the local elevation of radially-averaged concentrations near  $z = 0$  (fig. 27, solid lines).

In addition to the prediction of the upstream maximum in the radially-averaged concentration curves, the PMM has also captured the essential features of radial concentration variation in the ECS. For example, as is evident from fig. 28, the relative magnitudes of the inside-bore and outside-annulus concentrations at different axial positions predicted for experiment #2 are in very good agreement with the corresponding experimental profiles. Furthermore, the upstream concentration maximum for the same simulation conditions is correctly predicted to be present in both the inside-bore and outside-annulus curves (fig. 28). Despite the fact that the KCM results (figs. 25 and 27, dashed lines) are reasonably consistent with experimental data, the Krogh cylinder model, owing to its inherent limitations, could neither predict the existence of the upstream concentration maximum nor produce the radial variations depicted in fig. 28.

In all inoculation cases considered here, the local ECS Peclet numbers were of the order of hundreds, i.e., the protein transport was dominated by convection. Nonetheless, a dispersion of the predicted 2-D concentration front is clearly noticeable in the contour plots presented in fig. 26.<sup>15</sup> This was caused by the neglect of third- and higher-order terms in the finite-difference equations, a problem that could only partly be alleviated by refining the spatial grid. In contrast to the numerically-originated dispersion of the model-generated data, the washout of the protein front observed in the experiments was caused by concentration averaging within each cartridge section, as well as by local variations in the ECS hydraulic

---

<sup>15</sup> Note that a similar dispersion of the protein front in the PMM curves shown in figs. 25 and 27 can be partly explained by radial averaging.

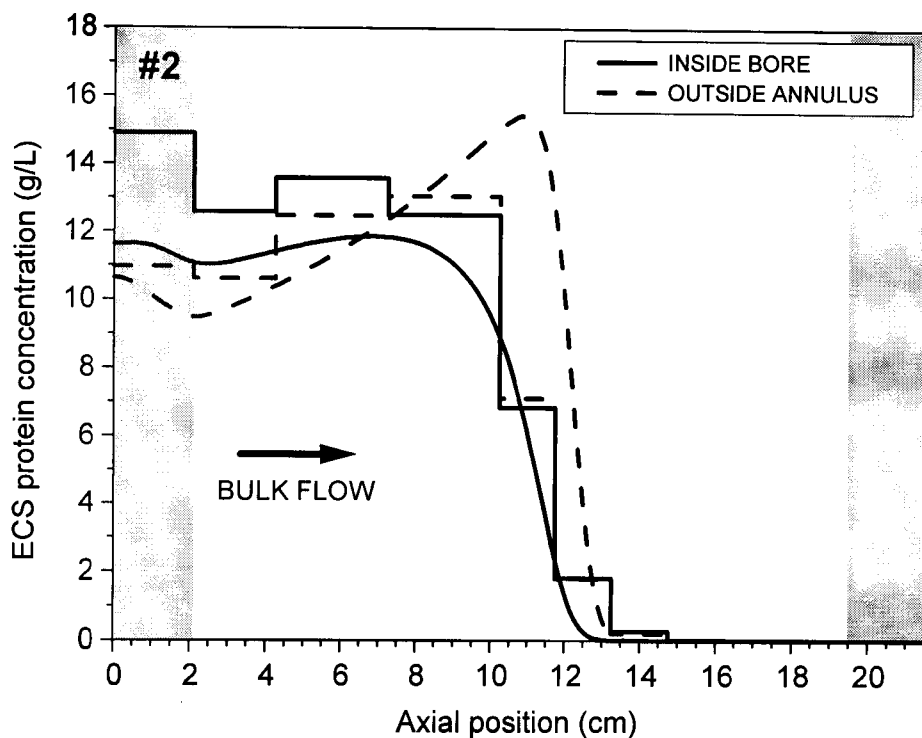


Fig. 28. Experimental (step lines) and PMM-predicted (smooth lines) axial ECS concentration profiles in the inside bore (solid lines) and the outside annulus (dashed lines) of the fibre bundle at  $t = t_{eff}$  for experiment #2. The PMM data have been averaged radially within each radial subsection. Shaded areas mark the positions of ECS manifolds. Adapted from Łabęcki et al. (1996).

permeability due to inhomogenous fibre packing, which were not taken into account in the model. The 2-D results for PMM simulations of various dead-end inoculation conditions are discussed in greater detail elsewhere (Łabęcki 1994).

In experiment #1, the first of the high- $N_V$  group, a significant discrepancy was encountered between the experimental and model-simulated protein distributions at  $t = t_{eff}$ . Another experiment carried out under similar conditions (#5) yielded similar results. As seen in figs. 29a and 30, which show the results for experiment #5, the PMM predicted a sharp rise of the downstream-end protein concentration to values exceeding 60 g/L. The experimental protein distribution, on the other hand, was much more uniform and displayed a broad peak at  $z \approx 16$  cm, with concentrations reaching about 15 g/L. The ECS

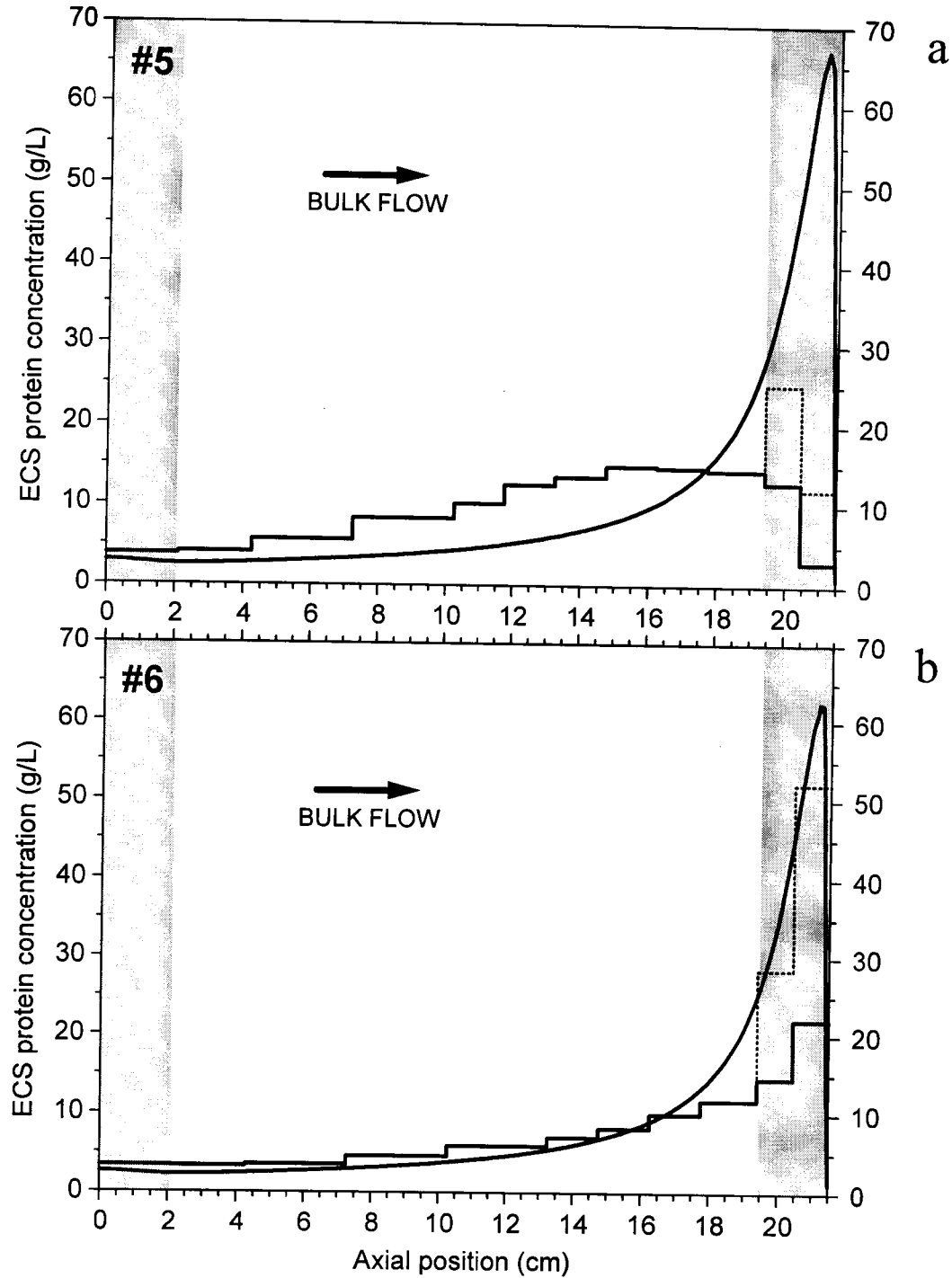


Fig. 29. Experimental versus model-simulated axial ECS protein concentration profiles at  $t = t_{eff}$ : *a*, experiment #5 (upward flow); *b*, experiment #6 (downward flow). Solid step lines – raw experimental data; dotted step lines – experimental data adjusted to account for protein present in the downstream manifold; smooth lines – radially-averaged 2-D PMM predictions. Shaded areas mark the positions of ECS manifolds. Adapted from Łabęcki et al. (1996).

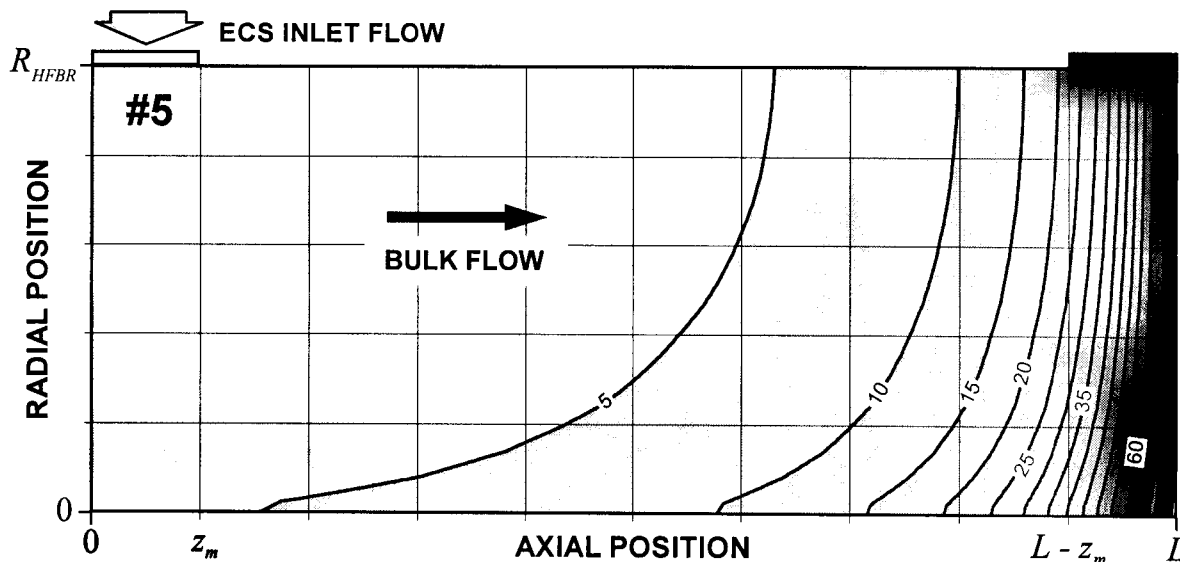


Fig. 30. PMM-predicted two-dimensional ECS protein concentration fields (g/L) at  $t = t_{eff}$  in experiment #5. The ECS concentration values have been scaled by a factor of  $m_{exp}/m_{eff} = 0.928$ . Domain dimensions are not to scale.

concentration adjustment, applied to the last two axial segments to allow for protein trapped in the downstream manifold (fig. 29a, dotted line), was not sufficient to eliminate the observed discrepancy. Clearly, an unaccounted-for mechanism delaying the downstream protein movement must have been involved in this case.

One such possible mechanism was hypothesised to be the convective protein polarisation at the surface of the filtering membranes, caused by transmembrane fluid passage from the ECS to the ICS in the presence of radial gradients of ECS axial velocity on the microscale of a single fibre. In assessing the significance of this phenomenon, the average radial Peclet number at the fibre surface was estimated to be  $Pe_r = v_m d/D \approx 0.1$ , where  $v_m \approx 4 \times 10^{-8}$  m/s is the average transmembrane velocity, and  $d \approx 10^{-4}$  m is the length scale, represented here by the average interfibre distance. The above result indicates that protein diffusion was more important than radial convection near the membrane surface and, therefore, the hypothetical radial distribution of the ECS axial velocity on the microscale likely played no role here. Moreover, the average axial Peclet numbers were, in this case, at least 3 orders of magnitude higher than  $Pe_r$ , which suggests that the protein should be

convectively swept downstream essentially unhindered by transmembrane flows. It is obvious that this mechanism does not provide a satisfactory explanation of the discrepancy observed for experiments #1 and #5.

Since cartridges #1 and #5 were operated for relatively long times in the vertical orientation with upward flow (see tables 6 and 8), significant upward gradients of protein concentration, and hence of fluid density, developed in the ECS in these two cases (see figs. 29a and 30). Thus, a likely mechanism responsible for impeding the upward movement of the protein could be the gravitational pull induced by density gradients, commonly referred to as buoyancy or simply free-convection (or natural convection).<sup>16</sup> The appropriate dimensionless group for assessing the relative importance of free- versus forced-convective transport is the so-called buoyancy parameter, which is the ratio of the Grashof number to the square of the Reynolds number (White 1991, p. 323), i.e.,

$$\frac{Gr}{Re^2} = \frac{g d \Delta\rho}{u^2 \rho}, \quad (90)$$

where  $g$  is the gravitational acceleration,  $d$  is a characteristic length,  $u$  is the fluid velocity,  $\rho$  is the fluid density, and  $\Delta\rho$  is the local change in density over the distance  $d$ . Natural convection can be considered important if  $Gr/Re^2$  is of order 1 or greater. Assuming that  $d \approx 10^{-4}$  m (average interfibre distance),  $\Delta\rho/\rho \approx 10^{-4}$  (corresponding, approximately, to the axial concentration gradient of 10 g/(L·cm)), and  $u_s \approx 10^{-4}$  m/s (maximum axial velocity in the ECS), the buoyancy parameter is estimated to be  $Gr/Re^2 \approx 10$ . This result indicates that free convection could have significantly influenced protein transport under the conditions of the inoculation experiments conducted here.

Because such buoyancy effects had been anticipated, upward flow was deliberately chosen for experiments #1-5. Had the flow been directed downward, the sharp concentration

---

<sup>16</sup> The terms *buoyancy* and *buoyant force* originate from the classical analysis of forces acting on a body immersed in a static fluid. In fluid dynamics, these terms are commonly used with reference to free-convective flows in the absence of immersed bodies. Such flows are also called *buoyant flows*, termed so because their driving force, proportional to the local density difference and to the acceleration of gravity, is analogous to the *buoyant force* known from the hydrostatic analysis. In this thesis, the terms *free-convective effects*, *gravitational effects*, or *buoyancy effects* are used to mean any modification to the forced-convective protein transport caused by local differences in fluid density due to gradients in concentration, under the influence of gravity (note that the effects of osmotic pressure or of variable viscosity on fluid flow may also result from concentration gradients but do not depend on gravity).

gradient existing at the boundary between the moving protein front and the protein-free ECS fluid would have induced free convection. The ECS flow channelling due to fibre maldistribution, leading to the washout of the protein front or even to the isolation of fast-moving streams of concentrated protein solution, could have further complicated the course of the downward-flow experiments. On the other hand, once the downward-moving boundary of the protein zone has reached the bottom end of the ECS, the associated buoyancy effects are expected to cease. Thus, if the final protein distributions were of most interest, the optimal strategy for minimising gravitational influences should be to use upward flow in short-term inoculation experiments and downward flow in long-term experiments. This proposition is supported by the observation that no free convection was apparent in the low- $N_V$  group experiments (#2-4), where the volume of protein solution introduced to the ECS was too small for significant upward concentration gradients to develop.

In view of the above, a downward-flow analogue of experiments #1 and #5 was conducted, labelled here as experiment #6. As is evident from a comparison of figs. 29a and 29b, a much better agreement between the PMM-simulated and experimental axial concentration profiles was indeed obtained when the flow was directed down rather than up. In particular, the model-predicted concentrations within the length of the downstream manifold are close to the adjusted experimental concentrations in the last two axial segments (fig. 29b, dotted line). The largest difference between the two profiles is observed in the third segment from the downstream end. That segment was likely involved to some extent in supplying protein to the downstream manifold, whereas the concentration adjustment was applied only to the segments between  $L - z_m$  and  $L$ .

Figure 31 plots the axial distributions of radial concentration gradients, determined experimentally and simulated by the PMM for cartridge #6 (cf. fig. 29b). Unlike in experiment #2 (fig. 28), where the inside bore and the outside annulus concentrations were of similar magnitudes, a relative rather than absolute difference between the two was plotted in this case. Overall, a good agreement between the simulated and experimental results is seen in fig. 31. Although the PMM curve drops steeply to negative values near the downstream end of the cartridge, its average over the length of the last axial segment is above zero, which qualitatively agrees with the experimental data.

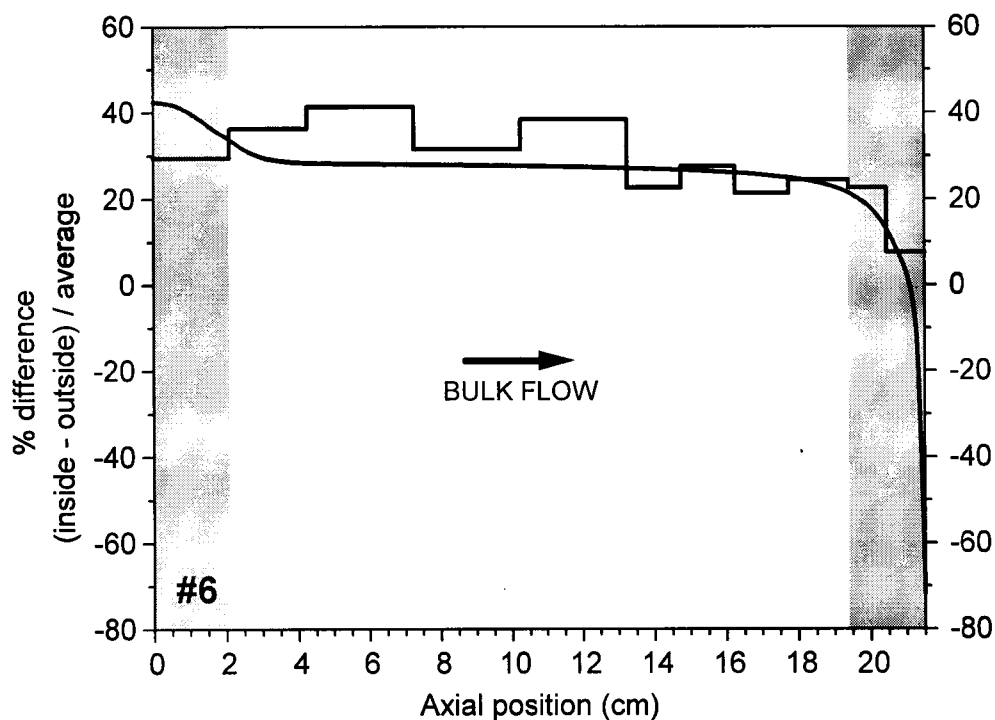


Fig. 31. Experimental (step line) versus PMM-predicted (smooth curve) radial protein concentration variation at  $t = t_{eff}$  in experiment #6. The plots express the difference between the average concentrations in the inside bore and the outside annulus of the fibre bundle, relative to the concentrations averaged radially over the whole bundle radius. Shaded areas mark the positions of ECS manifolds. Adapted from Łabecki et al. (1996).

Figure 32 illustrates the effect of flow direction on the transient position of the protein front, which was determined by observing the progress of the red azoalbumin solution through the transparent walls of the cartridge. Since, in both experiments #5 and #6, the front was usually distributed over about 2 cm of axial distance, its average position was plotted. The location of the front in the model simulations was defined as the maximum axial position (measured in the downstream direction) at which the local radially-averaged concentration exceeded 0.02 g/L. The initial time,  $t = 0$ , corresponds to the effective onset of inoculation, i.e., to the point at which the inlet fluid has apparently filled the fibre-free upstream manifold. In the downward-flow case (#6), strong natural convection effects caused the front to have travelled approximately 8 cm downstream by the time  $t = 0$ . Although narrow streams of protein solution could be seen forming and moving down ahead of the main protein front in cartridge #6, no flow channelling on a scale larger than the width of a few fibres was observed.

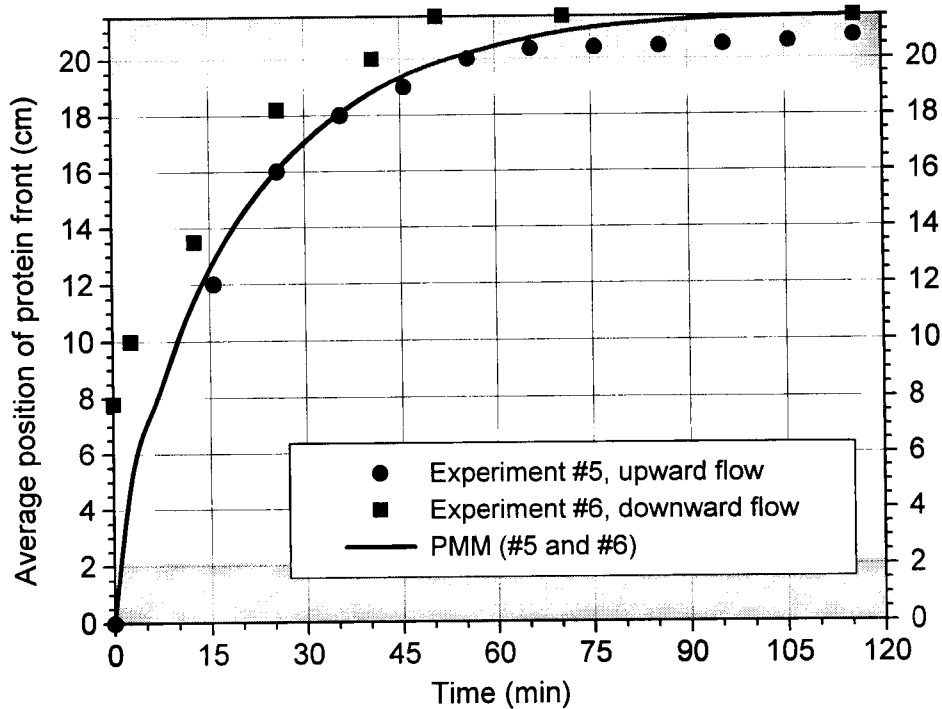


Fig. 32. Effect of flow direction on the axial progress of the protein front. Circles – experiment #5 (upward flow); squares - experiment #6 (upward flow); the PMM curves for both cases are indistinguishable. Shaded areas mark the positions of ECS manifolds. Adapted from Łabęcki et al. (1996).

The results plotted in fig. 32 confirm the validity of the earlier considerations regarding the anticipated influence of gravity and the choice of flow direction. It is seen that the PMM predictions agree well with the upward flow measurements (#5) for the initial phase of inoculation. The discrepancy between the model and the downward flow data over the first hour of experiment #6 indicates the importance of free convection, which significantly accelerated the axial protein transport. After about 1 h, the downstream protein movement in the upward cartridge (#5) slowed down to such an extent that the front position remained virtually unchanged for the next 60 min. This can be explained by the dominance of free over forced convection near the downstream end of the ECS, where the magnitude of ECS flow was very small owing to its transmembrane drainage over the length of the fibres. The PMM curve, which does not include buoyancy effects, shows that forced convection would have carried the protein front all the way to the downstream end by that time.

#### 4.4.2. Harvesting and ECS Shunt

Other open-shell operations studied within the scope of the present project are product harvesting and ECS medium recirculation (see fig. 23). In the 2-D PMM simulations of cocurrent and countercurrent harvesting processes, an ECS inlet flow of 1 mL/min was assumed, the ICS flow was 200 mL/min, and the average ECS protein concentration at the start of the simulation was 10 g/L. Two extreme cases of initial protein distribution were considered: uniform and steady-state downstream-polarised (fig. 33). Figure 34 compares the predicted efficiencies of cocurrent versus countercurrent harvesting of a model protein (BSA) from an essentially cell-free ECS, i.e., under conditions relevant to the early phase of HFBR operation. The ECS outlet concentration as a function of harvest volume for the two harvesting configurations is plotted in fig. 34a, while the corresponding product recovery curves are shown in fig. 34b.

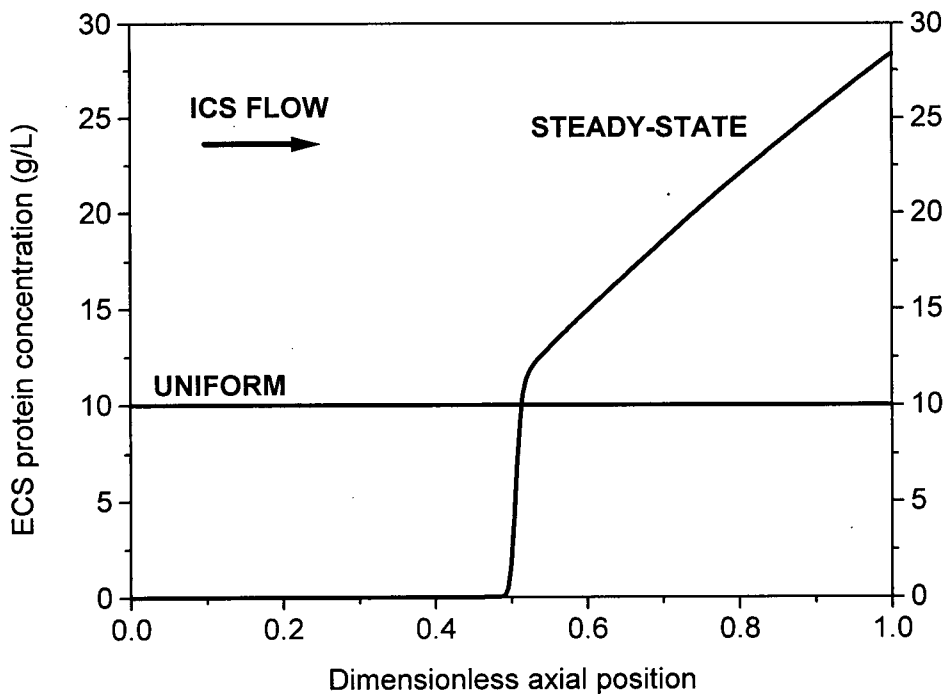


Fig. 33. Initial protein (BSA) distributions used in the PMM harvesting simulations; ICS flow rate  $Q_L = 200$  mL/min, average BSA concentration 10 g/L.

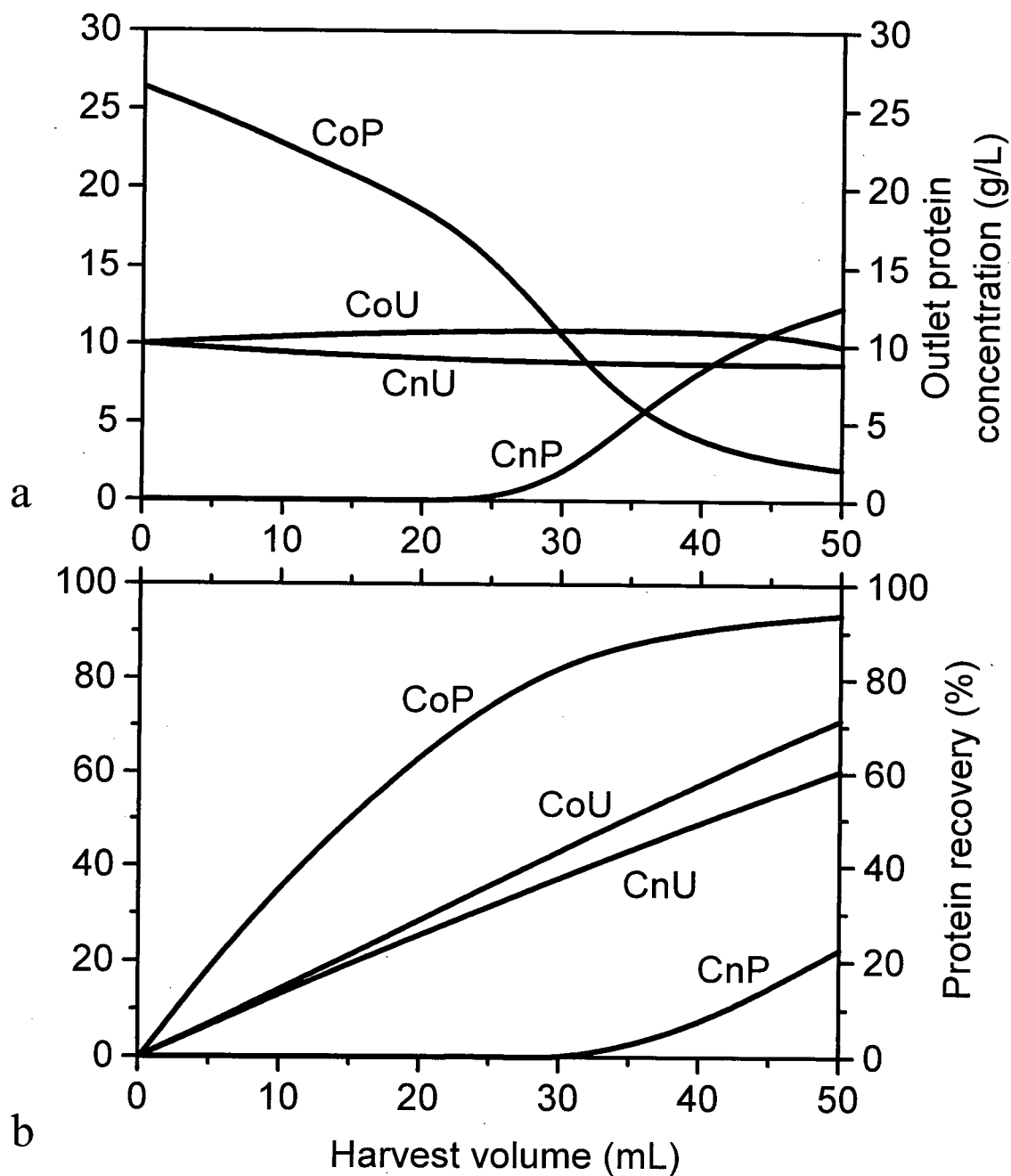


Fig. 34. PMM predictions of the outlet protein (BSA) concentration (*a*) and the fraction of protein removed from the ECS (*b*) for different harvesting modes: *Co*, cocurrent flow; *Cn*, countercurrent flow; *U*, uniform initial protein distribution; *P*, steady-state (polarised) initial protein distribution. The outlet concentrations were averaged over the ECS manifold length.

ICS flow rate  $Q_L = 200$  mL/min; ECS inlet flow rate 1 mL/min; average starting protein concentration 10 g/L. The ECS volume (not including manifolds) was 74.1 mL.

Certain general trends can be noticed from fig. 34. First, cocurrent harvesting is predicted to be more efficient than countercurrent harvesting regardless of the initial protein distribution. Second, the concentration of the product in the harvest should be maximised if the protein is downstream-polarised prior to harvesting (in the cocurrent configuration). By choosing cocurrent flow and taking advantage of the downstream protein polarisation, harvest volumes of only 30% of the ECS volume might be sufficient to recover about 75% of the protein at a mixing-cup harvest concentration of 20 g/L, i.e., twice the average initial concentration in the ECS. It should again be stressed that these results do not account for buoyancy effects, which depend on the orientation of bioreactor cartridge (see the following chapter 5), or for cell-packed conditions typical of the later stages of HFBR culture.

A continuous countercurrent flow configuration, or the countercurrent ECS shunt, can be used to reduce the heterogeneity of growth factor distribution caused by downstream polarisation. This is illustrated in fig. 35, which compares the steady-state results of PMM simulations for a closed-shell reactor and for an open-shell shunt system. Recirculation of the ECS fluid at a low flow rate (0.5 mL/min) countercurrently to the main ICS flow produced a considerably more uniform distribution of ECS protein (BSA). Other ECS flow rates were also investigated, but the resulting axial protein distributions (not shown) were less homogeneous than that predicted for 0.5 mL/min. The radial concentration variations were not significant in either of the two configurations, although the central core region was slightly enriched with protein in the open-shell case. The above results suggest that a properly optimised ECS shunt might be a feasible alternative to closed-shell operation of HFBRs.

#### 4.5. Conclusions

A series of dead-end inoculation experiments of different durations was carried out at different inlet protein concentrations, with either upward or downward flow. Each experiment yielded a set of axially as well as radially distributed ECS protein concentration data. In addition, the angular concentration variation was investigated in some of the cartridges. The angular effects were found to be of random nature, likely due to the nonuniform packing of the hollow fibres. The 2-D PMM simulations of the inoculation

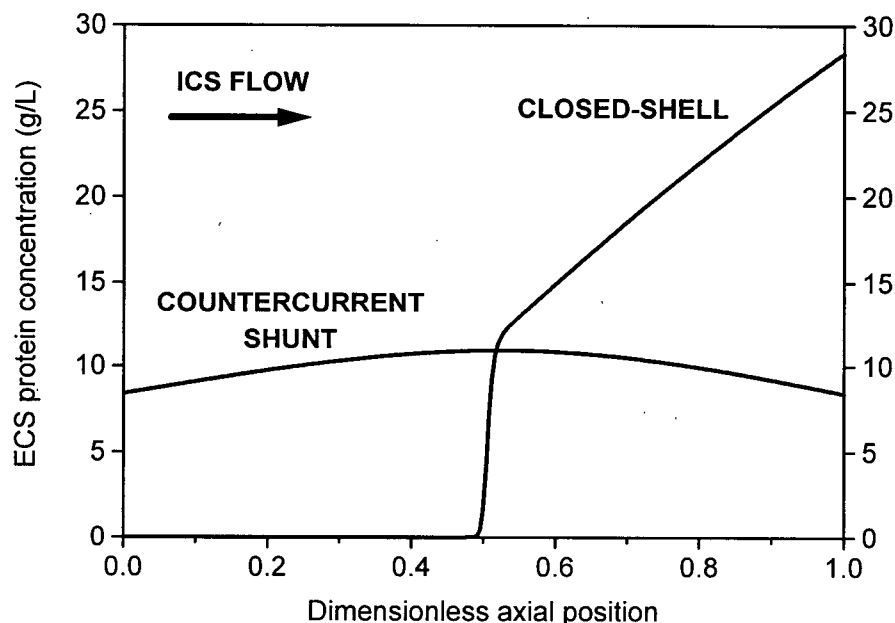


Fig. 35. PMM predictions of radially-averaged ECS protein (BSA) distribution at steady state in the countercurrent shunt and closed-shell configurations. ICS flow rate  $Q_L = 200$  mL/min, ECS inlet flow 0.5 mL/min, average initial ECS protein concentration 10 g/L.

experiments yielded results that reproduced well the radial concentration variation in each of the experimental cartridges.

The PMM-predicted radially-averaged axial protein distributions were in good agreement with the experimental data when the flow was directed upward and the number of fluid volumes displaced from the ECS,  $N_V$ , was relatively small, i.e., of the order of 1. In this case, the protein did not reach the downstream ECS manifold and the upward concentration gradients were relatively small. In contrast, when  $N_V$  was greater than 4 at the same flow orientation, the volume of the downstream manifold became filled with concentrated protein solution and significant upward concentration gradients developed in the ECS. In those experiments, the concentrations measured within the length of the downstream manifold were adjusted to account for the manifold-trapped protein (not included in the PMM domain) and thus allow more meaningful comparisons between the simulated and experimental data.

Despite the manifold concentration adjustment, significant differences between the measured and predicted results were observed for the high- $N_V$  experiments with upward flow. These discrepancies could be attributed to the effects of buoyancy, or free convection, which slowed the forced-convective, upward movement of protein. The results of a downward-flow experiment conducted under similar conditions confirmed this conclusion and demonstrated the PMM validity for high volumes of inoculation fluid passed through the cartridge. In the low- $N_V$  experiments (with upward flow), the upward concentration gradients were too small for the buoyancy effects to become apparent. The roles of free convection and of ECS manifolds in the redistribution of ECS proteins will constitute an important part of the 3-D PMM analyses presented in chapter 5.

Both the radially-averaged 2-D PMM and the 1-D KCM axial concentration profiles displayed a maximum located near the protein front, which was also observed experimentally. The differences between the predictions of the two models were more pronounced at low  $N_V$  than at high  $N_V$ . For example, the existence of another concentration maximum located upstream was correctly predicted by the PMM, but not by the KCM. This can be explained by a stronger influence of the radial entrance flow on the final protein distribution in the low- $N_V$  experiments. At high  $N_V$  values, the final ECS concentration field was mainly influenced by axial flow and the predictions of both models were similar. Owing to its intrinsic limitations, the KCM was not able to predict the macroscopic radial variation of ECS concentration for any of the experiments.

The experimental data collected here suggest that the conditions of upward flow and high  $N_V$  should favour the most uniform distributions of ECS inoculum if the dead-end flow configuration is used. The important point of this recommendation is that the inoculated solution reaches the downstream end of the ECS, while the development of upward density gradients due to downstream protein polarisation for this flow direction can facilitate homogenisation of the ECS contents by natural convection. For similar  $N_V$  values, factors such as the inlet protein concentration, the inoculation flow rate, and the total inoculum volume did not influence significantly the degree of heterogeneity for either transient or final protein distributions in the ECS. As was indicated at the beginning of this chapter, however, the main goal of the experimental inoculation study presented here was to validate the 2-D PMM predictions for an open-shell HFBR operation. The available data do not

allow formulation of more specific conclusions and recommendations about optimal inoculation conditions for cell culture HFBRs operated according to standard protocols (i.e., for inclined bioreactors inoculated countercurrently with an ICS upflow and an ECS downflow).

The results of the 2-D PMM simulations indicate that cocurrent harvesting from an essentially cell-free ECS should generally be more efficient than countercurrent harvesting, regardless of the initial protein distribution. This is evident from the predicted profiles of outlet protein concentration and of fractional product recovery, plotted as functions of harvest volume. The presented conclusions are expected to be even more valid at cell-packed ECS conditions, in which the larger transmembrane pressure difference existing in the countercurrent case would favour fluid bypassing from the ECS inlet to the ICS outlet at one end and from the ICS inlet to the ECS outlet at the other end of the cartridge. Downstream polarisation of the ECS product protein prior to its harvesting should further increase the efficiency of the cocurrent process.

The PMM also predicted that an external shunt configuration, in which the ECS medium is recirculated at a low flow rate countercurrently to the ICS flow, could be an effective way of controlling the magnitude of ECS convective transport and hence also the heterogeneity of ECS growth-factor and product protein concentrations in HFBRs. This suggests that the ECS shunt system has the potential to successfully compete with the conventional closed-shell HFBR, especially during the bioreactor startup phase, when rapid and uniform cell expansion is desired. However, adjustments to the shunt operation may be necessary to account for the changes in ECS flow conditions due to the presence of the growing cell mass at the later stages of culture.

The performance of a hollow-fibre hybridoma culture with continuously recirculated ECS fluid was analysed by Gramer et al. (1999). Their system was similar to the ECS shunt considered here, except that the flow arrangement was cocurrent rather than countercurrent. Compared with a traditional closed-shell HFBR which is harvested periodically, the continuous cocurrent open-shell system showed increases both in culture duration and in antibody yield, which might be attributed to a more homogeneous cell growth environment achieved by ECS fluid recirculation. However, neither of the two HFBR configurations was able to match the performance of an ECS cycling system (Acusyst) equipped with a

pressure-controlled expansion chamber (see fig. 4c and sections 2.1.3.4 and 2.1.3.5). A possible explanation for this difference might be the enhanced ECS mixing as well as effective flushing of cell debris from both the ECS and the membrane pores due to significant ECS transverse and transmembrane flows present in the Acusyst.

Although the countercurrent shunt proposed here is still a predominantly axial-flow configuration, it is premature to draw conclusions about its performance in cell culture, especially if small modifications can be made to improve the design of such a system. For example, an addition to the ECS loop of a reservoir similar to the Acusyst expansion chamber might facilitate the removal of dead cells and cell debris from the bioreactor, thus sustaining a more healthy environment for viable cells in the ECS. Also, optimisation of both the shunt flow rate and the cartridge inclination angle (see also chapter 5) might help maintain the cells in suspension, thus preventing formation of highly heterogeneous conditions in the ECS, with relatively few but large flow channels running through a densely-packed cell mass whose interior cells are prone to oxygen or nutrient starvation. (NMR imaging confirmed that, in contrast to the other two HFBR systems investigated by Gramer et al. (1999), such heterogeneous conditions did not exist in the Acusyst bioreactor.) On the other hand, a potential problem of shear-induced cell damage due to the repeated passage of cell suspension through the ECS recirculation pump may have to be addressed before the shunt system is implemented in practice (this might be partly resolved by positioning the ECS ports upwards and using a sufficiently low ECS flow rate). Further theoretical and experimental studies, preferably involving cell cultivation, are needed to elucidate the above issues.

## Chapter 5

### THREE-DIMENSIONAL ANALYSIS OF GRAVITY-INFLUENCED PROTEIN TRANSPORT IN CLOSED-SHELL HOLLOW-FIBRE BIOREACTORS

#### 5.1. Motivation and Objectives

The investigation of three-dimensional velocity and solute distributions in hollow-fibre reactors adds a considerable degree of realism to the description of HFBRs used for cell culture, where they are normally operated at nonvertical orientations (e.g., 45° with upward ICS flow). The combined effects of forced-convective downstream polarisation and gravity-induced natural convection in the ECS can bring about a spatial redistribution of growth-factor and product proteins; this – depending on the choice of operating conditions – may be used to the advantage or act to the disadvantage of cell culture. The fate of the ECS proteins (as well as of the cells) is further complicated by the influence of the fibre-free ECS manifolds. A good understanding of the transport phenomena occurring in all three dimensions of a hollow-fibre system is therefore prerequisite for the development of efficient and productive HFBR operation schemes.

The work described in this chapter focuses on closed-shell HFBRs, since the closed-shell phase is by far the longest in the overall duration of hollow-fibre cell culture. The essential proteins are assumed to be retained in the ECS by ultrafiltration membranes, which is usually true for medium proteins such as albumin or transferrin and for protein products such as antibodies. The main objective of the analysis presented here was to explore ways of improving HFBR productivity by shedding light on how gravity, ECS manifolds, and other factors affect the three-dimensional ECS protein distribution in hollow-fibre reactors.

## 5.2. Model Development

### 5.2.1. Underlying Assumptions

The model proposed here is a three-dimensional extension of the porous medium model of fluid flow and protein transport in HFBRs (Łabęcki et al. 1995, 1996), which was discussed in the preceding chapter. The most important new features of this extension are: the addition of density and viscosity gradients; the addition of angular position as another spatial dimension; and the inclusion, albeit simplified, of ECS manifolds. As before, the ICS and the ECS of the hollow-fibre bundle are treated as two interpenetrating porous media, with the constitutive equations formulated in a coupled form for both of these regions.<sup>17</sup> In the present analysis, the membranes are assumed impermeable to protein, although the general model formulation does account for transmembrane protein transport. Only the closed-shell reactor configuration is considered. A detailed list of the model assumptions is given as follows.

- (1) The fluid is incompressible and Newtonian. The incompressibility assumption holds also for fluids with variable fluid density, as long as the latter is a linear function of solute concentration.
- (2) The ECS porous medium is treated as inhomogeneous with respect to fluid density and viscosity; that is, these two properties can vary with position within the ECS (through their dependence on protein concentration). The ICS porous medium is treated as well-mixed, and hence homogeneous with respect to fluid density and viscosity. The porosity within each of the two spaces is assumed constant.
- (3) The HFBR system is isothermal; however, the dependence on temperature of fluid density, fluid viscosity, and protein diffusivity, is taken into account.
- (4) Dispersive fluid fluxes due to local fluctuations in ICS or ECS velocities are negligible, relative to the fluxes resulting from the average flows.
- (5) The ECS fluid flow is characterised by low Reynolds numbers ( $Re < 1$ ), making Darcy's law applicable to the ECS region. The ICS fluid flow, averaged over many fibres, is essentially one-dimensional and can therefore be described using an

---

<sup>17</sup> Strictly speaking, the membranes constitute a third porous region embedded within the other two. However, the PMM neglects transport phenomena in this region because of the membranes' negligible capacitance for fluid and protein.

expression similar to Darcy's law (i.e., a proportional relationship between the axial velocity and the axial pressure gradient).

- (6) The ECS porous medium is anisotropic with respect to the Darcy permeability and protein diffusivity; that is, these properties are assumed to depend on direction within the ECS. The transverse components of each of these two properties are the same (except when the HFBR cartridge is oriented vertically; see the next assumption); for example, in cylindrical co-ordinates, the radial and angular components are equal.
- (7) For nonvertical reactor orientations, planar symmetry of the system is assumed; the symmetry plane is determined by the reactor's longitudinal axis and by the direction of the vector of gravitational acceleration. For the vertical orientation, axial symmetry is assumed, with the reactor's longitudinal axis being the symmetry axis. In the latter case, the angular components of Darcy permeability and protein diffusivity are set to zero, which reflects the lack of net fluid and solute fluxes in the angular direction as a result of the assumed symmetry.
- (8) The membrane hydraulic permeability,  $L_p$ , fibre dimensions, as well as each of the components of the Darcy permeability and protein diffusivity tensors, are constant in space and in time.
- (9) The ECS manifold fluid is stagnant. At each time instant and over the whole circumference and axial length of the manifold, instantaneous diffusion-like equilibration of protein concentration occurs between the manifold and the adjacent layer of control volumes in the fibre bundle (i.e., in the radial direction). In addition, a similar instantaneous equilibration process takes place in any of the three dimensions within the manifold, as long as there exist concentration gradients such that natural convection would normally be expected to arise. See section 5.2.2.3 for more information on the manifold concentration adjustment schemes adopted here.

## 5.2.2. Mathematical Formulation

### 5.2.2.1. *Fluid Dynamics*

The equations governing the ICS and ECS hydrodynamics are derived by combining the Darcy and continuity laws for each of the two regions. The continuity equation for an

incompressible, inhomogeneous fluid in a porous medium, with velocity fluctuations neglected, has the form (Bear 1972, p. 103):

$$\varepsilon \frac{\partial \bar{\rho}}{\partial t} + \nabla \cdot (\bar{\rho} \bar{\mathbf{v}}) = 0, \quad (91)$$

where  $\varepsilon$  is the medium porosity (assumed constant),  $\rho$  is the fluid density,  $\mathbf{v}$  is the superficial fluid velocity vector, and the overbars signify averaging over the representative elementary volume (REV). For our purposes, since the ICS and ECS can exchange fluid through the membranes, a source/sink term must be added to the above equation; this leads to the following expression of fluid mass conservation for the ECS:

$$\varepsilon_S \frac{\partial \rho_S}{\partial t} + \nabla \cdot (\rho_S \mathbf{v}_S) = \rho_0 A_V J_{TMF}, \quad (92)$$

where the subscript  $S$  denotes the ECS (first letter of *shell* side), and the overbars have been omitted for convenience. On the right-hand side of eq. (92),  $\rho_0$  is the protein-free fluid density,  $A_V$  is the average membrane surface area per unit volume (eq. (30), section 2.2.2), and  $J_{TMF}$  is the transmembrane fluid flux (TMFF), expressed as (cf. eq. (49), section 3.2.2.1)

$$J_{TMF} = \frac{L_p}{\mu_0} (P_L - P_S - \Delta\Pi_{eff}), \quad (93)$$

where  $L_p$  is the membrane hydraulic permeability (eq. (1), section 2.1.2.2),  $\mu_0$  is the protein-free fluid viscosity,  $P_L$  and  $P_S$  are the ICS (*lumen* side) and ECS hydrostatic pressures, respectively, and  $\Delta\Pi_{eff}$  is the effective osmotic pressure difference (eq. (50), section 3.2.2.1). The protein-free medium density,  $\rho_0$ , and viscosity,  $\mu_0$ , were calculated here as the respective properties of pure water. Expansion of eq. (92) in cylindrical co-ordinates leads to

$$\varepsilon_S \frac{\partial \rho'_S}{\partial t} + v_{S,r} \frac{\partial \rho'_S}{\partial r} + \frac{v_{S,\theta}}{r} \frac{\partial \rho'_S}{\partial \theta} + v_{S,z} \frac{\partial \rho'_S}{\partial z} + \rho'_S \left[ \frac{1}{r} \frac{\partial (rv_{S,r})}{\partial r} + \frac{1}{r} \frac{\partial v_{S,\theta}}{\partial \theta} + \frac{\partial v_{S,z}}{\partial z} \right] = A_V J_{TMF}, \quad (94)$$

where  $\rho'_s = \rho_s / \rho_0$  is the dimensionless ECS fluid density. For the ICS, where the fluid is homogeneous and the flow is essentially one-dimensional in the  $z$ -direction, the continuity law has a simpler form, i.e.

$$\rho_L \frac{\partial v_{L,z}}{\partial z} = -\rho_0 A_V J_{TMF}, \quad (95)$$

or, in terms of the dimensionless ICS fluid density  $\rho'_L = \rho_L / \rho_0$ ,

$$-\rho'_L \frac{\partial v_{L,z}}{\partial z} = A_V J_{TMF}. \quad (96)$$

In writing eqs. (95) and (96) it has been assumed that the lumen side may, in general, contain a certain (spatially and temporally constant) quantity of non-leaking protein.

The general form of Darcy's law for an inhomogeneous medium is (Bear 1972, p. 106)

$$v_i = -\frac{k_i}{\mu} \left( \frac{\partial \bar{P}}{\partial x_i} + \bar{\rho} g \frac{\partial h}{\partial x_i} \right), \quad (97)$$

where  $k_i$  is the Darcy permeability in the  $i$ -direction,  $\mu$  is the fluid viscosity,  $P$  is the hydrostatic pressure,  $x_i$  is the  $i$ -th independent spatial variable,  $g = 9.807 \text{ m/s}^2$  is the acceleration of gravity, and  $h$  is the elevation of the centre of mass of the REV above a datum level. In our case, the spatial variables are  $r$ ,  $\theta$ , and  $z$ , and the datum level is conveniently set at the centre of the cartridge outlet area ( $r = 0$ ,  $z = L$ ), where the ICS pressure is specified as a boundary condition (fig. 36). In this arrangement,  $h$  assumes the following form:

$$h = r \sin \Psi \cos \theta + (L - z) \cos \Psi, \quad (98)$$

where  $\Psi$  is the cartridge inclination angle, defined as the angle between the direction of the bulk ICS flow and the direction of the gravity vector,  $L$  is the effective length of the porous medium domain, and  $\theta$  is the angular position measured from the highest point of a given

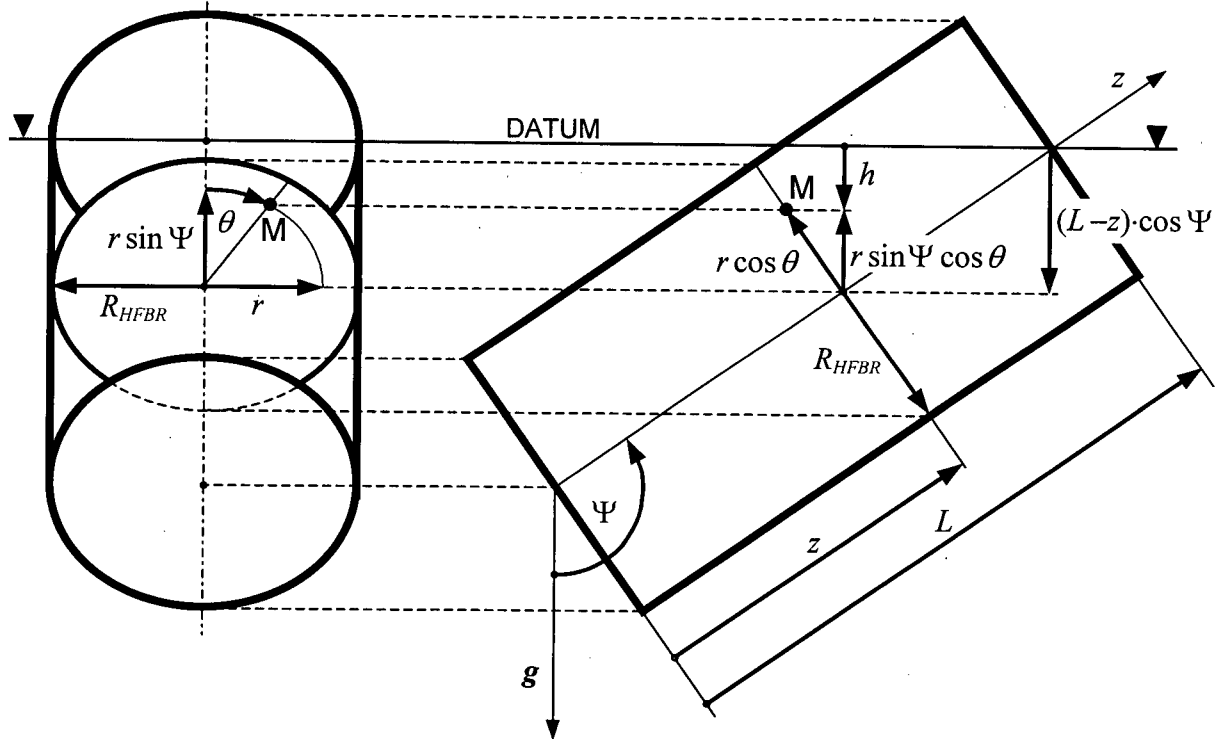


Fig. 36. Diagram illustrating the arrangement of spatial parameters in a three-dimensional cylindrical domain and the elevation  $h$  of a point  $M(r, \theta, z)$  relative to the datum level (dimensions not to scale).

circular cross-section through cartridge (see fig. 36).<sup>18</sup> Thus, the three components of fluid velocity for the ECS are obtained from eqs. (97) and (98) as:

$$v_{S,r} = -\frac{k_{S,r}}{\mu_S} \left( \frac{\partial P_S}{\partial r} + \rho_S g \sin \Psi \cos \theta \right) \quad (99a)$$

$$v_{S,\theta} = -\frac{k_{S,\theta}}{\mu_S} \left( \frac{1}{r} \frac{\partial P_S}{\partial \theta} - \rho_S g \sin \Psi \sin \theta \right) \quad (99b)$$

$$v_{S,z} = -\frac{k_{S,z}}{\mu_S} \left( \frac{\partial P_S}{\partial z} - \rho_S g \cos \Psi \right). \quad (99c)$$

Similarly, the only component of velocity in the ICS is

<sup>18</sup> Note that for vertical cartridges  $\theta$  becomes irrelevant because of axial symmetry. However, a general formalism is presented here, valid for all cartridge orientations (i.e., for all  $\Psi$ ).

$$v_{L,z} = -\frac{k_{L,z}}{\mu_L} \left( \frac{\partial P_L}{\partial z} - \rho_L g \cos \Psi \right). \quad (100)$$

At this point, it will be convenient to introduce two new variables, the piezometric pressure  $\hat{P}$  and the reduced density  $\Delta\rho$ , defined for both spaces as follows:

$$\hat{P}_S = P_S + \rho_0 g h \quad (101a)$$

$$\hat{P}_L = P_L + \rho_0 g h \quad (101b)$$

$$\Delta\rho_S = \rho_S - \rho_0 \quad (102a)$$

$$\Delta\rho_L = \rho_L - \rho_0. \quad (102b)$$

The term piezometric pressure is derived here from the engineering term piezometric head, which is defined as the sum of the pressure head  $P/(\rho g)$  and the elevation head  $h$  (Bear 1972, p. 64). Equations (99) and (100) can hence be rewritten as:

$$v_{S,r} = -\frac{k_{S,r}}{\mu_S} \left( \frac{\partial \hat{P}_S}{\partial r} + \Delta\rho_S g \sin \Psi \cos \theta \right), \quad (103a)$$

$$v_{S,\theta} = -\frac{k_{S,\theta}}{\mu_S} \left( \frac{1}{r} \frac{\partial \hat{P}_S}{\partial \theta} - \Delta\rho_S g \sin \Psi \sin \theta \right), \quad (103b)$$

$$v_{S,z} = -\frac{k_{S,z}}{\mu_S} \left( \frac{\partial \hat{P}_S}{\partial z} - \Delta\rho_S g \cos \Psi \right), \quad (103c)$$

and

$$v_{L,z} = -\frac{k_{L,z}}{\mu_L} \left( \frac{\partial \hat{P}_L}{\partial z} - \Delta\rho_L g \cos \Psi \right). \quad (104)$$

The above expressions of Darcy's law are perhaps more elegant than eqs. (99) and (100), since they treat the gravitational terms only as perturbations to the velocities of the solute-free flows. These formulations also avoid potential numerical inaccuracies resulting from the subtraction of two large terms of comparable magnitudes (i.e., the pressure gradient term and the gravitational term), as well as simplifying the specification of the ICS boundary conditions.

The HFBR fluid flow equations can now be formulated in terms of the piezometric pressures by inserting the velocity expressions (103) and (104) into the respective continuity equations (94) and (96). Making use of eqs. (101) and (102), and introducing a useful parameter  $F_1$ , the ECS continuity equation can be cast in the following, more general form:

$$F_1 \left\{ \epsilon_s \frac{\partial \Delta \rho'_s}{\partial t} + v_{s,r} \frac{\partial \Delta \rho'_s}{\partial r} + \frac{v_{s,\theta}}{r} \frac{\partial \Delta \rho'_s}{\partial \theta} + v_{s,z} \frac{\partial \Delta \rho'_s}{\partial z} + \Delta \rho'_s \left[ \frac{1}{r} \frac{\partial (rv_{s,r})}{\partial r} + \frac{1}{r} \frac{\partial v_{s,\theta}}{\partial \theta} + \frac{\partial v_{s,z}}{\partial z} \right] \right. \\ \left. + \frac{1}{r} \frac{\partial (rv_{s,r})}{\partial r} + \frac{1}{r} \frac{\partial v_{s,\theta}}{\partial \theta} + \frac{\partial v_{s,z}}{\partial z} = \frac{L_p A_v}{\mu_0} (\hat{p}_L - \hat{p}_S - \Delta \Pi_{eff}) \right\}, \quad (105)$$

where  $\Delta \rho'_s = \Delta \rho_s / \rho_0$  is the dimensionless reduced density of the ECS fluid, and  $F_1$  indicates whether the ECS is effectively treated, from the fluid continuity point of view, as a homogeneous ( $F_1 = 0$ ) or inhomogeneous ( $F_1 = 1$ ) porous medium. To be more explicit,  $F_1 = 0$  means that the only gradients of density and viscosity included in the ECS continuity equation are those obtained by differentiation of the velocity expressions in the homogeneous form of this equation. Upon rearranging the terms, a more orderly form of eq. (105) is obtained as

$$F_1 \epsilon_s \frac{\partial \Delta \rho'_s}{\partial t} + \left[ F_1 v_{s,r} \frac{\partial \Delta \rho'_s}{\partial r} + (1 + F_1 \Delta \rho'_s) \frac{1}{r} \frac{\partial (rv_{s,r})}{\partial r} \right] \\ + \left[ F_1 v_{s,\theta} \frac{1}{r} \frac{\partial \Delta \rho'_s}{\partial \theta} + (1 + F_1 \Delta \rho'_s) \frac{1}{r} \frac{\partial v_{s,\theta}}{\partial \theta} \right] \\ + \left[ F_1 v_{s,z} \frac{\partial \Delta \rho'_s}{\partial z} + (1 + F_1 \Delta \rho'_s) \frac{\partial v_{s,z}}{\partial z} \right] = \frac{L_p A_v}{\mu_0} (\hat{p}_L - \hat{p}_S - \Delta \Pi_{eff}). \quad (106)$$

Substitution of eqs. (103) into eq. (106), followed by extensive algebraic manipulation, yields eventually

$$A_{r2} \frac{1}{r} \frac{\partial}{\partial r} \left( r \frac{\partial \hat{p}_S}{\partial r} \right) + A_{r1} \frac{\partial \hat{p}_S}{\partial r} + A_{\theta 2} \frac{1}{r} \frac{\partial^2 \hat{p}_S}{\partial \theta^2} + A_{\theta 1} \frac{1}{r} \frac{\partial \hat{p}_S}{\partial \theta} \\ + A_{z2} \frac{\partial^2 \hat{p}_S}{\partial z^2} + A_{z1} \frac{\partial \hat{p}_S}{\partial z} + \hat{p}_S - \hat{p}_L = A_{SRHS}. \quad (107)$$

The  $1/r$  factor has been purposefully preserved in some of the terms above for convenience during discretisation, since the integration over a cylindrical elementary volume requires multiplication of integrand terms by  $r$ . The coefficients in eq. (107) are defined as follows:

$$A_{r2} = -k_{S,r} \mu_S^{-1} \frac{A_{F1}}{A_{Lp}}, \quad (108a)$$

$$A_{\theta 2} = -k_{S,\theta} \mu_S^{-1} \frac{1}{r} \frac{A_{F1}}{A_{Lp}}, \quad (108b)$$

$$A_{z2} = -k_{S,z} \mu_S^{-1} \frac{A_{F1}}{A_{Lp}}, \quad (108c)$$

$$A_{r1} = -\frac{k_{S,r}}{A_{Lp}} \left( F_1 \mu_S^{-1} \frac{\partial \Delta \rho'_S}{\partial r} + F_\mu A_{F1} \frac{\partial \mu_S^{-1}}{\partial r} \right), \quad (108d)$$

$$A_{\theta 1} = -\frac{k_{S,\theta}}{A_{Lp}} \frac{1}{r} \left( F_1 \mu_S^{-1} \frac{\partial \Delta \rho'_S}{\partial \theta} + F_\mu A_{F1} \frac{\partial \mu_S^{-1}}{\partial \theta} \right), \quad (108e)$$

$$A_{z1} = -\frac{k_{S,z}}{A_{Lp}} \left( F_1 \mu_S^{-1} \frac{\partial \Delta \rho'_S}{\partial z} + F_\mu A_{F1} \frac{\partial \mu_S^{-1}}{\partial z} \right), \quad (108f)$$

$$\begin{aligned} A_{SRHS} = & -\Delta \Pi_{eff} - \varepsilon_S \frac{F_1}{A_{Lp}} \frac{\partial \Delta \rho'_S}{\partial t} \\ & + \frac{k_{S,r}}{A_{Lp}} \rho_0 g \sin \Psi \cos \theta \left[ A_{F1} \frac{1}{r} \mu_S^{-1} \Delta \rho'_S + A_{F12} \mu_S^{-1} \frac{\partial \Delta \rho'_S}{\partial r} + F_\mu A_{F1} \Delta \rho'_S \frac{\partial \mu_S^{-1}}{\partial r} \right] \\ & - \frac{k_{S,\theta}}{A_{Lp}} \rho_0 g \sin \Psi \frac{1}{r} \left[ A_{F12} \mu_S^{-1} \sin \theta \frac{\partial \Delta \rho'_S}{\partial \theta} + A_{F1} \Delta \rho'_S \left( F_\mu \sin \theta \frac{\partial \mu_S^{-1}}{\partial \theta} + \mu_S^{-1} \cos \theta \right) \right] \\ & - \frac{k_{S,z}}{A_{Lp}} \rho_0 g \cos \Psi \left[ A_{F12} \mu_S^{-1} \frac{\partial \Delta \rho'_S}{\partial z} + F_\mu A_{F1} \Delta \rho'_S \frac{\partial \mu_S^{-1}}{\partial z} \right], \end{aligned} \quad (108g)$$

where

$$A_{F1} = 1 + F_1 \Delta \rho'_S, \quad (108h)$$

$$A_{F12} = 1 + 2 F_1 \Delta \rho'_S, \quad (108i)$$

$$A_{Lp} = L_p A_V / \mu_0, \quad (108j)$$

$\mu_S^{-1}$  is the reciprocal viscosity of the ECS fluid, and the parameter  $F_\mu$  has been introduced to allow convenient neglect ( $F_\mu = 0$ ) or inclusion ( $F_\mu = 1$ ) of ECS viscosity gradients. A similar procedure for the ICS, i.e., the combination of eqs. (105) and (113) (with density and viscosity assumed constant), leads to the comparatively simple equation:

$$A_{L2} \frac{\partial^2 \hat{P}_L}{\partial z^2} - \hat{P}_L + \hat{P}_S = A_{LRHS}, \quad (109)$$

where

$$A_{L2} = \rho'_L \frac{k_{L,z}}{\mu_L A_{Lp}} \quad (110a)$$

and

$$A_{LRHS} = -\Delta\Pi_{eff}. \quad (110b)$$

A consequence of the fluid incompressibility assumption is that the system hydrodynamics are always quasi-steady; i.e., any transient changes in the flow field are due only to changes in the protein concentration with time. In the present model formulation, the fluid flow can be influenced by the presence of protein through osmotic pressure, density, or viscosity variations. The concentration-dependence of the osmotic pressure in eqs. (108g) and (110b) was modelled using a virial relationship (eq. (52)), as described earlier in section 3.2.2.1. The fluid density was assumed to vary with protein concentration according to the following experimental formula obtained by Vilker et al. (1981a), valid for BSA concentrations up to 580 g/L:

$$\rho = \rho_0 + C(1 - \rho_0/\rho_A), \quad (111)$$

where  $C$  is the protein concentration,  $\rho_0$  is the density of the protein-free medium (water), and  $\rho_A = 1340$  g/L is referred to by the authors as the partial specific density of BSA. The relationship between fluid viscosity and protein concentration was assumed to be (Anderson et al. 1978)

$$\mu = \mu_0 (1 + A_{\mu 1} C + A_{\mu 2} C^2), \quad (112)$$

where  $\mu_0$  is the protein-free medium viscosity (assumed to be the viscosity of water),  $A_{\mu 1} = 3.8 \times 10^{-3}$  L/g, and  $A_{\mu 2} = 2.2 \times 10^{-5}$  L<sup>2</sup>/g<sup>2</sup> (valid for BSA solutions in 0.1 M KCl at pH  $\approx$  6.5). More details regarding the model parameters are provided in section 5.2.3.

The boundary conditions for the ECS equation (107) are, with one exception ( $r = 0$ ), derived by demanding that the normal velocity components become zero at the impermeable boundaries. It should be noted that the order of Darcy's law does not permit imposition of additional constraints, such as no-slip, on the tangential velocity components. Symmetry with respect to the  $\theta = 0$  (or  $\theta = \pi$ ) plane is assumed, which is also valid for axisymmetric vertical cartridges. At  $r = 0$ , the boundary degenerates from a two-dimensional surface to a one-dimensional line; hence, mass flow through it is zero and the boundary condition becomes immaterial. The radial velocity is discontinuous at  $r = 0$ , which seems at first to contradict fluid continuity; however, it is readily seen that all velocity components in Cartesian co-ordinates are continuous throughout the domain. For simplicity, the boundary at  $r = R_{HFBR}$  is treated as impermeable over its whole length, i.e., including the upstream and downstream segments where the fibre bundle adjoins the ECS manifolds.

For the ICS equation (109), a known axial velocity is specified at the lumen inlet,  $v_{L,in}$ , and a known value of the piezometric pressure,  $\hat{P}_{L,out}$ , is set at the lumen outlet. Both  $v_{L,in}$  and  $\hat{P}_{L,out}$  are assumed constant over the cartridge cross-section (note that, by definition, the piezometric pressure,  $\hat{P}_{L,out}$ , does not vary with elevation). Alternatively, a known and constant  $\hat{P}_{L,in}$  can be specified at the inlet, although the velocity condition is more consistent with the standard HFBR system configuration in which the ICS recycle pump circulates the liquid through the cartridge at an essentially constant flow rate (see fig. 2 in section 2.1.3.1). Table 9 summarises the boundary conditions for both eqs. (107) and (109).

#### 5.2.2.2. ECS Protein Transport

The time-dependent distribution of protein in the ECS, with the neglect of dispersive fluxes due to local velocity fluctuations, can be described using a standard convection-diffusion equation, which in cylindrical co-ordinates has the following form:

$$\varepsilon_S \frac{\partial C_S}{\partial t} = \frac{1}{r} \frac{\partial (r J_{P,r})}{\partial r} + \frac{1}{r} \frac{\partial J_{P,\theta}}{\partial \theta} + \frac{\partial J_{P,z}}{\partial z} + A_V J_{TMP}. \quad (113)$$

Table 9. Boundary conditions for the ECS and ICS pressure equations (107) and (109)

Boundary	Condition	Comment
$z = 0$	$\frac{\partial \hat{P}_S}{\partial z} = \Delta \rho_S g \cos \Psi$ $\frac{\partial \hat{P}_L}{\partial z} = \Delta \rho_L g \cos \Psi - v_{L,in} \mu_L / k_{L,z}$ or $\hat{P}_L = \hat{P}_{L,in}$	Impermeable boundary Known velocity or known pressure at ICS inlet
$z = L$	$\frac{\partial \hat{P}_S}{\partial z} = \Delta \rho_S g \cos \Psi$ $\hat{P}_L = \hat{P}_{L,out}$	Impermeable boundary Known pressure at ICS outlet
$\theta = 0, \theta = \pi$	$\frac{\partial \hat{P}_S}{\partial \theta} = 0$	Symmetry
$r = R_{HFBR}$	$\frac{\partial \hat{P}_S}{\partial r} = -\Delta \rho_S g \sin \Psi \cos \theta$	Impermeable boundary
$r = 0$	Immaterial	Degenerate boundary

Here,  $\varepsilon_S$  is the ECS porosity,  $C_S$  is the local interstitial protein concentration (i.e., mass of protein per unit volume of the ECS),  $J_{TMP}$  is the transmembrane protein flux, and  $J_P$  is the sum of the diffusive and convective components of the ECS protein flux in each spatial dimension, that is

$$J_{P,r} = D_{S,r} \frac{\partial C_S}{\partial r} - v_{S,r} C_S \quad (114a)$$

$$J_{P,\theta} = \frac{D_{S,\theta}}{r} \frac{\partial C_S}{\partial \theta} - v_{S,\theta} C_S \quad (114b)$$

$$J_{P,z} = D_{S,z} \frac{\partial C_S}{\partial z} - v_{S,z} C_S, \quad (114c)$$

where  $D_{S,r}$ ,  $D_{S,\theta}$ , and  $D_{S,z}$  are the protein diffusivities in the radial, angular, and axial directions, respectively, whereas  $v_{S,r}$ ,  $v_{S,\theta}$  and  $v_{S,z}$  are the superficial ECS velocity components expressed by eqs. (103). Since the protein is assumed to be completely retained in the ECS, the transmembrane flux term in eq. (113) will be neglected here (for a leaking protein,  $J_{TMP}$  can be modelled using eq. (68) derived in section 3.2.2.3). Thus, the following equation governing ECS protein transport is obtained:

$$\begin{aligned} \varepsilon_s \frac{\partial C_s}{\partial t} = & \frac{1}{r} \frac{\partial}{\partial r} \left( r D_{s,r} \frac{\partial C_s}{\partial r} - r v_{s,r} C_s \right) \\ & + \frac{1}{r} \frac{\partial}{\partial \theta} \left( \frac{D_{s,\theta}}{r} \frac{\partial C_s}{\partial \theta} - v_{s,\theta} C_s \right) + \frac{\partial}{\partial z} \left( D_{s,z} \frac{\partial C_s}{\partial z} - v_{s,z} C_s \right). \end{aligned} \quad (115)$$

This is coupled with the hydrodynamic eqs. (107) and (109) through the fluid velocities, which themselves depend on the protein distribution via the concentration-dependent density, viscosity, and osmotic pressure.

Equation (115) is subject to boundary conditions similar to those for the ECS fluid flow equation (107); namely, all physical boundaries, i.e.  $z = 0$ ,  $z = L$ , and  $r = R_{HFBR}$  are treated as impermeable, whereas planar symmetry is assumed at  $\theta = 0$  and  $\theta = \pi$ . Accordingly, at all boundaries but the centreline ( $r = 0$ ), where the condition is immaterial, it is stipulated that the protein flux into the boundary is zero. This is effectively equivalent to the requirement of a vanishing concentration gradient normal to the boundary, because the normal velocity component, and hence the corresponding convective flux, is also zero at each boundary (except at  $r = 0$ ). The initial condition for eq. (115) is a known ECS concentration distribution at time  $t = 0$ . In this study, the starting protein concentration was always assumed spatially constant and equal to  $C_0$  throughout the ECS, including the manifolds. Table 10 summarises the boundary and initial conditions for eq. (115).

Table 10. Boundary and initial conditions for the ECS protein concentration equation (115)

Boundary	Condition	Comment
$z = 0, z = L$	$\partial C_s / \partial z = 0$	Impermeable boundary
$\theta = 0, \theta = \pi$	$\partial C_s / \partial \theta = 0$	Symmetry
$r = R_{HFBR}$	$\partial C_s / \partial r = 0$	Impermeable boundary
$r = 0$	Immaterial	Degenerate boundary
$t = 0$	$C_s = C_0$	Uniform initial distribution

### 5.2.2.3. *Modelling of ECS Manifolds*

The main shortcoming of the three-dimensional model formulation presented above is that the fibre-free ECS manifolds, which comprise a significant portion of the total ECS volume, have not been included in the model domain. A rigorous description of hydrodynamics in these manifolds, even in the closed-shell case, would likely require employment of second-order differential equations such as the Navier-Stokes equations. This would considerably increase the level of algebraic and numerical challenge involved, owing to the added shear stress terms as well as the necessity to iterate the manifold pressure and velocity solutions at each time step. In addition, the fluid flow and protein distributions would have to be matched at the boundary between the manifold and the ECS fibre bundle. Since the latter condition can only be met if equations of the same order (i.e., second order) are used for both of these regions, it follows that the model complexity would be significantly increased throughout the ECS domain. The resulting set of model equations would be extremely tedious to discretise and difficult to solve numerically.

To avoid the above-mentioned complications, a simpler approach to the modelling of the ECS manifolds has been taken here, similar to the manifold extension scheme used in the one-dimensional protein leakage study described in chapter 3. Considering the significant role of the ECS manifolds observed thus far in all of the experimental studies of ECS protein redistribution, it is clear that these regions must be included in any realistic HFBR model, even if only in a very approximate manner. In the earlier approach (section 3.2.2.5), instantaneous equilibration of the protein was assumed to occur, at each time step, between each ECS manifold and the neighbouring portion of the fibre bundle (i.e., the sum of Krogh cylinder envelopes for all fibres). A natural extension of this procedure to the present three-dimensional system assumes that the protein equilibrates between each control volume (CV) in the radially-outermost layer of the fibre bundle and the corresponding, adjacent CV in the ECS manifold (fig. 37). Note that the manifold space is now subdivided not only into axial segments, but also into  $N_k$  angular sections (counted over half the circumference), as well as into  $N_m$  radial layers, each having the same volume. For geometrical simplicity, the volumes of the ECS port and of the small dead-end region near the fibre potting (see section 3.2.2.5) have both been neglected; thus, the manifolds are effectively treated as perfect annuli.

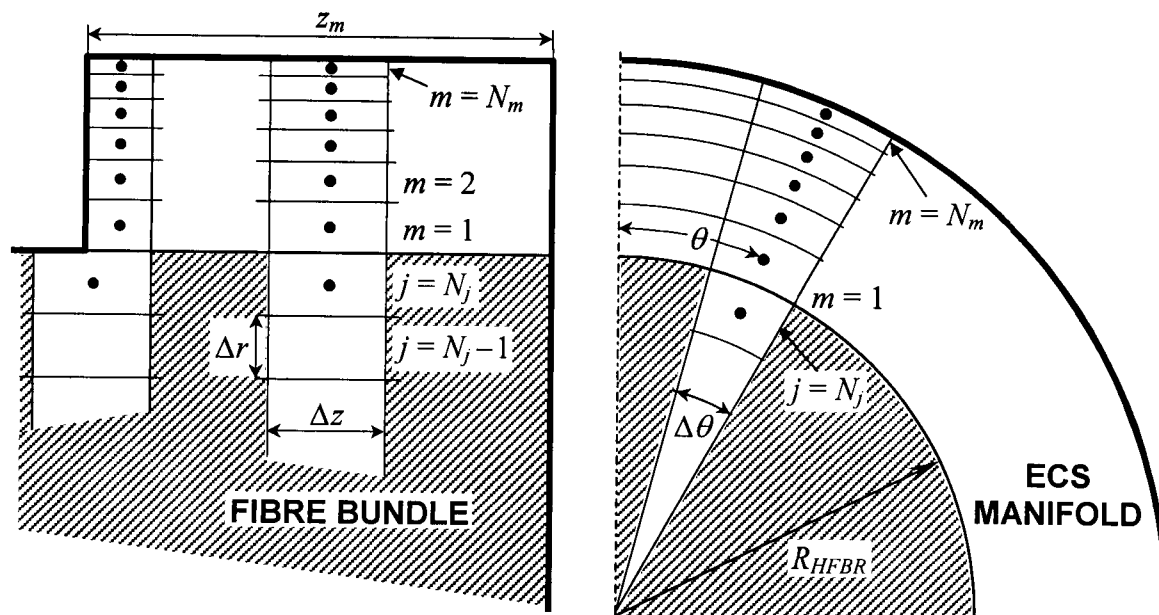


Fig. 37. Longitudinal (left) and cross-sectional (right) slices through an ECS manifold and the contiguous fibre bundle (not to scale). Black dots signify the centres of representative control volumes involved in the manifold concentration adjustment schemes (see text).

Two schemes for ECS concentration adjustment due to the presence of ECS manifolds have been implemented here. The first scheme assumes protein equilibration between neighbouring CVs in the radial direction, involving  $N_m$  layers within the manifold and the outermost layer ( $j = N_j$ ) of the fibre bundle (fig. 37), which is essentially a simplified view of the manifold-bundle protein exchange by radial diffusion. This scheme is termed here, in short, the *standard manifold adjustment*. Since radial diffusion cannot account for gravity-driven protein redistribution in the manifold, an additional procedure is employed here, referred to as the *natural-convective manifold adjustment*. This scheme assumes that instantaneous equilibration of the protein can occur between any two neighbouring CVs within the manifold, as long as their protein concentrations are different and the centre of the higher-concentration CV lies above or at the same level as the centre of the lower-concentration CV. This effectively means that the protein concentration in each ECS manifold is never allowed to increase with position horizontally or upwards, since the existence of such concentration gradients in the manifold would obviously induce protein

redistribution by natural convection. The details of both manifold adjustment schemes are presented below.

After the ECS concentration field at a given time is obtained as a solution of eq. (115), the standard scheme is employed by performing a radial sweep of concentration updates for each angular ( $k$ ) and each axial ( $i$ ) grid position within the length of each manifold. The procedure starts from the outermost radial layer in the fibre bundle and the first radial layer in the manifold, for which it is demanded that the CVs ( $i, j = N_j, k$ ) and ( $i, m = 1, k$ ) have equal protein concentrations (fig. 37). This artificial redistribution of the protein between two neighbouring CVs is hereafter referred to as instantaneous equilibration. The new concentration for ( $i, j = N_j, k$ ) and ( $i, m = 1, k$ ) is calculated as a volumetrically-weighted average of the previous values (these two CVs generally are of different sizes). The process is repeated for ( $i, m = 1, k$ ) and ( $i, m = 2, k$ ), then for ( $i, m = 2, k$ ) and ( $i, m = 3, k$ ), and so on until the last radial layer in the manifold ( $m = N_m$ ) is completed. Since all radial layers of manifold CVs have identical volumes, the new concentration for each pair ( $i, m, k$ ) and ( $i, m + 1, k$ ) is simply an arithmetic mean of their most recent concentrations. Note that the CVs bordering the edge of either manifold at  $z = z_m$  or  $z = L - z_m$  may, in general, be smaller than the CVs located at other axial positions in the manifold (fig. 37).

Next, the natural-convective concentration adjustment is carried out, which – in contrast to the standard scheme – involves only the manifold CVs. For each ECS manifold, the following algorithm is used:

- (1) calculate from eq. (98) the elevations  $h$  of the centres of all manifold CVs;
- (2) sort all CVs in order of their values of  $h$ ;
- (3) for each CV ( $i, m, k$ ), identify its significant neighbours; i.e., those of its neighbours whose value of  $h$  is larger than or equal to  $h(i, m, k)$ ;
- (4) starting from the CV with the lowest  $h$ , compare its concentration  $C(i, m, k)$  with that of its spatially-lowest significant neighbour (as defined in point (3) above); if  $C(i, m, k)$  is lower than the neighbour's concentration by more than a pre-specified tolerance (here:  $10^{-6}$  g/L), then set both of these concentrations to the same value, calculated as their volumetrically-weighted average;

- (5) repeat step (4) for the same CV and its next lowest significant neighbour, until all neighbours have been accounted for;
- (6) repeat steps (4) and (5) for a CV with the next lowest  $h$ , until all CVs have been accounted for.

### 5.2.3. Model Parameters

The major model parameters are listed in table 11. The fibre dimensions and other cartridge-specific parameters pertain to the Gambro GFE-15 hollow-fibre module and are essentially the same as those used in the myoglobin leakage study (see section 3.2.3). The fibre-free volumes for the upstream and downstream ECS manifolds were both assumed to be 13.63 mL, a value calculated by using the outer manifold radius of 0.0206 m and by neglecting the adjacent port and potting volumes. The cell-free ECS porosity,  $\varepsilon_S$ , was calculated as

$$\varepsilon_S = 1 - \frac{n R_F^2 L_F}{R_{HFBR}^2 L} \quad (116)$$

and the membrane surface area per unit volume,  $A_V$ , was evaluated from eq. (30). The values for the axial ICS and ECS hydraulic permeabilities,  $k_{L,z}$  and  $k_{S,z}$ , and for the membrane permeability,  $L_p$ , were taken from earlier measurements (see section 3.2.3), whereas the radial and angular ECS permeabilities,  $k_{S,r}$  and  $k_{S,\theta}$ , were both calculated from the same eq. (33), valid for flow across a bank of cylinders (see section 2.2.2).

The protein properties were all assumed to be the same as those for BSA. The fluid density and viscosity were evaluated using eqs. (111) and (112), respectively, with  $\rho_0$  and  $\mu_0$  varying with temperature as:

$$\rho_0 \text{ [g/L]} = 0.99986 + 6 \times 10^{-5} T - 7.74 \times 10^{-6} T^2 + 3.88 \times 10^{-8} T^3 \quad (117)$$

and

$$\log \left( \frac{\mu_0}{1.0021 \times 10^{-3}} \right) = \frac{1.3272(20-T) - 0.001053(20-T)^2}{T+105}, \quad (118)$$

Table 11. Parameters for the three-dimensional HFBR model

$n$	8128
$R_L$	$1.09 \times 10^{-4}$ m
$R_F$	$1.24 \times 10^{-4}$ m
$R_{HFBR}$	0.01575 m
$L$	0.215 m
$L_F$	0.238 m
$z_m$	0.021 m
$V_{ff}$	13.63 mL
$\varepsilon_S$	0.4423
$A_V$	$7907.1 \text{ m}^{-1}$
$L_p$	$7 \times 10^{-15}$ m
$k_{L,z}$	$5.23 \times 10^{-10} \text{ m}^2$
$k_{S,z}$	$9.39 \times 10^{-10} \text{ m}^2$
$k_{S,r}$	$2.01 \times 10^{-10} \text{ m}^2$
$k_{S,\theta}$	$2.01 \times 10^{-10} \text{ m}^2$
$T$	37°C
$M_A$	$69 \text{ kg mol}^{-1}$
$A_{\Pi 2,A}$	$10.473 \times 10^{-3} \text{ L g}^{-1}$
$A_{\Pi 3,A}$	$17.374 \times 10^{-6} \text{ L}^2 \text{ g}^{-2}$
$\rho_0$ (37°C)	$993.45 \text{ g L}^{-1}$
$\mu_0$ (37°C)	$6.9164 \times 10^{-4} \text{ Pa}\cdot\text{s}$
$A_{\mu 1}$	$3.8 \times 10^{-3} \text{ L g}^{-1}$
$A_{\mu 2}$	$2.2 \times 10^{-5} \text{ L}^2 \text{ g}^{-2}$
$D_{A0}$ (20°C)	$6.9 \times 10^{-11} \text{ m}^2 \text{ s}^{-1}$
$D_{S,z}$ (37°C)	$3.82 \times 10^{-11} \text{ m}^2 \text{ s}^{-1}$
$D_{S,r}$ (37°C)	$3.00 \times 10^{-11} \text{ m}^2 \text{ s}^{-1}$
$D_{S,\theta}$ (37°C)	$3.00 \times 10^{-11} \text{ m}^2 \text{ s}^{-1}$

where  $T$  is the temperature in °C, and  $1.0021 \times 10^{-3}$  Pa·s is the viscosity of water at 20°C. Equation (117) was obtained as a best cubic fit of tabulated data given in Perry and Green (1984, 3-75), and formula (118) was taken from Weast (1975, F-49). The osmotic pressure as a function of protein concentration and temperature was calculated from eq. (52) (see section 3.2.2.1), with the molar mass of BSA,  $M_A$ , taken as 69 kg/mol, and the virial

coefficients  $A_{\Gamma 2,A} = 10.473 \times 10^{-3} \text{ L/g}$  and  $A_{\Gamma 3,A} = 17.374 \times 10^{-6} \text{ L}^2/\text{g}^2$ , as before. The free-fluid protein diffusivity,  $D_A$ , was obtained by extrapolation of BSA diffusivity at 20°C ( $D_{A0} = 6.9 \times 10^{-11} \text{ m}^2/\text{s}$  as given by van den Berg and Smolders (1989)) to temperature  $T$ , with  $D\mu/T$  assumed constant. The ECS protein diffusivity components were calculated from  $D_A$  as before (section 2.2.2), i.e.,

$$D_{S,z} = D_A \varepsilon_S (L/L_F)^2 \quad (119)$$

and

$$D_{S,r} = D_A \frac{\varepsilon_S}{2 - \varepsilon_S}, \quad (120)$$

with the angular component  $D_{S,\theta} = D_{S,r}$ . Since diffusion plays a relatively insignificant role in the system of interest here, and since the BSA diffusivity changes only very little with protein concentration (Anderson et al. 1978), spatial variations of  $D_{S,z}$ ,  $D_{S,r}$ , and  $D_{S,\theta}$  were neglected.

The most important operating parameters varied in this study were (i) the cartridge inclination angle relative to the gravity vector,  $\Psi$ ; (ii) the inlet ICS flow rate,  $Q_L$ , which was converted to the inlet superficial velocity  $v_{L,in}$  required as a boundary condition for eq. (109); and (iii) the average ECS protein concentration,  $C_0$ . The ICS was usually assumed to be protein-free, although different levels of the mixing-cup ICS protein concentration,  $C_L$ , were considered. The temperature was normally taken to be 37°C, except in the simulations of room-temperature experiments. The outlet ICS pressure,  $\hat{P}_{L,out}$ , was always set to zero, whereas a fixed inlet pressure,  $\hat{P}_{L,in}$ , was only used in the initial stages of numerical code testing (see section 5.3.1.1).

### 5.3. Numerical Techniques

#### 5.3.1. Solution of the Pressure Equations

Discretisation of the hydrodynamic equations (107) and (109) was performed by integration over a cylindrical REV (or cylindrical CV), as recommended by Patankar (1980). A finite-difference, uniform grid was used in each spatial dimension. The pressure points were placed in the centres of the REV, and the velocity points were staggered half-way between the pressure nodes, i.e., in the centres of the faces normal to the direction of the particular velocity component (fig. 38). Within each REV, the pressure derivatives over one spatial variable were assumed constant over the remaining two dimensions; e.g.,  $\partial \hat{P}_s / \partial z$  and  $\partial^2 \hat{P}_s / \partial z^2$  in eq. (107) were assumed constant over  $r$  and  $\theta$ . Furthermore, all of the coefficients defined by eqs. (108) and (110) were assumed constant within each control volume. As a consequence of the latter assumption, additional integrals (such as those of a product of a density derivative and a pressure derivative) could be avoided, which greatly reduced the mathematical complexity of the discretisation. Rather than being included in the integration, the ECS density and viscosity terms in eqs. (108) were calculated as averages of their values at the two opposite faces of the REV in each direction. The discretisation produced a set of linear algebraic equations with the local ICS and ECS pressures as unknowns and with the coefficients varying in time and space through their dependence on protein concentration. These equations were solved at each time step, always using the most recent ECS concentration values to update the coefficients.

##### 5.3.1.1. *Iterative Solver*

Because of relatively large numbers of grid points involved in a three-dimensional analysis, a simple iterative solver, the Gauss-Seidel point algorithm (Anderson et al. 1984, p. 130; Burden and Faires 1997, p. 443), was initially employed for the solution of the ICS and ECS pressure equations. According to this method, initial guesses for  $\hat{P}_L$  and  $\hat{P}_S$  were first made<sup>19</sup>, then each of the unknown pressure values was updated iteratively in an explicit

---

<sup>19</sup> The initial guesses were usually obtained as analytical solutions of the one-dimensional protein-free problem, corrected by the value of the osmotic pressure (see appendix A).

fashion, i.e., by placing all of the other unknowns on the right-hand-side of the equation. The structure of the equations ensured that the magnitude of the coefficient for each pressure point was either equal to (whole ECS domain, ICS interior) or greater than (ICS outlet boundary) the sum of the magnitudes of all its neighbours' coefficients. Thereby, the sufficient criterion for convergence of the iterative procedure was always satisfied.

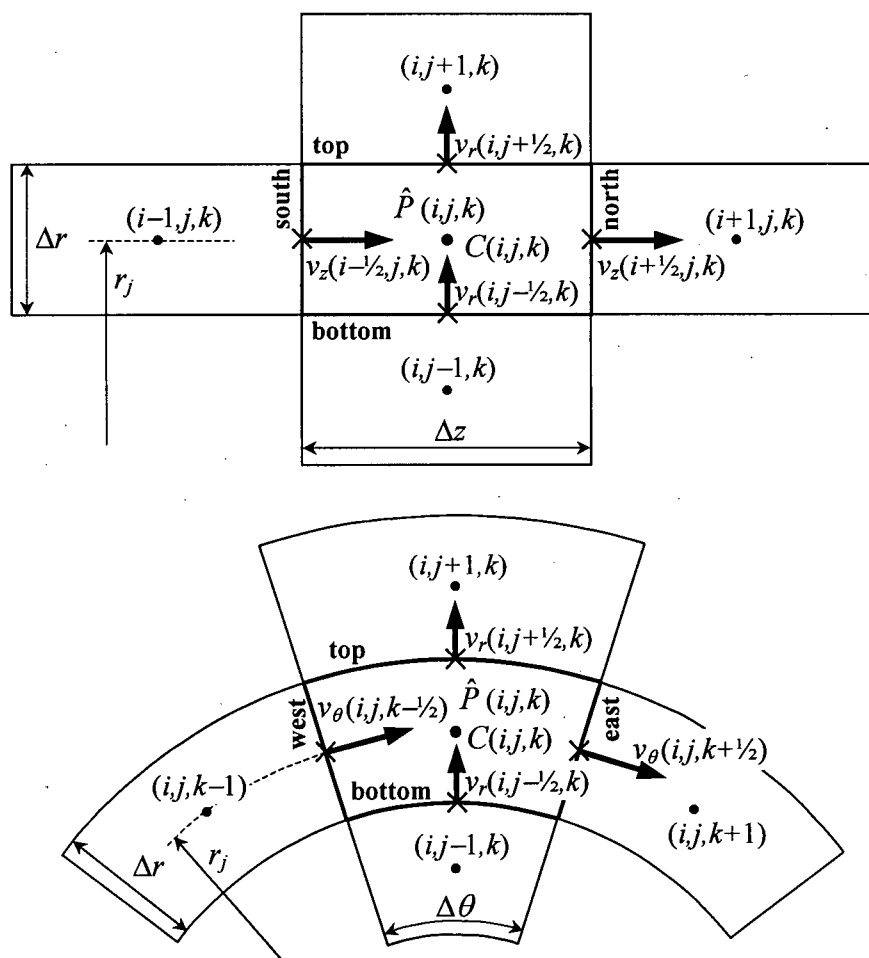


Fig. 38. Three-dimensional grid arrangement around an interior point  $(i, j, k)$  in a cylindrical domain. Upper diagram:  $z$ - $r$  projection, lower diagram:  $r$ - $\theta$  projection. The faces of the control volume are labelled as bottom and top ( $r$ -direction), west and east ( $\theta$ -direction), and south and north ( $z$ -direction).

To accelerate the convergence of the pressure solutions, successive over-relaxation was used (Anderson et al. 1984, p. 132), with the relaxation parameter specified separately for  $\hat{P}_L$  and  $\hat{P}_S$  and set usually between 1.00 and 1.98. Several different patterns for spatially updating the unknowns were considered, including (i) the regular point-by-point sweep in each direction; (ii) a “three-dimensional checkerboard” pattern, in which every second point was updated in one sweep and all of its neighbours in the next; and (iii) a “multiple skip” pattern, in which every third (fourth, fifth, etc.) point was updated in each of the total of three (four, five, etc.) sweeps, so that no point was ever updated in the same sweep as were its immediate neighbours. Of the above, the “checkerboard” update pattern turned out to be the most efficient, while the “multiple skip” patterns usually led to divergence for relaxation parameter values larger than about 1.6.

In spite of its simplicity and fast performance (per iteration), the application of the Gauss-Seidel method to the present numerical problem also caused some serious difficulties. These included:

- (1) increasingly unpredictable convergence behaviour as the protein distribution changed with time; this usually led to stalling, with the local  $\hat{P}_S$  difference from one iteration to next levelling out at around  $10^{-4}$  Pa, a value too high to ensure a satisfactory fluid mass balance;
- (2) development of artificial pressure gradients in the direction of sweep for the point update method, resulting in numerically-originated mass imbalances; and
- (3) strong dependence of the speed and success of convergence on the number of grid points in each direction, with the maximum grid size limited by the amount of available computer memory; this seriously compromised the accuracy of the solution.

Owing to these difficulties, the iterative point algorithm was eventually abandoned as the method for solving the ECS pressure problem; it was subsequently employed only to solve the  $\hat{P}_L$  equations. In the latter case, with the  $\hat{P}_S$  field generated by using a direct solver (see the following section), the convergence of the  $\hat{P}_L$  solution was very fast (1-2 iterations) and, hence, no over- or under-relaxation was necessary.

### 5.3.1.2. Direct Solver for the ECS Pressure Problem

In most simulations,  $N_i = 50$  axial,  $N_j = 10$  radial, and  $N_k = 9$  angular points were used in the fibre bundle domain, reflecting roughly the geometric aspect ratio for the HFBR cartridge considered here (see table 11). Thus, with the total of  $50 \times 10 \times 9 = 4500$  grid points, a direct solution by Gaussian elimination (Anderson et al. 1980, p. 130; Burden and Faires 1997, p. 350) of the resulting set of algebraic equations for either  $\hat{P}_S$  or  $\hat{P}_L$  would require manipulation of a  $4500 \times 4501$  matrix occupying at least  $4500 \times 4501 \times 8$  bytes  $\approx 162$  MB of computer RAM (based on double-precision arithmetic). Fortunately, since the structure of the finite-difference equations is such that each point is affected only by its direct neighbours, many of the elements of this Gauss matrix are zero. In fact, it can be easily shown that all non-zero elements are contained within a diagonal strip having a width of only  $2 \cdot N_j \cdot N_k + 1 = 181$ . This suggests that the elimination matrix need not, in this case, occupy more than  $4500 \times 182 \times 8$  bytes  $\approx 6.5$  MB of RAM, i.e., only about 4% of its original size. Based on this premise, a modified Gaussian elimination procedure was developed here, making it possible to solve the pressure equations directly, without exceeding the limits of the available computer memory (128 MB RAM). This modified procedure can also be used for the solution of any system of algebraic equations obtained by a standard finite-difference discretisation<sup>20</sup> in three spatial dimensions. The Fortran code of the modified Gauss elimination routine is listed in appendix C.

Figure 39 illustrates how the coefficient matrix was transformed to its condensed form used as input to the modified Gauss routine. The shaded squares identify all non-zero elements, the open circles indicate elements that are initially zero but may change their values in the course of the elimination, and the blank squares indicate zero elements that remain unaffected by the elimination process. In the example shown,  $N_i = 3$ ,  $N_j = 2$ , and  $N_k = 3$ ; thus, the original matrix (upper diagram) has  $N_i \times N_j \times N_k = 18$  rows and  $N_i \times N_j \times N_k + 1 = 19$  columns. Each row corresponds to a single equation formulated for point  $(i, j, k)$  (identified by the indices on the main diagonal), with the right-hand-side values assigned to the last

<sup>20</sup>A standard discretisation is understood here to mean that each point has either one or two neighbours in each direction, depending on whether it lies on a boundary or in the interior of the domain, respectively.



column. The transformed matrix (lower diagram) has 18 rows and  $2 \times N_j \times N_k + 2 = 14$  columns, and its elements are re-arranged such that the south ( $i-1$ ), bottom ( $j-1$ ), west ( $k-1$ ), north ( $i+1$ ), top ( $j+1$ ), and east ( $k+1$ ) neighbours of  $(i,j,k)$  are grouped in separate columns. The indices shown in the filled squares of both arrays identify the positions of the points that contribute to each equation.

An important advantage of using a direct solver for the present hydrodynamic problem was the eradication of numerically-originated radial and angular pressure gradients that typically arise during iterative procedures. Such artificial gradients upset the fluid mass balance and are normally very difficult to minimise. A convenient feature of the direct approach was also an easy prediction and control of the duration of each simulation run.

### 5.3.2. Solution of the ECS Concentration Problem

The ECS protein concentration equation (eq. 113) was solved by means of a three-dimensional Alternate Direction Implicit (ADI) method utilising the Crank-Nicolson discretisation scheme (Douglas, 1962) combined with Patankar's (1980) hybrid scheme for upwinding control. According to this ADI formulation, the concentration distribution at each time level was recalculated in three consecutive steps. At each step, a set of one-dimensional solutions was obtained with respect to a different spatial variable using the Thomas algorithm (for all discrete values of the other two variables), from which a three-dimensional concentration field was then generated. For more details about the ADI solver and the upwind control scheme used here see appendix D. The ECS concentration problem was also solved by a direct method using the modified Gauss elimination routine described in the previous section. This approach yielded the same results (within 4 significant digits) as the ADI method, but was less efficient than the latter in terms of computational time.

As was mentioned earlier in section 5.2.2, the  $r = 0$  centreline in a three-dimensional cylindrical system represents a degenerate boundary. In the results of many simulations performed in this study, distortions of the concentration profiles in longitudinal planes passing through the centre line were observed, particularly in the vertical plane. This was partly a consequence of the singularity existing at  $r = 0$  for a finite number of grid points (since the accuracy was limited by the finest grid for a given memory size), and partly also

due to inter- and extrapolation errors (since the data in the planes of interest were inter- or extrapolated from the original grid). The origin of these distortions can also be understood better by recalling the structure of finite-difference equations in cylindrical co-ordinates (see fig. 39). Namely, some grid points (or control volumes) that are physically proximal can be very distant from one another in the numerical sense; i.e., one point may influence another point's equation only through a chain of other points. For example, points  $(i, 1, 1)$  and  $(i, 1, N_k)$  of the first radial layer ( $j = 1$ ), which lie respectively just above and just below the centreline, are separated in the set of finite-difference equations by points  $(i, 1, 2)$ ,  $(i, 1, 3)$ , ...,  $(i, 1, N_k - 1)$ . As a result of poor numerical communication between  $(i, 1, 1)$  and  $(i, 1, N_k)$  in the finite-grid system, an apparent discontinuity of the concentration profiles in the vertical plane  $\theta = 0$  could be observed at  $r = 0$ .

To overcome the difficulties described above and smooth the distorted concentration profiles, a method involving angular averaging of the central core ( $j = 1$ ) was implemented. Since the thickness of the central core is  $2\Delta r$ , whereas the thickness of any other radial layer ( $j > 1$ ) is  $\Delta r$ , the core was divided into its upper and lower halves for the purpose of the smoothing. Accordingly, at each new time level, the innermost concentrations  $C(i, 1, k)$  were averaged separately for  $k = 1, \dots, N_{k, half}$  and for  $k = N_{k, half} + 1, \dots, N_k$ , where  $N_{k, half}$  is the largest integer of  $N_k/2$ . The concentration distribution so modified was then used as input to generate a solution at the subsequent time step. Thus, the averaging procedure was a part of the solution algorithm, and not merely a cosmetic alteration of the output data; the latter measure by itself failed to provide satisfactory smoothing.

### 5.3.3. Organisation of Numerical Input and Output

#### 5.3.3.1. *Input*

One group of parameters used as input to the numerical code is the set of model parameters listed in table 11 (section 5.2.3). The remaining input parameters along with their typical values are summarised in table 12. These can be roughly categorised as operating variables of primary interest with respect to their effects on protein distribution (e.g., ICS flow rate or cartridge inclination angle), or as parameters controlling numerical performance

Table 12. Essential input parameters for the numerical code of the three-dimensional HFBR model (default or commonly used values are given in boldface)

Parameter	Meaning	Values
$Q_L$	ICS flow rate (mL/min)	200, <b>600</b>
$C_0$	Initial ECS protein concentration (g/L)	<b>5</b> , 20
$\Psi$	Angle between the ICS flow and gravity vectors	<b>0°</b> , 0.1°, <b>45°</b> , 60°, <b>90°</b> , 105°, 120°, <b>135°</b> , 160°, 170°, 175°, <b>179°</b> , 179.9°, <b>180°</b>
$C_L$	Mixing-cup ICS protein concentration (g/L)	<b>0</b> , 5, 10
$IndPLin$	Use fixed-flow or fixed-pressure boundary condition at ICS inlet (eq. (107) and table 9)	<b>0</b> (fixed-flow), 1 (fixed-pressure)
$\hat{P}_{L,in}$	Inlet ICS pressure (if $IndPLin = 1$ ) (Pa)	~3647 Pa to generate $Q_L \approx 600$ mL/min
$\hat{P}_{L,out}$	Outlet ICS pressure (Pa)	<b>0</b>
$IADJMan$	Include or neglect the presence of ECS manifolds	0 (neglect), <b>1</b> (include)
$IManNC$	Switch on/off natural-convective manifold adjustment (section 5.2.2.3)	0 (off), <b>1</b> (on)
$F_1$	Use homogeneous or inhomogeneous form of ECS continuity equation (eqs. (105), (106), and (108))	<b>0</b> (homogeneous), 1 (inhomogeneous)
$F_\mu$	Include or neglect viscosity gradients in eq. (108)	<b>0</b> (neglect), 1 (include)
$F_\rho$	Include or neglect density gradients in eq. (108)	0 (neglect), <b>1</b> (include)
$ConvPL$	Convergence criterion for $\hat{P}_L$ iteration (Pa)	$10^{-6}$ , <b><math>10^{-8}</math></b> , $10^{-10}$
$AlphaPL$	Relaxation parameter for $\hat{P}_L$ iteration	0.5, <b>1.0</b> , 1.5, 1.9
$IStSt$	Use steady-state or maximum-time criterion to terminate simulation	0 (maximum-time), <b>1</b> (steady-state)
$EpsStSt$	Threshold for steady-state protein distribution (if $IStSt = 1$ ) ( $\text{g L}^{-1} \text{s}^{-1}$ )	$10^{-4}$ , <b><math>10^{-5}</math></b> , $10^{-6}$
$\Delta t$	Initial time step for the protein transport equation (eqs. (115) and (D7-D9)) (s)	1, 2, 5, <b>10</b> , 20, 30, 60
$IDTCtrl$	Switch on/off $\Delta t$ control from external file	0 (off), <b>1</b> (on)
$Ir0$	Switch on/off angular averaging of concentrations at $j = 1$ (section 5.3.2)	0 (off), <b>1</b> (on)
$N_i$	Number of axial grid points	20, 25, <b>50</b> , 100
$N_j$	Number of radial grid points	5, 6, <b>10</b> , 12, 18
$N_k$	Number of angular grid points	5, 6, <b>9</b> , 12, 18
$N_m$	Number of radial grid points in the ECS manifolds	<b>1</b> , 10

(e.g., grid size).<sup>21</sup> Excluded from table 12 are the numbers of grid points used for interpolation and extrapolation of output data to various lines and planes of interest. Also omitted are parameters used to optimise the convergence of the iterative  $\hat{P}_s$  solution (section 5.3.1.1), including parameters controlling the time step adjustment schemes developed for this purpose. See section 5.3.5.2 for more information on the results of sensitivity analyses performed on some input parameters in order to optimise the numerical performance.

### 5.3.3.2. Output

All of the transient and steady-state output data were saved in a number of files organised by output variable and by output time<sup>22</sup>. Table 13 summarises the different output files created at each desired time. To facilitate the analysis and graphical presentation of the results, a variety of different sets and subsets of the data were created; these included three-dimensional (3-D) distributions, as well as various averaged or interpolated two-dimensional (2-D) and one-dimensional (1-D) distributions. Each 3-D output was organised as a double set of 2-D arrays: the  $z$ - $r$  distributions for all discrete values of  $\theta$ , and the  $z$ - $\theta$  distributions for all discrete values of  $r$ . In addition, several input files for Tecplot (an advanced plotting package from Amtec Engineering, Bellevue, Washington) were generated at each output time. Aside from their main contents specified in table 13, all output files (except the Tecplot files) included data such as: the CPU time, average ECS protein concentrations in the fibre bundle and in the manifolds (if included), as well as global fluid mass balances based on the transmembrane (TMFF) and ICS fluid fluxes.

Another important output file, not included in table 13, was updated at every time step and listed variations with time of the following parameters:

- 1) maximum local magnitude of  $dC/dt$  ( $dCdtMax$ ) and its location in the spatial domain;
- 2) average global magnitude of  $dC/dt$  ( $dCdtAve$ ), i.e., the sum of the magnitudes of all local  $dC/dt$  values, divided by the total number of grid points  $N_{ijk}$  ( $= N_i \cdot N_j \cdot N_k$ );
- 3) ECS protein heterogeneity index ( $HetIx$ ) – see discussion later in this section;

<sup>21</sup> The boundary between these two groups is not sharp. For instance, the ECS manifold effect was investigated by means of a numerical parameter,  $IADJMan$ , set to either 1 (manifolds present) or 0 (manifolds absent).

<sup>22</sup> The output time, or time of simulation, is distinguished here from the execution or CPU time. The former measures the progress of a simulated protein redistribution, while the latter indicates how long the numerical code is executed on a given computer.

Table 13. Output files generated at each desired time; the ?? symbol in the file name denotes a two-digit code identifying the output time

File name	Output variable	Main contents
output???.out	Local ECS fluid and protein mass balances	3-D distributions
output???.PL3	ICS pressure	3-D distribution
output???.PS3	ECS pressure	3-D distribution
output???.VzL	ICS superficial fluid velocity, $z$ -component	3-D distribution, radially-averaged and angularly-averaged 2-D distributions
output???.VzS	ECS superficial fluid velocity, $z$ -component	3-D distribution, radially-averaged and angularly-averaged 2-D distributions, interpolated 2-D distributions in selected $z$ - $r$ sections
output???.VrS	ECS superficial fluid velocity, $r$ -component	3-D distribution, radially-averaged and angularly-averaged 2-D distributions, interpolated 2-D distributions in selected $z$ - $r$ and $r$ - $\theta$ sections
output???.VtS	ECS superficial fluid velocity, $\theta$ -component	3-D distribution, radially-averaged and angularly-averaged 2-D distributions, interpolated 2-D distributions in selected $r$ - $\theta$ sections
output???.TMF	TMFF	3-D distribution, radially-averaged and angularly-averaged 2-D distributions, interpolated 2-D distributions in selected $r$ - $\theta$ sections
output???.C_E	ECS concentration	3-D distribution in the fibre bundle and manifolds (if $IADJMan = 1$ ), radially-averaged and angularly-averaged 2-D distributions, interpolated 2-D distributions in selected $r$ - $\theta$ sections, 3-D distribution of $dC/dt$
output???.rt_	All velocity components, ECS concentration, TMFF	Radially- and angularly-averaged 1-D distributions
output???.INT	ECS concentration, TMFF	Interpolated 2-D distributions in selected $z$ - $r$ sections
tpl3DC???.dat	ECS concentration, TMFF	Tecplot input: 3-D distributions interpolated to desired $r$ - $\theta$ - $z$ grid
tpl3DV???.dat	All ECS velocity components	Tecplot input: 3-D distributions interpolated to desired $r$ - $\theta$ - $z$ grid (cell corners)
tplzrV???.dat	$z$ and $r$ ECS velocity components	Tecplot input: interpolated 2-D distributions in selected $r$ - $z$ sections
tplrtV???.dat	ECS velocities in cartesian co-ordinates	Tecplot input: interpolated 2-D distributions in selected $r$ - $\theta$ sections (half-circle)
tplftV???.dat	ECS velocities in cartesian co-ordinates	Tecplot input: interpolated 2-D distributions in selected $r$ - $\theta$ sections (full-circle)
tpl_CV???.dat	ECS velocities in cartesian co-ordinates, ECS concentration	Tecplot input: interpolated 2-D distributions in selected $r$ - $\theta$ sections (half-circle)

- 4) average protein concentration in the ECS fibre bundle ( $C_{Bundle}$ ), calculated as a volumetric average of all local concentrations; and
- 5) number of cycles required to converge the natural-convective manifold adjustment procedure (if included) to the desired accuracy (usually  $10^{-6}$  g/L).

The temporal changes of  $dCdtMax$  and  $dCdtAve$  provided a great deal of insight into the numerical properties of the system under investigation, particularly with regard to convergence to steady state (see section 5.5.2). It is worth noting that the maximum local  $|dC/dt|$  is perhaps more meaningful than  $dCdtAve$  in measuring the 'distance from steady state' in situations where the process of protein redistribution is confined to a small part of the reactor volume; for example, when the protein is polarised to the downstream end of the ECS or when the main changes in concentration occur in the boundary zone between the bundle and the manifold. Since such situations were frequently encountered in the simulations performed in this study,  $dCdtMax$  rather than  $dCdtAve$  was chosen to determine how far the system was from steady state (which was done by comparing the current value of  $dCdtMax$  with  $EpsStSt$  from table 12).

The ECS heterogeneity index,  $HetIx$ , was introduced here as a parameter that conveniently quantifies the nonuniformity of solute distribution in the ECS. This issue is of importance in HFBR cell culture, where it is desired to minimise spatial heterogeneities of growth factors and nutrients. The following definition of  $HetIx$  was adopted:

$$HetIx = \frac{\sum_i |C_i - C_{Bundle}| V_{i,ECS}}{2 C_{Bundle} V_{ECS}}, \quad (121)$$

where the summation is taken over all  $N_{ijk}$  grid points,  $C_i$  is the local ECS solute (protein) concentration,  $C_{Bundle} = \sum_i C_i V_{i,ECS} / V_{ECS}$ ,  $V_{i,ECS}$  is the ECS part of the  $i$ th cell volume, and  $V_{ECS}$  is the total ECS volume (excluding manifolds). The heterogeneity index defined by eq. (127) can vary between 0, corresponding to a perfectly uniform concentration field, and an upper limit, corresponding to a distribution in which all of the ECS solute (protein) is confined to the smallest control volume. Although this upper limit of  $HetIx$  depends on  $N_{ijk}$ , it quickly approaches 1 as the grid is refined (it equals 0.999989 for the  $50 \times 10 \times 9$  cylindrical grid used here). An alternative definition,  $HetIx'$ , was also considered, in which the linear

term  $|C_i - C_{Bundle}|/C_{Bundle}$  was replaced with its square. However, the value of *HetIx'* (especially its upper limit) was found to depend much more strongly on  $N_{ijk}$ , a property found to be generally less convenient for the analyses of interest here.<sup>23</sup>

Interpolation and extrapolation of the data constituted the largest part of the output routine and was also performed using external programs. The interpolated functions were the ECS concentration, the transmembrane fluid flux, and the components of ECS fluid velocity. The main purposes of interpolation and extrapolation were: (1) to increase the number of data points in the spatial domain for smoother graphical presentation (such as contour plotting); (2) to extend the range of the data to the domain boundaries (most of the original solutions did not include boundary points); and (3) to obtain data points in desired sections through the cartridge (e.g., rectangular sections at selected angular positions, or circular sections at selected axial positions). In all cases, the functions of interest were approximated using cubic splines (Burden and Faires 1997, p. 143) with clamped boundary conditions (vanishing first derivative) imposed at all no-flux and symmetry boundaries and with natural boundary conditions (vanishing second derivative) applied elsewhere. This process required special caution because of the differences in the arrangement of grid points and in the behaviour of the various interpolated variables at different boundaries.<sup>24</sup> In some cases, the inter- and extrapolated sets of results were additionally linked together to illustrate data variation in a particular plane of interest. For example, the  $\theta = 0$  set was linked to the  $\theta = \pi$  set to show variation in the vertical longitudinal section passing through the centreline, while the combined  $\theta = \pi/4$  and  $\theta = 3\pi/4$  data sets provided information on how the results varied in a similar longitudinal section inclined at  $45^\circ$  to the vertical.

---

<sup>23</sup> Consider, for example, a solute distribution on a grid composed of  $N_{ijk} = 8$  equisized control volumes, such that all of the solute is packed into a single CV. In this case, the corresponding upper limit for *HetIx* is 0.875, and the upper limit for *HetIx'* is 3.5. Upon twofold grid refinement to  $N_{ijk} = 16$ , these upper limits increase respectively to 0.9375 and to 7.5. Thus, a visually small change in solute distribution can produce a relatively insignificant change in *HetIx*, but a fairly dramatic change in *HetIx'*.

<sup>24</sup> The peripheral data points for concentration, TMFF, and tangent velocity components were located a half grid-increment from the boundary, whereas those for normal velocity components were located on the boundary (cf. fig. 101). Thus in the latter case, the number of points for each interpolated vector was 1 larger than in the former. At  $r = 0$ , natural conditions were used for all interpolated variables. For TMFF, clamped conditions were imposed at  $\theta = 0$  and  $\theta = \pi$  (symmetry plane), and natural conditions at all other boundaries.

#### 5.3.4. Computational System

All numerical simulations were carried out using a Celeron 533 personal computer equipped with a 66 MHz bus, 128 kB on-die L2 cache, and 128 MB RAM.<sup>25</sup> Microsoft Visual Fortran 5.0 was used for the compilation, linking, and execution of the numerical source code. For a  $50 \times 10 \times 9$  ( $N_i \times N_j \times N_k$ ) grid, the required CPU time was about 1.4 s per simulation time step or about 1 h 25 min per each 10 h of simulation at  $\Delta t = 10$  s (with optimum utilisation of the system resources).<sup>26</sup>

On several occasions, problems were encountered as a consequence of limitations or mismanagement of the RAM. These included: (1) unexpected zeroing of some array elements, resulting likely from excessive memory requirements by the interpolation subroutines; (2) occurrence of a stack-overflow run-time error when the individual subprograms and COMMON blocks in the code exceeded a certain critical size for a given grid; (3) faulty display in the Fortran editor when the code length exceeded approximately 6500 lines. These problems seemed to have been resolved by splitting some of the routines and program blocks into smaller parts and by keeping the grid size within moderate limits.

#### 5.3.5. Preliminary Model Simulations

This section will present the essential results of preliminary simulations which included consistency tests and sensitivity analyses. The aim of the consistency tests was to verify that the results of simulations using the present 3-D numerical code would agree with the predictions of the 2-D PMM and 1-D KCM in the absence of gravity and angular gradients in the HFBR. The sensitivity analyses were conducted in order to identify factors that had negligible effects on the results and to optimise the performance of the subsequent numerical simulations.

---

<sup>25</sup> This system proved to be about 20% less expensive and about 30% faster in the solution of the 3-D problem of interest here than were comparable Pentium III systems equipped with a 100 MHz bus and 512 kB external L2 cache.

<sup>26</sup> Excessive RAM occupation by other residing software was found to cause up to twofold increase in the CPU time. Similarly, oversize declaration of arrays in the Fortran source code could dramatically (5-10 times) slow down program execution, even if the actual input grid was unchanged. This was due to the relatively slow handling of hard drive resources utilised as virtual memory when the RAM had become exhausted.

### 5.3.5.1. Consistency with 2-D and 1-D Formulations

Several tests were performed to demonstrate the consistency of the present 3-D model and numerical code with the 2-D PMM formulation described in section 2.2.2. As an example, a case was considered in which radial ICS pressure gradients were imposed at the entrance to ( $z = 0$ ) and exit from ( $z = L$ ) the fibre bundle in order to induce a two-dimensional (i.e., axisymmetric) variation of the ECS protein concentration. The essential input and output parameters for this test are listed in tables 14 and 15, respectively. Note that the 2-D PMM did not include the ECS manifolds, which were therefore neglected in this comparison.

As can be seen from table 15, the corresponding output data for the two PMM formulations are fairly consistent with one another. The quantitative discrepancies are generally less than 1% (or less than 0.05 g/L for the local concentrations), the differences

Table 14. Input parameters for the test of consistency between the 3-D and 2-D PMM codes  
( $\hat{P}_L = P_L$  in the 2-D model)

$N_i$	Number of axial grid points	100
$N_j$	Number of radial grid points	12
$N_k$	Number of angular grid points (3-D only)	2
$\Delta\hat{P}_L$	Axial centreline ICS pressure drop	3000 Pa
$\hat{P}_{L,in}(r)$	Radial variation of inlet ICS pressure	$\Delta\hat{P}_L(1 - \frac{1}{2} r/R_{HFBR})$
$\hat{P}_{L,out}(r)$	Radial variation of outlet ICS pressure	$\frac{1}{2} \Delta\hat{P}_L r/R_{HFBR}$
$C_0$	Initial ECS protein concentration	20 g/L
$\Delta t$	Time step	5 s
$AlphaPS$	$P_S$ over-relaxation factor (2-D only)	1.98
$AlphaPL$	$\hat{P}_L$ over-relaxation factor	1.00
$ConvPS$	$P_S$ convergence criterion (2-D only)	$10^{-8}$ Pa
$ConvPL$	$\hat{P}_L$ convergence criterion	$10^{-6}$ Pa
$T$	Temperature	37°C
$t_{final}$	Total simulation time	6 h

Table 15. Selected results of the numerical consistency test for the 3-D and 2-D PMMs; the overbars denote radially-averaged quantities;  $C_{AVE}$  is the final average ECS concentration (including the manifolds)

Parameter	2-D PMM	3-D PMM	Difference
$C(1,1)$ [g/L]	1.3453	1.3025	+0.0428 (+3.3%)
$C(N_i,1)$ [g/L]	42.2878	42.3210	-0.0332 (-0.078%)
$C(1,N_j)$ [g/L]	18.6412	18.6538	-0.0126 (-0.068%)
$C(N_i,N_j)$ [g/L]	21.7096	21.7103	-0.0007 (-0.003%)
$\bar{C}$ at $i = 1$ [g/L]	11.0775	11.0721	+0.0054 (+0.049%)
$\bar{C}$ at $i = N_i$ [g/L]	28.6378	28.6504	-0.0126 (-0.044%)
$ C_{AVE} - C_0 $ [g/L]	0.0002499	0.0000002	+0.0002497 (1250×)
Axial ECS flow at $z = \frac{1}{2}L$ [mL/min]	$1.774 \times 10^{-3}$	$1.755 \times 10^{-3}$	$+0.019 \times 10^{-3}$ (+1.1%)
$\bar{v}_r$ at $z = \frac{1}{2}L$ [m/s]	$-1.186 \times 10^{-9}$	$-1.173 \times 10^{-9}$	$-0.013 \times 10^{-9}$ (-1.1%)
$Q_{L,out}$ [mL/min]	164.502	165.028	-0.526 (-0.32%)
$ Q_{L,out} - Q_{L,in} $ [mL/min]	$3.076 \times 10^{-7}$	$5.802 \times 10^{-7}$	$-2.726 \times 10^{-7}$ (0.53×)
Total average TMFF [m/s]	$-9.792 \times 10^{-14}$	$0.730 \times 10^{-14}$	$-10.522 \times 10^{-14}$ (13.4×)
CPU time	38 h 22 min	19 min	38 h 03 min (121×)

being mainly due to the use of different solvers for the ECS pressure equations. Note that the values of the total unbalanced TMFF and of  $|C_{AVE} - C_0|$ , which can be regarded as respective indicators of fluid and protein mass imbalance, suggest a greater accuracy of the results generated using the 3-D code, compared with the 2-D simulation. Even so, a satisfactory level of accuracy in the latter case was only achieved at the expense of an exceedingly long computational time.

The 2-D PMM had already been previously verified for consistency with the 1-D KCM in the absence of radial gradients. Additional tests using the present code for the solution of a 1-D ECS protein transport problem (results not shown) confirmed the numerical and mathematical consistency of the 3-D PMM with the Krogh cylinder model.

### 5.3.5.2. Sensitivity Analyses

#### *Effect of grid size*

A number of preliminary simulations were performed for various combinations of operating conditions in order to determine a grid arrangement that would lead to satisfactory levels of solution accuracy within the capabilities of the available computational system. As was mentioned in section 5.3.4, excessive grid refinement could result in the exhaustion of RAM and a dramatic slowdown of code execution. The  $50 \times 10 \times 9$  ( $N_i \times N_j \times N_k$ ) grid chosen here allowed most of the simulations to be completed within about half a day, and almost all of them within 24 h. As an example, a typical steady-state run for  $\Psi = 90^\circ$ , with all essential input parameters set to their default values (table 12), required about 6.5 h execution time. In general, the CPU time was found to be proportional, approximately, to  $N_i$ , to  $N_j^{3.42}$ , and to  $N_k^{3.5}$ ; for instance, a twofold increase in  $N_j$  would slow down the computation by about  $2^{3.42} \approx 11.7$  times.

Table 16 summarises the effects of spatial grid coarsening for the above-mentioned steady-state run at  $\Psi = 90^\circ$ . Remarkably, a twofold reduction in  $N_j$  caused, in fact, a marginal improvement in the fluid mass balance, whereas a similar change to either  $N_i$  or  $N_k$  increased the unbalanced ICS and transmembrane fluxes by up to 1.5 times. For most of the output data, the changes engendered by the imposed grid coarsening were roughly 0.2-4.0%. Although larger relative errors (up to 180%) appear in the predictions of the average upstream ECS manifold concentration ( $C_{UpMan}$ ), the corresponding differences expressed in concentration units do not exceed 0.03 g/L. The data listed in the last column of table 16 (grid  $25 \times 5 \times 5$ ) suggest that the observed effects of  $N_i$ ,  $N_j$ , and  $N_k$  are cumulative.

An additional set of simulations was performed for various cartridge orientations to investigate the effect of the number of radial grid points within each ECS manifold ( $N_m$ ). The steady-state concentration distributions obtained for  $N_m = 1$  and for  $N_m = 10$  did not differ locally by more than 0.02%. Also, the plots of either  $dCdtMax$ ,  $dCdtAve$ ,  $HetIx$ , or  $C_{Bundle}$  versus time, as well as various 2-D concentration contour graphs, were undistinguishable for these two  $N_m$  values. Based on these results, all subsequent model simulations used the input value of  $N_m = 1$ .

Table 16. Effects of grid coarsening on steady-state results for  $\Psi = 90^\circ$ ,  $Q_L = 600$  mL/min,  $C_0 = 5$  g/L (other input parameters at their defaults, see table 12); original grid  $50 \times 10 \times 9$ , the changed values are underlined;  $C_{UpMan}$  and  $C_{DnMan}$  are the average concentrations in the upstream and downstream ECS manifold, respectively; the double overbar denotes a quantity averaged both radially and angularly

Parameter	Grid ( $N_i \times N_j \times N_k$ )				
	$50 \times 10 \times 9$	<u><math>25 \times 10 \times 9</math></u>	$50 \times \underline{5} \times 9$	$50 \times 10 \times \underline{5}$	<u><math>25 \times \underline{5} \times \underline{5}</math></u>
$C_{Bundle}$	4.1344 g/L	+0.16%	+1.1%	-0.008%	+1.1%
$C_{UpMan}$	0.03413 g/L	+35%	-84%	+180%	-37%
$C_{DnMan}$	14.6720 g/L	-0.33%	-1.4%	-0.17%	-1.6%
$\overline{\overline{C}}$ at $z = L$ (extrapolated)	13.1018 g/L	-0.56%	+2.0%	+2.5%	+4.0%
$HetIx$	0.7346	-1.8%	-1.1%	-1.4%	-4.0%
Axial ECS flow at $z = \frac{1}{2}L$	0.2933 mL/min	-0.06%	-0.40%	+0.06%	-0.40%
$ Q_{L,out} - Q_{L,in} $	$1.475 \times 10^{-7}$ mL/min	1.5×	0.61×	1.4×	1.3×
Total average TMFF	$1.853 \times 10^{-15}$ m/s	1.5×	0.61×	1.4×	1.3×
Time to steady state	47 h 30 min	-14%	-16%	-12%	-36%

#### *Effect of time increment*

As in the case of spatial grid, the time step for the solution of the protein transport problem ( $\Delta t$ ) was chosen based on considerations of CPU time and solution accuracy. For  $\Delta t$  varied between 5 s and 60 s, the corresponding changes in local concentration values did not exceed 0.5%. Time increments smaller than 5 s were found impractical because of excessively long times of code execution (for the given  $50 \times 10 \times 9$  grid). The main effect of  $\Delta t$  on the results was observed in the fluid mass balances (i.e., in the unbalanced  $Q_L$  and TMFF), which would usually deteriorate by about the same factor as the increase in time step. The value of  $\Delta t = 10$  s was eventually chosen for all subsequent simulations. The run-time  $\Delta t$  adjustment schemes developed initially for the purpose of accelerating the convergence of ECS pressure iteration at each time level (the initial guess of the pressure field for the next time level was better when  $\Delta t$  was smaller) were not used after the implementation of a direct ECS pressure solver (section 5.3.1.1).

### *Effect of angular concentration averaging in the central core*

At every time level and for every axial grid point  $i$ , the protein concentrations in the central core of the domain ( $j = 1$ ) were angularly averaged in order to smooth out the transverse concentration profiles in the vicinity of the cartridge centreline (section 5.3.2). The averaging was implemented by setting the input parameter  $Ir0$  to 1. The results of simulations performed for  $Ir0 = 1$  and for  $Ir0 = 0$ , including the indicators of fluid mass balance and distance from steady state, differed by less than 0.4%. In various graphs plotting the concentration data, the effects of angular averaging, if noticeable, were apparent only inside the central core region.

### *Homogeneous versus inhomogeneous fluid continuity equation*

The ECS fluid continuity equation (eq. 105, section 5.2.2) could be greatly simplified by setting the parameter  $F_1$  to 0, i.e., by assuming that the fluid flow in the (inhomogeneous) ECS porous medium could be adequately described using a homogeneous form of the continuity law. The validity of this assumption was tested in several preliminary simulations for different cartridge orientations. At either  $\Psi = 90^\circ$  or  $\Psi = 135^\circ$ , the local concentrations and other output parameters at steady state for  $F_1 = 0$  and  $F_1 = 1$  differed by less than 0.05%. However, the choice of  $F_1$  had a dramatic effect on the fluid mass balance, which was usually 2-3 orders of magnitude worse when the inhomogeneous continuity equation was used. Since the simulation results were virtually unaffected by the value of  $F_1$ , and because of the significant deterioration of the fluid mass balance at  $F_1 = 1$ , the subsequent simulations were performed with  $F_1$  set to 0.

### *Influence of viscosity gradients*

The differences in most of the output data due to cancellation of viscosity gradients in the ECS pressure equation ( $F_\mu = 0$ ) were less than 1%, although some of the concentration values in protein-enriched regions could change locally by up to 3%. However, no differences were evident in the graphical appearance of the results for  $F_\mu = 0$  and for  $F_\mu = 1$ . On the other hand, the inclusion of viscosity gradients had a serious adverse effect on the fluid mass balance, causing its deterioration by as much as 3-5 orders of magnitude (depending on  $\Psi$ ). Consequently,  $F_\mu = 0$  was chosen as an input value for all later simulations.

### *Effect of natural-convective manifold adjustment*

For a horizontal cartridge ( $\Psi = 90^\circ$ ), cancellation of the natural-convective manifold adjustment scheme<sup>27</sup> (see section 5.2.2.3) produced less than 0.5% changes to the output parameters such as those listed in table 16. In the inclined-upward case ( $\Psi = 135^\circ$ ), these differences were slightly more pronounced, with the concentration changes inside and near the upstream ECS manifold reaching 5-6%. Overall, the scheme did not affect significantly the fluid and protein mass balances or the graphical appearance of the results at  $\Psi \leq 135^\circ$ . However, much more pronounced influences, with local concentration changes up to 4 g/L and with significant alteration of the  $dCdtMax$  and  $dCdtAve$  profiles, were observed at higher inclination angles (i.e., closer to the vertical-upward orientation). For that reason, the input parameter  $IManNC$  in the subsequent simulations was always set to 1.

### *Influence of lumen-side protein concentration*

The lumen-side protein concentration ( $C_L$ ), treated as spatially constant for the ICS flow rates of interest here, had practically no effect on fluid flow and ECS protein transport in a closed-shell HFBR. For  $C_L \geq 5$  g/L, all steady-state ECS concentration data were identical within at least 6 significant figures to those obtained for  $C_L = 0$  g/L, while the fluid mass balance was affected by less than 0.15%. This outcome could be expected, because the elevation of lumen-side osmotic pressure due to the presence of protein in the ICS produced the same shift of transmembrane pressure at all locations within the HFBR. Thus, by fluid continuity, there was no change in the transmembrane fluid flux and hence no change in the ECS convective flow anywhere in the bioreactor. For such changes to occur, gradients of osmotic pressure would have to exist, for example, as a result of spatial variation in the ICS protein concentration. By the same token, the magnitude and distribution of Starling flow in the ECS filled with protein is initially the same as in a protein-free HFBR, as long as the starting protein distribution is uniform.

---

<sup>27</sup> Note that the diffusive adjustment scheme could not be cancelled or the manifold effect would not be accounted for. Section 5.5.2.2 of Results and Discussion will further elaborate on the role of ECS manifolds in HFBR protein redistribution.

#### 5.4. Experimental Procedures

In the experimental investigation of gravity-influenced 3-D ECS protein transport, several factors seriously limit the use of invasive methods such as the freeze-and-thaw technique (see section 3.3.3) to quantitate the HFBR protein distribution. For instance, one is likely to encounter problems such as (1) instability of some of the protein distributions upon the stoppage of ICS flow (e.g., when the ICS flow was directed upward); (2) large numbers of cartridge sections required for a three-dimensional analysis; or (3) a limit of one data set per experiment, which stipulates that a large number of cartridges be available at a reasonable cost. Noninvasive analytical methods, on the other hand, are generally more sophisticated, expensive, and time-consuming, and may also require some specific technical problems to be addressed. For example, the possibility of flow disturbances due to local heating in magnetic resonance imaging (MRI) should be considered, and equipment constraints such as the size of the magnet bore may limit the use of this method to study the effects of HFBR orientation. For the above reasons, the experimental studies conducted here were mainly focused on visual observation and qualitative analysis.

As in the one- and two-dimensional investigations described earlier, a Cuprophan membrane GFE-15 hollow-fibre cartridge was used in these experiments. This was the last cartridge of this type available in our laboratory and probably one of very few still available anywhere, as Gambro has recently discontinued the GFE-15 series and replaced it on the market with GFS-Plus-16 dialysers utilising Hemophan membranes. The present experimental work was carried out in spite of some problems with azoalbumin leakage to the ICS, possibly caused by fibre breakage in the several-year-old GFE-15 cartridge. However, the extra time and effort required to characterise in detail a new type of hollow-fibre device (needed for model simulations) as well as the focus on qualitative aspects of the results were factors that justified limiting the scope of this study to one type of HFBR.

Azoalbumin (Sigma, St. Louis, Missouri), a red-coloured derivative of bovine serum albumin (BSA), was used as a test protein whose redistribution throughout the ECS could be observed through the transparent walls of the cartridge. The physical properties of azoalbumin (except its colour) were assumed to be essentially the same as for BSA. The azoalbumin concentrations were determined by spectrophotometric analysis using a Spectronic 601 device (Milton Roy, Rochester, New York). Solution absorbance was

measured at 450 nm, corresponding to the maximum absorption of the protein's azo group; additional measurements were also carried out at 280 nm (absorption of aromatic rings in the polypeptide chain) to confirm that the observed colour intensity was indeed representative of the protein concentration.

Prior to the experiments, the hollow-fibre membranes were thoroughly rinsed using a mixture of phosphate-buffered saline (PBS) and distilled water, according to the protocol described earlier (section 3.3.1). Following the rinsing and overnight equilibration of the membranes, the fluid was drained from the cartridge and the ICS was filled with PBS containing 0.1% NaN<sub>3</sub> (Baker, Phillipsburg, New Jersey) to inhibit bacterial growth. Next, the ICS ports were closed, and a solution of azoalbumin in PBS (also with 0.1% NaN<sub>3</sub>) was recirculated through the ECS at 100-200 mL/min for 15-20 min using a peristaltic pump (Cole-Parmer, Barrington, Illinois), in order to ensure a homogeneous distribution of the protein in that space. After the cartridge orientation was adjusted to the desired angle, the ECS ports were clamped and a sample was taken to determine the initial ECS concentration. The ICS fluid recirculation at a desired flow rate was then started using another peristaltic pump (Cole-Parmer), which marked the onset of an experiment ( $t = 0$ ).

The conditions of the azoalbumin transport experiments are summarised in table 17. All of them were conducted at room temperature (21-25°C) (variations in fluid density and viscosity and in protein diffusivity resulting from the temperature fluctuations were neglected in the subsequent model simulations). Five different cartridge orientations were investigated: vertical with downward ICS flow ( $\Psi = 0^\circ$ ), inclined with downward ICS flow ( $\Psi = 45^\circ$ ), horizontal ( $\Psi = 90^\circ$ ), inclined with upward ICS flow ( $\Psi = 135^\circ$ ), and vertical with upward ICS flow ( $\Psi = 180^\circ$ ). The ICS flow rate was set to 850 mL/min, a value higher than those normally used in cell culture but chosen here purposefully in order to amplify the significance of convective protein transport. The initial protein concentrations in the ECS ranged from 3.08 g/L to 6.16 g/L, which are realistic values for proteins in mammalian cell culture media.<sup>28</sup> A typical experiment was carried out until an apparent steady state was

---

<sup>28</sup> Typically, 5-20% serum is used to supplement the ECS medium in HFBR mammalian cell culture. Assuming that the serum composition is similar to that of physiological plasma in humans, which contains 60-84 g/L total proteins, the approximate range of growth-factor protein concentrations in the ECS should be 3.0-16.8 g/L. This estimation neglects other proteins, such as the product antibody, whose concentrations in the ECS during most of the culture are usually much lower.

Table 17. Summary of azoalbumin transport experiments for different cartridge orientations ( $Q_L = 850$  mL/min); the initial ECS concentrations in 6B-D, denoted with an asterix, were determined from the ICS concentration data; the extent of protein leakage, i.e., the fraction of ECS protein that has leaked to the ICS over the experiment duration, was calculated based on the known ICS recycle volumes and the approximate total ECS volume of 100 mL

#	$\Psi$ (orientation)	Duration	Initial ECS distribution	Initial ECS concentration (g/L)	Final ICS concentration (g/L)	Extent of protein leakage
1	90° (horizontal)	6 h	uniform	6.16	0.153	12%
2	90° (horizontal)	6 h	uniform	4.37	0.125	14%
3	135° (inclined up)	9 h	uniform	4.71	0.302	26%
4	45° (inclined down)	6 h	uniform	4.38	0.044	29%
5	180° (vertical up)	32 h	uniform	4.09	0.095	63%
6A	0° (vertical down)	6 h	uniform	3.08	0.042	38%
6B	90° (horizontal)	20 h	final of 6A	2.01*	0.064	31%
6C	45° (inclined down)	26 h	final of 6B	1.45*	0.074	19%
6D	135° (inclined up)	50 h	final of 6C	1.20*	0.100	61%

reached; i.e., until no further changes to the protein distribution were noticeable over a sufficiently long time, relative to the experiment's time scale.

In the course of each experiment, photographs of the side view of the cartridge were taken periodically. This enabled the monitoring of the transient changes in azoalbumin distribution, since the red-coloured protein solution was clearly visible through the transparent walls of the HFBR. The protein distribution captured in each picture was, in fact, a superposition of many ECS concentration distributions existing in the various vertical sections perpendicular to the direction of viewing (over the cartridge thickness), blended additionally with the faint background colour due to a small quantity of the protein present in the ICS. Nevertheless, the photographic images collected in this fashion were sufficient for qualitative analysis purposes.

ICS fluid samples were taken regularly to monitor the extent of azoalbumin leakage to the lumen side in each experiment. In order to lower the ICS protein concentration and thereby enhance the ICS-ECS contrast in the photographs, the ICS recycle volume was increased from the initial 400-500 mL in experiments 1-3 to 2.7-2.9 L in the subsequent

runs. Between experiments (except 6A-D), the ECS contents were homogenised by fluid recirculation, and an ECS sample was taken to determine the azoalbumin concentration. In the 6A-D series, the cartridge orientation was changed while maintaining the ICS flow and with ECS ports closed; the intermediate ECS concentrations in this series were determined indirectly from the ICS concentration data, by calculating the amount of protein that had leaked to the lumen side.

Similar ECS azoalbumin transport experiments were also conducted using a GFS Plus 16 Hemophan membrane dialyser. The results of these studies, not shown here for better clarity of the discussion, do not differ qualitatively from those obtained for the GFE-15 cartridge. The trends of protein redistribution in the GFS Plus 16 reactor were generally less pronounced because of the reduced convective polarisation and longer transients involved, which could be attributed to the differences in geometry and in membrane permeability for the two HFBRs. Also, since the GFS cartridge was not characterised independently to verify the manufacturer's specifications of its essential parameters such as the fibre dimensions, reliable model simulations could not be carried out in this case. In conclusion, no additional information was gained from the GFS Plus 16 experiments that further benefitted the qualitative analysis of HFBR protein transport presented below.

## **5.5. Results and Discussion**

This part of the thesis will start with a summary of the experimental distributions of azoalbumin in the ECS of a GFE-15 hollow-fibre cartridge, juxtaposed with the corresponding distributions obtained by model simulations (section 5.5.1). The comparison between the observed and simulated results will focus on general trends related mainly to the effects of gravity and natural convection. Its primary purpose will be to demonstrate the model validity in a qualitative sense, while an accompanying discussion will attempt to explain any quantitative differences. Section 5.5.2 will follow with a more comprehensive presentation of the modelling results for different operating conditions and a discussion of the relevant mechanisms involved in gravity-influenced ECS protein redistribution.

### 5.5.1. Experimental Observations and Model Validation

Figures 40-44 show a representative selection of transient and steady-state experimental distributions of ECS azoalbumin for different HFBR orientations. Also presented in figs. 40-43 are the corresponding model predictions, plotted as two-dimensional concentration contour graphs in the vertical section through cartridge centre line. Since this particular section belongs to the symmetry plane and has the largest surface area (equal to  $2R_{HFBR}L$ ) of all vertical sections parallel to the cartridge axis, its protein distribution was chosen as a sufficiently adequate representation of the depth-averaged experimental distribution viewed in the photographic images. For the benefit of visual comparison, an attempt was made to reproduce the appearance of azoalbumin-filled cartridges by relating (in a nonlinear fashion) the hue and intensity of the colour in the graphs to the setup of the contour levels. Owing to a lack of relevant experimental data, however, quantitative comparisons of the local concentration values were not possible; hence, the contour labels in figs. 40-43 have been omitted. The small rectangles (not drawn to scale) outside the ECS domain in the graphs illustrating the model predictions mark the positions of the ECS manifolds. For simplicity, the manifold concentration distributions predicted by means of the adjustment schemes outlined in section 5.2.2.3 are not shown.<sup>29</sup>

An important assumption made in order to simplify the simulations of the experimental runs was the constancy of the total ECS azoalbumin content in each experiment. In reality, as was mentioned in section 5.4 and demonstrated in table 17, the protein was progressively leaking from the ECS to the lumen recycle stream at an average rate varying, for different experiments, from about 1% to about 5% per hour (the leakage rate was usually declining with time). Note that larger errors might be associated with the estimates of azoalbumin leakage in experiments 4-6, where the lumen-side protein was diluted to a relatively small concentration in a large ICS recycle volume (2.7-2.9 L). The neglect of azoalbumin leakage over the time periods of interest here was assumed to have no significant bearing on the qualitative features of protein redistribution in the ECS. Thus, the essential conclusions regarding the validation of the present model, at least in the qualitative sense, are expected to remain unchanged.

---

<sup>29</sup> The same convention has been applied to all contour plots presented hereafter. Note, however, that the concentrations in the manifolds are essentially the same as those in the adjacent parts of the ECS fibre bundle.

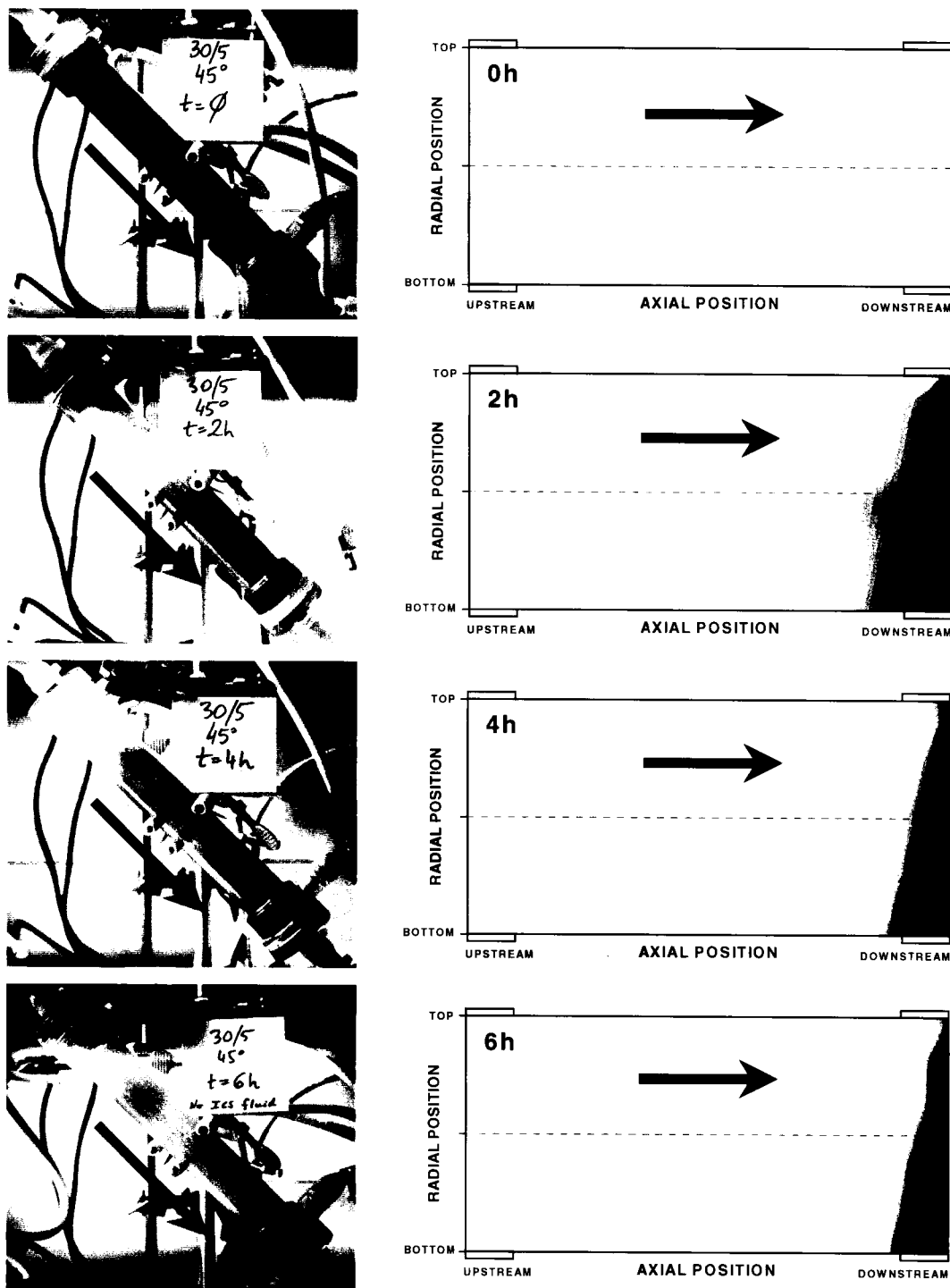


Fig. 40. Experimental (left) and model-simulated (right) transient distributions of ECS azoalbumin in a GFE-15 cartridge inclined at 45°. Conditions of experiment 4 (table 17),  $Q_L = 850$  mL/min,  $C_0 = 4.38$  g/L (assumed unchanged over the experiment duration). Black arrows indicate the direction of bulk ICS flow. The lumen space in the last photograph was emptied to increase contrast between the ICS and ECS. All panels have been resized for the convenience of arrangement in the layout and hence the cartridges are not shown to scale.

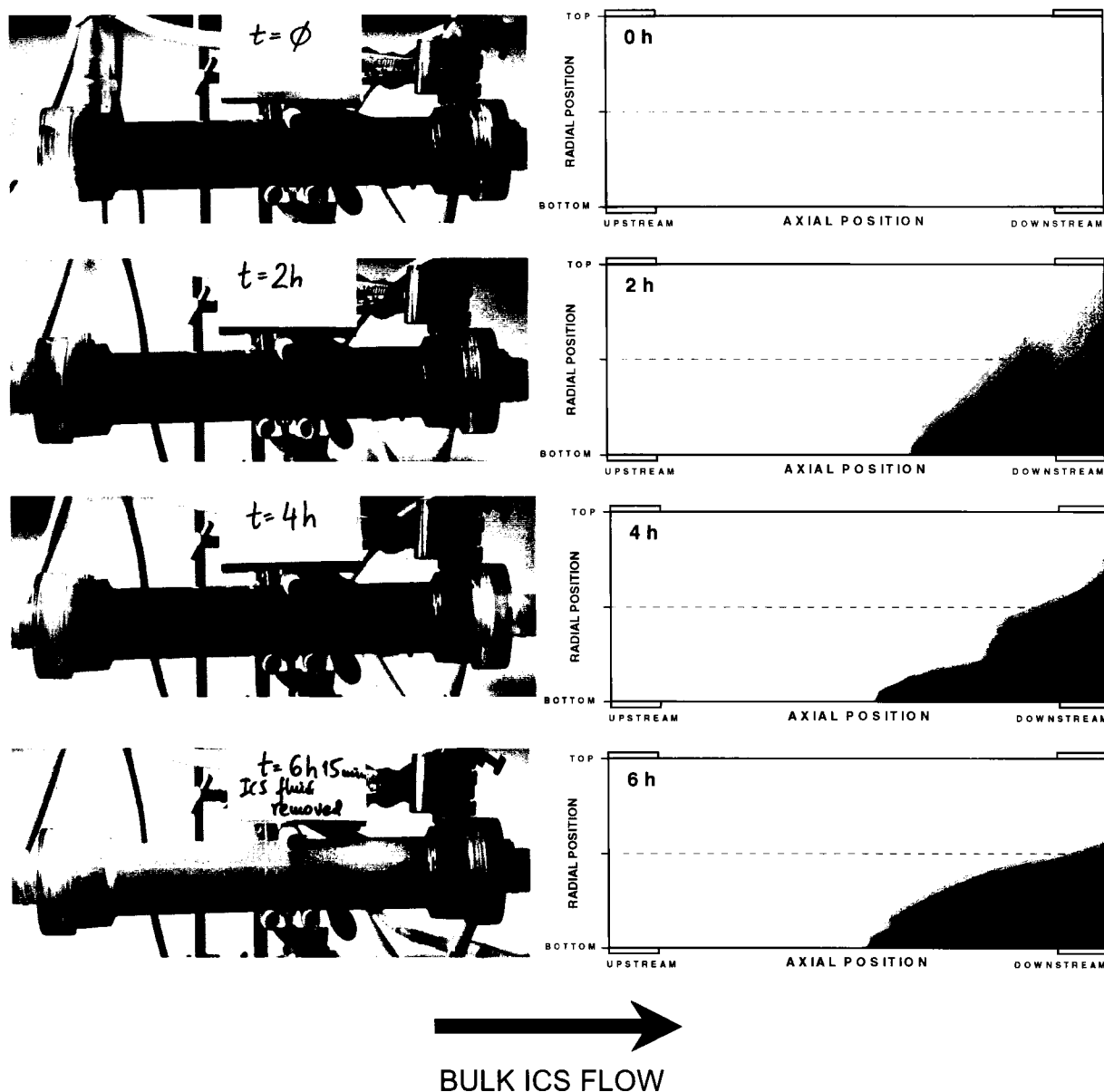


Fig. 41. Experimental (left) and model-simulated (right) transient distributions of ECS azoalbumin in a horizontal GFE-15 hollow-fibre cartridge. Conditions of experiment 1 (table 17),  $Q_L = 850$  mL/min,  $C_0 = 6.16$  g/L (assumed unchanged over the experiment duration). The lumen space in the last photograph was emptied to increase contrast between the ICS and ECS. All panels have been resized for the convenience of arrangement in the layout and hence the cartridges are not shown to scale.

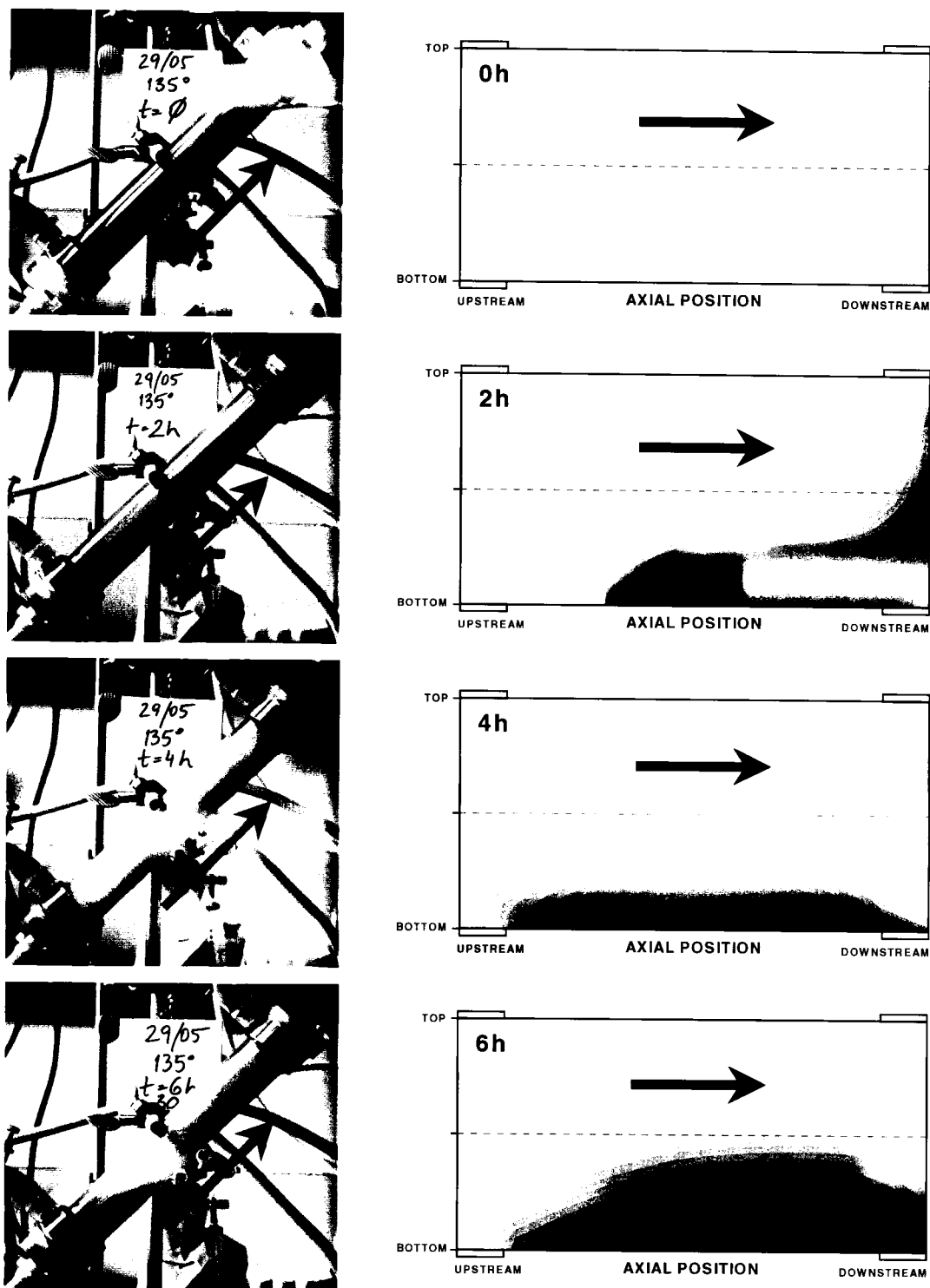


Fig. 42. Experimental (left) and model-simulated (right) transient distributions of ECS azoalbumin in a GFE-15 cartridge inclined at  $135^\circ$ . Conditions of experiment 3 (table 17),  $Q_L = 850$  mL/min,  $C_0 = 4.71$  g/L (assumed unchanged over the experiment duration). Black arrows indicate the direction of bulk ICS flow. All panels have been resized for the convenience of arrangement in the layout and hence the cartridges are not shown to scale.

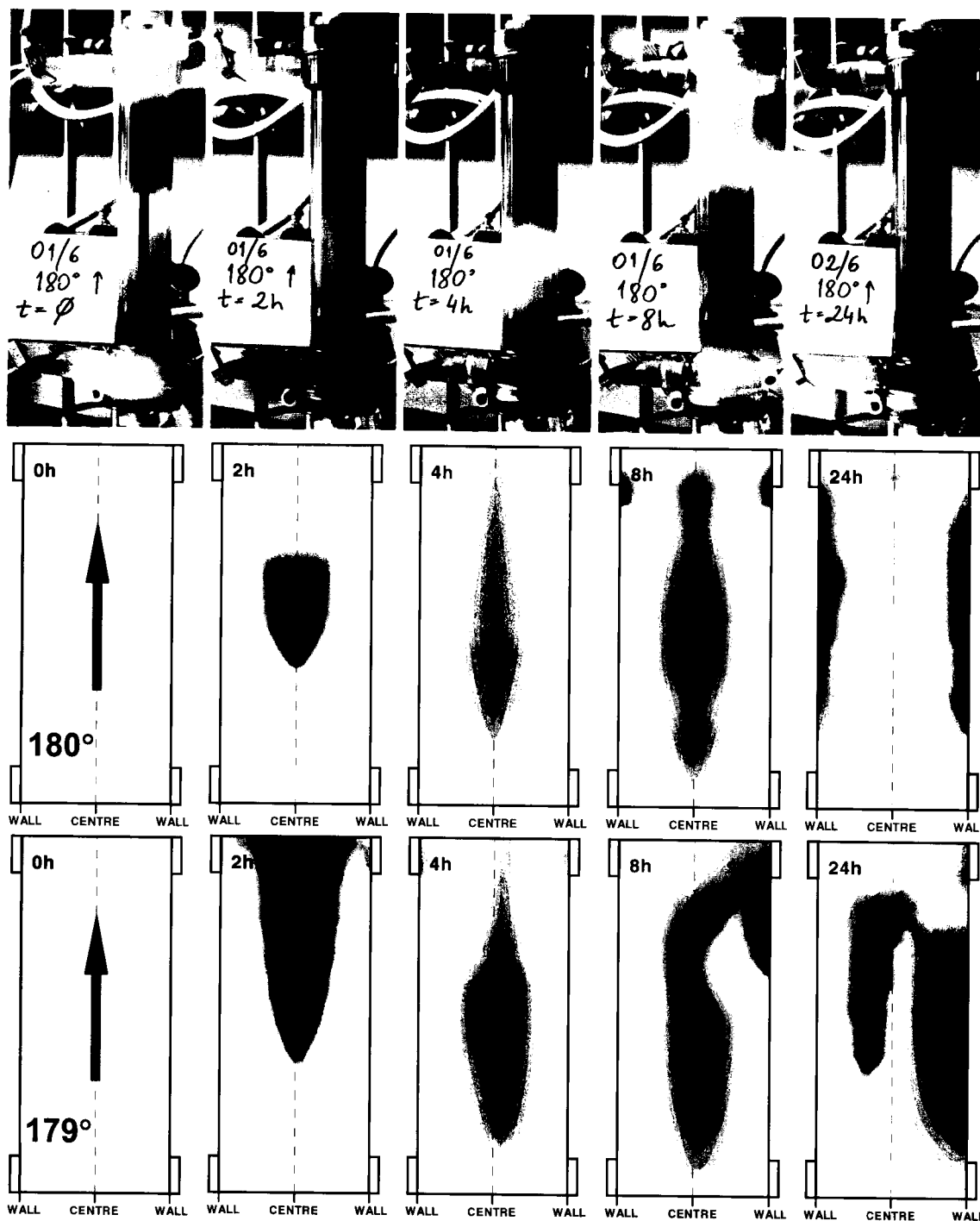


Fig. 43. Experimental (top panels) and model-simulated (middle and bottom panels) transient distributions of ECS azoalbumin in a vertical GFE-15 cartridge with upward ICS flow (indicated by black arrows). Conditions of experiment 5 (table 17),  $Q_L = 850$  mL/min,  $C_0 = 4.09$  g/L (assumed unchanged over the experiment duration). The bottom panels show the predicted effect of a  $1^\circ$  deviation from the vertical orientation towards the right (i.e.,  $\Psi = 179^\circ$ ) for the same simulation conditions. All panels have been resized for the convenience of arrangement in the layout and hence the cartridges are not shown to scale.

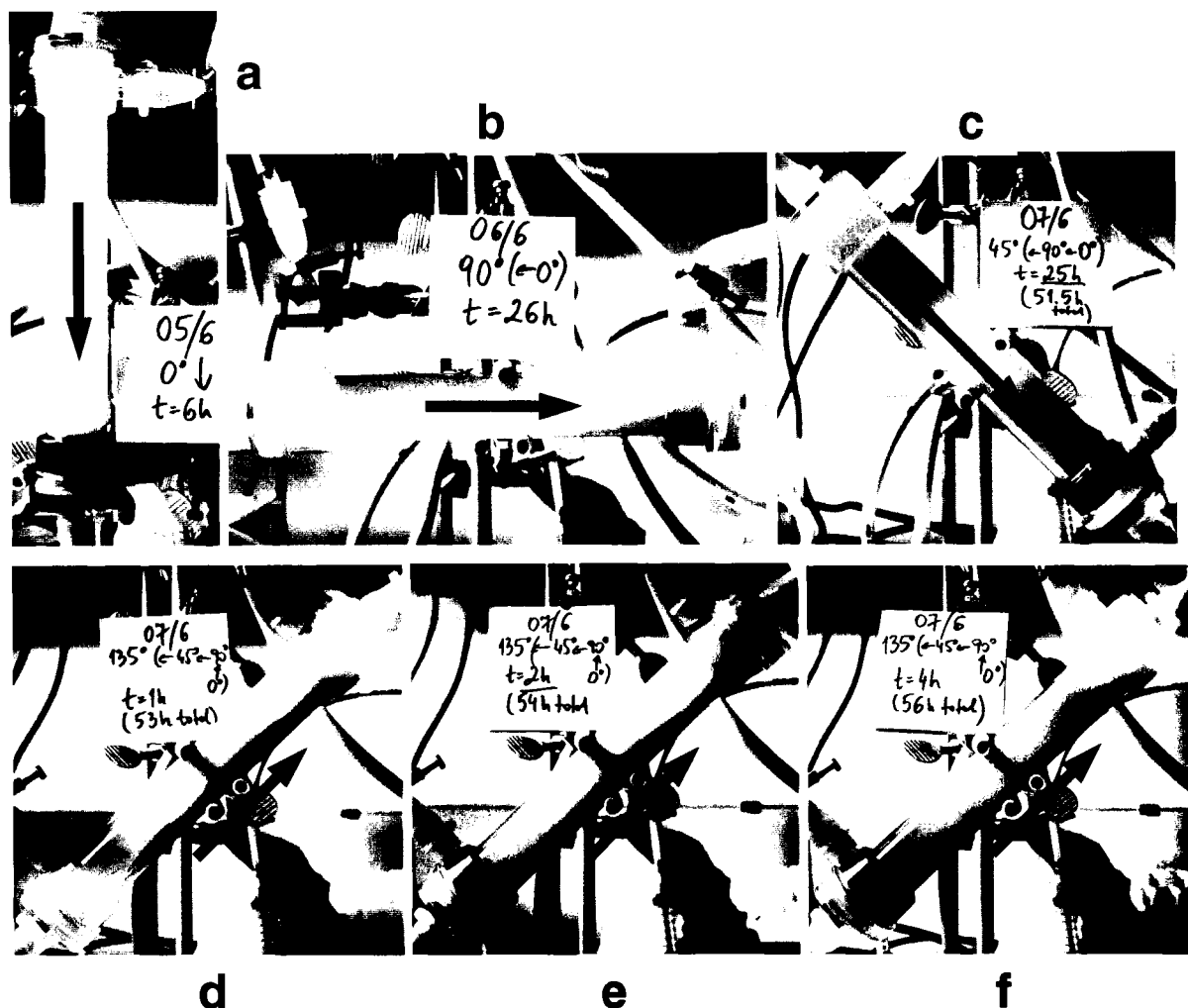


Fig. 44. Azoalbumin distributions in a GFE-15 cartridge for the experimental series 6A-D (table 17): *a*,  $\Psi = 0^\circ$ , at the end of 6A (6 h); *b*,  $\Psi = 90^\circ$ , at the end of 6B (20 h, considered to be steady state); *c*,  $\Psi = 45^\circ$ , at the end of 6C (26 h, considered to be steady state); *d*,  $\Psi = 135^\circ$ , 1 h of 6D; *e*,  $\Psi = 135^\circ$ , 2 h of 6D; *f*,  $\Psi = 135^\circ$ , 4 h of 6D. The final distribution for  $\Psi = 135^\circ$  (case 6D) is not shown because of significant protein depletion from the ECS due to leakage, but is qualitatively similar to the 4 h transient in panel *f*. Black arrows indicate the direction of bulk ICS flow.

The transient changes to the initially uniform distribution of azoalbumin in the ECS of an inclined HFBR cartridge with downward ICS flow ( $\Psi = 45^\circ$ ) are illustrated in fig. 40. The results shown correspond to the conditions of experiment 4 (see table 17). Within 2 h of the experiment, some extent of downstream polarisation of the protein was already evident, although it appeared less pronounced than predicted by the model. The accumulation of the protein at the downstream end of the ECS continued over the next 4 h or so, until a nearly horizontal boundary of the polarised zone became visible, as was expected of a protein distribution at or close to steady state for this HFBR orientation. The final experimental transient at  $t = 6$  h (fig. 40, bottom left) shows the azoalbumin packed to approximately 10% of the ECS volume and filling up the downstream ECS manifold. The corresponding model-simulated protein distribution at  $t = 6$  h exhibits lower concentrations in the top portion of the ECS near its downstream end (suggesting less involvement of the downstream manifold) as well as noticeably less axial dispersion (suggesting that this phenomenon should perhaps be included in an extended version of the model). Nonetheless, the overall trends shown in all of the predicted transients appear consistent with the experimental observations.

Figure 41 shows the dynamics of ECS azoalbumin redistribution in a horizontal HFBR cartridge (conditions of experiment 1). In addition to the forced-convective polarisation downstream, a downward polarisation of the protein occurs, resulting in a characteristically skewed profile observed earlier by Piret and Cooney (1990b). The model has generally well reproduced the experimental results, with some minor discrepancies in the axial extent of the polarised zone at  $t = 6$  h and in the amount of protein present in the upper part of the downstream ECS manifold. The first of these discrepancies could possibly be explained by the existence of a small gap between the fibre bundle and the cartridge wall, which might facilitate fluid movement – and hence convective transport – in the upstream direction along the bottom of the bioreactor. The second discrepancy likely relates to the simplified manner in which the ECS manifolds are treated in the present model. Although the phenomena of dynamic protein release and absorption by the manifolds are predicted by the model as indicated, for example, by the concentration gradients existing near the downstream manifold for the 2 h and 4 h transients in the right panels of fig. 41, these effects appeared to exhibit more inertia in a real system than is suggested by the simulations.

The inclined orientation with upward ICS flow ( $\Psi = 135^\circ$ ), depicted in fig. 42, is commonly used in commercial HFBR systems. The images assembled in fig. 42 illustrate the results pertaining to experiment 3 (see table 17). In this case, the initial stage of downstream polarisation of azoalbumin was followed by its redistribution back upstream along the bottom of the cartridge ( $t \geq 2$  h). This process was similar to that occurring in a horizontal cartridge (fig. 41), except that now – owing to a nonzero axial component<sup>30</sup> of gravitational acceleration – the magnitude of the natural-convective backflow was much larger. Consequently, the protein was carried all the way back to the upstream end of the ECS and its subsequent distribution was much more uniform than those observed in the cases discussed above, i.e., at lower values of  $\Psi$ . No significant changes to the azoalbumin distribution were seen after 6 h of experiment 3 (fig. 42, bottom panels). Again, judging by the appearance, the model seems to have somewhat underestimated the amount of azoalbumin held up within the ECS manifold volumes. However, the existence of a top-to-bottom concentration gradient over most of the ECS length at  $t \geq 4$  h has been correctly predicted by the simulations.

The process of ECS protein redistribution in a vertical cartridge with upward ICS flow, corresponding to experiment 5, is depicted in fig. 43. The transient distributions developed after the initial stage of upward downstream polarisation ( $t > 2$  h) display almost no heterogeneity at all, which proves the existence of a very effective mixing mechanism due to natural convection. This mechanism is self-regulating, i.e., it is based on negative feedback – the more the protein is polarised downstream by forced convection, the larger the upward fluid density gradients and hence the stronger the resulting natural-convective downward flows. The model-simulated transients shown in the middle panels of fig. 43 are clearly highly idealised, mainly because of the assumed axial symmetry of the cartridge at  $\Psi = 180^\circ$ . Nonetheless, the prediction of more uniform protein distributions at this HFBR orientation, compared with the previously discussed cases, is in qualitative agreement with the experimental observations.<sup>31</sup>

---

<sup>30</sup> A reminder: the axial (or  $z$ -) component is in the direction of the longitudinal axis of HFBR cartridge.

<sup>31</sup> Recall, again, that the concentration contours plot the data in a section through the HFBR, whereas the experimental photographs show azoalbumin distributions as seen over the entire thickness of the cartridge.

The simulation results obtained for the same experimental conditions, but with  $\Psi = 179^\circ$  (fig. 43, bottom panels), demonstrate how sensitive the protein redistribution in a vertical cartridge can be to variations in system parameters. Owing to the highly nonlinear characteristics of mixed-convective protein transport and the unstable nature of upward-polarised concentration fields, even a small perturbation – such as a  $1^\circ$  deviation from the vertical orientation – can lead to distributions that are markedly different from those predicted for the perfectly axisymmetric vertical case. By a similar token, it is expected that other nonideal and random factors, e.g., nonuniformity in fibre packing, could also have a perturbing effect on the convective flow patterns and the resulting protein distributions. The task of quantifying such nonidealities, however, which would likely require significant additional experimental as well as modelling work, was not undertaken within the scope of this project.

Figure 44 shows some of the photographs taken over the course of the experimental series 6A-D. Simulations of this case were not performed for several reasons. First, they would require additional code modification to allow initialisation of nonuniform concentration fields at a variable  $\Psi$ . Second, the simulations were not expected to yield significantly different predictions from those depicted in figs. 40-42. Third, the extent of protein leakage at the end of the series was considerably higher than in any of experiments 1-4 (conducted at the same orientations as 6B-D; see table 17), which would increase the error due to the neglect of protein leakage in the simulations.

The series was designed to examine if the expected trends in protein redistribution toward steady state would also manifest themselves when the experimental system was started from a highly nonuniform initial state. Moreover, it was anticipated that many of the observed transients could be shortened (since the redistribution process at any orientation typically started with downstream polarisation, as is evident from figs. 40-43) and the contrast between the ECS and ICS improved<sup>32</sup> if the starting distribution had already been polarised downstream, as was the case at the end of run 6A ( $\Psi = 0^\circ$ , fig. 44a). The final distributions in the subsequent runs 6B ( $\Psi = 90^\circ$ , fig. 44b) and 6C ( $\Psi = 45^\circ$ , fig. 44c) appear

---

<sup>32</sup> If the location of the fibre breakage was confined to the upstream or middle part of the cartridge, then the azoalbumin leakage could be diminished under the conditions of rapid downstream polarisation, thus reducing the background tint of the ICS fluid.

to represent steady states for these two reactor orientations (neglecting protein leakage to ICS), a conclusion supported by the existence of sharp boundaries between the protein-rich and protein-poor zones, particularly within the ECS manifolds. Figure 44*d-f* shows some of the transient azoalbumin distributions in an inclined cartridge with an upward ICS flow (6D,  $\Psi = 135^\circ$ ). The protein is seen to spread gradually along the bottom wall of the cartridge toward the upstream manifold and, afterwards, throughout the rest of the ECS. The 4-h transient distribution in run 6D does not differ qualitatively from the final distribution at 50 h (the latter is not shown because of a considerable loss of ECS azoalbumin due to leakage). Thus, as can be seen from fig. 44, the results of the 6A-D series exhibit the same general trends as those shown in figs. 40-42, where the starting protein distribution was uniform.

The results presented above clearly demonstrate a strong influence of HFBR orientation on ECS protein redistribution, with an increasing role of natural-convective transport as the direction of bulk ICS flow changes from vertical-downward ( $\Psi = 0^\circ$ ) to horizontal ( $\Psi = 90^\circ$ ) to vertical-upward ( $\Psi = 180^\circ$ ). This has important practical implications, since the heterogeneity of ECS growth factor distribution at certain reactor orientations may seriously impair cell growth and the overall productivity of the culture. In this respect, the available data strongly suggest that configurations with upward ICS flows ( $\Psi > 90^\circ$ ), in which most advantage can be taken of the natural-convective mixing in the ECS, are the best options for HFBR operation. In particular, the vertical-upward flow configuration ( $\Psi = 180^\circ$ ) – currently uncommon for HFBR cell culture systems – seems quite promising from this point of view, as long as the process of cell sedimentation can be kept under reasonable control (see also the discussion on Starling flow in section 2.1.3.3).

The present 3-D porous medium model has reproduced most of the essential features of gravity-influenced protein distributions observed in the experiments. In this sense, a qualitative validation of the model has arguably been accomplished. The majority of the quantitative differences between the experimental and simulated results can be attributed to the simplistic way of modelling the ECS manifolds and to the neglect of nonidealities, such as the nonuniformity of fibre packing, existing in the real hollow-fibre cartridge. The following section will take a closer look at the mechanisms of the ECS mass transfer phenomena illustrated above, as well as presenting analyses of the most significant effects of various parameters on the 3-D hydrodynamics and protein transport in HFBRs.

### 5.5.2. Model Predictions

This section will discuss the effects of the most important factors playing a role in gravity-influenced ECS protein redistribution in HFBRs. Four such major factors have been identified: the cartridge inclination angle ( $\Psi$ ), the presence and size of ECS manifolds, the ICS flow rate ( $Q_L$ ), and the initial protein concentration in the ECS ( $C_0$ ). It was not the aim of this section to present a complete analysis of model-generated data for all possible combinations of the various levels of these factors. Rather, only the essential aspects of the results are discussed, emphasising the overall characteristics of ECS protein transport at different bioreactor orientations and highlighting possible implications of these results to mammalian cell culture. The discussion has been divided into four subsections, each one concentrating on a different factor, with most attention given to the influence of the inclination angle. Obviously, some of the effects could not be completely separated; thus although each subsection does maintain its intended focus, the material has been organised in a fairly flexible manner.

#### 5.5.2.1. *Effect of HFBR Inclination Angle*

The model simulations carried out for different HFBR orientations assumed a uniform initial ECS protein concentration of 5 g/L (including manifolds), an ICS flow rate of 600 mL/min, a spatial grid of  $50 \times 10 \times 9$  ( $N_i \times N_j \times N_k$ ), a time step  $\Delta t = 10$  s, and other input parameters at their default values given in table 12. Some of the steady-state output data predicted by the model are summarised in table 18 and plotted in fig. 45. In addition to the 5 inclination angles used in the experimental studies (section 5.4), other values of  $\Psi$  were also considered in order to confirm the validity of the observed trends. Investigation of several orientations at  $\Psi \geq 170^\circ$  demonstrated a strong sensitivity of the simulation results to  $\Psi$  for near-vertical cartridges with upward ICS flow. On the other hand, no similarly sensitive dependence on  $\Psi$  was found near  $\Psi = 0^\circ$  or for any orientation with downward ICS flow, which can probably be explained by the lesser significance of gravity-induced free-convective phenomena in these cases.<sup>33</sup>

---

<sup>33</sup> Note that the symmetry of the model system changes from planar to axial as the cartridge becomes vertical, e.g., as  $\Psi$  is changed from  $179.9^\circ$  to  $180^\circ$  or from  $0.1^\circ$  to  $0^\circ$ . However, the results are very sensitive to  $\Psi$  only in the former case, i.e., when the ICS flow is directed upward.

Table 18. Model predictions of ECS heterogeneity index ( $HetIx$ ), ECS protein concentration in the fibre bundle ( $C_{Bundle}$ ), and average global magnitude of  $dC/dt$  ( $dCdtAve$ ) for different HFBR orientations at steady state; times needed to reach steady state ( $t_{StSt}$ ) are also given

$\Psi$ (cartridge orientation)	$t_{StSt}$ (h)	Steady-state $dCdtAve$ (g/L/s)	Steady-state $HetIx$	Steady-state $C_{Bundle}$ (g/L)
0° (vertical down)	33.1	$3.78 \times 10^{-07}$	0.918	2.37
0.1° (near-vertical down)	33.2	$3.72 \times 10^{-07}$	0.918	2.37
45° (inclined down)	26.5	$4.39 \times 10^{-07}$	0.885	2.65
60° (inclined down)	31.6	$3.97 \times 10^{-07}$	0.868	2.94
90° (horizontal)	47.5	$5.28 \times 10^{-07}$	0.735	4.13
105° (inclined up)	32.8	$1.05 \times 10^{-06}$	0.470	5.09
120° (inclined up)	26.9	$1.04 \times 10^{-06}$	0.351	5.23
135° (inclined up)	25.0	$8.90 \times 10^{-07}$	0.300	5.26
160° (inclined up)	25.0	$9.05 \times 10^{-07}$	0.267	5.36
170° (near-vertical up)	n/a <sup>a</sup>	$9.23 \times 10^{-06}$ <sup>b</sup>	0.256 <sup>c</sup>	5.65 <sup>d</sup>
175° (near-vertical up)	54.8	$1.63 \times 10^{-06}$	0.264	5.53
179° (near-vertical up)	155.0	$1.16 \times 10^{-06}$	0.247	5.84
179.9° (near-vertical up)	123.8	$2.39 \times 10^{-07}$	0.244	5.67
180° (vertical up)	28.4	$1.15 \times 10^{-06}$	0.287	5.29

<sup>a</sup> Steady state not attained in > 400 h; solution oscillates at 0.033 mHz (period 8.5 h). <sup>b</sup> Logarithmic mean of the lower and upper limits for an oscillating periodic solution. <sup>c</sup> Arithmetic mean of the lower and upper limits for an oscillating periodic solution, amplitude 0.29%. <sup>d</sup> Arithmetic mean of the lower and upper limits for an oscillating periodic solution, amplitude 0.028%.

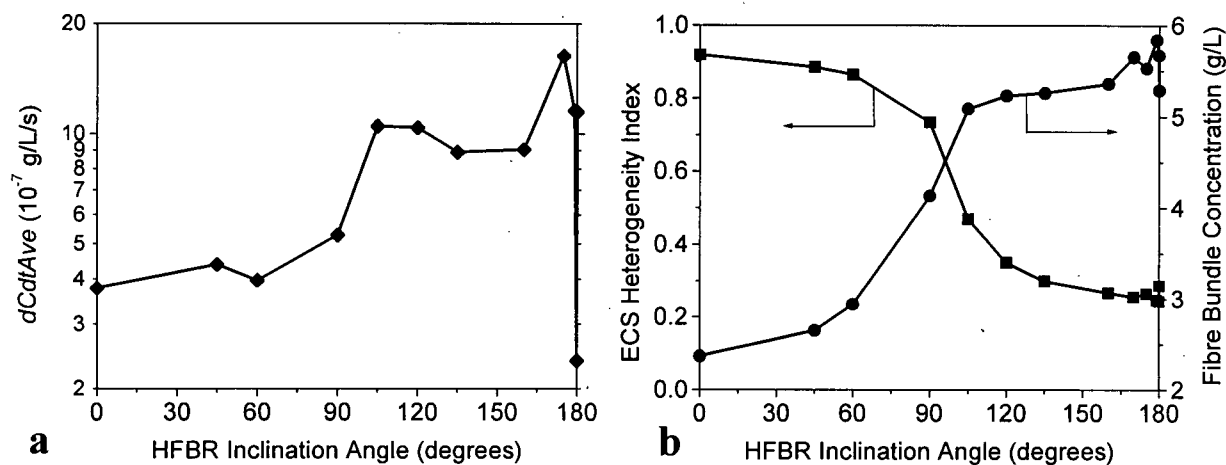


Fig. 45. Steady-state output parameters as functions of the HFBR inclination angle: *a*, global average magnitude of  $dC/dt$ ; *b*, ECS heterogeneity index (squares, left axis) and ECS fibre bundle concentration (circles, right axis). At  $\Psi = 170^\circ$ , no data point is plotted for  $dCdtAve$ , and the mean values from table 49 are plotted for  $HetIx$  and  $C_{Bundle}$ .

As was mentioned earlier in section 5.3.3.2, the criterion adopted here assumed that steady state was reached as soon as the value of  $dCdtMax$  dropped below the threshold value of  $EpsStSt = 10^{-5}$  g/(L·s).  $dCdtMax$  (maximum local magnitude) rather than  $dCdtAve$  (average global magnitude) was chosen for this criterion in order to account for local changes in concentration that might be confined to a small part of the ECS, e.g., as a result of significant downstream polarisation or exchange of the protein between the fibre bundle and the manifolds. Indeed, despite some anomalies in the trend, especially for upward-flow orientations, the steady-state  $dCdtAve$  is seen to generally increase with  $\Psi$  (table 18 and fig. 108a). This indicates that, had the criterion been based on  $dCdtAve$ , the highly polarised distributions at low inclination angles could have been identified as being at steady state, even though significant local changes in concentration – indicated by the value of  $dCdtMax$  – might still be taking place in the polarised region.

The trends of variation with cartridge inclination angle are fairly clear for the steady-state ECS heterogeneity index,  $HetIx$ , and the steady-state average protein concentration in the fibre bundle,  $C_{Bundle}$  (fig. 45b).<sup>34</sup> Both of these parameters are important from a cell culture point of view. Heterogeneous distribution of ECS growth factors may lead to nonuniform cell growth and inefficient use of HFBR space, whereas a decrease in  $C_{Bundle}$  below the initial level ( $C_0 = 5$  g/L) indicates the possibility of growth factor depletion due to accumulation in the ECS manifolds. As fig. 45b shows, the S-shaped profiles of  $HetIx$  and  $C_{Bundle}$  have their inflexion points (i.e., points of maximum change) near  $\Psi = 90^\circ$ , which emphasises the fundamental difference between the downward- and upward-flow orientations. From the plotted data, it is clear that inclination angles of at least  $120^\circ$  are the ones of practical interest for HFBR cell culture. Furthermore, since  $HetIx$  is lowest and  $C_{Bundle}$  is highest at  $\Psi$  close to  $180^\circ$ , it appears that vertical or near-vertical orientations with upward flow may have the potential of successfully competing with the standard HFBR inclination of  $135^\circ$ .

The history of system convergence to steady state (or lack thereof) can be followed by plotting  $dCdtMax$  versus time. Such plots for different HFBR inclinations are presented in fig. 46. At the lowest  $\Psi$  values, the  $dCdtMax$  profiles have a similar appearance; in

<sup>34</sup> The shapes of the curves in fig. 45b remain virtually unchanged if  $HetIx$  and  $C_{Bundle}$  are plotted at a sufficiently long time (the same for all orientations, e.g., at  $t = 24$  h) rather than at steady state.

particular, the curve for  $\Psi = 0.1^\circ$  (not shown) is undistinguishable from that shown for  $0^\circ$ . On the other hand, a very sensitive dependence on  $\Psi$  (as noted earlier) exists at near-vertical orientations. For each inclination angle, a local peak in the  $dCdtMax$  curve typically appears at  $t \approx 1.5-2.5$  h, corresponding to the formation of the downstream-polarised protein zone. The height of this peak is seen to generally increase with  $\Psi$ , which correlates with the increasing magnitude of the natural-convective redistribution of the polarised protein. As time passes, the  $dCdtMax$  profiles for different inclination angles become more distinctive. The relatively noisy appearance of the plots for vertical and near-vertical upward cartridges can be attributed to the complexity of local convective flows and protein distributions that arise at various times at these orientations (see discussion later in this section).

The HFBR inclination of  $170^\circ$  represents an interesting case in which no steady state was reached in more than 400 h of simulation time (table 18, fig. 46). Instead, after about 50 h, a periodic solution emerged oscillating with a frequency of about 0.033 mHz (period 8.5 h). A question arises whether this periodicity reflected an intrinsic property of the differential equation system (or, for that matter, the modelled hollow-fibre system) or was merely a numerical artifact. Additional simulations for this orientation performed using several variations of coarser grid ( $N_i = 20$ ,  $N_j = 5$ ,  $\Delta t = 30$  s) did yield steady states within 20-30 h. On the other hand, a periodic solution oscillating with the same frequency as the original one was also obtained when the spatial mesh was refined to  $N_i = 100$  and  $N_j = 12$  (with  $\Delta t = 10$  s or 30 s making no difference). This suggests that such periodic numerical behaviour might indeed be characteristic of this HFBR orientation but could perhaps only arise at a grid fine enough to ensure sufficient spatial resolution of the concentration field. Although it seems reasonable to treat finer-mesh solutions as more accurate, it is not perfectly clear whether the same behaviour would be reproduced at grids refined even further (note that the finest mesh size is limited by computer RAM constraints). It is therefore difficult to prove beyond any doubt the validity of the periodic solution in this case. The concentration and hydrodynamic results generated for the  $\Psi = 170^\circ$  orientation will be discussed later in this section.

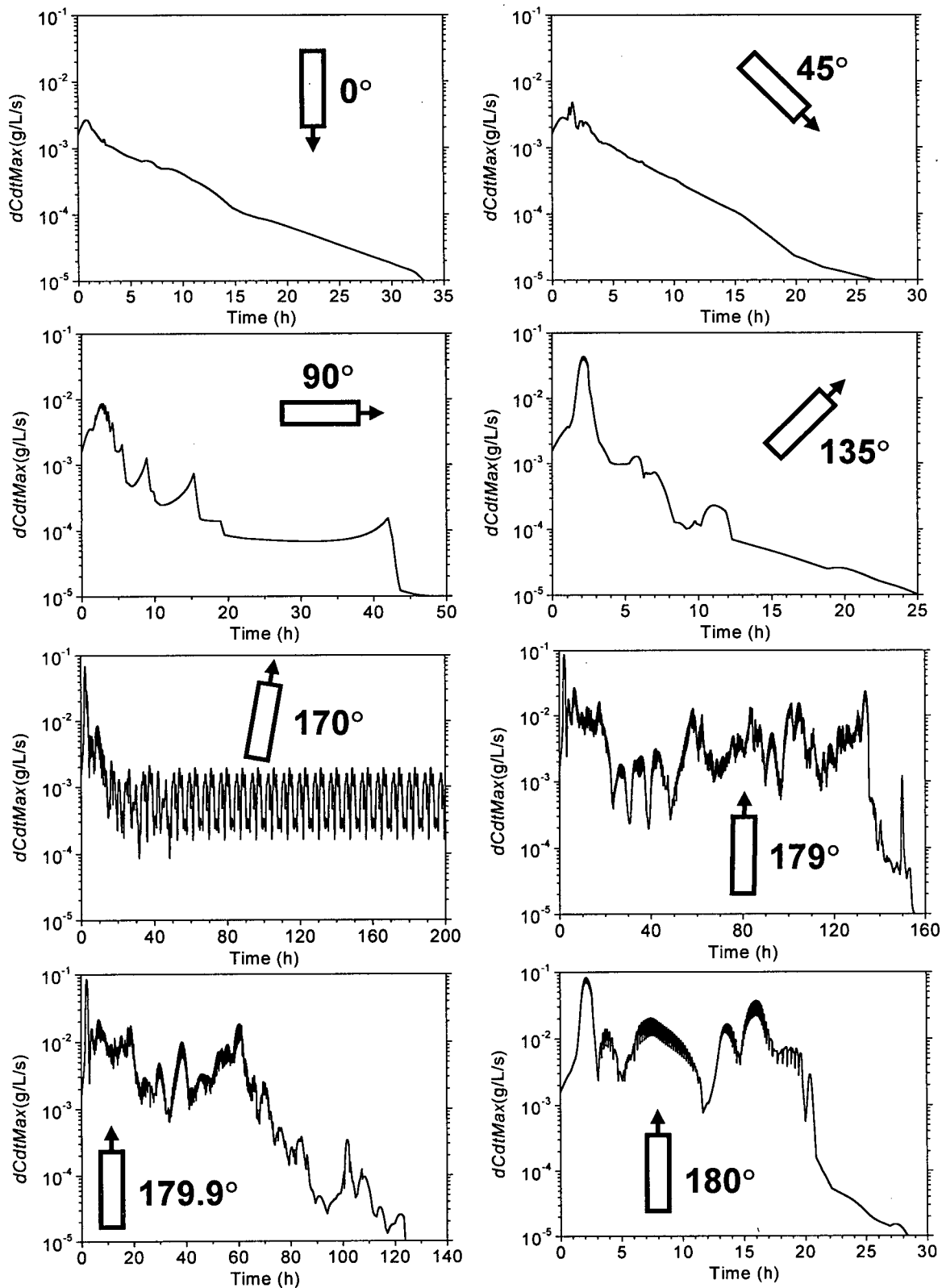


Fig. 46. Temporal changes of  $dCdtMax$  for different HFBR orientations (all other parameters at their default values – see table 12).

The local minima, or dips, in the curve plotting  $dCdtMax$  versus time are usually associated with spatial relocation of the maximum  $|dC/dt|$ . Initially,  $dCdtMax$  is located in the region of fastest concentration change due to convective polarisation, i.e., at the downstream end and the bottom wall of the cartridge. Later, as time passes, several – either gradual or abrupt – relocations of  $dCdtMax$  usually take place towards the axial half-length (for  $\Psi = 90^\circ$ ) or all the way to the upstream end (for  $\Psi \geq 135^\circ$ ), then back to the vicinity of the downstream manifold, and so on. A local rise and then drop in  $|dC/dt|$  at a given position often occurs between such two subsequent relocation events, which is seen in the  $dCdtMax$  curve as a spike or a hill. The maximum  $|dC/dt|$  is typically located either in a region adjacent to an ECS manifold (e.g., from 12 h to 18 h at  $\Psi = 135^\circ$ ), at the boundary of the protein polarisation zone (e.g., from 11 h to 45 h at  $\Psi = 90^\circ$ ), or near a local concentration maximum (e.g., from 22 h to steady state at  $\Psi = 180^\circ$ ).

The plots of  $dCdtAve$  versus time (not shown) are generally much smoother than the  $dCdtMax$  curves, since the information they carry has been averaged over the entire volume of the reactor. Because of their smoother appearance, the overall trend of convergence towards steady state is usually more obvious from the  $dCdtAve$  profiles. On the other hand, some of the information related to local events may be lost; for example, a prominent spike visible at  $t \approx 150$  h for  $\Psi = 179^\circ$  (fig. 46) is totally absent from the  $dCdtAve$  curve. The spike marks the local changes in concentration at the periphery of a protein accumulation zone ( $i = 29, j = 8, k = 9$ ), corresponding to the last significant protein redistribution event preceding steady state. Since the plots of  $dCdtMax$  and, to a lesser degree,  $dCdtAve$  versus time contain very specific information about the behaviour of the protein in the ECS, they can be regarded as a type of numerical fingerprint of the HFBR system dynamics for a given set of conditions. In this sense, these plots were helpful, for example, in assessing the significance of various input parameters by means of the sensitivity analyses described in section 5.3.5.2.

Figures 47 and 48 plot the steady-state ECS concentration contours and velocity vectors for a representative selection of inclination angles. Three nonvertical orientations are considered in fig. 47, which shows the protein and flow distributions in the vertical section through the cartridge centreline for  $\Psi = 45^\circ, 90^\circ$ , and  $135^\circ$ . The results of the essentially one-dimensional vertical-down case ( $\Psi = 0^\circ$ ) are similar to those at  $\Psi = 45^\circ$  and have been

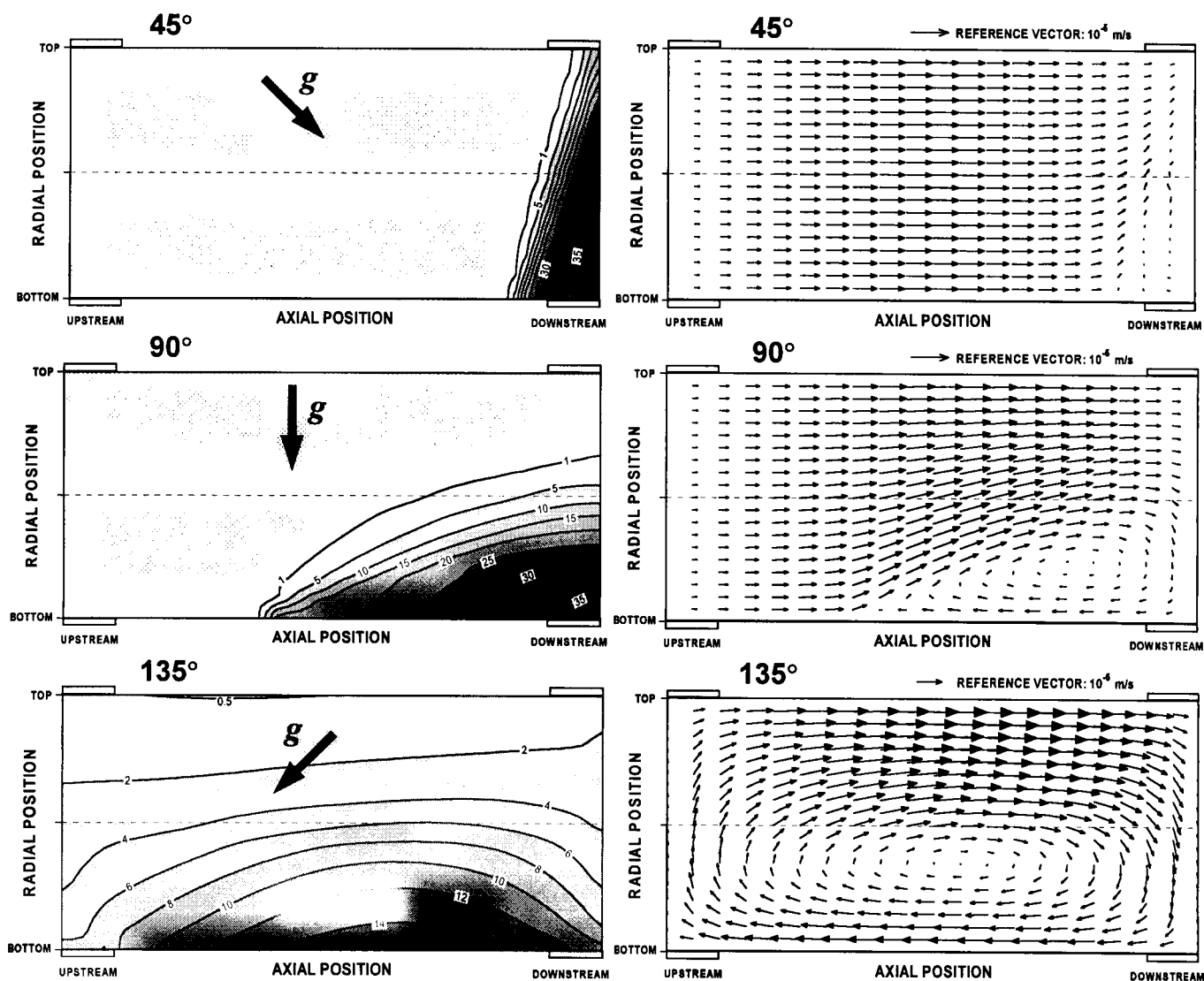


Fig. 47. Model-predicted steady-state protein concentrations (g/L; left panels) and ECS flow patterns (superficial velocities, right panels) at nonvertical orientations of HFBR cartridge:  $\Psi = 45^\circ$  (inclined-down),  $\Psi = 90^\circ$  (horizontal), and  $\Psi = 135^\circ$  (inclined-up). Shown are longitudinal sections in the vertical plane passing through cartridge centerline (not to scale). ICS flow is from left to right and the thick arrows indicate the direction of the gravity vector ( $g$ ). See also table 17 for more of the relevant steady-state data.

Fig. 48 (next page). Model-predicted steady-state protein concentrations (g/L) and ECS superficial velocity vectors at the vertical and near-vertical orientations of HFBR cartridge (top inclined to the right). Left column:  $\Psi = 179^\circ$ , middle column:  $\Psi = 179.9^\circ$ , right column:  $\Psi = 180^\circ$ . The top two rows show longitudinal sections in the vertical plane passing through cartridge centerline (not to scale), with the upward arrows on the left-hand side marking the direction of ICS flow. The third and fourth rows of graphs show cross-sections at  $z = 0.5L$  (axial half-length) and at  $z = 0.9L$  (edge of the downstream ECS manifold), respectively, with the ICS flow coming out of the paper plane. See also table 17 for more of the relevant steady-state data.

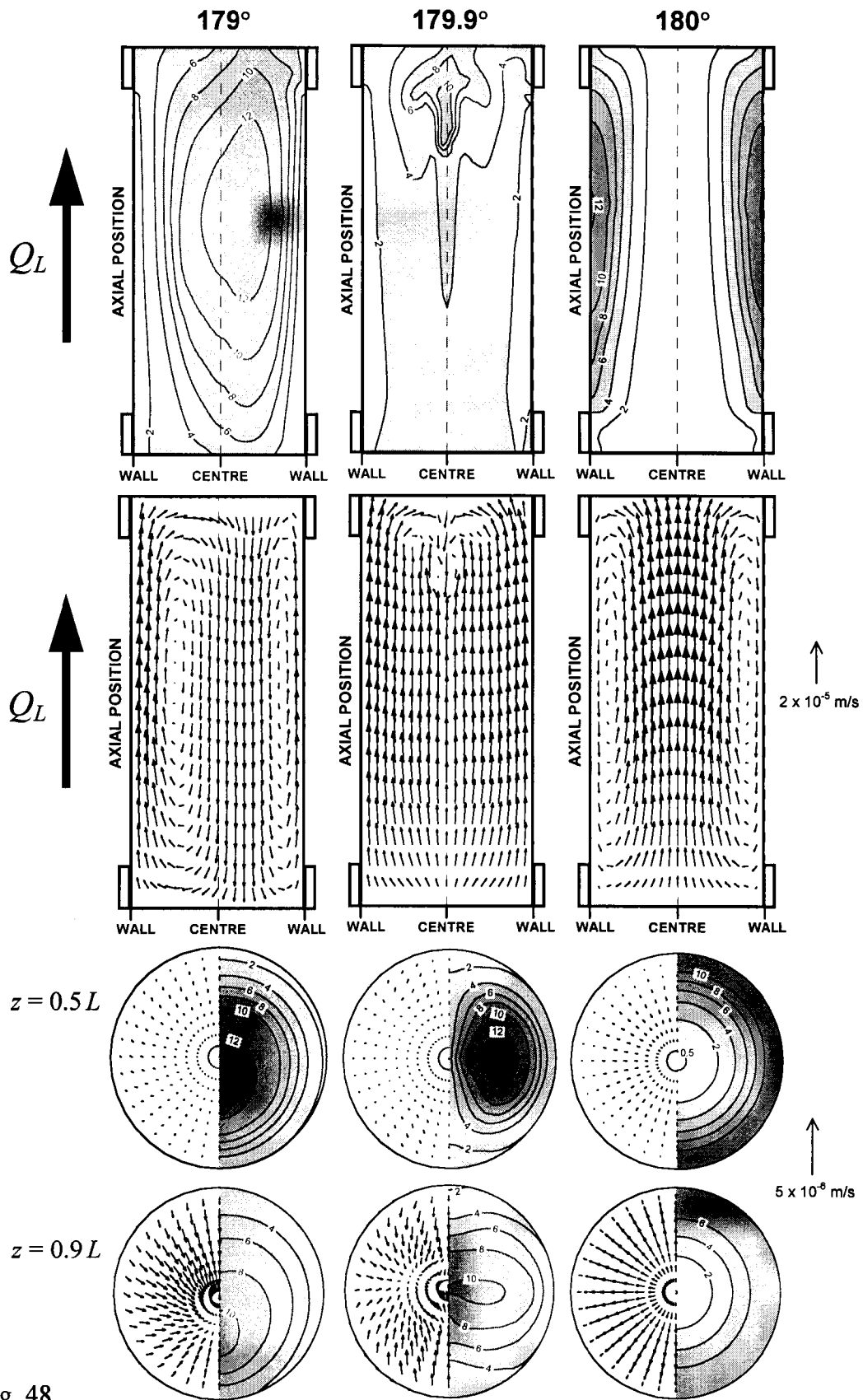


Fig. 48.

omitted from this presentation. The concentration contours plotted in fig. 47 resemble qualitatively the protein distributions at  $t = 6$  h shown in figs. 40 ( $\Psi = 45^\circ$ ), 41 ( $\Psi = 90^\circ$ ), and 42 ( $\Psi = 135^\circ$ ), which compared the results of protein transport experiments with the model predictions (section 5.5.1). As can be seen from fig. 47, the steady-state protein distributions, in addition to being polarised downstream, are generally shifted in the direction of the gravity vector ( $\mathbf{g}$ ). This is a result of superposition of forced-convective Starling flow, induced by the axial ICS pressure drop, and free-convective flows that develop in the ECS whenever the direction of the local increase in protein concentration is not aligned with  $\mathbf{g}$ .<sup>35</sup>

As fig. 47 demonstrates, there is virtually no steady-state natural convection at  $\Psi = 45^\circ$ . In the horizontal case ( $\Psi = 90^\circ$ ), a free-convective recirculation flow is present that coincides with the location of the polarised protein zone. At  $\Psi = 135^\circ$ , as the gravitational contribution and the resulting free-convective flows grow even stronger, the fluid recirculation loop extends over the entire ECS. Interestingly enough, despite the significant ECS convective protein transport at  $90^\circ$  and  $135^\circ$ , the protein distributions do remain unchanged, i.e., the system is indeed at steady state. This is because a dynamic balance is established at every point of the domain, in which the rates of local protein removal and delivery are equal. Moreover, in contrast to the downward-flow cases, neither the transmembrane fluid exchange (results not shown) nor the ECS flow (fig. 47) in the protein-rich region is diminished at  $\Psi \geq 90^\circ$ , i.e., in the presence of significant free convection.

Figure 48 presents the steady-state results for near-vertical and vertical orientations with upward ICS flow, i.e.,  $\Psi = 179^\circ$ ,  $179.9^\circ$ , and  $180^\circ$ . Juxtaposition of these  $\Psi$  values seems justified, since each of them could probably be regarded in an experimental setup as practically vertical. That notwithstanding, the model predicts very different ECS protein and fluid flow distributions for each of these three cases. For  $179^\circ$ , the protein at steady state is mainly concentrated about the bioreactor's centreline and close to its axial half-length. This distribution is almost axisymmetric, with a slight distortion due to the  $1^\circ$  off-vertical cartridge tilting. The corresponding ECS flow pattern in the  $z$ - $r$  section consists of two

---

<sup>35</sup> Note that the boundary of the polarisation zone at  $\Psi = 45^\circ$  in fig. 47 is, in reality, nearly perpendicular to  $\mathbf{g}$ , but does not appear so because the cartridge section is not drawn to scale.

asymmetric recirculation loops, with the fluid ascending near the wall and descending in the central core. In the perfectly vertical case,  $\Psi = 180^\circ$ , the hydrodynamic pattern is essentially reversed, whereas the protein is accumulated along the circumference and away from the centreline. At an intermediate angle of  $179.9^\circ$ , the steady-state protein concentrations are predicted to be highest at radial positions of about half the cartridge radius, i.e., away both from the centreline and from the wall; and at angular position of about  $90^\circ$ , i.e., largely out of sight in the vertical section shown in the uppermost image of fig. 48. This somewhat unusual distribution is revealed more clearly in the cross-sectional  $r-\theta$  plots (bottom two rows in fig. 48). The steady-state ECS flow at  $\Psi = 179.9^\circ$  is best visualised in the  $\theta = 90^\circ$  longitudinal  $z-r$  section (perpendicular to the plane passing vertically through the cartridge centreline), which reveals a triple loop of recirculating fluid (results not shown). Despite their considerable differences<sup>36</sup>, the near-vertical and vertical cases discussed here also share an important similarity. Namely, the vigorous convective flows that exist in the ECS represent a very effective mechanism of homogenising the contents of the extracapillary space, thus creating favourable conditions for cell growth in HFBRs at these orientations. Note also that radially-polarised protein distributions such as those shown in fig. 48 may be difficult to identify in experimental cartridges merely by visual inspection.

It is instructive to inspect the temporal development of protein distributions in the presence of significant free-convective flows in the ECS. To that end, three upward-flow HFBR orientations were chosen:  $\Psi = 135^\circ$ ,  $170^\circ$ , and  $179^\circ$ . Figures 49-51 plot selected transient ECS concentration contours and velocity vectors for these three cases. For convenience, the gravity vector is also shown in figs. 49 and 50, and arrows marking the direction of ICS flow are drawn in fig. 51. The off-vertical inclination of  $179^\circ$  was chosen here as being perhaps a more realistic representation of a nonideal vertical cartridge with upward ICS flow than was the perfectly axisymmetric orientation of  $\Psi = 180^\circ$  (cf. fig. 43 in section 5.5.1).

---

<sup>36</sup> Some of these differences are due to the different symmetries assumed for the vertical (axial) and off-vertical orientations (planar). For example, when the  $\Psi = 180^\circ$  case was simulated assuming planar symmetry, its results were very close to those predicted for  $\Psi = 179.9^\circ$  (see also discussion of transients for  $\Psi = 180^\circ$  later in this section).

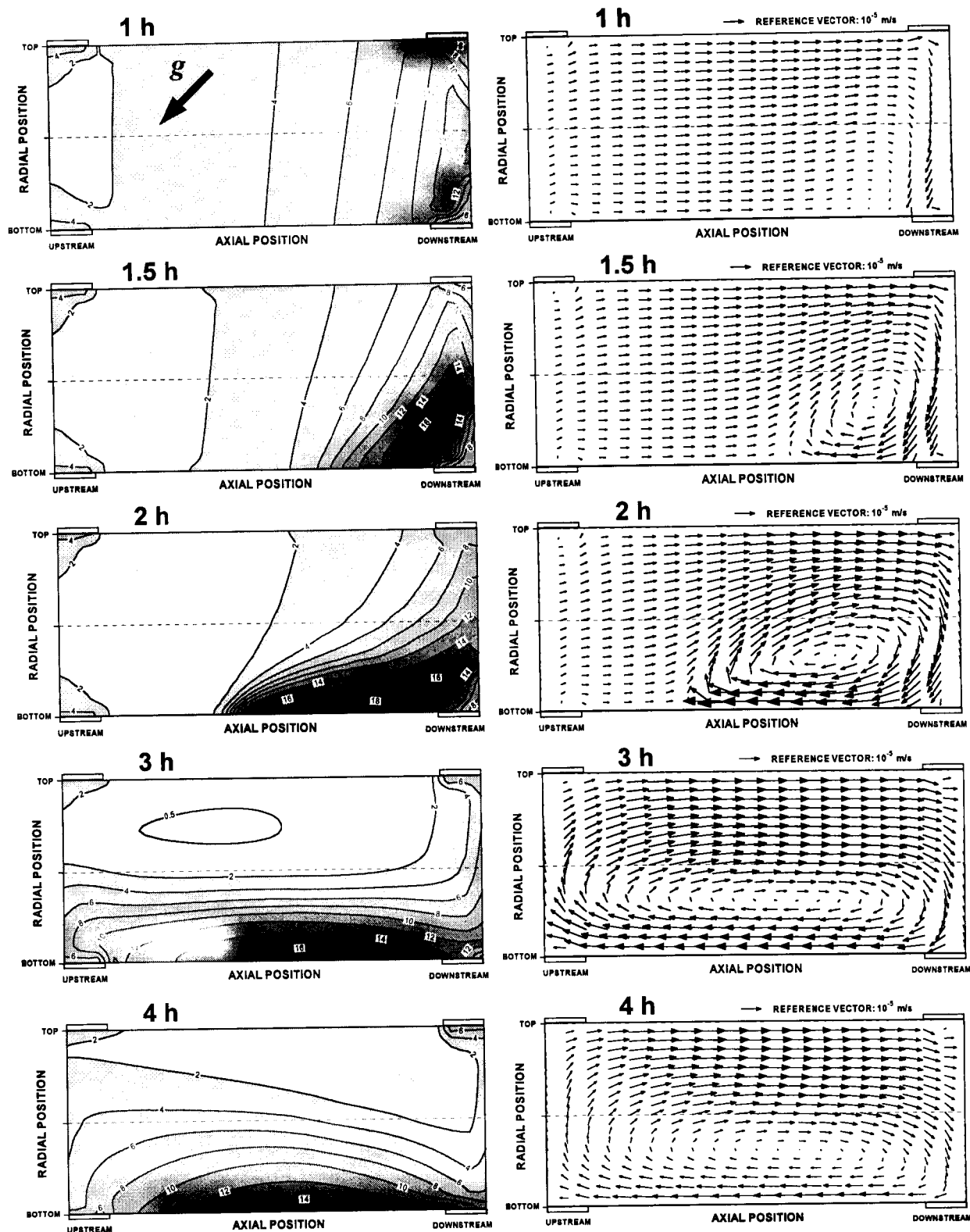


Fig. 49. Selected transients for  $\Psi = 135^\circ$ , plotted in the vertical section through the cartridge centreline. Left panels: ECS protein concentration contours (g/L), right panels: ECS superficial fluid velocity vectors. ICS flow from left to right,  $Q_L = 600$  mL/min,  $C_0 = 5$  g/L.

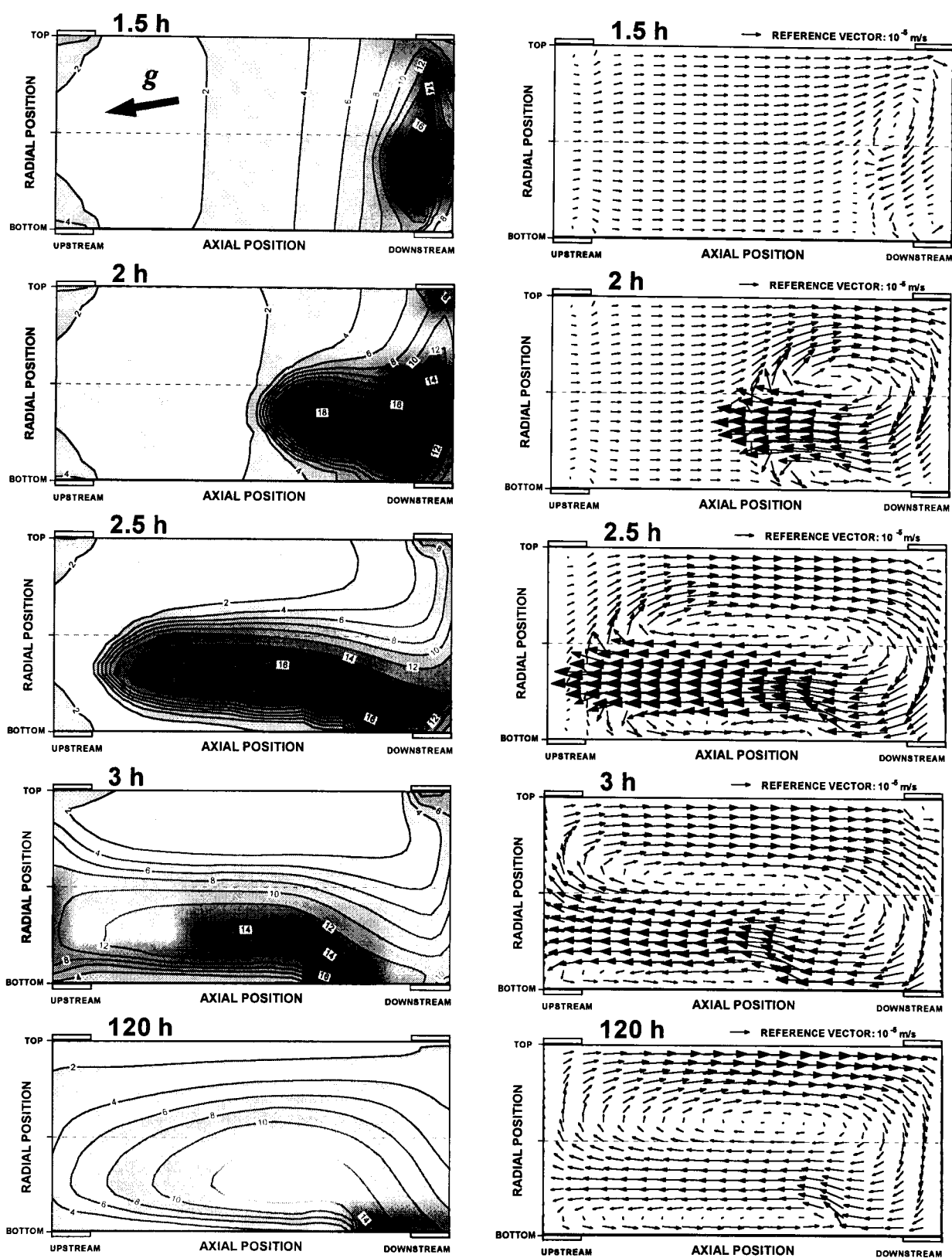
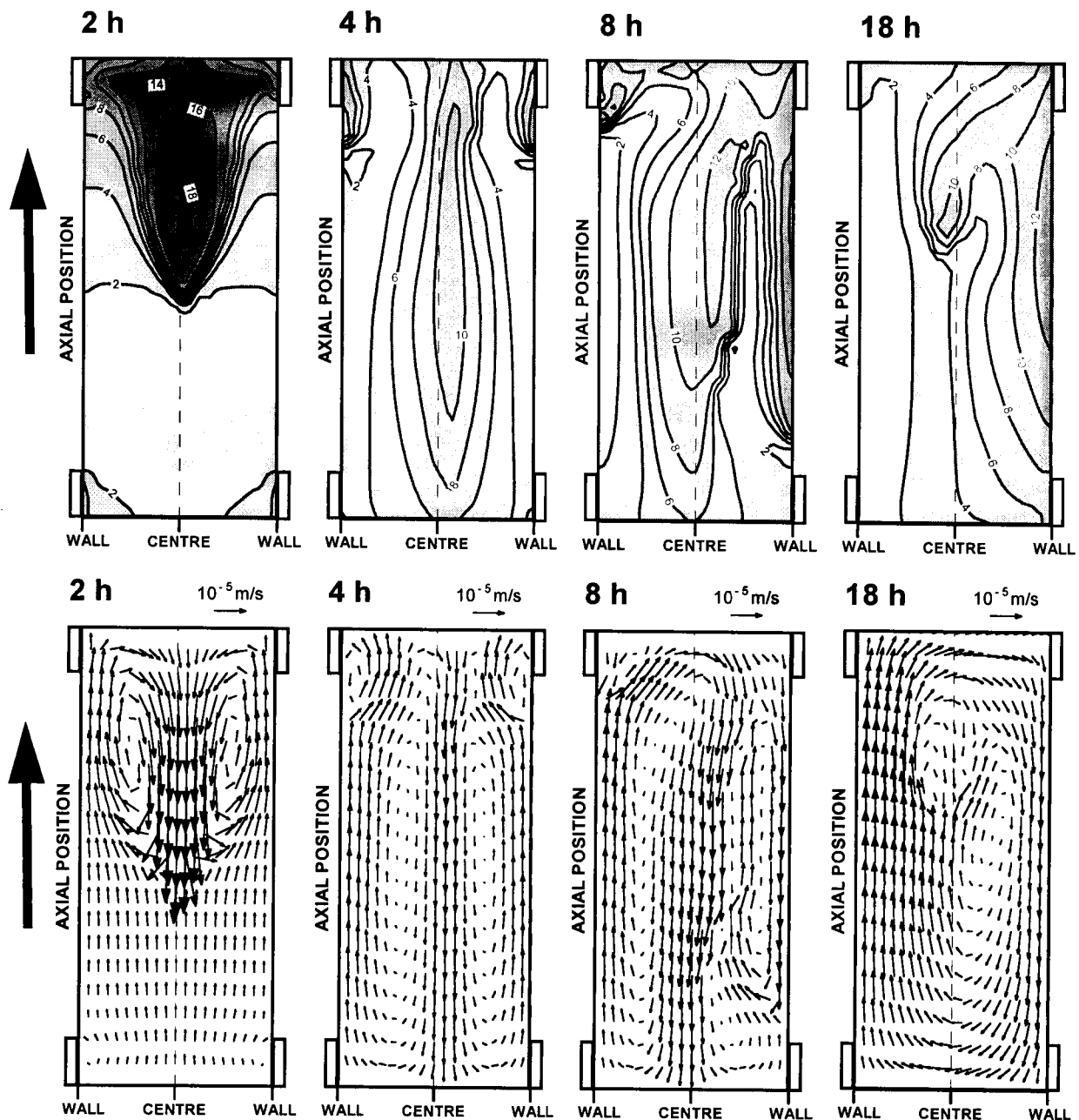


Fig. 50. Selected transients predicted for  $\Psi = 170^\circ$ , plotted in the vertical section through the cartridge centreline. Left panels: ECS protein concentration contours (g/L), right panels: ECS superficial fluid velocity vectors. ICS flow left to right,  $Q_L = 600$  mL/min,  $C_0 = 5$  g/L.



(continued on next page)

Fig. 51. Selected transients predicted for  $\Psi = 179^\circ$  (top of the cartridge inclined to the right). Upper panels: ECS protein concentration contours (g/L), lower panels: ECS superficial fluid velocity vectors. All plots are shown in the vertical section through the cartridge centreline (not to scale). The upward arrows on the left-hand side mark the direction of ICS flow.

$$C_0 = 5 \text{ g/L}, Q_L = 600 \text{ mL/min.}$$

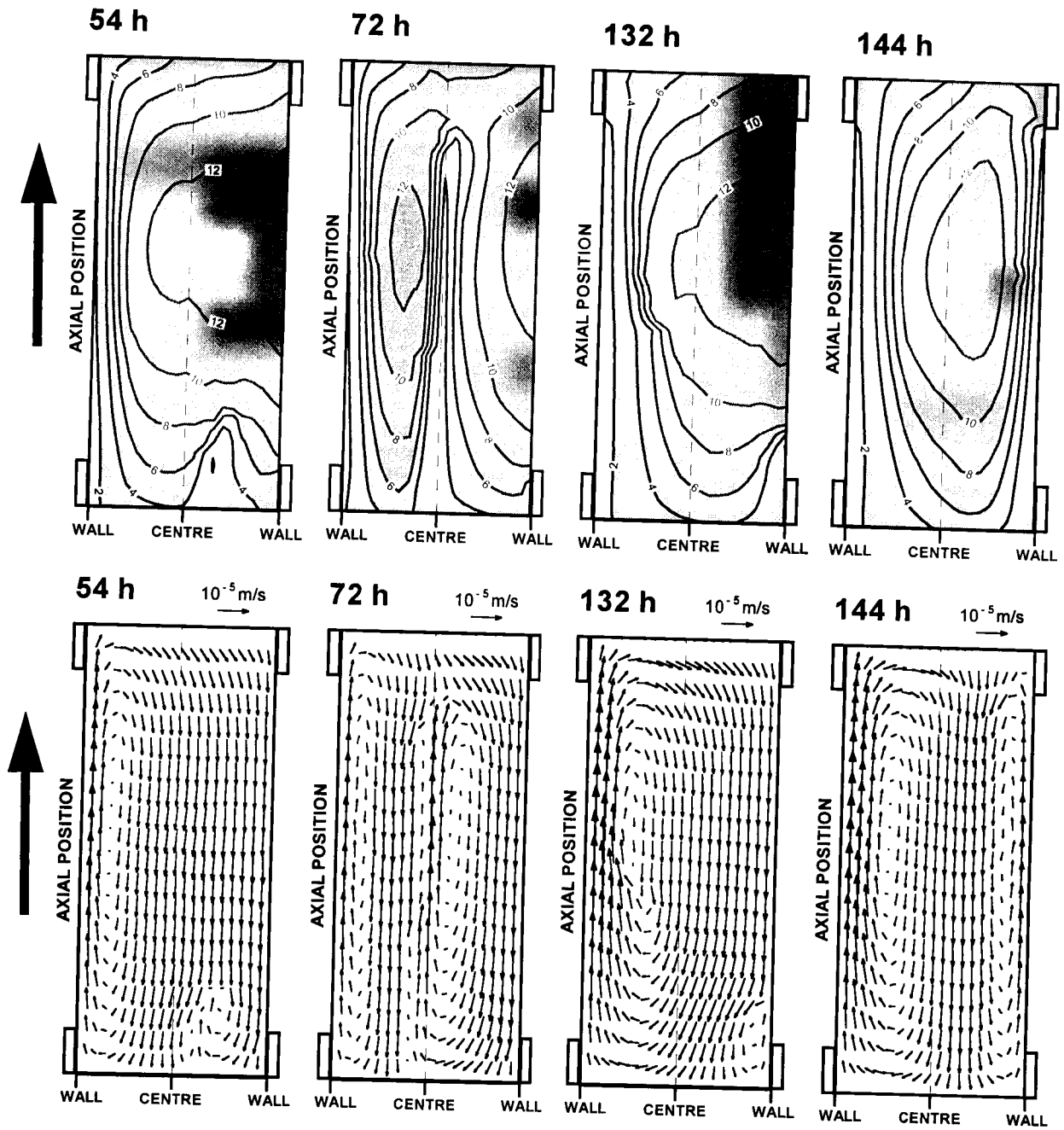


Fig. 51 – continued from previous page.

During the first hour of ICS fluid recirculation in a cartridge inclined upward at  $\Psi = 135^\circ$  (fig. 49), protein is primarily polarised downstream by the forced-convective Starling flow. This process is to some extent delayed by protein exchange with the ECS manifolds, as a result of which the concentration in the outer portion of the fibre bundle increases upstream and decreases downstream. A characteristic free-convective swirl soon develops in the region of protein accumulation, pulling the more-concentrated fluid towards the bottom of the cartridge ( $t = 1.5$  h) and then upstream ( $t = 2$  h). As the bottom-polarised protein spreads over the entire length of the bioreactor, the upstream-moving fluid finds its way back downstream through the upper portion of the ECS, where the concentration is lower ( $t = 3$  h). Thus, the fluid recirculation loop is closed, encompassing now the whole ECS and carrying the protein along by convective motion. Later ( $t \geq 4$  h), the concentration gradients decrease somewhat and the natural-convective flows abate, as the system gradually approaches its steady state. After  $t = 4$  h, no more major changes occur to the ECS hydrodynamics or concentration distribution, with the protein spread mainly along the bottom of the cartridge (see also fig. 47, bottom panels).

A discussion of the transient results for  $\Psi = 170^\circ$  (fig. 50) provides some valuable insight into the origin of the periodic solution obtained in this case. The initial stage of downstream polarisation at this orientation is very similar to that occurring at  $\Psi = 135^\circ$  (fig. 47), except for a less asymmetric protein distribution (fig. 50,  $t = 1.5$  h). At  $t = 2$  h, a distinct zone of high protein concentration ( $> 18$  g/L) is already formed near the downstream end of the ECS, which induces a powerful free-convective flow spreading the protein back upstream ( $t = 2.5$  h). The concentration fields that develop from this moment onward share an important feature related to their distinctive geometry. Namely, although the protein-rich zone eventually reaches the upstream end of the ECS ( $t = 3$  h), it also remains attached to the radial boundary just outside the downstream manifold, with a narrow radial gap separating it from the bottom wall of the cartridge further upstream. Between  $t = 2$  h and 3 h, a small anticlockwise fluid recirculation loop can be seen forming within this gap as the latter grows in length. At  $t = 3$  h and later, most of the ECS fluid travels in the major free-convective loop recirculating clockwise. As we will soon see, the specific flow pattern existing in a boundary region between these two loops is responsible for the persistent attachment of the protein-rich zone to the bottom wall near the downstream manifold and is also a crucial

factor leading to the oscillating behaviour of the concentration and hydrodynamic solutions at this HFBR orientation. With the exception of these local concentration oscillations, the overall ECS protein and flow distributions existing at  $t = 120$  h remain virtually unchanged at later times. Essentially the same transient results as those shown in fig. 50 were also obtained using a refined spatial grid ( $100 \times 12 \times 9$ ).

To gain a better understanding of the dynamics of this system, let us take a closer look at the phenomena taking place in the region of confluence, i.e., where the two flow streams coming from different directions meet. A noteworthy property of such a region is that it may enable protein exchange between two convective loops, which can then lead to the growth of one of them and decline of the other. Because of a highly nonlinear relation between protein distribution and hydrodynamics, the fluid flow in a confluence region is very sensitive to even slight changes in the local concentration, while the latter is sensitive to the changes in convective flow. This interdependence is especially noticeable at high protein concentrations, as is the case for  $\Psi = 170^\circ$  at the position of protein attachment to the wall near the downstream manifold (fig. 50,  $t \geq 2.5$  h). There was apparently no effective mechanism for breaking this attachment, as the protein was continuously removed from and supplied into the confluence region by convective flow. At the same time, the concentration field throughout most of the ECS was stabilised by the major (clockwise) recirculation flow, whereby the stability of the minor (anticlockwise) loop was also ensured. Existence of high local concentrations in a region of confluence of two stable convective loops (fig. 50,  $t = 120$  h) created favourable conditions for the development of oscillations in the position of the local concentration maximum, thus leading to a periodic solution for this HFBR orientation.

A detailed study of these oscillations goes beyond the scope of this thesis, but a likely mechanism may be hypothesised as follows. The concentration on the downstream side of the confluence region was mainly influenced by protein transport via the major convective loop. A transient increase in this downstream-side concentration would cause a corresponding local increase in the magnitude of free-convective flow in the negative axial direction. Consequently, the flow path out of the confluence region would change its direction to more upstream, thus causing convective transfer of some of the protein to the small loop. This would lead to a local decrease in concentration on the downstream side and

a buildup of concentration on the upstream side of the confluence region. Ultimately, the local flow path out of the region would change its direction to its original state, thus favouring protein transfer from the small convective loop back to the major loop. The whole process would then repeat itself in cycles, with oscillations in the flow direction causing shifts in the protein distribution and vice versa. Such periodic changes in the direction of local fluid velocity vector and in the position of local concentration maximum were indeed observed in the results (not shown).

Verification of this hypothesis would require a detailed analysis of transient fluxes in the region of confluence as well as generation of additional output data, which was not attempted here because of limited significance to cell culture. However, the following simple examination based on the available data was carried out to strengthen the above postulate. The cycle of the hypothesised periodic exchange of the protein between the two convective loops should repeat itself after the fluid has completed a full lap moving in one loop and then another lap moving in the other. Thus, the cycle duration is expected to be a sum of the circulation periods for the two loops. Fluid moving along the circumference of the major (clockwise) loop shown in fig. 50 ( $t = 120$  h) travels a lap distance of about  $2(L + 2R_{HFBR}) \approx 0.5$  m at the average interstitial velocity of  $2-4 \times 10^{-5}$  m/s (i.e., about twice the superficial velocity, since the ECS porosity is close to 0.5). This corresponds to an approximate frequency range of 0.04-0.08 mHz. The lap distance for the minor (anticlockwise) loop is roughly  $2 \times 0.75L \approx 0.3$  m, and the average interstitial fluid velocity is about  $2 \times 10^{-5}$  m/s, corresponding to a frequency of 0.067 mHz. Harmonic superposition of these two results yields an approximate frequency range of 0.025-0.036 mHz (period range 7.7-11.1 h). This is indeed consistent with the properties of the periodic solution at  $\Psi = 170^\circ$ , which oscillated with a frequency of 0.033 mHz (period 8.5 h).

Why are there no periodic solutions at lower or higher inclination angles, e.g.,  $\Psi = 160^\circ$  or  $175^\circ$ ? In the former case (results not shown), the protein-rich zone forms too far from the centreline and is pushed by convective flow against the bottom wall (similarly as for  $\Psi = 135^\circ$ , fig. 49). Consequently, the anticlockwise flow loop never arises, and all of the ECS fluid recirculates longitudinally in the clockwise direction. At  $\Psi = 175^\circ$  (results not shown), the concentrated protein zone forms closer to the centreline and is therefore always on the path of the major convective flow. Although a minor (anticlockwise) loop does arise

at the bottom wall, it is larger than that at  $170^\circ$  and hence more effective in redistributing the protein throughout the ECS. As transfer of the protein continuously occurs from the minor to the major convective flow, the anticlockwise loop gradually shrinks and eventually disappears (at  $t \approx 8$  h). Past that time, only the clockwise recirculating flow exists in the ECS and the system readily reaches steady state.

The transient results for  $179^\circ$  (fig. 51) are more complicated than those discussed so far for the lower  $\Psi$  values. Until about 2 h into the simulation, the  $1^\circ$  off-vertical inclination has virtually no effect on the results, and the protein concentration and fluid velocity distributions are almost exactly axisymmetric. As the maximum extent of downstream protein polarisation is reached and free-convective flows begin to spread the protein downwards ( $t = 2$  h), nonlinear-dynamic mechanisms are set in motion which cause the system perturbation due to cartridge inclination to grow ( $t = 4$  h) and the axial symmetry to eventually disappear ( $t \approx 8$  h). A major convective flow loop recirculating clockwise becomes apparent ( $t \geq 8$  h), which henceforth maintains the protein distribution generally polarised in the direction of cartridge tilting, i.e., toward the right-hand-side wall in fig. 51. Numerous transient loops arise locally near regions of high upward concentration gradients (e.g., at  $t = 4$  h or  $t = 18$  h), forming confluence points with the major recirculation flow, and then disappearing along with those regions as the concentration distribution locally changes because of interloop protein transfer.

It is interesting to inspect some of the transients closer to steady state for this HFBR orientation (fig. 51,  $t \geq 54$  h). The protein and flow distributions shown for  $t = 54$  h (or, more exactly, those just preceding them) could almost be taken as steady-state ones, as the transient local flows seem to have practically died out and the results agree with intuitive expectations.<sup>37</sup> However, the upstream region of the ECS, or the bottom of the cartridge, is still prone to hydrodynamic instabilities, since that is where the strong downward flow must reverse its direction. It is conceivable that the upstream manifold may also contribute to flow perturbation, owing to the radial concentration gradient existing across the bundle-manifold

---

<sup>37</sup> The distributions between  $t \approx 32$  h and  $t \approx 50$  h appear more steady than those at  $t = 54$  h, but the latter case is shown to demonstrate the development of a new convective loop and hence indicate the direction of further changes.

boundary<sup>38</sup>, although instabilities similar to that developing at  $t = 54$  h were also observed in the simulations of a hypothetical cartridge without manifolds (see section 5.5.2.2). Whatever its origin, the result of the perturbation to the major recirculation flow is a small clockwise loop forming at the bottom end of the ECS, slightly away from the side wall and the upstream manifold (fig. 51,  $t = 54$  h). Within the subsequent 18 h or so, this minor loop stimulates its own growth by recirculating the protein towards the high-concentration zone, which increases the concentration gradient in the confluence region and hence enhances the local free-convective flow. The result is a growing split of the protein distribution into two distinct zones, each with its own concentration maximum ( $t = 72$  h). Interestingly enough, the newly formed convective loop now becomes dominant and grows in size, as the protein from the left-hand-side zone is gradually transferred towards the right-hand side wall ( $t = 132$  h). This leads to a distribution bearing a close resemblance to that of  $t = 54$  h, with a small convective loop forming again at the bottom of the ECS, except that the direction of flow in this minor loop is now reversed, i.e., anticlockwise. The reason for this difference is not clear, but it may be attributable to minor local changes in the concentration field near the upstream (bottom) manifold, on the right-hand side of the section shown in fig. 51. The subsequent upward growth of the new loop, by the same mechanism as before, leads eventually to the formation of a stable protein zone away from the wall ( $t = 144$  h), whereafter a steady state is quickly reached (at  $t = 155$  h, see fig. 48).

Owing to the imposed axial symmetry of the cartridge, the dynamics of the system at  $\Psi = 180^\circ$  (results not shown) are less complex than those in the off-vertical case discussed above. After the initial stage of downstream polarisation, strong free-convective flows begin to recirculate the protein downwards along the centreline and then upwards in the outer parts of the fibre bundle. The outward protein redistribution gives rise to a new, angular-independent (because of symmetry) convective loop, countercurrent to the existing ECS flow, which grows in size until all of the protein has been removed from the central core region. The resulting concentration and flow fields, with the protein accumulated near the wall and the fluid ascending in the centre, are stable and lead to steady state as soon as the equilibrium between the manifolds and the fibre bundle is reached ( $t = 28.4$  h). It can be

---

<sup>38</sup> The influence of the downstream (top) manifold on convective flow is negligible, because the concentration in the top half of the ECS generally increases in the downward direction.

noted that sideways-polarised transient concentration fields such as those at  $t = 54$  h or 132 h for  $\Psi = 179^\circ$  (fig. 51) cannot arise in an axisymmetric system ( $180^\circ$ ). Therefore, no mechanism existed in the latter case that would lead to a steady-state distribution similar to that for  $\Psi = 179^\circ$ , i.e., with the protein accumulated in the centre of the fibre bundle (cf. fig. 48). Such mechanisms did become active, however, when the  $180^\circ$  case was simulated assuming planar symmetry (i.e., as for nonvertical orientations); the steady-state results were then virtually identical to those plotted in fig. 48 for  $\Psi = 179.9^\circ$ .

In situations where a detailed analysis of transient three-dimensional flows and protein distributions is not necessary but, instead, a quick assessment of the ECS state at a given instant is needed, plots of the ECS protein heterogeneity index (*HetIx*) versus time can be a simple alternative to the velocity vector and concentration contour graphs shown in figs. 49-51. For example, examination of the temporal changes in *HetIx* for a growth-factor or product protein at a particular combination of operating conditions can provide some guidelines as to whether these conditions are suitable for application in HFBR cell culture. Figure 52 plots the temporal profiles of *HetIx* for selected cartridge orientations during the initial 30 h of the simulation. For clarity, since the curves for  $\Psi = 170^\circ$ ,  $179^\circ$ ,  $179.9^\circ$ , and  $180^\circ$  all look very similar, only one near-vertical case is depicted, namely  $\Psi = 179^\circ$ .

As can be seen, all of the curves in fig. 52 appear to level off within approximately 15 h, although steady state may, in some cases, not be attained until much later (see table 49). For the horizontal and downward-flow cartridges, the profiles rise monotonically and reach plateau values exceeding 0.7. As the cartridge orientation changes from horizontal towards vertical-up, damped oscillations of the curves become increasingly noticeable and the plateau values of *HetIx* decrease to less than 0.3. These oscillations reflect the alternating patterns of forced- and free-convective protein polarisation and redistribution taking place at higher inclination angles. Interestingly enough, between about 1 h and 5 h, the *HetIx* values at  $\Psi = 0^\circ$  and  $45^\circ$  temporarily fall below those for the other cartridge orientations, particularly the horizontal one. This can be mainly attributed to the less uniform cross-sectional distribution of the downstream-polarised protein at  $t < 5$  h for inclination angles near  $90^\circ$ .

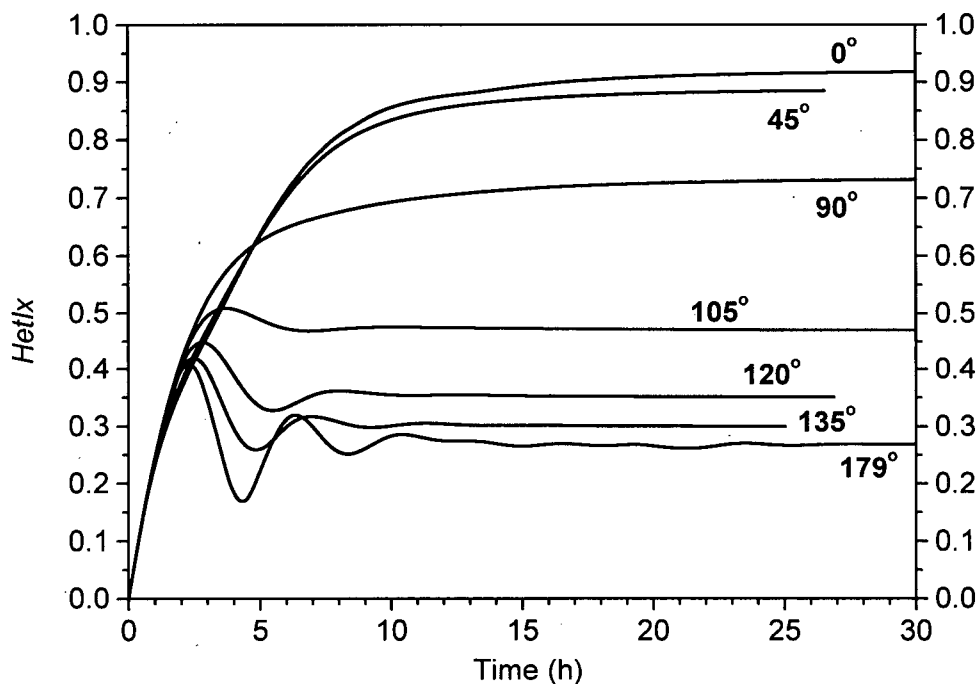


Fig. 52. Model-predicted temporal changes of the ECS protein heterogeneity index for different orientations of HFBR cartridge; uniform initial concentration field,  $C_0 = 5 \text{ g/L}$ ,  $Q_L = 600 \text{ mL/min}$ , other input parameters at their default values (see table 12).

#### 5.5.2.2. Effect of ECS Manifolds

To investigate the effect of ECS manifolds, two hypothetical HFBR cartridges were simulated for comparison with the normal case discussed so far: (1) a cartridge with no manifolds and (2) a cartridge with manifolds of twice the normal size. The imposed changes to the manifold volume had an effect on the convergence of model simulations to steady state; this was reflected, for example, in the altered shapes of the  $dCdtMax$  profiles versus time, compared with those plotted in fig. 46. From the point of view of protein distribution in a cell culture HFBR, the most important aspect of the manifolds' involvement, as predicted by the model, was their influence on the heterogeneity of the ECS concentration field and on the amount of protein present in the fibre bundle. Table 19 illustrates these effects by listing the changes in steady-state  $HetIx$  and  $C_{Bundle}$  due to the addition of manifolds to a hypothetical, manifold-free cartridge.

Table 19. Model-predicted effects of normal and double-size manifolds on the ECS protein heterogeneity index ( $HetI_x$ ) and on the average protein concentration in the fibre bundle ( $C_{Bundle}$ ) at steady state for different cartridge orientations;  $C_0 = 5$  g/L,  $Q_L = 600$  mL/min; the listed values represent changes relative to the case of a hypothetical cartridge with no ECS manifolds

Cartridge orientation	Change in steady-state $HetI_x$ due to ECS manifolds		Change in steady-state $C_{Bundle}$ due to ECS manifolds	
	Normal manifolds	Double-size manifolds	Normal manifolds	Double-size manifolds
0° (vertical down)	+0.076	+0.091	-53%	-64%
45° (inclined down)	+0.059	+0.075	-47%	-62%
90° (horizontal)	+0.036	+0.059	-17%	-28%
135° (inclined up)	-0.007	-0.011	+5%	+8%
179° (near-vertical up) †	-0.022	-0.033	+17%	+28%
180° (vertical up)	-0.004	-0.045	+6%	+20%

† Very similar effects are predicted for 179.9°.

By and large, the manifolds were responsible for increased  $HetI_x$  values and decreased  $C_{Bundle}$  values in horizontal and downward-flow cartridges, while opposite trends were observed for upward-flow cartridges (table 19). There appeared to be no proportional relationship between the magnitude of these effects and the change in manifold size, which can probably be explained by the fact that the surface area of the manifold-bundle boundary was the same in both cases where the manifolds were included. Since, for growth-factor proteins,  $HetI_x$  should ideally be low and  $C_{Bundle}$  high, the results in table 19 clearly suggest that high HFBR inclination angles,  $\Psi \geq 135^\circ$  or so, should be used in order to avoid the adverse effects of the manifolds. It may be recalled that a similar conclusion regarding the most suitable HFBR orientations was drawn based on the shapes of the  $HetI_x$  and  $C_{Bundle}$  profiles plotted versus  $\Psi$  in fig. 45b (section 5.5.2.1).

The trends revealed in table 19 can be understood better upon examination of the temporal changes of the average protein concentrations in the fibre bundle ( $C_{Bundle}$ ) and in the manifolds ( $C_{UpMan}$  and  $C_{DnMan}$ ), which are plotted for different HFBR orientations in figs.

53 and 54. Figure 53 focuses on the influence of manifold size on  $C_{Bundle}$ , while fig. 54 illustrates protein redistribution between the bundle and the manifolds during the first 24 h. In both figures, the manifold effects are depicted as deviations of the concentration profiles from the horizontal line  $C_S = C_0 = 5$  g/L, which corresponds to a manifold-free cartridge. In addition, steady-state values of  $C_{Bundle}$ ,  $C_{UpMan}$ , and  $C_{DnMan}$  for different orientations of a cartridge with normal-size manifolds have been listed in table 20.

Table 20. Average protein concentrations in the ECS fibre bundle ( $C_{Bundle}$ ), in the upstream manifold ( $C_{UpMan}$ ), and in the downstream manifold ( $C_{DnMan}$ ) for different cartridge orientations at steady state;  $C_0 = 5$  g/L,  $Q_L = 600$  mL/min, normal manifolds

Cartridge orientation	$C_{Bundle}$ (g/L)	$C_{UpMan}$ (g/L)	$C_{DnMan}$ (g/L)
0° (vertical down)	2.37	0.01	24.27
45° (inclined down)	2.65	0.04	22.74
90° (horizontal)	4.13	0.03	14.67
135° (inclined up)	5.26	2.76	5.82
179° (near-vertical up)	5.84	1.82	3.59
180° (vertical up)	5.29	2.41	6.01

As can be seen from fig. 53, the twofold increase in manifold size affected mainly the magnitude of the  $C_{Bundle}$  deviation from  $C_0$ , but not so much the shapes of the curves at each inclination angle. Most of the transient and steady-state protein distributions predicted for cartridges with double-size manifolds (results not shown) were also qualitatively similar to those for cartridges with normal manifolds, with the exception of the  $\Psi = 180^\circ$  case, where the protein at steady state was concentrated along the centreline rather than near the wall (cf. fig. 48). At all inclinations, as figs. 53 and 54 indicate, significant amounts of the protein were transferred within the first few hours into the downstream manifold as a result of downstream polarisation. Although a simultaneous release of the protein from the upstream manifold was taking place (fig. 54), the net effect was a decrease in  $C_{Bundle}$ . The subsequent changes in the bundle concentration depended on cartridge orientation. At  $\Psi = 0^\circ$  and  $45^\circ$ , the  $C_{Bundle}$  profiles continued to decline and then began to level off at  $t \approx 10$  h,

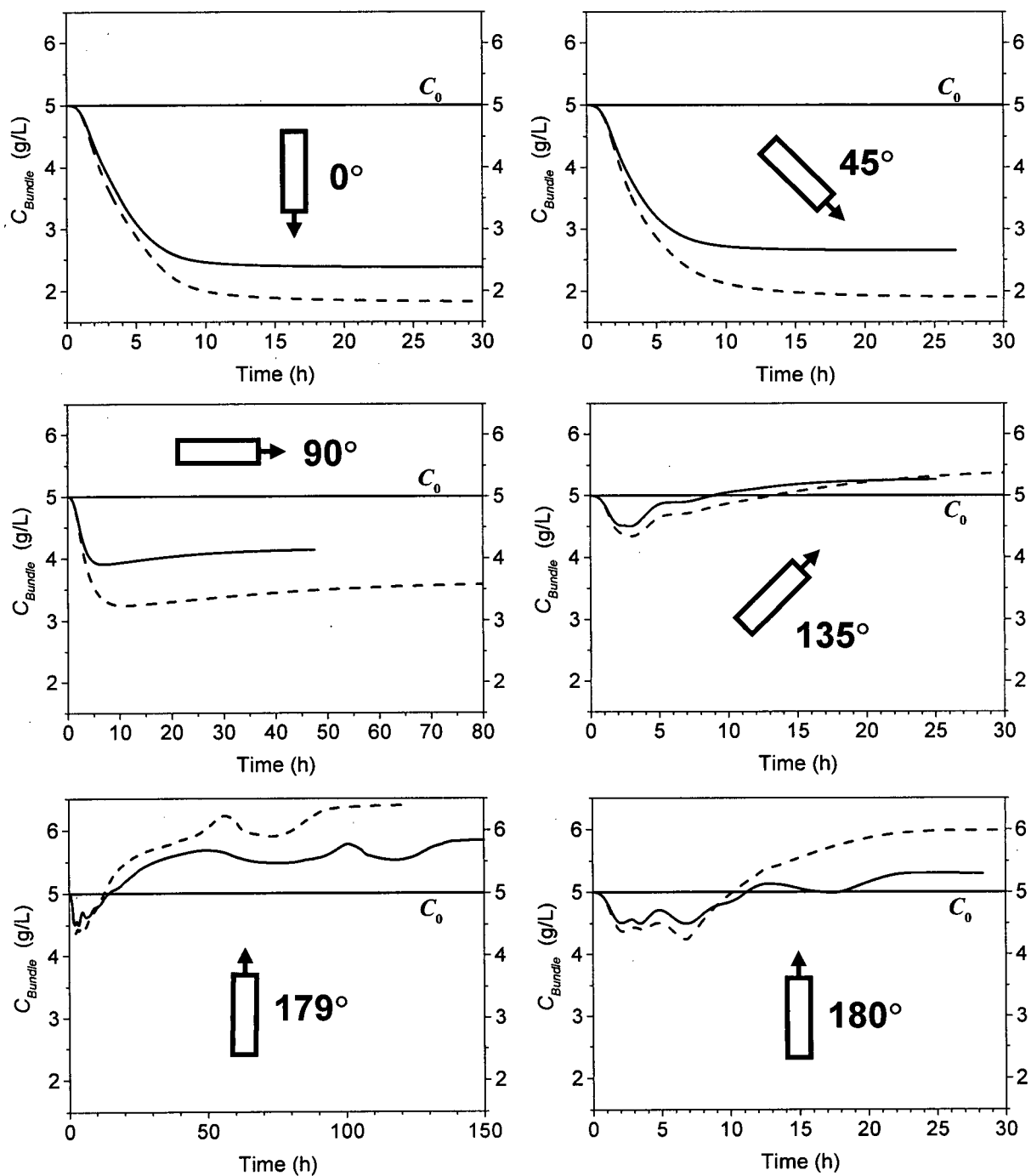


Fig. 53. Temporal changes of the average protein concentration in the ECS fibre bundle for cartridges with normal (solid lines) and double-size manifolds (dashed lines) at different HFBR orientations;  $C_0 = 5$  g/L,  $Q_L = 600$  mL/min.

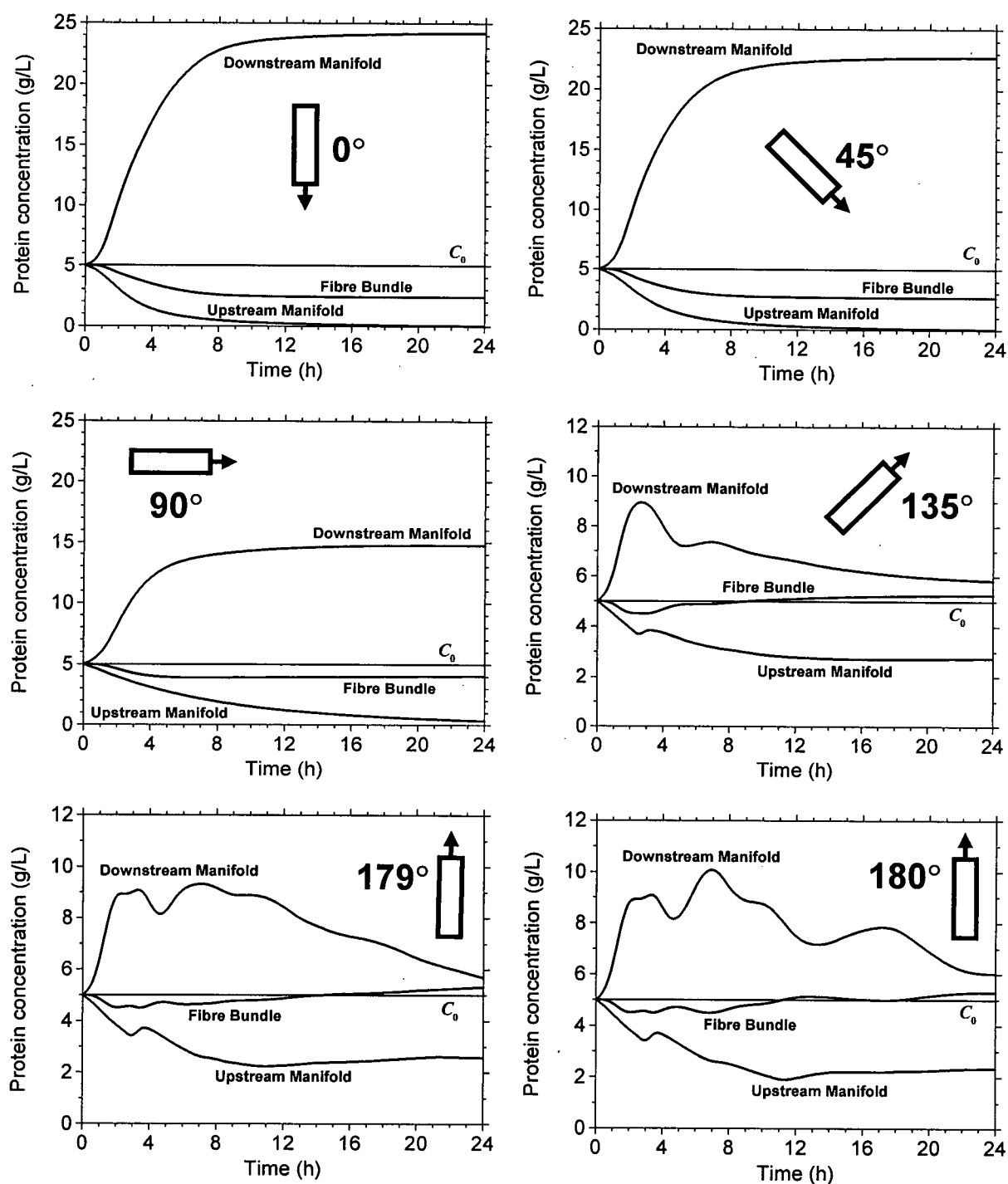


Fig. 54. Temporal changes of the average protein concentrations in the ECS fibre bundle and in the manifolds at different HFBR orientations (cartridge with normal-size manifolds);  $C_0 = 5$  g/L,  $Q_L = 600$  mL/min. Note that different concentration scales are used for  $\Psi \leq 90^\circ$  and for  $\Psi > 90^\circ$ .

reaching a value of about 2.5 g/L for normal manifolds and less than 2 g/L for double-size manifolds (fig. 53). This translates into about 50% or more of the protein being effectively trapped in the downstream manifold (table 19). In the horizontal case ( $\Psi = 90^\circ$ ),  $C_{Bundle}$  rose slightly after 10 h, reflecting a slow release of residual protein from the upstream manifold. Note that, according to the predictions, the cartridge orientation had a marked effect on the rate of this release process. For example, despite the fact that the ECS protein distributions at  $t = 6$  h for  $\Psi = 90^\circ$  and  $\Psi = 45^\circ$  were both already strongly polarised downstream, the average concentration in the normal-size upstream manifold at that time was still as high as 2.4 g/L for  $\Psi = 90^\circ$ , versus 1.0 g/L for  $\Psi = 45^\circ$  (fig. 54).

A noticeable difference between the manifold and bundle concentration profiles for  $\Psi \leq 90^\circ$  and for  $\Psi > 90^\circ$  is that they change monotonically in the former case, while displaying the presence of local extrema in the latter (fig. 54). This is because the distributions resulting from the initial stage of downstream polarisation at  $\Psi > 90^\circ$  are not stable, and the protein is shifted by natural convection back upstream, as was discussed in section 5.5.2.1 above. This is accompanied by protein release from the downstream manifold into the bundle, which causes an increase in  $C_{Bundle}$  (figs. 53 and 54). Since the magnitude of free-convective flows decreases as the protein is being spread more evenly throughout the ECS, there is no polarising mechanism that might lead to significant protein accumulation upstream. Consequently, the concentration in the upstream manifold never reaches the high levels observed for its downstream counterpart; in fact,  $C_{UpMan}$  is always (at  $t > 0$ ) lower than both  $C_{Bundle}$  and  $C_0$  for all HFBR orientations. On the other hand, the downstream manifold concentration remains above the  $C_{Bundle}$  level over the first 24 h (fig. 54) for all inclination angles, although it is predicted to be lower than  $C_{Bundle}$  and  $C_0$  at steady state for  $\Psi = 179^\circ$  (table 20).

It is interesting to compare the transient protein distributions in manifold-free versus normal cartridges (see section 5.5.2.1). The vertical and near-vertical upward-flow cases ( $\Psi = 180^\circ$  and  $179^\circ$ ) seem especially compelling, because of the highly nonlinear dynamics of the system at these HFBR orientations and a potential sensitivity of the simulation results to the presence of manifolds. An intriguing example of those nonlinearities is the protein and fluid flow behaviours at and after  $t \approx 66$  h and  $t \approx 144$  h in a manifold-free cartridge inclined at  $\Psi = 179^\circ$  (fig. 55). At either time, a virtually identical sideways-polarised concentration

field arises – very similar to that in a normal cartridge at  $t = 132$  h (fig. 51) – and a minor anticlockwise convective loop begins to grow near the bottom of the ECS. Yet at the earlier time, the growing loop detaches at some point from the right-hand-side wall (fig. 55,  $t = 78$  h), resulting in a longitudinal split of the concentration field, similar to that at 72 h in fig. 51; while in the other case, the new loop remains attached to the wall (fig. 55,  $t = 150$  h) and

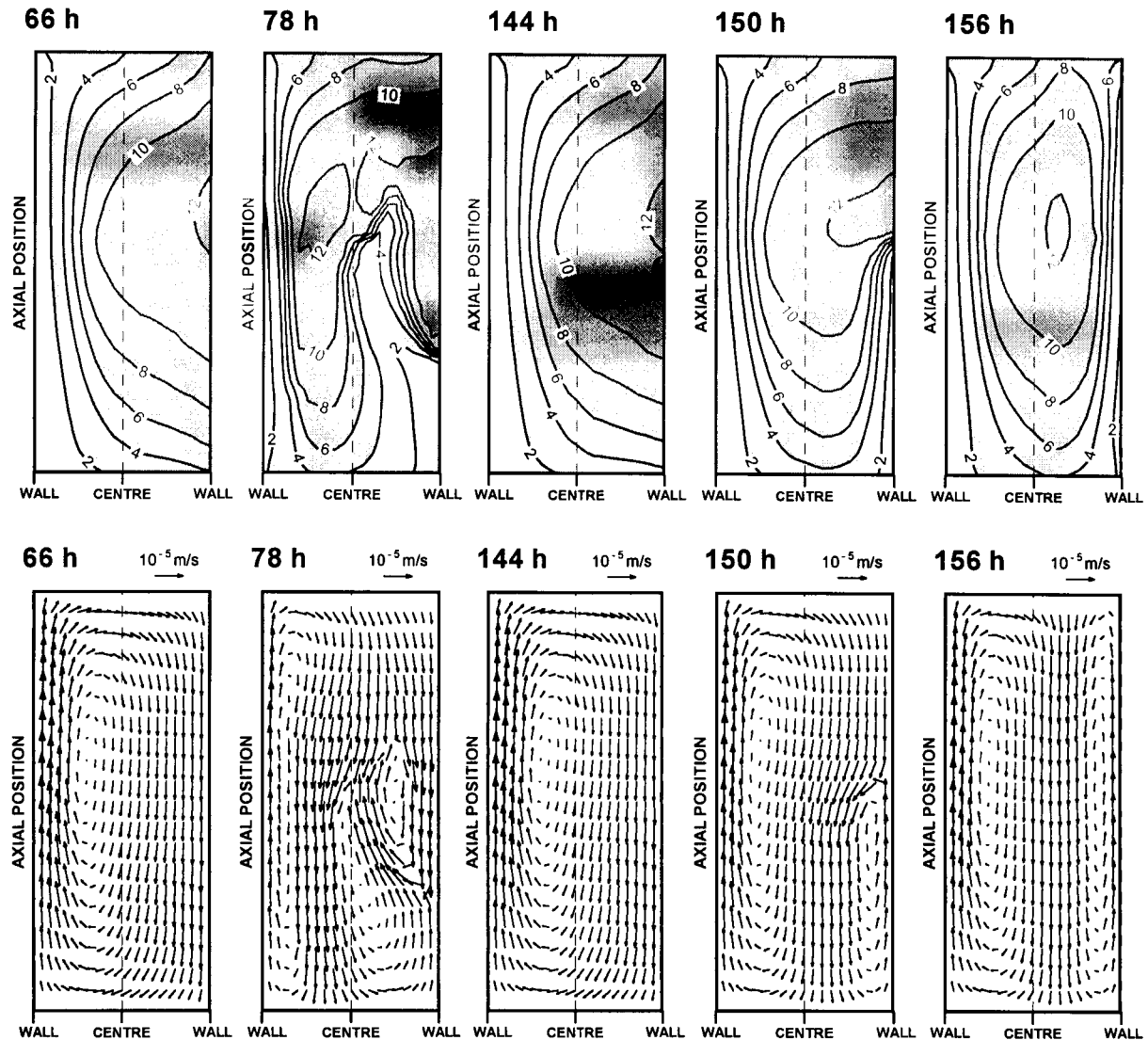


Fig. 55. Selected transients predicted for a hypothetical manifold-free cartridge at  $\Psi = 179^\circ$  (top inclined to the right). Upper panels: ECS protein concentration contours (g/L), lower panels: ECS superficial fluid velocity vectors. All plots are shown in the vertical section through the cartridge centreline (not to scale).  $C_0 = 5$  g/L,  $Q_L = 600$  mL/min (upward ICS flow).

reaches the top boundary of the ECS ( $t = 156$  h). This leads directly to a steady state (at  $t \approx 170$  h), characterised by ECS protein and flow distributions that are qualitatively the same as those in a normal cartridge (fig. 48,  $\Psi = 179^\circ$ ). It is not clear why two almost identical states, at 66 h and at 144 h, should give rise to completely different transients afterwards. Nonetheless, this example demonstrates how sensitive the system dynamics can be to subtle details of the ECS concentration and velocity fields at near-vertical orientations, especially in the absence of the perturbing influence of the manifolds.

At the vertical orientation ( $\Psi = 180^\circ$ ), the difference in the ECS dynamics for a normal and a manifold-free cartridge was even more dramatic. In the absence of manifolds, no radial (or angular) gradients were present at the outset, and the initial downstream polarisation process was essentially one-dimensional (fig. 56,  $t = 2.5$  h). It is hypothesised that the instability leading to downward protein redistribution did not develop until the numerical round-off errors were large enough, which occurred at  $t \approx 3$  h. The resulting radial gradients gave rise to disordered free-convective flows, which gradually became more regular as the protein was spread throughout the ECS (fig. 56,  $t = 4$  h and 8 h). In contrast, radial gradients existed right from the outset in a normal cartridge because of the bundle-manifold concentration differences. Hence, the instability developed about an hour earlier, i.e., at  $t \approx 2$  h, and the resulting convective flow patterns were much more orderly (see also fig. 51 – the distributions at 2 h are virtually identical for  $\Psi = 179^\circ$  and for  $\Psi = 180^\circ$ ). The manifold-free system reached steady state at  $t = 32.9$  h (fig. 56), revealing the existence in the ECS of a quadruple convective loop (in the section shown) and a protein distribution clearly different from that in a normal cartridge (cf. fig. 48,  $\Psi = 180^\circ$ ), although displaying a similar degree of heterogeneity ( $HetIx = 0.291$  versus 0.287 with manifolds).

As was just mentioned, the presence of ECS manifolds was found to shorten the time needed for the development of free-convective instabilities in vertical-upward cartridges. From a fundamental point of view, it might be of interest to characterise the onset of this phenomenon by means of a rigorous stability analysis. However, this is not a trivial task. Owing to the presence of forced-convective flow in the ECS and the influence of the manifolds, the analogy with a heat-transfer system such as a liquid-filled porous cylinder heated from below and the traditional definition of a related dimensionless parameter such as the Rayleigh number (e.g., Wooding 1959, Nield and Bejan 1992) do not apply to this

case. Further investigation of this issue has not been pursued within the scope of this thesis because of its limited significance to HFBR cell culture.

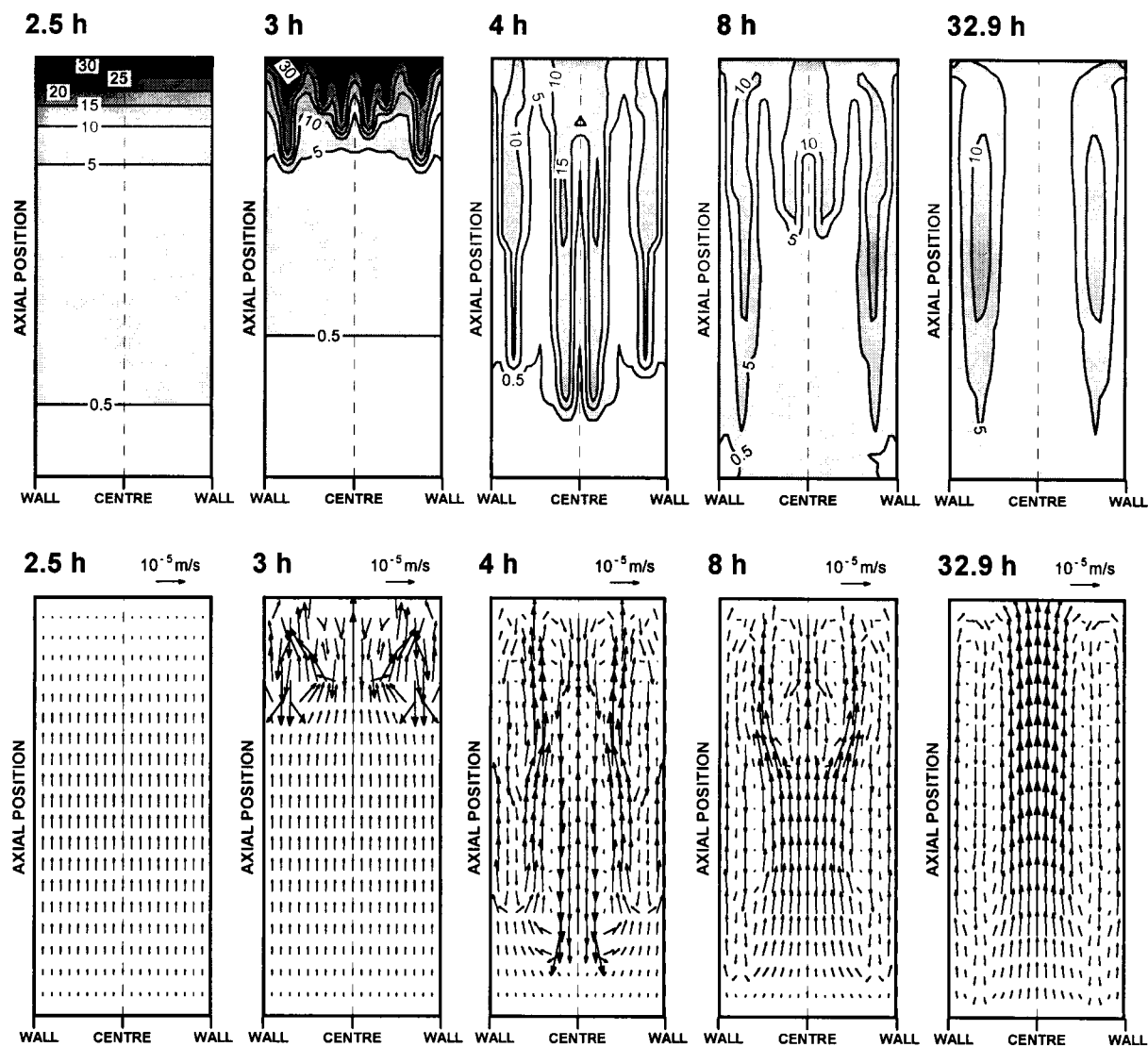


Fig. 56. Selected transients predicted for a hypothetical manifold-free cartridge at the vertical-upward orientation ( $\Psi = 180^\circ$ ). Upper panels: ECS protein concentration contours (g/L), lower panels: ECS superficial fluid velocity vectors. All plots are shown in the vertical section through the cartridge centreline (not to scale).  $C_0 = 5$  g/L,  $Q_L = 600$  mL/min;  $t = 32.9$  h marks the steady state for this case.

### 5.5.2.3. Effect of ICS Flow Rate

The choice of  $Q_L = 600$  mL/min as a default input for the model simulations was intended to accentuate the role of free convection in protein transport by producing a sufficiently strong Starling flow in the ECS. For the GFE-15 cartridge simulated here, this high  $Q_L$  value may still be acceptable for use in mammalian cell culture, although more typical ICS flow rates are about 200-300 mL/min. This section will briefly discuss the predicted effects of a decrease in  $Q_L$  from 600 mL/min to 200 mL/min.

The imposed change in  $Q_L$ , and hence in the magnitude of ECS forced-convective flow, did influence the convergence to steady state, although the effect was not simply – as might have been anticipated – a threefold increase in the time needed to reach steady state ( $t_{StSt}$ ). At  $\Psi = 0^\circ, 45^\circ$ , and  $179.9^\circ$ ,  $t_{StSt}$  was increased by a factor of two, whereas at  $\Psi = 90^\circ$  and  $135^\circ$ , the change in  $t_{StSt}$  was marginal ( $\pm 7\%$ ). At  $\Psi = 179^\circ$  and  $180^\circ$ , only periodic solutions were obtained, oscillating with respective frequencies of 0.0021 mHz and 0.0062 mHz (periods 132 h and 45 h, respectively). Recall from section 5.5.2.1 that a periodic solution (oscillation frequency 0.033 mHz) was also obtained at 600 mL/min for  $\Psi = 170^\circ$ .

Figure 57 illustrates the changes in protein distribution at  $179^\circ$  ( $Q_L = 200$  mL/min) over the duration of one oscillation cycle, i.e., 132 h. Some of the features displayed in this figure can be recognised as familiar from the examples discussed earlier for  $Q_L = 600$  mL/min (cf. figs. 51 and 55). Following the development of a sideways-polarised concentration field (fig. 57,  $t = 228$  h), an anticlockwise convective loop begins to grow upward from the upstream end of the ECS, with its top detaching from the right-hand-side wall within about 20-24 h ( $t = 252$  h). This causes a split in the concentration field and a corresponding change in the convective flow pattern ( $t = 312$  h). Eventually, the original distribution is restored ( $t = 360$  h). Had the growing flow loop remained attached to the wall, steady state would have likely resulted, with the protein accumulated near the centre of the ECS, as in fig. 51 at  $t = 144$  h. Note that, in contrast to the previously discussed periodic solution for  $\Psi = 170^\circ$  at 600 mL/min, as much as about half of the ECS protein is now involved in the oscillatory movement and the ECS hydrodynamics are much more complicated. Therefore, a detailed explanation of the mechanism of oscillations, or prediction of their frequency, is in the present case much more difficult. The most important

practical aspect of the results shown in fig. 57 is the continuing protein redistribution, which may benefit the cells cultivated in the ECS by virtue of periodic enrichment in growth factors of regions where their local concentration is below average.

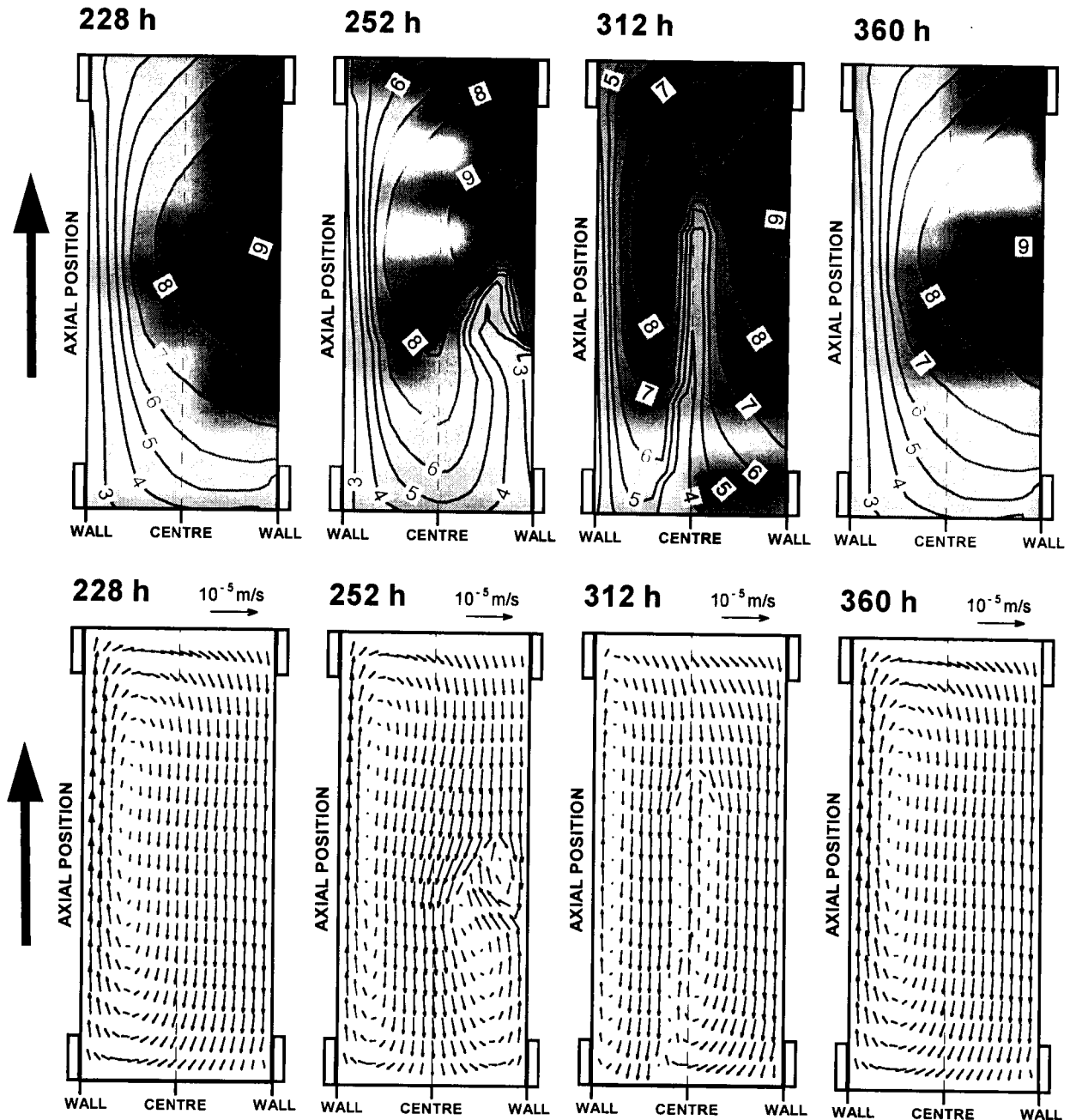


Fig. 57. Periodic protein redistribution over one oscillation cycle (132 h) in the vertical section through the cartridge centreline at  $\Psi = 179^\circ$ . Upper panels – ECS concentration contours (g/L), lower panels – ECS velocity vectors. Thick arrows on the left mark the direction of ICS flow.  $Q_L = 200$  mL/min,  $C_0 = 5$  g/L.

Figure 58 compares the steady-state ECS heterogeneity indices and protein concentrations in the fibre bundle at 600 mL/min and at 200 mL/min. For the two periodic solutions at the lower flow rate, mean values are plotted along with error bars signifying the amplitudes of oscillation ( $HetIx = 0.148 \pm 0.004$ ,  $C_{Bundle} = 5.33 \pm 0.11$  at  $179^\circ$ ;  $HetIx = 0.155 \pm 0.002$ ,  $C_{Bundle} = 4.97 \pm 0.03$  at  $180^\circ$ ). As can be seen from the figure, a decrease in  $Q_L$  has generally moderated both the degree of ECS protein heterogeneity and the deviations of the ECS bundle concentration from its initial level of  $C_0 = 5$  g/L. Although more uniform growth factor distributions are definitely desirable in cell culture, a side-effect for the upward-flow orientations ( $\Psi > 90^\circ$ ) is that some of the protein is shifted from the bundle to the manifolds, as is indicated by the decreased  $C_{Bundle}$  values (fig. 58). Nevertheless, the overall qualitative features of manifold involvement remain the same at both ICS flow rates; viz., the fibre bundle is depleted of protein for  $\Psi \leq 90^\circ$  and enriched with protein – albeit marginally at 200 mL/min – for  $\Psi > 90^\circ$ .

#### 5.5.2.4. *Effect of Initial ECS Protein Concentration*

As was demonstrated in the previous section, the heterogeneity of ECS protein distribution could be reduced by using a lower ICS flow rate. The same goal might also be achieved by loading the ECS with more protein, i.e., by increasing the initial ECS concentration ( $C_0$ ).<sup>39</sup> The  $C_0$  value of 5 g/L, used thus far, represented a realistic concentration level for a mammalian cell culture HFBR with serum-supplemented medium, and also enabled fairly clear manifestations of forced- and free-convective polarisation phenomena in the ECS. This section will briefly discuss two cases simulated using different  $C_0$  values (at  $Q_L = 600$  mL/min). In one case, the initial concentration was increased to 20 g/L, i.e., roughly to the upper limit of what can be reasonably expected to be valid for a typical ECS cell culture medium containing serum. In the other case,  $C_0$  was reduced to 1 g/L, which is more representative of protein concentrations in a serum-free media supplemented with growth factors.

---

<sup>39</sup> This is because there exists a maximum level of local protein accumulation, which is determined by the distributions of pressures on both sides of the membrane. Addition of more protein into the ECS will not cause the concentration to increase above that level, but rather will cause the protein to spread over a larger part of the HFBR.

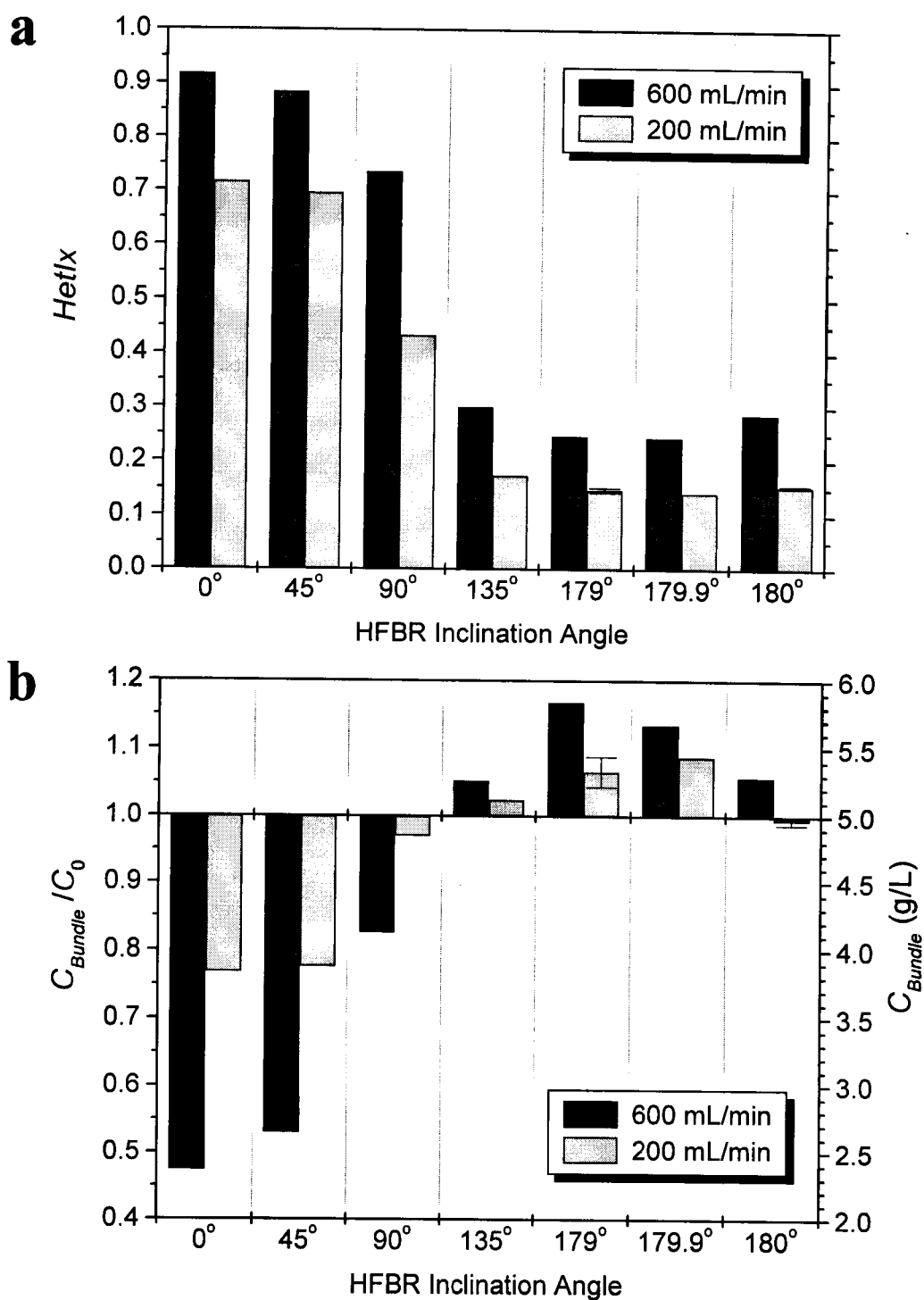


Fig. 58. Effects of ICS flow rate on the protein heterogeneity index (a) and on the protein concentration in the fibre bundle (b) at steady state for different HFBR orientations. No steady-state solutions were obtained at 179° and 180°; error bars signify the oscillation amplitudes for the periodic solutions in these two cases.

The increase in  $C_0$  from 5 g/L to 20 g/L extended up to 40% the time to steady state ( $t_{SS}$ ) for downward-flow cartridges ( $\Psi < 90^\circ$ ), while shortening it about twice for the horizontal and upward-flow cartridges ( $\Psi \geq 90^\circ$ ). Interestingly, a similar pattern of  $t_{SS}$  changes was also observed when  $C_0$  was reduced from 5 g/L to 1 g/L. An exception was the vertical-up orientation ( $\Psi = 180^\circ$ ), for which  $t_{SS}$  was slightly increased at  $C_0 = 1$  g/L, while no steady state was attained at  $C_0 = 20$  g/L (solution oscillating at frequency 0.022 mHz, period 12.5 h). In the latter case, however, unlike in the example of a periodic solution discussed in the previous section ( $\Psi = 179^\circ$ ,  $Q_L = 200$  mL/min,  $C_0 = 5$  g/L), the changes in the oscillating concentration field were barely noticeable.

The effects of the simulated changes in  $C_0$  on the protein distribution heterogeneity and the average protein concentration in the fibre bundle at steady state are illustrated in fig. 59. The error bars shown for  $\Psi = 180^\circ$  at  $C_0 = 20$  g/L quantitate the oscillation amplitudes for  $HetIx$  and  $C_{Bundle}$ . As can be seen, the fourfold elevation of  $C_0$  has caused about a twofold decrease in  $HetIx$  at all inclination angles (fig. 59a). Similarly, the heterogeneity index was approximately doubled as a result of fivefold  $C_0$  reduction to 1 g/L, but only for upward-flow orientations. At  $\Psi \leq 90^\circ$ , the increases in the steady-state  $HetIx$  were much less pronounced, since the index at  $C_0 = 5$  g/L for these orientations was already close to its saturation level (i.e., close to 1). At  $C_0 = 1$  g/L, the predicted steady-state  $HetIx$  values remained above 0.5 even at the highest inclination angles.

As can be seen from fig. 59b, the deviation of  $C_{Bundle}$  from  $C_0$  has been reduced to less than 8% at the highest protein loading (20 g/L), which clearly indicates a diminished involvement of the ECS manifolds. Conversely, a significant impact of the manifolds is evident from the  $C_{Bundle}$  results for  $C_0 = 1$  g/L. In this case, the model has predicted that the bundle will be enriched with protein (released from the manifolds) by more than 30% at  $\Psi \approx 180^\circ$  and will be depleted of protein by more than 50% at  $\Psi \leq 90^\circ$ . At  $\Psi = 135^\circ$ , the steady-state  $C_{Bundle}/C_0$  ratio is almost unaffected by the initial protein concentration and remains close to 1. The somewhat unexpected decline in  $C_{Bundle}$  with  $\Psi$  increasing from  $0^\circ$  to  $45^\circ$  at  $C_0 = 1$  g/L can be attributed to the more favourable conditions of protein transfer from the bundle to the downstream manifold at an inclined rather than vertical orientation. Such an

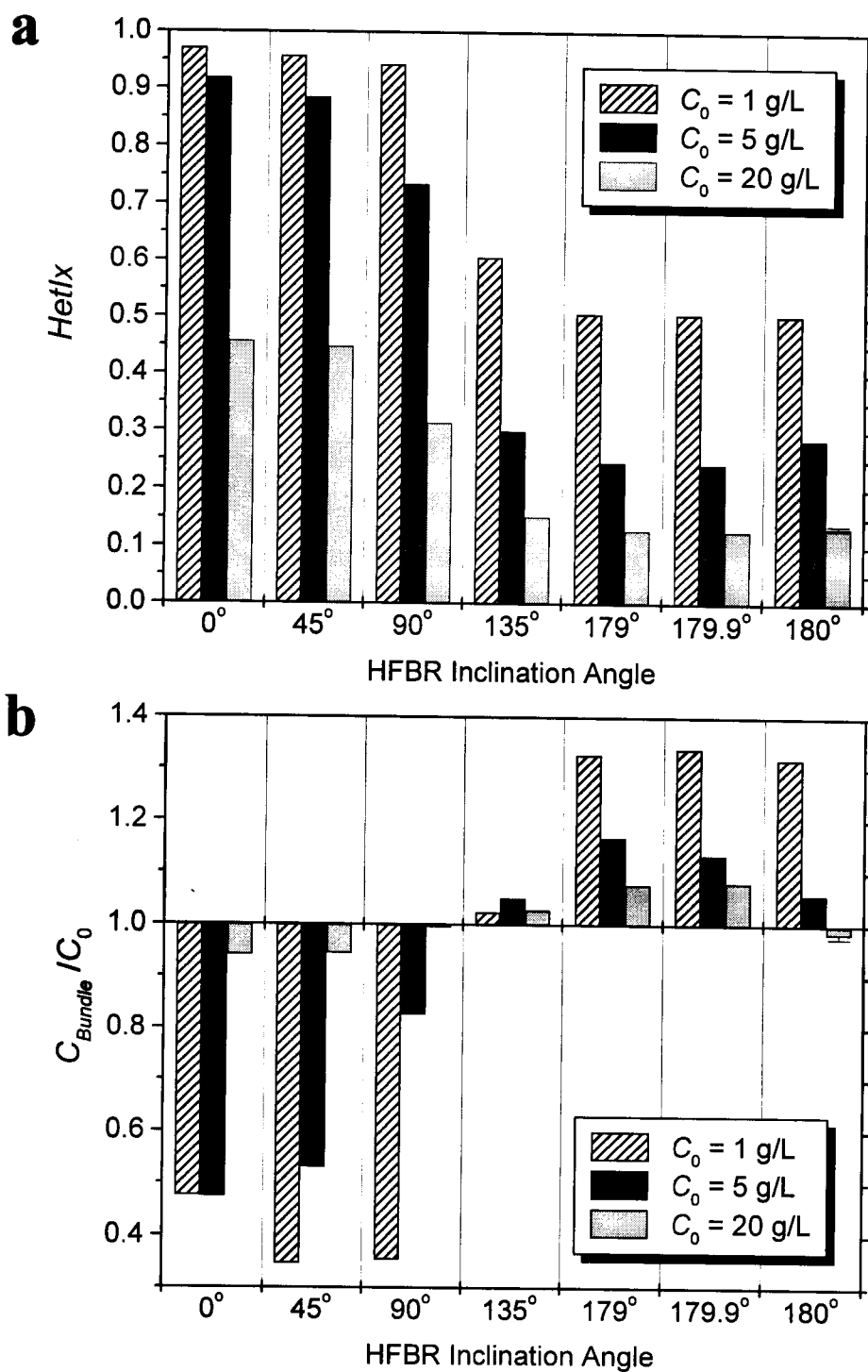


Fig. 59. Effects of the initial ECS protein concentration on the heterogeneity index (a) and the concentration in the fibre bundle (b) at steady state for different HFBR orientations ( $Q_L = 600 \text{ mL/min}$ ). Error bars signify the oscillation amplitudes of a periodic solution obtained for  $180^\circ$  at  $C_0 = 20 \text{ g/L}$ .

anomaly, opposing the trend predicted for the higher protein loadings, could only be observed at sufficiently low ECS protein contents for the given volume of the manifold.<sup>40</sup>

As expected, the trends of the *HetIx* and  $C_{Bundle}$  changes with an increase in  $C_0$  are qualitatively the same as those resulting from a reduction in  $Q_L$  (cf. figs. 58 and 59). Quantitatively, the strongest dependence of *HetIx* on  $\Psi$  was predicted for the moderate protein loading (5 g/L), while the weakest dependence on  $\Psi$ , both for *HetIx* and for  $C_{Bundle}$ , was predicted to exist at the highest  $C_0$  level (20 g/L). The above results suggest that the heterogeneity of growth factor distribution in cell culture HFBRs at a given inclination angle may perhaps be more conveniently and effectively controlled through an increase in the ECS protein content (e.g., by adding an inexpensive medium protein such as BSA) rather than through manipulation of the ICS flow rate, especially since the latter parameter also determines the rate of oxygen supply to the bioreactor. However, the consequences of the protein addition with respect to the efficiency of downstream product separation would have to be considered before such a measure is implemented in cell culture.

## 5.6. Conclusions

The study described in this chapter was concerned with the dynamics of ECS protein transport and fluid flow in closed-shell HFBRs under the influence of gravity. A three-dimensional porous medium model has been developed, which accounts for spatial and temporal variations of osmotic pressure, fluid density, and fluid viscosity with protein concentration, as well as including the effect of protein exchange between the fibre bundle and the fibre-free ECS manifolds. The model was qualitatively validated by comparing the predicted two-dimensional protein concentration fields in the vertical section through the

---

<sup>40</sup> Assuming that the concentration in the protein-rich zone after a sufficiently long time of downstream polarisation is approximately the same for both orientations (and equal to its maximum value determined by the distributions of hydrostatic pressure on both sides of the membrane), the volume of the zone should also be similar in both cases. Geometric considerations show that the lateral area of a truncated portion of cylinder, which is the shape of the protein-rich zone (within the fibre bundle) in an inclined cartridge, is greater than the lateral area of a plain cylinder having the same volume, which is the shape of the zone in the vertical case. Thus, the surface area for bundle-manifold protein exchange, and hence also the portion of the manifold volume available to the protein at steady state (according to the manifold adjustment scheme used here), is expected to be larger at  $\Psi = 45^\circ$  than at  $\Psi = 0^\circ$ . This conclusion should be valid as long as the protein zone does not extend beyond the length of the downstream manifold, i.e., at sufficiently low ECS protein loadings and for sufficiently large manifolds (note also that the volume of the zone decreases with time until steady state because of protein transfer from the bundle into the manifold).

cartridge centreline with the experimentally observed distributions of azoalbumin as a test protein. The reasonable agreement between these two sets of results at several HFBR orientations suggest that the protein distribution in the selected longitudinal section was fairly representative of the thickness-averaged distribution observed via a side view of the cartridge. Quantitative validation of the model proved more difficult because of the limitations of the available techniques for protein analysis, which compromised the ability to determine the transient 3-D protein distributions during each experiment. In addition, the comparisons between the predicted and experimental data were obscured by the complex influences of the ECS manifolds and of various random factors, such as the nonuniformity of fibre packing, existing in real HFBR cartridges. Sufficiently accurate model simulations were obtained by neglecting the viscosity gradients and by assuming a simplified, homogeneous form of the fluid continuity equation for the ECS.

The ECS fluid density gradients associated with the existence of nonuniform concentration fields can give rise to free-convective protein redistribution. A number of model simulations were performed to investigate in detail the mechanisms of this phenomenon at various operating conditions, with a particular emphasis on understanding the effect of the cartridge inclination angle and the role of ECS manifolds. For certain combinations of input parameters, periodic rather than steady-state solutions were obtained. A thorough investigation of their origin and dynamic properties, however, is beyond the scope of this thesis.

The extent and magnitude of free convection in the ECS depends most dramatically on the angle between the direction of bulk ICS flow and the direction of gravitational force ( $\Psi$ ). In horizontal and downward-flow cartridges ( $\Psi \leq 90^\circ$ ), natural-convective flows are limited in scope, and fairly nonuniform protein distributions prevail at steady state, with most of the ECS clear of protein. This indicates a potential limitation to cell growth, owing to the high degree of heterogeneity of the ECS culture environment. In inclined and vertical cartridges with upward ICS flow ( $\Psi > 90^\circ$ ), on the other hand, free-convective protein recirculation usually extends over the entire ECS volume, thus providing much more favourable conditions for cell growth. In particular, the vigorous free-convective flows at  $\Psi \approx 180^\circ$  represent a very effective mechanism of mixing the ECS contents, which suggests that the vertical-up orientation may be a promising configuration for use in HFBR cell

culture. Additional studies will be required to verify the feasibility of this proposition by considering the combined effects of natural convection and sedimentation on the distribution of cells in the ECS.

According to the model predictions, the heterogeneity of ECS protein distribution should increase as a result of the ECS manifolds' influence in horizontal and downward-flow cartridges, while a reduced protein heterogeneity can be expected in upward-flow cartridges. The manifolds were predicted to accelerate the development of free-convective instabilities and to stimulate the formation of transient local flows, particularly in vertical cartridges with upward ICS flow. In addition, the average steady-state protein concentration in the fibre bundle was found to decrease below its initial level for  $\Psi \leq 90^\circ$  and increase above its initial level for  $\Psi > 90^\circ$ , owing to the ECS manifolds. These results can have important implications for HFBR cell culture, since the accumulation of medium proteins within the manifold spaces will limit their availability to the cells cultivated in the ECS fibre bundle. In particular, the choice of upward-flow bioreactor orientations may be critical in minimising the manifold entrapment of low-concentration ( $C_0 < 1$  g/L) growth factors if serum-free media are used. Lower ICS flow rates and higher ECS protein loadings were both found to moderate the influence of the manifolds and to reduce the heterogeneity of protein distribution. All of these effects should be carefully considered in the planning of HFBR operation strategies.

## Chapter 6

### OVERALL CONCLUSIONS AND RECOMMENDATIONS

#### 6.1. Conclusions

The establishment of uniform cell growth conditions in hollow-fibre bioreactors for mammalian cell culture is an important factor in their successful operation. Earlier studies (Piret and Cooney 1990b) demonstrated that the distribution of cells in the ECS approximately followed the distribution of growth-factor proteins, although an exact correlation between these two was difficult to determine and quantify. Nonetheless, knowledge of ECS protein transport and redistribution, investigated here both experimentally and theoretically for a variety of flow configurations and operating conditions, may serve to indicate where the ECS cells will proliferate, at least during the early stages of bioreactor operation (i.e., at low cell densities in the ECS). An analysis of protein behaviour in the HFBR could also facilitate identification of critical factors and conditions that may lead to cell culture failure, an all too common feature of HFBR startup. In addition, some of the present results should be helpful in designing optimal strategies for harvesting the useful product proteins from the bioreactor.

The theoretical part of this project comprised the development of several mathematical models which can be used as simulation tools for the analysis of different aspects of protein transport in HFBRs. Each of the models was, to the best of the available laboratory resources and within the given time constraints, tested and validated against protein concentration data collected from a corresponding series of hollow-fibre protein transport experiments. The model of transmembrane protein leakage in closed-shell HFBRs (chapter 3) was based on a one-dimensional Krogh cylinder approximation, modified to include the effects of ECS manifolds and wet fibre expansion. Selected open-shell HFBR operations such as inoculation, harvesting, and ECS shunting (chapter 4) were studied using

a two-dimensional porous medium model (PMM) that had been developed earlier (Oabcki 1994). The most demanding modelling endeavour was associated with the analysis of forced- and free-convective ECS protein transport under the influence of gravity. This task required inclusion of body force terms with a concentration-dependent fluid density in the PMM equations, extension of the model to three spatial dimensions, a more advanced treatment of the ECS manifold effects, and development of a more sophisticated numerical approach.

The 1-D leakage model presented in chapter 3 was based on the use of a single adjustable parameter, the membrane constant ( $k_m$ ), whose value was estimated by forcing the model predictions to fit the experimental ICS protein concentration data. The inclusion of ECS manifolds, modelled in a simplified manner as fibre-free spaces accessible to the protein solution, turned out to be particularly important from the point of view of matching the experimental and predicted results. The proposed model provided good quantitative descriptions of ICS, ECS, and transmembrane protein transport in closed-shell cell-free hollow-fibre cartridges operated vertically with downward ICS flow to minimise the free-convection effects. The redistribution of a leaking protein on both sides of the hollow-fibre membranes was found to be a complex process dependent primarily on the ICS flow rate, the involvement of ECS manifolds, the presence of a nonleaking protein in the ECS, the membrane pretreatment procedure, the experiment duration, and the addition of a surfactant.

The transmembrane protein transport studied here is most relevant to the leakage of growth-factor proteins from the ECS of HFBRs. Such losses not only lead to the dilution of expensive ECS media proteins in the large ICS recycle volume, but may also pose a severe limitation to cell growth in the bioreactor. The results of this study indicate that, at the high ICS flow rates typically used in HFBR cell culture, the ECS protein distributions can be highly heterogeneous, even for proteins that can pass readily through the membrane. However, the distributions of smaller proteins can be rendered more uniform by the addition of a nonleaking solute to the ECS, which – by supplementing the ECS osmotic pressure – can modify the magnitude and pattern of transmembrane flow. It should be noted that other phenomena that are not included in the present leakage model, such as gravity-induced free convection, are likely to influence the rates of transmembrane protein passage in nonvertical

or upward-flow HFBR cartridges. These effects may need further research, possibly in conjunction with investigations making use of the 3-D PMM described in chapter 5.

The results of simulations using the 2-D PMM (chapter 4) show that, regardless of the initial protein distribution, cocurrent harvesting should be more efficient than countercurrent harvesting. An external ECS shunt, in which the medium is recirculated at a low flow rate countercurrently to the ICS flow, has the potential of neutralising the polarising effects of ECS Starling flow. This suggests that, with proper optimisation, the shunt may be an effective means of controlling the heterogeneity of ECS protein and cell distributions in HFBRs. A slight modification of the shunt system, e.g., by changing the cartridge orientation angle and using cocurrent flow, or by adding an external ECS reservoir (similar to the Acusyst expansion chamber (Gramer et al. 1999)) for enhanced removal of dead cells and cell debris, might also benefit the HFBR performance in this configuration. The feasibility of the ESC shunt as an alternative to closed-shell HFBR operation requires more testing on an experimental cell culture system.

The 2-D PMM simulations of a series of dead-end inoculation experiments (chapter 4) yielded results that reproduced well the measured radial variations of ECS protein concentration. The observed angular concentration variations were mostly random and likely related to nonuniform fibre packing. The model-predicted axial protein concentrations (averaged both radially and angularly) were in best agreement with experimental data when the ICS flow was directed upward and the number of fluid volumes displaced from the ECS,  $N_V$ , was less than or approximately equal to 1. In this case, the extent of ECS penetration by the incoming protein solution was too small for the downstream ECS manifold to absorb any of the protein and for axial concentration gradients to become significant. At the same flow orientation but with greater  $N_V$  ( $\approx 4-5$ ), the concentrated protein solution reached the downstream manifold and substantial upward concentration gradients developed in the ECS. The resulting buoyancy or free-convection effects slowed the upward protein movement, leading to discrepancies between the measured and predicted data. In a similar experiment with downward ICS flow, the free-convection influence was greatly reduced and the agreement between the predicted and experimental protein distributions at the end of the inoculation period was markedly improved.

The above results demonstrate that the neglect of gravitational effects represents a significant limitation in both the 1-D leakage model and the 2-D PMM. Thus, the subsequent modelling efforts aimed at the development of a more general simulation tool that would combine the features of the two earlier models with the ability to realistically describe the HFBR protein transport and hydrodynamics at various cartridge orientations. The formulation of the 3-D PMM for closed-shell HFBRs (chapter 5) was the first step in accomplishing this task (the next two obvious steps, i.e., the extensions of the 3-D PMM to include transmembrane protein transport and open-shell operations, were not undertaken within the scope of this thesis). The model was validated qualitatively, although the comparisons of its predictions with experimental results were complicated by a lack of analytical methods for obtaining the 3-D ECS protein distribution data in a noninvasive manner, as well as by influences of interfering factors such as the protein accumulation in the fibre-free ECS manifolds and the nonuniformity of fibre packing. The difficulty of quantifying this last effect, for example, justified the neglect in the model of transport phenomena such as hydrodynamic dispersion, whose existence may need to be acknowledged in future mathematical formulations if a more realistic representation of protein behaviour in HFBRs is to be obtained. The neglect of concentration-dependent viscosity gradients in the PMM equations or the use of a homogeneous form of the fluid continuity equation for the ECS did not compromise the accuracy of the predicted results.

The parameter that most dramatically influenced the ECS convective flow and protein transport was the cartridge inclination angle, i.e., the angle between the directions of bulk ICS flow and the gravity vector. Drastically different ECS protein distributions and flow patterns were predicted to exist in horizontal and downward-flow cartridges on the one hand, and in upward-flow cartridges on the other. This can be attributed to the different scales and magnitudes of gravity-induced free-convection, which was most effective in redistributing the ECS proteins when the ICS recirculation flow was directed upward. The most homogeneous ECS protein distributions were predicted for the vertical-up (or near-vertical-up) orientation, which suggests that this flow configuration – owing to its potential for supporting a uniform growth environment – may be of interest in HFBR cell culture. Whether this expectation is justified remains to be verified experimentally. Future modelling studies relevant to this issue may consider the combined influences of free convection and

sedimentation on the cell distribution in the ECS, as well as possible effects of the cells on the ECS hydrodynamics.

An important aspect of the HFBR studies conducted here was the analysis of the ECS manifold involvement in the protein redistribution process. In cell culture HFBRs, entrapment of growth-factor proteins within fibre-free spaces such as the manifolds limits their availability to the cells, thus increasing the cost of bioreactor operation and a risk of culture failure. In order to remain viable, the cells must be in close proximity to the oxygen source, i.e., to the hollow fibres, which excludes the possibility of their cultivation in fibre-free regions. The results of 3-D PMM simulations indicate that an upward ICS flow could be used in order to minimise the adverse effects of the manifolds. According to the predictions, an addition of ECS manifolds to a hypothetical manifold-free cartridge would increase the heterogeneity of protein distributions in horizontal and downward-flow HFBRs, while more homogeneous distributions would result from the manifold addition for upward-flow orientations. Furthermore, the average protein concentration in the fibre bundle was predicted to increase above its initial level, as a consequence of protein release from the manifolds, when the ICS flow was directed upward. In the horizontal and downward-flow cases, on the other hand, the fibre bundle was found to be significantly depleted as a result of protein transfer to the downstream manifold. This effect was most pronounced at low ECS protein loadings which are typical of growth factor levels encountered in serum-free culture media.

From the point of view of maximising the harvesting efficiency, accumulation of the protein in the downstream manifold near the outlet ECS port may be used to increase the product concentration in the harvest. The presence of fibre-free spaces can also be used to the benefit of the culture if the manifolds absorb any inhibitory proteins or proteases that may be released by the cells. Sometimes, the useful product itself may be inhibitory (e.g., tissue plasminogen activator secreted by CHO cells investigated by Dowd et al. (2000)), in which case its transfer from the bundle to the manifolds in a hollow-fibre culture might be particularly desired. The potential advantages of the manifolds, however, should be carefully weighed against the downside associated with the entrapment of cells and growth factors. If the manifolds are too large, for example, then the concentration of viable cells introduced

into the ECS may be significantly reduced, thereby jeopardising the success of culture startup.

According to the PMM simulation results, the intensity and complexity of natural-convective phenomena in the ECS should increase with the HFBR inclination angle. The predicted protein and fluid flow distributions became particularly sensitive to variation in system parameters as the cartridge inclination approached the vertical with an upward ICS flow. At this orientation, the perturbing influence of the manifolds on ECS flow became evident. For example, the onset of free-convective protein redistribution in a hypothetical manifold-free cartridge was significantly delayed, relative to that in a normal cartridge. For upward-flow HFBRs inclined at  $10^\circ$  or less from the vertical, certain combinations of input parameters yielded periodic rather than steady-state solutions. A possible mechanism was hypothesised to explain the oscillations of the ECS protein concentration and fluid velocity fields in one of those cases. However, a more in-depth investigation of the origin and dynamic properties of these periodic solutions exceeds the scope of the present work.

## 6.2. Recommendations

As a continuation of the studies described in this thesis, several future research projects related to hollow-fibre bioreactors can be suggested. For instance, the following directions of HFBR modelling work might be pursued:

- 1) *Development of a higher-level HFBR simulation tool able to realistically describe protein transport for a broader variety of operating conditions.* The resulting “supermodel” should include open-shell operations, leakage of proteins across the membrane, as well as gravitational effects and free convection. The 3-D open-shell extension might be implemented by using the Navier-Stokes and Brinkman equations to describe the hydrodynamics in the ECS manifolds and fibre bundle, respectively, although some drastic simplifications may be required to reduce the complexity of the resulting formulation (due to the presence of shear stress terms and the necessity to iterate the velocity and pressure fields). Ideally, the new model should also include hydrodynamic dispersion of ECS proteins, provided a reliable method is in place for estimating the ECS dispersion coefficients (e.g., by using NMR image analysis). In addition, the presence of

cells might indirectly be taken into account by considering temporal changes in the fluid and mass transport conditions due to the increase in cell mass, as well as by including the kinetics of protein production or consumption by the cells. A more general model formulation valid for both isotropic and asymmetric membranes might also be of interest.

- 2) *Development of a 3-D model of transport and growth of cells in HFBRs.* This model might ultimately be combined with the protein transport simulator mentioned above. The cells could be modelled, in a first approximation, as rigid spherical particles redistributing by forced convection, free convection, and sedimentation. Their spatial distribution and growth could be assumed to depend on the availability and local concentrations not only of growth-factor proteins, but also of nutrients and oxygen. The distributions of small solutes in the bioreactor should be possible to model without any additional difficulties, because of the dominant role of diffusive transport in this case.

Formulation of any realistic HFBR model will not be complete without experimental validation. This suggests a need for the following project:

- 3) *Implementation of a robust experimental technique for the analysis of 3-D distributions of (a) proteins and (b) cells in the ECS of HFBRs.* The method should be noninvasive to enable the collection of transient data. The most promising analytical technique for this purpose seems to be NMR spectroscopy (Mancusco et al. 1990, Williams et al. 1997, Gramer et al. 1999).

Examples of projects that could balance the experimental and theoretical aspects of HFBR research, while not necessarily involving cell cultivation, are:

- 4) *Optimisation of the inoculation procedure.* The initial distributions of cells and media proteins in the ECS are often far from uniform and can be influenced by random factors such as flow channelling due to fibre maldistribution in the HFBR cartridge. The aim of this study would be to minimise these random effects by finding a flow configuration and operating conditions which would ensure that the inoculum is most uniformly distributed throughout the fibre bundle and that the cells do not accumulate excessively in the ECS manifolds (studies by Gramer et al. (1999) suggest that uniform cell distributions are optimal for a productive long-term HFBR operation).
- 5) *Optimisation of the harvesting strategy.* The most promising harvesting protocols predicted by model simulations could be verified and screened experimentally in a series

of interactive modelling and laboratory studies. The factors varied during the harvest optimisation procedure might include the configuration of open ports, the ECS and ICS flow rates, the harvested fluid volume, harvesting mode (batch versus continuous) and frequency (batch), changes to the ICS flow rate and/or the cartridge inclination angle prior to harvesting, the value of hydrostatic pressure head at each of the open ports, etc.

The recommended future work involving HFBR cell culture includes:

- 6) *Verification of the feasibility of the vertical-up HFBR orientation as an alternative to the inclined-up orientation.* Ideally, two bioreactors inclined at different angles could be run in parallel under otherwise identical operating conditions. Even better, the same experiment should be repeated to minimise the possible influence of random factors.
- 7) *Verification of the feasibility of an external ECS shunt as an alternative to the closed-shell HFBR operation.* Similarly as above, it would be ideal to conduct a duplicate experiment using two parallel HFBR systems, one with and one without the shunt. The shunt flow rate and the cartridge inclination angle should be optimised for the best system performance. A small reservoir could be installed within the external ECS loop for more effective removal of dead cells and better control of ECS culture conditions. The harvesting protocol will require considerable modification in the shunt configuration.

It seems generally advisable that any future research strategies devote an increasing amount of attention to bridging of the gap between modelling and laboratory endeavours. New simulation tools should be devised in such a way that they can be applied directly and straightforwardly by cell culture experimenters. In some cases, this might mean sacrifices of scientific rigour or fulfilment of research curiosity for the sake of simplicity and applicability to practical problems encountered during HFBR operation. On the other hand, the qualitative and quantitative information gathered during cell culture runs should be utilised to the best possible extent for the validation and improvement of the models. The experimenters, in turn, should realise that the practice of treating cell culture HFBRs as black boxes is coming to an end, and that mathematical modelling and interactions with modellers will benefit all parties concerned. This author firmly believes that this type of feedback-based research philosophy will best serve future investigations and is the best recipe for maximising progress in the area of HFBR protein production.

## Nomenclature

### *Latin letters*

$a_1$ - $a_7$	constants in eq. (86)	(-)
$a_m$	parameter defined by eq. (79)	(-)
$a_{edg}$	parameter defined by eq. (80)	(-)
$a_{pot}$	parameter defined by eq. (81)	(-)
$A$	(1) total membrane area (2) upwinding coefficients (appendix D)	( $m^2$ ) (-)
$A_1$	coefficient in eq. (17)	( $L^2 g^{-2}$ )
$A_2$	coefficient in eq. (17)	( $L^3 g^{-3}$ )
$A_{F1}$	parameter defined by eq. (108h)	(-)
$A_{F2}$	parameter defined by eq. (108i)	(-)
$A_{L2}$	coefficient defined by eq. (110a)	( $m^2$ )
$A_{Lp}$	parameter defined by eq. (108j)	( $m s kg^{-1}$ )
$A_{LRHS}$	coefficient defined by eq. (110b)	(Pa)
$A_p$	pore area measured in the $x$ -direction (ellipse)	( $m^2$ )
$A_{p,eff}$	pore area in the direction normal to the pore axis (circle)	( $m^2$ )
$A_{r1}$	coefficient defined by eq. (108d)	(m)
$A_{r2}$	coefficient defined by eq. (108a)	( $m^2$ )
$A_{SRHS}$	coefficient defined by eq. (108g)	(Pa)
$A_V$	membrane surface area per unit volume, eq. (30)	( $m^{-1}$ )
$A_{z1}$	coefficient defined by eq. (108f)	(m)
$A_{z2}$	coefficient defined by eq. (108c)	( $m^2$ )
$A_{\mu 1}$	coefficient in eq. (112)	( $L g^{-1}$ )
$A_{\mu 2}$	coefficient in eq. (112)	( $L^2 g^{-2}$ )
$A_{\Pi 2}$	coefficient in eq. (52)	( $L^2 g^{-2}$ )

$A_{\Gamma 3}$	coefficient in eq. (52)	$(L^3 g^{-3})$
$A_{\theta 1}$	coefficient defined by eq. (108e)	(m)
$A_{\theta 2}$	coefficient defined by eq. (108b)	(m)
<i>AlphaPL</i>	relaxation parameter for ICS pressure iteration (tables 12, 14)	(-)
<i>AlphaPS</i>	relaxation parameter for ECS pressure iteration (table 14)	(-)
$b_1$ - $b_7$	constants in eq. (86)	(-)
$B$	upwinding coefficients (appendix D)	(-)
$B_1$ - $B_4$	parameters in eqs. (A3, A4)	(Pa)
$C$	protein concentration	$(g L^{-1})$
$C^*$ , $C^{**}$	intermediate concentration solutions (appendix D)	$(g L^{-1})$
$C_{Bundle}$	average protein concentration in the ECS fibre bundle (chapter 5)	$(g L^{-1})$
$C_{crit}$	critical concentration parameter, eq. (88)	$(g L^{-1})$
$C_{exp}$	sampled ICS protein concentration (chapter 3)	$(g L^{-1})$
$C_L$	mixing-cup ICS protein concentration	$(g L^{-1})$
$C_{max}$	local concentration parameter (section 3.4.3.2)	$(g L^{-1})$
$C_N$	parameter in eqs. (B13-B17)	$(m^{-2})$
$C_{S0}^{crit}$	critical initial protein concentration (section 2.2.1)	$(g L^{-1})$
$C_{S,ad}$	adjusted local ECS protein concentration, eq. (78)	$(g L^{-1})$
<i>ConvPL</i>	convergence criterion for ICS pressure iteration (tables 12, 14)	(Pa)
<i>ConvPS</i>	convergence criterion for ECS pressure iteration (table 14)	(Pa)
$d$	length scale for dimensionless parameter estimation (usually taken as average interfibre distance)	(m)
$dCdtAve$	average global magnitude of $dC/dt$ (chapter 5)	$(g L^{-1} s^{-1})$
$dCdtMax$	maximum local magnitude of $dC/dt$ (chapter 5)	$(g L^{-1} s^{-1})$
$D$	protein diffusivity	$(m^2 s^{-1})$
<i>EpsStSt</i>	steady-state criterion (table 12)	$(g L^{-1} s^{-1})$
$f_{eff}$	effective fractional recovery of protein (chapter 4)	(-)
$F_1$	homogeneity parameter for ECS continuity eq. (105)	(-)
$F_{\mu}$	viscosity gradient parameter, eqs. (108d-g)	(-)
$F_{\rho}$	density gradient parameter (table 12)	(-)

$g$	acceleration of gravity	( $\text{m s}^{-2}$ )
$Gr$	Grashof number, eq. (90)	(-)
$h$	elevation of the REV centre of mass above a datum level, eq. (98)	(m)
$h_p$	radial position along the direction of pore axis	(m)
$HetIx$	ECS protein heterogeneity index, eq. (121)	(-)
$i$	axial grid point index	(-)
$IADJMan$	manifold adjustment parameter (table 12)	(-)
$IDTCtrl$	time step control parameter (table 12)	(-)
$IManNC$	natural-convective manifold adjustment parameter (table 12)	(-)
$IndPLin$	ICS inlet boundary condition parameter (table 12)	(-)
$Ir0$	angular concentration averaging parameter (table 12)	(-)
$IStSt$	termination criterion for numerical simulations (table 12)	(-)
$j$	radial grid point index	(-)
$J_M$	transmembrane myoglobin flux (chapter 3)	( $\text{g L}^{-1} \text{m s}^{-1}$ )
$J_P$	protein flux, eqs. (113, 114)	( $\text{g L}^{-1} \text{m s}^{-1}$ )
$J_{TMF}$	transmembrane fluid flux	( $\text{m s}^{-1}$ )
$J_{TMP}$	transmembrane protein flux, eq. (113)	( $\text{g L}^{-1} \text{m s}^{-1}$ )
$k$	(1) Darcy permeability (2) angular grid point index (chapter 5)	( $\text{m}^2$ ) (-)
$k_m$	membrane constant, eq. (56)	(-)
$K_c$	(1) convective hindrance factor for cell-packed ECS, eq. (25) (2) convective hindrance factor for transmembrane protein transport (chapter 3)	(-) (-)
$K_d$	(1) diffusive hindrance factor for cell-packed ECS, eq. (25) (2) diffusive hindrance factor for transmembrane protein transport (chapter 3)	(-) (-)
$K_s, K_t$	parameters in eq. (86)	(-)
$L$	ECS length	(m)
$L_F$	permeable length of the wet fibre	(m)
$L_p$	membrane hydraulic permeability	(m)
$m$	(1) number of angular sections per axial segment, eq. (89) (2) radial grid point index for ECS manifolds (section 5.2.2.3)	(-) (-)

$m_{app}$	mass of protein introduced into the cartridge over the actual experiment duration (chapter 4)	(g)
$m_{eff}$	mass of protein introduced into the cartridge over the effective experiment duration (chapter 4)	(g)
$m_{exp}$	mass of protein recovered from the fibre bundle and from the downstream manifold and tubing (chapter 4)	(g)
$m_L$	mass of protein recovered from the lumen side (chapter 4)	(g)
$m_s$	molar salt concentration, eq. (17)	(mmol L <sup>-1</sup> )
$M$	molar mass	(kg mol <sup>-1</sup> )
$n$	(1) number of fibres in the HFBR cartridge (2) time level index (appendix D)	(-) (-)
$N$	number of axial grid points (chapter 3)	(-)
$N_0$	number of pores at the maximum of the distribution function (appendix B)	(-)
$N_d$	number of pores having radius $r_d$ (appendix B)	(-)
$N_{el}$	number of pores within a differential membrane element	(-)
$N_{exp}$	number of ICS samples for a given experiment (chapter 3)	(-)
$N_i$	number of axial grid points (chapter 5)	(-)
$N_{ijk}$	total number of grid points in the 3-D domain (chapter 5)	(-)
$N_j$	number of radial grid points (chapter 5)	(-)
$N_k$	number of angular grid points (chapter 5)	(-)
$N_{k,half}$	largest integer of $N_k/2$ (section 5.3.2)	(-)
$N_m$	number of radial grid points in the ECS manifold (section 5.2.2.3)	(-)
$N_p$	number of pores per unit area of the membrane at $r = R_L$	(m <sup>-2</sup> )
$N_V$	number of fluid volumes displaced from the ECS (chapter 4)	(-)
$P$	hydrostatic pressure	(Pa)
$\hat{p}$	piezometric pressure (chapter 5)	(Pa)
$\Delta P_L$	axial centreline ICS pressure drop	(Pa)
$\Delta P_m$	effective transmembrane pressure difference	(Pa)
$P_S^{up}$	hydrostatic pressure in the ECS protein-free region, eq. (20)	(Pa)
$Pe$	Peclet number, $vd/D$	(-)

$Pe_m$	pore Peclet number, eq. (69)	(-)
$Pe_r$	radial Peclet number at the fibre surface (chapter 4)	(-)
$P_f$	probability of pore plugging (section 3.4.3.2)	(-)
$Q$	fluid flow rate	(mL min <sup>-1</sup> )
$Q_{in}$	inoculation flow rate (chapter 4)	(mL min <sup>-1</sup> )
$r$	radial position	(m)
$\Delta r$	radial grid increment	(m)
$r_d$	pore radius in a membrane with distributed pore sizes (appendix B)	(m)
$r_0$	pore radius at the maximum of the distribution function (appendix B)	(m)
$r_M$	effective myoglobin radius (chapter 3)	(m)
$r_p$	pore radius measured in the x-direction	(m)
$r_{p,eff}$	effective pore radius (normal to the pore axis)	(m)
$R_g$	universal gas constant	(J mol <sup>-1</sup> K <sup>-1</sup> )
$R_{HFBR}$	inner radius of HFBR cartridge	(m)
$R_K$	Krogh cylinder radius	(m)
$R_L$	fibre lumen radius	(m)
$R_F$	fibre outer radius	(m)
$R_m$	ECS manifold radius	(m)
$Re$	Reynolds number, $vd\rho/\mu$	(-)
$SD$	standard deviation, eq. (87)	(-)
$t$	time	(s)
$\Delta t$	time step	(s)
$t_{act}$	actual experiment duration (chapter 4)	(min)
$t_{eff}$	effective experiment duration (chapter 4)	(min)
$t_{final}$	total simulation time (table 14)	(h)
$t_{StSt}$	time to reach steady state (section 5.5.2)	(h)
$T$	temperature	(K, °C)
$u$	axial fluid velocity (chapters 2, 3)	(m s <sup>-1</sup> )
$u_0$	centreline velocity at the lumen inlet, eqs. (10-13)	(m s <sup>-1</sup> )

$v$	(1) fluid velocity; (2) radial fluid velocity (chapters 2, 3)	$(\text{m s}^{-1})$ $(\text{m s}^{-1})$
$\mathbf{v}$	superficial fluid velocity vector (section 5.2.2.1)	$(\text{m s}^{-1})$
$v_m$	radial superficial velocity in the membrane	$(\text{m s}^{-1})$
$v_p$	interstitial pore velocity, eqs. (58, 59)	$(\text{m s}^{-1})$
$V$	volume	$(\text{m}^3, \text{mL})$
$V_{ECS}$	ECS volume	$(\text{mL})$
$V_{exp}$	ICS sample volume (chapter 3)	$(\text{mL})$
$V_{EXT}$	external volume (chapter 3)	$(\text{mL})$
$V_{ff}$	fibre-free ECS region volume (section 5.2.3)	$(\text{mL})$
$V_L$	ICS volume	$(\text{mL})$
$V_m$	ECS manifold region volume	$(\text{mL})$
$V_{pot}$	ECS potting region volume (chapter 3)	$(\text{mL})$
$V_{REC}$	ICS recycle volume (chapter 3)	$(\text{mL})$
$V_p$	membrane pore volume	$(\text{m}^3)$
$x$	axial position measured along the axis of a tortuous fibre	$(\text{m})$
$\Delta x$	axial grid increment in the $x$ -direction	$(\text{m})$
$z$	axial position measured along the cartridge axis	$(\text{m})$
$\Delta z$	axial grid increment in the $z$ -direction	$(\text{m})$
$z_m$	axial length of the ECS manifold	$(\text{m})$
$z_s$	axial position of ECS division into protein-free and protein-filled zones (section 2.2.1)	$(\text{m})$
$Z_p$	protein charge number, eq. (17)	$(-)$

#### *Greek letters*

$\alpha$	parameter in eqs. (A5, A6)	$(\text{m}^4 \text{s kg}^{-1})$
$\chi_{ins}$	rate of insulin production, eq. (3)	$(\text{g L}^{-1} \text{s}^{-1})$
$\varepsilon$	(1) porosity (2) local surface or cross-sectional porosity (chapter 3)	$(-)$ $(-)$
$\varepsilon_S$	cell-free ECS porosity, eq. (116)	$(-)$
$\varepsilon_V$	local volumetric porosity (chapter 3)	$(-)$

$\overline{\varepsilon}_v$	mean volumetric porosity, eq. (47)	(-)
$\gamma$	ECS to ICS hydraulic permeability ratio, eqs. (8, 9)	(-)
$\phi$	fraction of reactor volume occupied by the fibres	(-)
$\Phi$	equilibrium partition coefficient, eq. (82)	(-)
$\lambda$	(1) parameter defined by eq. (14) (2) ratio of effective solute and pore radii (section 3.2.3)	(-) (-)
$\mu$	fluid viscosity	(kg m <sup>-1</sup> s <sup>-1</sup> )
$\mu_0$	protein-free fluid viscosity, eq. (118)	(kg m <sup>-1</sup> s <sup>-1</sup> )
$\mu_s^{-1}$	reciprocal ECS fluid viscosity (chapter 5)	(m s kg <sup>-1</sup> )
$\pi$	3.14159265358979...	(-)
$\Pi$	osmotic pressure	(Pa)
$\Delta\Pi_{eff}$	effective osmotic pressure difference, eq. (50)	(Pa)
$\rho$	fluid density	(kg m <sup>-3</sup> )
$\Delta\rho$	(1) local change in fluid density (chapter 4) (2) reduced density, eqs. (102a, b)	(kg m <sup>-3</sup> ) (kg m <sup>-3</sup> )
$\rho'$	dimensionless fluid density (chapter 5)	(-)
$\Delta\rho'$	dimensionless reduced fluid density (chapter 5)	(-)
$\rho_0$	protein-free fluid density, eq. (117)	(kg m <sup>-3</sup> )
$\rho_A$	partial specific density of BSA, eq. (111)	(kg m <sup>-3</sup> )
$\sigma_0^2$	apparent variance of the log-normal distribution function, eq. (B4)	(-)
$\sigma_{re}$	osmotic reflection coefficient, eq. (83)	(-)
$\Omega$	function defined by eq. (15)	(-)
$\tau$	pore tortuosity	(-)
$\theta$	angular position	(°, rad)
$\Delta\theta$	angular grid increment (chapter 5)	(°, rad)
$\Psi$	(1) angle between the ICS flow and gravity vectors (chapter 5) (2) general transmission parameter, eq. (B13)	(°, rad) (-)

*Subscripts*

0	initial
<i>A</i>	albumin
<i>AVE</i>	average
<i>b</i>	bottom face of a 3-D REV (radial direction)
<i>DnMan</i>	upstream manifold (chapter 5)
<i>e</i>	east face of a 3-D REV (angular direction)
<i>exp</i>	experimental
<i>in</i>	inlet
<i>L</i>	lumen side
<i>m</i>	(1) membrane (2) manifold (chapter 3)
<i>max</i>	maximum
<i>M</i>	myoglobin
<i>n</i>	north face of a 3-D REV (axial direction)
<i>out</i>	outlet
<i>p</i>	(1) protein (2) membrane pore (chapter 3)
<i>s</i>	south face of a 3-D REV (axial direction)
<i>S</i>	shell side
<i>s</i>	south face of a 3-D REV (axial direction)
<i>t</i>	top face of a 3-D REV (radial direction)
<i>UpMan</i>	upstream manifold (chapter 5)
<i>w</i>	west face of a 3-D REV (angular direction)

*Superscripts*

•	cell-packed
— (overbar)	(1) radially-averaged (2) pore-size-averaged (appendix B) (3) averaged over the REV (section 5.2.2.1)
= (double overbar)	radially- and angularly-averaged

*Abbreviations*

1-D	one-dimensional
2-D	two-dimensional
3-D	three-dimensional
ADI	Alternate Directions Implicit
ASD	angular standard deviation, eq. (89)
BAL	bioartificial liver
BHK	baby hamster kidney
BSA	bovine serum albumin
CA	cellulose acetate
CHO	Chinese hamster ovary
CPU	central processing unit
CTA	cellulose triacetate
CV	control volume
DNA	deoxyribonucleic acid
DO	dissolved oxygen
ECM	extracellular matrix
ECS	extracapillary space
FBS	foetal bovine serum
ICS	intracapillary space
IgG	immunoglobulin G
HFBR	hollow-fibre bioreactor
KCM	Krogh cylinder model
MAb	monoclonal antibody
MCT	Mass Culturing Technique
MM	molar mass
MRI	magnetic resonance imaging
MWCO	molecular weight cutoff
NINT	nearest integer function
NMR	nuclear magnetic resonance

NPS	nominal pore size
PAN	polyacrylonitrile
PBS	phosphate-buffered saline
PMM	porous medium model
PMMA	poly(methylmethacrylate)
POENP	polyoxyethelene nonyl-phenol
RAM	random access memory
REV	representative elementary volume
TGF- $\beta$	transforming growth factor beta
TMFF	transmembrane fluid flux

## References

- Adamson, S. R., L. A. Behie, G. M. Gaucher, and B. H. Lesser. 1987. Metabolism of hybridoma cells in suspension culture: evaluation of three commercially available media. In *Commercial Production of Monoclonal Antibodies. A Guide for Scale-Up*, ed. Sally S. Seaver, 17-34. New York: Marcel-Dekker.
- Adema, E., and A. J. Sinskey. 1987. An analysis of intra- versus extracapillary growth in a hollow fiber reactor. *Biotechnol. Prog.* 1987; 3: 74-79.
- Alberts, Bruce, Dennis Bray, Julian Lewis, Martin Raff, Keith Roberts, and James D. Watson. 1994. *Molecular Biology of the Cell*. New York: Garland Publishing.
- Altshuler, G. L., D. M. Dziewulski, J. A. Soweck, and G. Belfort. 1986. Continuous hybridoma growth and monoclonal antibody production in hollow fiber reactors-separators. *Biotechnol. Bioeng.* 28: 646-658.
- Andersen, B. G., and M. L. Gruenberg. 1987. Optimization techniques for the production of monoclonal antibodies utilizing hollow-fiber technology. In *Commercial Production of Monoclonal Antibodies. A Guide for Scale-Up*, ed. Sally S. Seaver, 175-195. New York: Marcel-Dekker.
- Anderson, Dale A., John C. Tannehill, and Richard H. Pletcher. 1984. *Computational Fluid Mechanics and Heat Transfer*. Washington: Hemisphere.
- Anderson, J. L., and D. M. Malone. 1974. Mechanism of osmotic flow in porous membranes. *Biophys. J.* 14: 957-982.
- Anderson, J. L., and J.A. Quinn. 1974. Restricted transport in small pores. A model for steric exclusion and hindered particle motion. *Biophys. J.* 14: 130-150.
- Anderson, J. L., F. Rauh, and A. Morales. 1978. Particle diffusion as a function of concentration and ionic strength. *J. Phys. Chem.* 82: 608-616.
- Apelblat, A., A. Katzir-Katchalsky, and A. Silberberg. 1974. A mathematical analysis of capillary-tissue fluid exchange. *Biorheology* 11: 1-49.
- Balakrishnan, M., G. P. Agarwal, and C. L. Cooney. 1993. Study of protein transmission through ultrafiltration membranes. *J. Membrane Sci.* 85: 111-128.

- Baltus, R. E. 1997. Characterization of the pore area distribution in porous membranes using transport measurements. *J. Membrane Sci.* 123: 165-184.
- Barnes, D. 1984. Attachment factors in cell culture. In *Mammalian Cell Culture. The Use of Serum-Free Hormone-Supplemented Media*, ed. Jennie P. Mather, 195-237. New York: Plenum Press.
- Bear, Jacob. 1972. *Dynamics of Fluid in Porous Media*. New York: Dover Publications.
- Beavers, G. S., and D. D. Joseph. 1967. Boundary conditions at a naturally permeable wall. *J. Fluid Mech.* 30: 197-207.
- Becher, P. 1961. Nonionic surface-active compounds. IV. Micelle formation by polyoxyethylene alkanols and alkyl phenols in aqueous solution. *J. Colloid Sci.* 16: 49-56.
- Belfort, G. 1989. Membranes and bioreactors: A technical challenge in biotechnology. *Biotechnol. Bioeng.* 33: 1047-1066.
- Birch, J. R., P. W. Thompson, K. Lambert, and R. Boraston. 1985. The large scale cultivation of hybridoma cells producing monoclonal antibodies. In *Large-Scale Mammalian Cell Culture*, ed. Joseph Feder and William R. Tolbert, 1-16. Orlando: Academic Press.
- Blatt, W. F., A. Dravid, A. S. Michaels, and L. Nelsen. 1970. Solute polarization and cake formation in membrane ultrafiltration: causes, consequences, and control techniques. In *Membrane Science and Technology. Industrial, Biological, and Waste Treatment Processes*, ed. James E. Flinn, 47-97. New York: Plenum Press.
- Broek, A. P., H. A. Teunis, D. Bargeman, E. D. Sprengers, H. Strathmann, and C. A. Smolders. 1995. Characterization of hemodialysis membranes by inverse size exclusion chromatography. *J. Membrane Sci.* 99: 217-228.
- Brotherton, J. D., and P. C. Chau. 1990. Modeling analysis of an intercalated-spiral alternate-dead-ended hollow fiber bioreactor for mammalian cell cultures. *Biotechnol. Bioeng.* 35: 375-394.
- Brotherton, J. D., and P. C. Chau. 1995. Protein-free human-human hybridoma cultures in an intercalated-spiral alternate-dead-ended hollow fiber bioreactor. *Biotechnol. Bioeng.* 47: 384-400.
- Brotherton, J. D., and P. C. Chau. 1996. Modeling of axial-flow hollow fiber cell culture bioreactors. *Biotechnol. Prog.* 12: 575-590.

- Brown, B. L. 1987. Reducing costs upfront: Two methods for adapting hybridoma cells to an inexpensive, chemically defined serum-free medium. In *Commercial Production of Monoclonal Antibodies. A Guide for Scale-Up*, ed. Sally S. Seaver, 35-48. New York: Marcel-Dekker.
- Brown, P. C., M. A. C. Costello, R. Oakley, and J. L. Lewis. 1985. Applications of the mass culturing technique (MCT) in the large scale growth of mammalian cells. In *Large-Scale Mammalian Cell Culture*, ed. Joseph Feder and William R. Tolbert, 59-71. Orlando: Academic Press.
- Bungay, P. M., and H. Brenner. 1973. The motion of a closely-fitting sphere in a fluid-filled tube. *Int. J. Multiphase Flow* 1: 25-56.
- Burden, Richard L., and J. Douglas Faires. 1997. *Numerical Analysis*. 6<sup>th</sup> ed. Pacific Grove: Brooks/Cole.
- Butler, Michael. 1987. *Animal Cell Technology. Principles and Products*. New York: Taylor and Francis.
- Butler, M., and M. Dawson. 1992. *Cell Culture. Labfax*. Oxford: BIOS Scientific Publishers.
- Carman, P. C. 1937. Fluid flow through a granular bed. *Trans. Inst. Chem. Eng. London* 15: 150-156.
- Cartwright, Terence. 1994. *Animal Cells as Bioreactors*. New York: Cambridge University Press.
- Catapano, G. 1996. Mass transfer limitations to the performance of membrane bioartificial liver support devices. *Int. J. Artif. Organs* 19: 18-35.
- Chen, V., K. J. Kim, and A. G. Fane. 1995. Effect of membrane morphology and operation on protein deposition in ultrafiltration membranes. *Biotechnol. Bioeng.* 47: 174-180.
- Chick, W. L., A. A. Like, and V. Lauris. 1975. Beta cell culture on synthetic capillaries: An artificial endocrine pancreas. *Science* 187: 847-949.
- Chresand, T. J., R. J. Gillies, and B. E. Dale. 1988. Optimum fibre spacing in a hollow fiber bioreactor. *Biotechnol. Bioeng.* 32: 983-992.
- Colton, C. K., K. A. Smith, E. W. Merrill, and P. C. Farrell. 1971. Permeability studies with cellulosic membranes. *J. Biomed. Mater. Res.* 5: 459-488.
- Davis, J. M., J. A. J. Hanak, G. M. Lewis, R. Chung, and J. Faulkner. 1991. Long term serum-free hollow-fibre culture of cell lines producing monoclonal antibodies: Metabolic aspects. In *Production of Biologicals from Animal Cells in Culture*, ed. R. E. Spier, J. B. Griffiths, and B. Meignier, 130-133. Oxford: Butterworth-Heinemann.

- Davis, M. E., and L.T. Watson. 1986. Mathematical modeling of annular reactors. *Chem. Eng. J.* 33: 133-142.
- Deen, W. M. 1987. Hindered transport of large molecules in liquid-filled pores. *AIChE J.* 33: 1409-1425.
- Dhainaut, F., L. Pouget, M. J. Richer-Hers, and G. Mignot. 1991. Optimization of human anti-rhesus IgG production using hollow fiber technology. In *Production of Biologicals from Animal Cells in Culture*, ed. R. E. Spier, J. B. Griffiths, and B. Meignier, 495-497. Oxford: Butterworth-Heinemann.
- Douglas, J. 1962. Alternating direction methods for three space variables. *Numer. Math.* 4: 41-63.
- Dowd, J. E., K. E. Kwok, and J. M. Piret. 2000. Increased t-PA yields using ultrafiltration of an inhibitory product from CHO fed-batch culture. *Biotechnol. Prog.* 16: 786-794.
- Enyart, C. R. 1967. Polyoxyethylene alkylphenols. In *Nonionic Surfactants*, ed. Martin J. Schick, 44-85. Marcel Dekker, New York.
- Evans, T. L., and R. A. Miller. 1988. Large-scale production of murine monoclonal antibodies using hollow fiber bioreactors. *BioTechniques* 6: 762-767.
- Filho, G. R., and W. A. Bueno. 1992. Water state of Cuprophane (hemodialysis membrane). *J. Membrane Sci.* 74: 19-27.
- Fleischaker, R. J., Jr., and A. J. Sinskey. 1981. Oxygen demand and supply in cell culture. *European J. Appl. Microbiol. Biotechnol.* 12: 193-197.
- Freshney, R. Ian. 1994. *Culture of Animal Cells. A Manual of Basic Technique*, 3<sup>rd</sup> ed. New York: Wiley-Liss.
- Gartner, Leslie P., and James L. Hiatt. 1997. *Color Textbook of Histology*. Philadelphia: W. B. Saunders Company.
- Glacken, M. W., E. Adema, and A. J. Sinskey. 1988. Mathematical description of hybridoma culture kinetics: I. Initial metabolic rates. *Biotechnol. Bioeng.* 32: 491-506.
- Gramer, M. J., and S. M. Keznoff. 1998. Optimizing hollow-fiber bioreactors: EC cycling technology for cell culture production. *Gen. Eng. News* 18: 21.
- Gramer, M. J., and D. M. Poeschl. 1998. Screening tool for hollow-fiber bioreactor process development. *Biotechnol. Prog.* 14: 203-209.

- Gramer, M. J., D. M. Poeschl, M. J. Conroy, and B. E. Hammer. 1999. Effect of harvesting protocol on performance of a hollow fiber bioreactor. *Biotechnol. Bioeng.* 65: 334-340.
- Griffiths, B. 1986. Scaling-up of animal cell cultures. In *Animal Cell Culture. A Practical Approach*, ed. R. I. Freshney, 33-69. Oxford: IRL Press.
- Griffiths, B. 1990. Perfusion systems for cell cultivation. In *Large-Scale Mammalian Cell Culture Technology*, ed. Anthony S. Lubiniecki, 217-250. New York: Marcel-Dekker.
- Gullino, P. M., and R. A. Knazek. 1979. Tissue culture on artificial capillaries. *Meth. Enzymol.* 58: 178-184.
- Hammer, B. E., C. A. Heath, S. D. Mirer, and G. Belfort. 1990. Quantitative flow measurements in bioreactors by nuclear magnetic resonance imaging. *Bio/Technology* 8: 327-330.
- Handa-Corrigan, A., S. Nikolay, and R. E. Spier. 1992. Biochemical control of monoclonal antibody secretion in hollow fibre bioreactors. In *Animal Cell Technology. Developments, Processes and Products*, ed. R. E. Spier, J. B. Griffiths, and C. MacDonald, 489-493. Oxford: Butterworth-Heinemann.
- Happel, J. 1959. Viscous flow relative to arrays of cylinders. *AIChE J.* 5: 174-177.
- Harrington, T. J., J. L. Gainer, and D. J. Kirwan. 1991. Effects of fluid shear on immobilized enzyme kinetics. *Enz. Microb. Technol.* 13: 610-616.
- Heath, C., and G. Belfort. 1987. Immobilization of suspended mammalian cells: Analysis of hollow fibre and microcapsule bioreactors. *Adv. Biochem. Eng. Biotechnol.* 34: 2-31.
- Heifetz, A. H., J. A. Braatz, R. A. Wolfe, R. M. Barry, D. A. Miller, and B. A. Solomon. 1989. Monoclonal antibody production in hollow fiber bioreactors using serum-free medium. *BioTechniques* 7(2): 192-199.
- Inloes, D. S., W. J. Smith, D. P. Taylor, S. N. Cohen, A. S. Michaels, and C. R. Robertson. 1983. Hollow-fiber membrane bioreactors using immobilized *E. coli* for protein synthesis. *Biotechnol. Bioeng.* 25: 2653-2681.
- Jackson, L. R., L. J. Trudel, J. G. Fox, and N. S. Lipman. 1996. Evaluation of hollow fiber bioreactors as an alternative to murine ascites production for small scale monoclonal antibody production. *J. Immunol. Methods* 189: 217-231.
- Jaffrin, M. Y., G. Reach, and D. Notelet. 1988. Analysis of ultrafiltration and mass transfer in a bioartificial pancreas. *J. Biomech. Eng. (Trans. ASME)* 110: 1-10.

- Jäger, V. 1991. Serum-free media suitable for upstream and downstream processing. In *Production of Biologicals from Animal Cells in Culture*, ed. R. E. Spier, J. B. Griffiths, and B. Meignier, 155-164. Oxford: Butterworth-Heinemann.
- Jayaraman, V. K. 1993. Solution of hollow fibre bioreactor design equations for zero-order limit of Michaelis-Menten kinetics. *Chem. Eng. J.* 51: B63-B66.
- Kedem, O., and A. Katchalsky. 1958. Thermodynamic analysis of permeability of biological membranes to non-electrolytes. *Biochim. Biophys. Acta* 27: 229-246.
- Kelsey, L. J., M. R. Pillarella, and A. L. Zydney. 1990. Theoretical analysis of convective flow profiles in a hollow-fiber membrane bioreactor. *Chem. Eng. Sci.* 45: 3211-3220.
- Kessler, N., G. Thomas, L. Gerentes, G. Delfosse, and M. Aymard. 1997. Hybridoma growth in a new generation hollow fibre bioreactor: Antibody productivity and consistency. *Cytotechnology* 24: 109-119.
- Kessler, S. B., and E. Klein. 1992. *Dialysis*. In *Membrane Handbook*, ed. W. S. Winston Ho and Kamallesh K. Sirkar, 161-215. New York: Van Nostrand Reinhold.
- Kidwell, W., R. Knazek, and Y. Wu. 1989. Effect of fiber pore size on performance of cells in hollow fiber bioreactors. In *Trends in Animal Cell Culture Technology*, ed. Hiroki Murakami, 29-33. Tokyo: Kodansha.
- Kilburn, D. G., and F. C. Webb. 1968. The cultivation of animal cells at controlled dissolved oxygen partial pressure. *Biotechnol. Bioeng.* 10: 801-814.
- Kim, S.-S., and D. O. Cooney. 1976. An improved theoretical model for hollow-fiber enzyme reactors. *Chem. Eng. Sci.* 31: 289-294.
- Kitano K., K. Iwamoto, Y. Shintani, and R. Sasada. 1989. Improvement in cell lines for effective production of human monoclonal antibodies by human-human hybridomas. In *Trends in Animal Cell Culture Technology*, ed. Hiroki Murakami, 285-290. Tokyo: Kodansha.
- Klein, E., F. F. Holland, A. Donnaud, A. Lebeouf, and K. Eberle. 1977. Diffusive and hydraulic permeabilities of commercially available cellulosic hemodialysis films and hollow fibers. *J. Membrane Sci.* 2: 349-364.
- Kleinstreuer, C., and S. S. Agarwal. 1986. Analysis and simulation of hollow-fiber bioreactor dynamics. *Biotechnol. Bioeng.* 28: 1233-1240.
- Knazek, R. A. 1974. Solid tissue masses formed in vitro from cells cultured on artificial capillaries. *Federation Proc.* 33: 1978-1981.

- Knazek, R. A., P. M. Gullino, P. O. Kohler, and R. L. Dedrick. 1972. Cell culture on artificial capillaries: An approach to tissue growth in vitro. *Science* 178: 65-67.
- Köhler, G., and C. Milstein. 1975. Continuous cultures of fused cells secreting antibody of predefined specificity. *Nature* 256: 495-497.
- Koska, J., B. D. Bowen, and J. M. Piret. 1997. Protein transport in packed-bed ultrafiltration hollow-fibre bioreactors. *Chem. Eng. Sci.* 52: 2251-2263.
- Kretzmer, G., T. Buch, K. Konstantinov, and D. Naveh. 1998. The temperature effect in mammalian cell culture: An Arrhenius interpretation. In *New Developments and New Applications in Animal Cell Technology*, ed. Otto-Wilhelm Merten, Pierre Perrin, and Bryan Griffiths, 363-366. Dordrecht: Kluwer Academic Publishers.
- Krogh, A. 1919. The number and distribution of capillaries in muscles with calculations of the oxygen pressure head necessary for supplying the tissue. *J. Physiol.* 52: 409-415.
- Ku, K., M. J. Kuo, J. Delente, B. S. Wildi, and J. Feder. 1981. Development of a hollow-fiber system for large-scale culture of mammalian cells. *Biotechnol. Bioeng.* 23: 79-95.
- Kulkarni, S. S., E. W. Funk, and N. N. Li. 1992. *Ultrafiltration*. In *Membrane Handbook*, ed. W. S. Winston Ho and Kamalesh K. Sirkar, 391-453. New York: Van Nostrand Reinhold.
- Łabęcki, Marek. 1994. Modelling of fluid flow and protein transport in hollow-fibre bioreactors. M.A.Sc. thesis, University of British Columbia.
- Łabęcki, M., J. M. Piret, and B. D. Bowen. 1995. Two-dimensional analysis of fluid flow in hollow-fibre modules. *Chem. Eng. Sci.* 50: 3369-3384.
- Łabęcki, M., B. D. Bowen, and J. M. Piret. 1996. Two-dimensional analysis of protein transport in the extracapillary space of hollow-fibre bioreactors. *Chem. Eng. Sci.* 51: 4197-4213.
- Łabęcki, M., I. Weber, Y. Dudal, J. Koska, J. M. Piret, and B. D. Bowen. 1998. Hindered transmembrane protein transport in hollow-fibre devices. *J. Membrane Sci.* 146: 197-216.
- Langsdorf, L. J., and A. L. Zydney. 1994. Effect of blood contact on the transport properties of hemodialysis membranes: A two-layer membrane model. *Blood Purif.* 12: 292-307.
- Laukemper-Ostendorf, S., H. D. Lemke, P. Blümmler, and B. Blümich. 1998. NMR imaging of flow in hollow fiber hemodialyzers. *J. Membrane Sci.* 138: 287-295.

- Lee, S. H., and E. Ruckenstein. 1988. Adsorption of proteins onto polymeric surfaces of different hydrophilicities – a case study with bovine serum albumin. *J. Coll. Interface Sci.* 125: 365-379.
- Levick, J. R. 1987. Flow through interstitium and other fibrous matrices. *Quart. J. Experim. Physiol.* 72: 409-438.
- Lowrey, D., S. Murphy, and R. A. Goffe. 1994. A comparison of monoclonal antibody productivity in different hollow fiber bioreactors. *J. Biotechnol.* 36: 35-38.
- Lysaght, M. J. 1995. Evolution of hemodialysis membranes. In *Contributions to Nephrology*, ed. G. M. Berlyne and S. Giovannetti, vol. 113, *Dialysis Membranes. Structure and Predictions*, ed. V. Bonomini and Y. Berland, 1-10. Basel: Karger.
- Mancusco, A., E. J. Fernandez, H. W. Blanch, and D. S. Clark. 1990. A nuclear magnetic resonance technique for determining hybridoma cell concentration in hollow fiber bioreactors. *Bio/Technology* 8: 1282-1285.
- Marx, U., D. Roggenbuck, M. Wilding, H. Tanzmann, and S. Jahn. 1994. Pitfalls of bioprocessing a human monoclonal multireactive IgM antibody. In *Animal Cell Technology. Products of Today, Prospects for Tomorrow*, ed. R. E. Spier, J. B. Griffiths, and W. Berthold, 278-280. Oxford: Butterworth-Heinemann.
- Mather, J. P., and M. Tsao. 1990. Expression of cloned proteins in mammalian cells: Regulation of cell-associated parameters. In *Large-Scale Mammalian Cell Culture Technology*, ed. Anthony S. Lubiniecki, 161-177. New York: Marcel-Dekker.
- Matthiasson, E. 1983. The role of macromolecular adsorption in fouling of ultrafiltration membranes. *J. Membrane Sci.* 16: 23-36.
- Maurer, H. R. 1986. Towards chemically-defined, serum-free media for mammalian cell culture. In *Animal Cell Culture. A Practical Approach*, ed. R. I. Freshney, 13-31. Oxford: IRL Press.
- McCullough, Kenneth C., and Raymond E. Spier. 1990. *Monoclonal Antibodies in Biology and Biotechnology. Theoretical and Practical Aspects*. Cambridge: University Press.
- Meireles, M., P. Aimar, and V. Sanchez. 1991. Albumin denaturation during ultrafiltration: Effects of operating conditions and consequences on membrane fouling. *Biotechnol. Bioeng.* 38: 528-534.
- Merten, O-W. 1989. Culture of hybridomas – a survey. In *Advanced Research on Animal Cell Technology*, ed. Alain O. A. Miller, 367-398. Dordrecht: Kluwer Academic Publishers.

- Michaels, A. S. 1980. Analysis and prediction of sieving curves for ultrafiltration membranes: a universal correlation? *Sep. Sci. Technol.* 15: 1305-1322.
- Miller, W. M., H. W. Blanch, and C. R. Wilke. 1988. A kinetic analysis of hybridoma growth and metabolism in batch and continuous suspension culture: Effect of nutrient concentration, dilution rate, and pH. *Biotechnol. Bioeng.* 32: 947-965.
- Mochizuki, S., and A. L. Zydney. 1993. Theoretical analysis of pore size distribution effects on membrane transport. *J. Membrane Sci.* 82: 211-227.
- Mulder, Marcel. 1991. *Basic Principles of Membrane Technology*. Dordrecht: Kluwer Academic Publishers.
- Neale, G. H., and W. K. Nader. 1973. Prediction of transport processes within porous media: Diffusive flow processes within an homogeneous swarm of spherical particles. *AIChE J.* 19: 112-119.
- Nield, Donald A., and Adrian Bejan. 1992. *Convection in Porous Media*. New York: Springer-Verlag.
- Norde, W. 1986. Adsorption of proteins from solution at the solid-liquid interface. *Adv. Coll. Interface Sci.* 25: 267-340.
- Nyberg, S. L., R. A. Shatford, W. D. Payne, W.-S. Hu, and F. B. Cerra. 1992. Primary culture of rat hepatocytes entrapped in cylindrical collagen gels: An *in vitro* system with application to the bioartificial liver. *Cytotechnology* 8: 205-216.
- Ozturk, S. S., and B. O. Palsson. 1990. Chemical decomposition of glutamine in cell culture media: Effect of media type, pH, and serum concentration. *Biotechnol. Prog.* 6: 121-128.
- Park, J. K., and H. N. Chang. 1986. Flow distribution in the fiber lumen side of a hollow-fiber module. *AIChE J.* 32: 1937-1947.
- Patankar, Suhas V. 1980. *Numerical Heat Transfer and Fluid Flow*. Washington: Hemisphere.
- Patkar, A. Y., J. Koska, D. G. Taylor, B. D. Bowen, and J. M. Piret. 1995. Protein transport in ultrafiltration hollow fiber bioreactors. *AIChE J.* 41: 415-425.
- Perry, Robert H., and Don Green, eds. 1984. *Perry's Chemical Engineering Handbook*. 6<sup>th</sup> ed. New York: McGraw-Hill.
- Pillarella, M. R., and A. L. Zydney. 1990. Theoretical analysis of the effect of convective flow on solute transport and insulin release in a hollow fiber bioartificial pancreas. *J. Biomech. Eng. (Trans. ASME)* 112: 220-228.

- Pinton, H., A. L. da Silva, J. L. Goergen, A. Marc, J. M. Engasser, J. N. Rabaud, and G. Pierry. 1994. Control of the maximal cell density in a membrane perfusion reactor. In *Animal Cell Technology. Products of Today, Prospects for Tomorrow*, ed. R. E. Spier, J. B. Griffiths, and W. Berthold, 470-475. Oxford: Butterworth-Heinemann.
- Piret, J. M., and C. L. Cooney. 1990a. Immobilized mammalian cell cultivation in hollow fiber bioreactors. *Biotechnol. Adv.* 8: 763-783.
- Piret, J. M., and C. L. Cooney. 1990b. Mammalian cell and protein distributions in ultrafiltration hollow-fiber bioreactors. *Biotechnol. Bioeng.* 36: 902-910.
- Piret, J. M., and C. L. Cooney. 1991. Model of oxygen transport limitations in hollow fiber bioreactors. *Biotechnol. Bioeng.* 37: 80-92.
- Piret, J. M., D. A. Devens, and C. L. Cooney. 1991. Nutrient and metabolite gradients in mammalian cell hollow fiber bioreactors. *Can. J. Chem. Eng.* 69: 421-428.
- Radovich, J. M. 1995. Composition of polymer membranes for therapies of end-stage renal disease. In *Contributions to Nephrology*, ed. G. M. Berlyne and S. Giovannetti, vol. 113, *Dialysis Membranes. Structure and Predictions*, ed. V. Bonomini and Y. Berland, 11-24. Basel: Karger.
- Renkin, E. M. 1954. Filtration, diffusion, and molecular sieving through porous cellulose membranes. *J. Gen. Physiol.* 38: 225-243.
- Reuveny, S., D. Velez, F. Riske, J. D. Macmillan, and L. Miller. 1985. Production of monoclonal antibodies in culture. *Develop. Biol. Standard.* 60: 185-197.
- Rony, P. R. 1971. Multiphase catalysis. II. Hollow-fiber catalysts. *Biotechnol. Bioeng.* 13: 431-447.
- Ryan, G. B., M. T. Simpson, W. T. Jones, M. J. Nicol, and P. H. P. Reynolds. 1994. Effect of dissolved oxygen on monoclonal antibody production from hybridoma cultured in haemodialysers. In *Animal Cell Technology. Products of Today, Prospects for Tomorrow*, ed. R. E. Spier, J. B. Griffiths, and W. Berthold, 437-456. Oxford: Butterworth-Heinemann.
- Ryll, T., M. Lucki-Lange, V. Jäger, and R. Wagner. 1990. Production of recombinant human interleukin-2 with BHK cells in a hollow fibre and a stirred tank reactor with protein-free medium. *J. Biotechnol.* 14: 377-392.
- Saffman, P. G. 1971. On the boundary condition at the surface of a porous medium. *Studies Appl. Math.* L: 93-101.

- Sakai, K., S. Takesawa, R. Mimura, and H. Ohashi. 1987. Structural analysis of hollow fiber dialysis membranes for clinical use. *J. Chem. Eng. Japan* 20: 351-356.
- Salmon, P. M., S. B. Libicki, and C. R. Robertson. 1988. A theoretical investigation of convective transport in the hollow-fiber reactor. *Chem. Eng. Commun.* 66: 221-248.
- Sardonini, C. A., and D. DiBiasio. 1993. Growth of animal cells around hollow fibers: Multifiber studies. *AIChE J.* 39: 1415-1419.
- Schneider, Y.-J., and A. Lavoix. 1990. Monoclonal antibody production in semi-continuous serum- and protein-free culture. Effect of glutamine concentration and culture conditions on cell growth and antibody secretion. *J. Immunol. Methods* 129: 251-268.
- Schonberg, J. A., and G. Belfort. 1987. Enhanced nutrient transport in hollow fiber perfusion bioreactors: A theoretical analysis. *Biotechnol. Prog.* 3: 80-89.
- Schönherr, O. T., and P. T. J. A. van Gelder. 1988. Culture of animal cells in hollow-fibre dialysis systems. In *Animal Cell Biotechnology*, ed. R. E. Spier and J. B. Griffiths, 3: 337-355. Oxford: Academic Press.
- Starling, E. H. 1896. On the absorption of fluids from the connective tissue spaces. *J. Physiol.* 19: 312-326.
- Staverman, A. J. 1951. The theory of measurement of osmotic pressure. *Rec. Trav. Chim.* 70: 344-352.
- Swabb, E. A., J. Wei, and P. M. Gullino. 1974. Diffusion and convection in normal and neoplastic tissues. *Cancer Res.* 34: 2814-2822.
- Taylor, D. G., J. M. Piret, and B. D. Bowen. 1994. Protein polarisation in isotropic membrane hollow-fiber bioreactors. *AIChE J.* 40: 321-333.
- Tharakan, J. P., and P. C. Chau. 1986a. A radial flow hollow fiber bioreactor for the large-scale culture of mammalian cells. *Biotechnol. Bioeng.* 28: 329-342.
- Tharakan, J. P., and P. C. Chau. 1986b. Operation and pressure distribution of immobilized cell hollow fiber bioreactors. *Biotechnol. Bioeng.* 28: 1064-1071.
- Tharakan, J. P., and P. C. Chau. 1987. Modeling and analysis of radial flow mammalian cell culture. *Biotechnol. Bioeng.* 29: 657-671.
- Tharakan, J. P., S. Gallagher, and P. C. Chau. 1988. Hollow fiber bioreactors in mammalian cell culture. *Adv. Biotechnol. Process.* 7: 153-184.
- Thomas, J. N. 1990. Mammalian cell physiology. In *Large-Scale Mammalian Cell Culture Technology*, ed. Anthony S. Lubiniecki, 93-145. New York: Marcel-Dekker.

- Todisco, S., V. Calabro, and G. Iorio. 1995. A lumped parameter mathematical model of a hollow fiber membrane device for the controlled insulin release. *J. Membrane Sci.* 106: 221-232.
- Tyo, M. A., B. J. Bulbulian, B. Z. Menken, and T. J. Murphy. 1988. Large-scale mammalian cell culture utilizing ACUSYST technology. In *Animal Cell Biotechnology*, ed. R. E. Spier and J. B. Griffiths, 3: 357-371. Oxford: Academic Press.
- Tzianabos, A. O., and R. Smith. 1995. Use of hollow-fiber bioreactor for production in problematic cell lines. *Gen. Eng. News* 1: 24.
- van den Berg, G.B., and C. A. Smolders. 1989. The boundary-layer resistance model for unstirred ultrafiltration. A new approach. *J. Membrane Sci.* 40: 149-172.
- Vilker, V. L., C. K. Colton, and K. A. Smith. 1981a. The osmotic pressure of concentrated protein solutions: Effect of concentration and pH in saline solutions of bovine serum albumin. *J. Coll. Interface Sci.* 79: 548-565.
- Vilker, V. L., C. K. Colton, and K. A. Smith. 1981b. Concentration polarization in protein ultrafiltration. Part II: Theoretical and experimental study of albumin ultrafiltered in an unstirred cell. *AIChE J.* 27: 637-645.
- von Wedel, R. J. 1987. Mass culture of mouse and human hybridoma cells in hollow-fiber culture. In *Commercial Production of Monoclonal Antibodies. A Guide for Scale-Up*, ed. Sally S. Seaver, 159-173. New York: Marcel-Dekker.
- Waterland, L. R., A. S. Michaels, and C. R. Robertson. 1974. A theoretical model for enzymatic catalysis using asymmetric hollow-fiber membranes. *AIChE J.* 20: 50-59.
- Waterland, L. R., C. R. Robertson, and A. S. Michaels. 1975. Enzymatic catalysis using asymmetric hollow fiber membranes. *Chem. Eng. Commun.* 2: 37-47.
- Weast, Robert C., ed. 1975. *Handbook of Chemistry and Physics*. 56<sup>th</sup> ed. Boca Raton: CRC Press.
- Webster, I. A., and M. L. Shuler. 1978. Mathematical models for hollow-fiber enzyme reactors. *Biotechnol. Bioeng.* 20: 1541-1556.
- Wei, J., and M. B. Russ. 1977. Convection and diffusion in tissues and tissue cultures. *J. Theor. Biol.* 66: 775-787.
- White, Frank M. 1991. *Viscous Fluid Flow*. 2<sup>nd</sup> ed. New York: McGraw-Hill.

- Williams, S. N. O., R. M. Callies, and K. M. Brindle. 1997. Mapping of oxygen tension and cell distribution in a hollow-fiber bioreactor using magnetic resonance imaging. *Biotechnol. Bioeng.* 56: 1997.
- Wolf, C. F. W., C. R. Minick, and C. H. McCoy. 1978. Morphologic examination of a prototype liver assist device composed of cultured cells and artificial capillaries. *Int. J. Artif. Organs* 1: 45-51.
- Wooding, R. A. 1959. The stability of a viscous liquid in a vertical tube containing porous material. *Proc. Royal Soc. London, Ser. A.* 252: 120-134.
- Wurm, F. M., K. A. Gwinn, and R. E. Kingston. 1986. Inducible overproduction of the mouse c-myc protein in mammalian cells. *Proc. Natl. Acad. Sci. USA* 83: 5414-5418.
- Wyatt, D. E. 1994. Adaptation of mammalian cells to protein-free growth. In *Animal Cell Technology. Products of Today, Prospects for Tomorrow*, ed. R. E. Spier, J. B. Griffiths, and W. Berthold, 144-146. Oxford: Butterworth-Heinemann.
- Zeman, Leos J., and Andrew L. Zydney. 1996. *Microfiltration and Ultrafiltration. Principles and Applications*. New York: Marcel Dekker.
- Zydney, A. L. 1993. Bulk mass transfer limitations during high-flux hemodialysis. *Artif. Organs* 17: 919-924.
- Zydney, A. L., P. Aimar, M. Meireles, J.M. Pimbley, and G. Belfort. 1994. Use of the log-normal probability density function to analyze membrane pore size distributions: functional forms and discrepancies. *J. Membrane Sci.* 91: 293-298.

## Appendix A

### ONE-DIMENSIONAL HYDRODYNAMIC SOLUTIONS FOR A TORTUOUS KROGH CYLINDER

The tortuosity of the flow path can be taken into account in the tortuous Krogh cylinder model by replacing the axial co-ordinate  $z$  with  $x = zL_F/L$ . The 1-D KCM pressure equations (7) and (8) become then (Łabęcki et al. 1995)

$$\frac{d^2 P_L}{dx^2} = \frac{16 L_p}{R_L^3} [P_L(x) - P_S(x)] \quad (\text{A1})$$

and

$$\frac{d^2 P_S}{dx^2} = -\frac{16 L_p}{\gamma R_L^3} [P_L(x) - P_S(x)], \quad (\text{A2})$$

where  $\gamma$  is defined by eq. (9). The boundary conditions for eqs. (A1) and (A2) depend on the flow configuration. At an open ICS or ECS port, either a known pressure or a known pressure derivative (fluid velocity) can be assumed. At a closed port, a no-flux condition is imposed, i.e., the pressure derivative is forced to zero. The general solutions of eqs. (A1) and (A2) are

$$P_L(x) = B_1 \sinh\left(\lambda \frac{x}{L_F}\right) + B_2 \cosh\left(\lambda \frac{x}{L_F}\right) + B_3 \frac{x}{L_F} + B_4 \quad (\text{A3})$$

and

$$P_S(x) = -\frac{B_1}{\gamma} \sinh\left(\lambda \frac{x}{L_F}\right) - \frac{B_2}{\gamma} \cosh\left(\lambda \frac{x}{L_F}\right) + B_3 \frac{x}{L_F} + B_4, \quad (\text{A4})$$

where  $\lambda$  is defined by eq. (14),  $L_F$  is the wet fibre length, and the parameters  $B_1$ - $B_4$  depend on the boundary conditions as well as being functions of  $\gamma$  and  $\lambda$  (the algebraic forms of parameters  $B_1$ - $B_4$  for different flow configurations are given in Łabęcki et al. 1995). The local ICS and ECS flow rates can be calculated from the above pressure distributions as follows:

$$Q_L(x) = \alpha L_F \frac{dP_L}{dx} \quad (\text{A5})$$

and

$$Q_S(x) = \alpha \gamma L_F \frac{dP_S}{dx}, \quad (\text{A6})$$

where

$$\alpha = -\frac{n\pi R_L^4}{8\mu L_F}. \quad (\text{A7})$$

In particular, the general forms of expressions for the flow rates at open ICS and ECS ports are

$$Q_{L,x=0} = \alpha(B_1 \lambda + B_3), \quad (\text{A8})$$

$$Q_{L,x=L_F} = \alpha[B_1 \lambda \cosh(\lambda) + B_1 \lambda \sinh(\lambda) + B_3], \quad (\text{A9})$$

$$Q_{S,x=0} = \alpha(-B_1 \lambda + B_3 \gamma), \quad (\text{A10})$$

and

$$Q_{S,x=L_F} = \alpha[-B_1 \lambda \cosh(\lambda) - B_1 \lambda \sinh(\lambda) + B_3 \gamma]. \quad (\text{A11})$$

## Appendix B

### HINDERED TRANSMEMBRANE PROTEIN TRANSPORT ANALYSIS INCLUDING PORE SIZE DISTRIBUTION

For a membrane having a distribution of pore sizes, the Hagen-Poiseuille fluid flux equation (53) for a differential membrane element is replaced by

$$dJ_v(R_L) = \frac{\pi r_d^4}{8\mu A} \cdot \frac{(P_L - P_S - \Delta\Pi_{eff})}{\tau(R_F - R_L)} \cdot \frac{dN_d}{dr_d} dr_d, \quad (B1)$$

where  $r_d$  is the pore radius (equivalent to  $r_{p,eff}$  for a homoporous membrane),  $dJ_v(R_L)$  is the flux contribution from the pores with radii between  $r_d$  and  $r_d + dr_d$ ,  $dN_d$  is the number of pores of that size, and  $A = 2\pi n R_L L_F$  is the total membrane area. Integration of eq. (B1) over all pore radii, followed by the combination of the result with eq. (49), yields

$$\int_0^{\infty} \frac{dN_d}{dr_d} r_d^4 dr_d = \frac{8AL_p(R_F - R_L)\tau}{\pi}. \quad (B2)$$

Similarly, the definition of surface porosity at  $r = R_L$  leads to

$$\int_0^{\infty} \frac{dN_d}{dr_d} r_d^2 dr_d = \frac{A\varepsilon(R_L)}{\pi\tau}. \quad (B3)$$

If the following log-normal pore size distribution is assumed (Michaels 1980, Mochizuki and Zydny 1993),

$$\frac{dN_d}{dr_d} = N_0 \exp\left\{-\frac{[\ln(r_d/r_0)]^2}{2\sigma_0^2}\right\} \quad (B4)$$

then equations (B2) and (B3) become, respectively,

$$\int_0^{\infty} \exp\left\{-\frac{[\ln(r_d/r_0)]^2}{2\sigma_0^2}\right\} r_d^4 dr_d = \frac{8AL_p(R_F - R_L)\tau}{\pi N_0} \quad (\text{B5})$$

and

$$\int_0^{\infty} \exp\left\{-\frac{[\ln(r_d/r_0)]^2}{2\sigma_0^2}\right\} r_d^2 dr_d = \frac{A\tau}{k_m \pi N_0}, \quad (\text{B6})$$

where  $k_m = \tau^2/\varepsilon(R_L)$ ,  $N_0$  and  $r_0$  are the number of pores and the pore radius at the maximum of the distribution function, and  $\sigma_0^2$  is the apparent variance (for more discussion of different forms and parameters of the log-normal distribution function see Zydney et al. (1994)). Analytical solutions of the integrals in eqs. (B5) and (B6) are easily obtained upon changing the integration variable to  $\alpha = \ln(r_d/r_0)/(\sqrt{2}\sigma_0) - \frac{m+1}{2}\sqrt{2}\sigma_0$ , where  $m$  is the exponent of the  $r_d^m$  term in the integrand expression. Thus, by recalling that

$$\int_{-\infty}^{\infty} \exp(-\alpha^2) d\alpha = \sqrt{\pi}, \text{ one arrives at}$$

$$\int_0^{\infty} \exp\left\{-\frac{[\ln(r_d/r_0)]^2}{2\sigma_0^2}\right\} r_d^4 dr_d = \sqrt{2\pi}\sigma_0 r_0^5 \exp\left(\frac{25}{2}\sigma_0^2\right) \quad (\text{B7})$$

and

$$\int_0^{\infty} \exp\left\{-\frac{[\ln(r_d/r_0)]^2}{2\sigma_0^2}\right\} r_d^2 dr_d = \sqrt{2\pi}\sigma_0 r_0^3 \exp\left(\frac{9}{2}\sigma_0^2\right), \quad (\text{B8})$$

which, upon substitution into eqs. (B5) and (B6), yield

$$\sqrt{2\pi}\sigma_0 r_0^5 \exp\left(\frac{25}{2}\sigma_0^2\right) = \frac{8AL_p(R_F - R_L)\tau}{\pi N_0} \quad (\text{B9})$$

and

$$\sqrt{2\pi}\sigma_0 r_0^3 \exp\left(\frac{9}{2}\sigma_0^2\right) = \frac{A\tau}{\pi k_m N_0}, \quad (\text{B10})$$

respectively. The two equations above have four unknowns,  $r_0$ ,  $N_0/\tau$ ,  $k_m$ , and  $\sigma_0^2$ , the last two of which are treated here as fitting parameters. Upon assuming values for  $k_m$  and  $\sigma_0^2$ , the other two parameters can be calculated from eqs. (B9) and (B10) as

$$r_0 = \frac{\sqrt{8L_p(R_F - R_L)k_m}}{\exp(4\sigma_0^2)} \quad (\text{B11})$$

and

$$\frac{N_0}{\tau} = \frac{A}{\pi\sqrt{2\pi}\sigma_0 k_m r_0^3 \exp\left(\frac{9}{2}\sigma_0^2\right)}. \quad (\text{B12})$$

It is easy to show that the pore-size-averaged transmission parameters can then be determined from the following general formula:

$$\bar{\Psi} = C_N \int_0^\infty \Psi(r_d) \exp\left\{-\frac{[\ln(r_d/r_0)]^2}{2\sigma_0^2}\right\} r_d^2 dr_d \quad (\text{B13})$$

where  $\Psi = \sigma_{re}$ ,  $\Phi$ ,  $K_c$  or  $K_d$ , and  $C_N = \pi k_m N_0 / (A\tau)$ . Substitution into eq. (B13) of the appropriate analytical expressions for  $\Psi(r_d)$  given by eqs. (82)-(85) yields eventually

$$\bar{\Phi} = C_N \int_0^\infty (1 - r_M/r_d)^2 \exp\left\{-\frac{[\ln(r_d/r_0)]^2}{2\sigma_0^2}\right\} r_d^2 dr_d, \quad (\text{B14})$$

$$\bar{\sigma}_{re} = C_N \int_0^\infty [1 - (1 - r_M/r_d)^2]^2 \exp\left\{-\frac{[\ln(r_d/r_0)]^2}{2\sigma_0^2}\right\} r_d^2 dr_d, \quad (\text{B15})$$

$$\bar{K}_c = C_N \int_0^\infty \frac{[2 - (1 - r_M/r_d)^2] K_s(r_d)}{2 K_t(r_d)} \exp\left\{-\frac{[\ln(r_d/r_0)]^2}{2\sigma_0^2}\right\} r_d^2 dr_d, \quad (\text{B16})$$

and

$$\bar{K}_d = C_N \int_0^\infty \frac{6\pi}{K_t(r_d)} \exp\left\{-\frac{[\ln(r_d/r_0)]^2}{2\sigma_0^2}\right\} r_d^2 dr_d, \quad (\text{B17})$$

where  $K_t$  and  $K_s$  are evaluated as functions of  $r_d$  using eq. (86).

The general solution algorithm taking into account the pore size distribution becomes then as follows:

- (1) assume a value for  $k_m$ ;
- (2) assume a value for  $\sigma_0^2$ ;
- (3) calculate  $r_0$  and  $N_0/\tau$  from eqs. (B11) and (B12);
- (4) calculate the pore-size-averaged transmission parameters,  $\overline{\sigma_{re}}$ ,  $\overline{\Phi}$ ,  $\overline{K_c}$  and  $\overline{K_d}$ , from eqs. (B14)-(B17);
- (5) run model simulations using  $\overline{\sigma_{re}}$ ,  $\overline{\Phi}$ ,  $\overline{K_c}$  and  $\overline{K_d}$ ;
- (6) repeat steps 2-5 to find the best-fit  $\sigma_0^2$  value (i.e., one minimising the standard deviation defined by eq. (87));
- (7) repeat steps 1-6 to find the best-fit pair of  $k_m$  and  $\sigma_0^2$ .

## Appendix C

## FORTRAN CODE OF THE MODIFIED GAUSS ELIMINATION ROUTINE

```

*****
*
*      SUBROUTINE GAUSS3D (AS,Ni,Nj,Nk,PL,PS,RNORM,RNORM_)
*
*      IMPLICIT REAL*8 (A-H,O-Z)
*      PARAMETER (NiMAX=50,NjMAX=10,NkMAX=9,NmMAX=1)
*      DIMENSION PS(0:NiMAX+1,0:NjMAX+1,0:NkMAX+1),
>             PL(0:NiMAX+1,0:NjMAX+1,0:NkMAX+1),
>             AS(NiMAX,NjMAX,NkMAX,9),
>             X(NiMAX*NjMAX*NkMAX),
>             B(NiMAX*NjMAX*NkMAX,2*NjMAX*NkMAX+2)
*
*      PS:  the sought-after ECS pressure distribution
*      PL:  the known ICS pressure distribution
*      AS:  matrix of coefficients for the PS equations
*      B:   the compacted Gauss coefficient matrix
*      NDr: number of rows in B
*      NDc: number of columns in B
*      m1:  column index of the axial neighbour behind, (i-1,j,k)
*      m2:  column index of the axial neighbour ahead, (i+1,j,k)
*      m3:  column index of the radial neighbour behind, (i,j-1,k)
*      m4:  column index of the radial neighbour ahead, (i,j+1,k)
*      m5:  column index of the angular neighbour behind, (i,j,k-1)
*      m6:  column index of the angular neighbour ahead, (i,j,k+1)
*      m8:  column index of the central point, (i,j,k)
*
*      NDr = Ni*Nj*Nk
*      NDr1 = (Ni-1)*Nj*Nk
*      NDc = 2*Nj*Nk+2
*      m1 = 1
*      m2 = NDc-1
*      m3 = (Nj-1)*Nk+1
*      m4 = (Nj+1)*Nk+1
*      m8 = Nj*Nk+1
*      m5 = m8-1
*      m6 = m8+1
*
*      Set up matrix B
*
*      B = 0.D0
*      DO i=1,Ni
*      DO j=1,Nj
*      DO k=1,Nk
*         id = (i-1)*Nj*Nk + (j-1)*Nk + k
*         B(id,m1) = AS(i,j,k,1)
*         B(id,m2) = AS(i,j,k,2)

```

```

      B(id,m3) = AS(i,j,k,3)
      B(id,m4) = AS(i,j,k,4)
      B(id,m5) = AS(i,j,k,5)
      B(id,m6) = AS(i,j,k,6)
      B(id,m8) = AS(i,j,k,8)
      B(id,NDc) = AS(i,j,k,9) - AS(i,j,k,7)*PL(i,j,k)
    END DO
  END DO
END DO

```

```

*
*   The diagonal dominance is already reflected in B, so there is no
*   need for pivot selection. The next step is elimination.
*

```

```

DO k=1,NDr-1
  mk = MAX(0,k-NDr1)
  DO i=1,m5-mk
    id = k+i
    jd = m8-i
    mjd = m2-i-mk
    QUOT = B(id,jd)/B(k,m8)
    B(id,jd) = 0.DO
    DO j=jd+1,mjd
      B(id,j) = B(id,j) - QUOT*B(k,j+i)
    END DO
    B(id,NDc) = B(id,NDc) - QUOT*B(k,NDc)
  END DO
END DO

```

```

*
*   Back substitution
*

```

```

IF (DABS(B(NDr,m8)).LE.1.D-12) THEN
  WRITE(6,*)'ZERO DIAGONAL ELEMENT at row',NDr
  STOP
END IF
X(NDr) = B(NDr,NDc)/B(NDr,m8)
DO k=NDr-1,1,-1
  mk = MAX(0,k-NDr1)
  SUM = 0.DO
  DO j=m8+1,m2-mk
    SUM = SUM + B(k,j)*X(k+j-m8)
  END DO
  IF (DABS(B(k,m8)).LE.1.D-12) THEN
    WRITE(6,*)'ZERO DIAGONAL ELEMENT at row',k
    STOP
  END IF
  X(k) = (B(k,NDc)-SUM)/B(k,m8)
END DO

```

```

*
*   Conversion of X to PS
*

```

```

DO i=1,Ni
  DO j=1,Nj
    DO k=1,Nk
      id = (i-1)*Nj*Nk + (j-1)*Nk + k
      PS(i,j,k) = X(id)
    END DO
  END DO
END DO

```

```

*
*   Estimate accuracy by calculating the norm of residual vector
*   (global, RNORM, and average per grid point, RNORM_)
*

```

```
*
RNORM = 0.DO
DO i=1,Ni
DO j=1,Nj
DO k=1,Nk
  SUM = AS(i,j,k,9) - AS(i,j,k,7)*PL(i,j,k)
  > - AS(i,j,k,1)*PS(i-1,j,k)
  > - AS(i,j,k,2)*PS(i+1,j,k)
  > - AS(i,j,k,3)*PS(i,j-1,k)
  > - AS(i,j,k,4)*PS(i,j+1,k)
  > - AS(i,j,k,5)*PS(i,j,k-1)
  > - AS(i,j,k,6)*PS(i,j,k+1)
  > - AS(i,j,k,8)*PS(i,j,k)
  RNORM = RNORM + DABS(SUM)
END DO
END DO
END DO
RNORM_ = RNORM/DBLE(NDr)
*
RETURN
END
*
*****
```

### Appendix D

#### ADI METHOD AND UPWIND CONTROL SCHEME FOR THE SOLUTION OF THREE-DIMENSIONAL ECS CONCENTRATION PROBLEM

The protein transport equation (113) (or its equivalent form, eq. (115)) was discretised by integration over a representative elementary volume (REV) in three cylindrical dimensions. Integration of the spatial derivatives on the right-hand side of the equation yielded protein flux terms at the different faces of the REV, which were calculated by employing an upwinding hybrid scheme developed by Patankar (1980, p. 92), i.e.,

$$J_{z,s} = \frac{D_z}{\Delta z} (A_s C_{i,j,k} - B_s C_{i-1,j,k}), \quad (\text{D1a})$$

$$J_{z,n} = \frac{D_z}{\Delta z} (A_n C_{i+1,j,k} - B_n C_{i,j,k}), \quad (\text{D1b})$$

$$J_{r,b} = \frac{D_r}{\Delta r} (A_b C_{i,j,k} - B_b C_{i,j-1,k}), \quad (\text{D1c})$$

$$J_{r,t} = \frac{D_r}{\Delta r} (A_t C_{i,j+1,k} - B_t C_{i,j,k}), \quad (\text{D1d})$$

$$J_{\theta,w} = \frac{D_\theta}{r_j \Delta \theta} (A_w C_{i,j,k} - B_w C_{i,j,k-1}), \quad (\text{D1e})$$

and

$$J_{\theta,e} = \frac{D_\theta}{r_j \Delta \theta} (A_e C_{i,j,k+1} - B_e C_{i,j,k}), \quad (\text{D1f})$$

where the subscripts  $z$ ,  $r$ , and  $\theta$  identify the directions of the flux and diffusivity components;  $s$ ,  $n$ ,  $b$ ,  $t$ ,  $w$ , and  $e$  denote the south, north, bottom, top, west, and east faces of the REV, respectively (see fig. 38, section 5.3.1.1); and subscript  $S$  has been omitted for clarity. The upwinding coefficients  $A$  and  $B$  in the above equations are calculated as

$$A(Pe) = \max\left(0, 1 - \frac{1}{2}|Pe|\right) + \max(-Pe, 0) \quad (D2a)$$

and

$$B(Pe) = \max\left(0, 1 - \frac{1}{2}|Pe|\right) + \max(Pe, 0), \quad (D2b)$$

where  $Pe$  is the local Peclet number at each face of the REV, i.e.,

$$Pe_s = \frac{v_{i-\frac{1}{2},j,k} \Delta z}{D_z}, \quad (D3a)$$

$$Pe_n = \frac{v_{i+\frac{1}{2},j,k} \Delta z}{D_z}, \quad (D3b)$$

$$Pe_b = \frac{v_{i,j-\frac{1}{2},k} \Delta r}{D_r}, \quad (D3c)$$

$$Pe_t = \frac{v_{i,j+\frac{1}{2},k} \Delta r}{D_r}, \quad (D3d)$$

$$Pe_w = \frac{v_{i,j,k-\frac{1}{2}} r_j \Delta \theta}{D_\theta}, \quad (D3e)$$

and

$$Pe_e = \frac{v_{i,j,k+\frac{1}{2}} r_j \Delta \theta}{D_\theta}, \quad (D3f)$$

with the fluid velocities indexed as shown in fig. 38. In writing eqs. (D1) and (D3), the flux component through each face of the REV was assumed constant over the surface of that face. In particular, the explicit radial dependence of  $J_\theta$  (see eq. (114b)) was neglected, which avoided the appearance of the logarithmic term  $\ln(r_{j+\frac{1}{2}}/r_{j-\frac{1}{2}})$  and the consequent complication due to division by  $r_{j-\frac{1}{2}} = 0$  at  $j = 1$  (innermost radial core). The velocity field needed to evaluate the Peclet numbers in eqs. (D3) was always taken from the most recent ECS pressure solution.

The advancement of the concentration solution to the next time level was performed by means of a 3-D alternate direction implicit (ADI) method formulated by Douglas (1962) and based on the Crank-Nicolson scheme. Accordingly, the following three-step procedure was implemented:

*Step 1.* Obtain the first intermediate concentration field,  $C^*$ , by solving a tridiagonal set of finite-difference equations in which the temporal derivative on the left-hand side of eq. (113) is expressed as

$$\frac{\partial C}{\partial t} \approx \frac{C_{i,j,k}^* - C_{i,j,k}^{(n)}}{\Delta t} \quad (\text{D4a})$$

and the concentrations in the axial flux terms (eqs. (D1a) and (D1b)) are taken as

$$C = \frac{1}{2}(C^* + C^{(n)}), \quad (\text{D4b})$$

where the superscript  $(n)$  denotes the most recent time level.

*Step 2.* Obtain the second intermediate concentration field,  $C^{**}$ , by solving a tridiagonal set of finite-difference equations in which the temporal derivative on the left-hand side of eq. (113) is expressed as

$$\frac{\partial C}{\partial t} \approx \frac{C_{i,j,k}^{**} - C_{i,j,k}^{(n)}}{\Delta t}, \quad (\text{D5a})$$

the concentrations in the radial flux terms (eqs. (D1c) and (D1d)) are taken as

$$C = \frac{1}{2}(C^{**} + C^{(n)}), \quad (\text{D5b})$$

and the concentrations in the axial flux terms (eqs. (D1a) and (D1b)) are calculated from eq. (D4b).

*Step 3.* Obtain the concentration field at the next time step,  $C^{(n+1)}$ , by solving a tridiagonal set of finite-difference equations in which the temporal derivative on the left-hand side of eq. (113) is expressed as

$$\frac{\partial C}{\partial t} \approx \frac{C_{i,j,k}^{(n+1)} - C_{i,j,k}^{(n)}}{\Delta t}, \quad (\text{D6a})$$

the concentrations in the angular flux terms (eqs. (D1e) and (D4f)) are taken as

$$C = \frac{1}{2}(C^{(n+1)} + C^{(n)}), \quad (\text{D6b})$$

and the concentrations in the axial (eqs. (D1a) and (D1b)) and radial (eqs. (D1c) and (D1d)) flux terms are calculated from eqs. (D4b) and (D5b), respectively.

The set of the finite-difference equations for each of the above steps was obtained by combining eqs. (113), (D1), and (D3)-(D6), with the coefficients  $A$  and  $B$  evaluated using the most recent ECS velocity field (similarly, the most recent ECS and ICS pressure fields could be used to evaluate the transmembrane protein flux term,  $J_{TMP}$ ). The subsequent algebraic manipulations led eventually to the formulation of the following algorithm for the generation of the 3-D concentration field at the new time level ( $n + 1$ ):

*Step 1.* For each  $j$  and  $k$ , obtain a  $C_j^*$  concentration vector by solving

$$\begin{aligned}
 & C_{i-1,j,k}^* \left[ -\frac{D_z \Delta t}{2 \varepsilon_S (\Delta z)^2} B_s \right] + C_{i,j,k}^* \left[ 1 + \frac{D_z \Delta t}{2 \varepsilon_S (\Delta z)^2} (A_s + B_n) \right] + C_{i+1,j,k}^* \left[ -\frac{D_z \Delta t}{2 \varepsilon_S (\Delta z)^2} A_n \right] = \\
 & = C_{i,j,k}^{(n)} \left[ 1 - \frac{D_z \Delta t}{2 \varepsilon_S (\Delta z)^2} (A_s + B_n) - \frac{D_r \Delta t}{\varepsilon_S (\Delta r)^2} \frac{1}{r_j} (B_t r_{j+\frac{1}{2}} + A_b r_{j-\frac{1}{2}}) - \frac{D_\theta \Delta t}{\varepsilon_S (r_j \Delta \theta)^2} (A_w + B_e) \right] \\
 & + \frac{D_r \Delta t}{\varepsilon_S (\Delta r)^2} \frac{1}{r_j} \left[ C_{i,j+1,k}^{(n)} A_t r_{j+\frac{1}{2}} + C_{i,j-1,k}^{(n)} B_b r_{j-\frac{1}{2}} \right] + \frac{D_\theta \Delta t}{\varepsilon_S (r_j \Delta \theta)^2} \left[ C_{i,j,k+1}^{(n)} A_e + C_{i,j,k-1}^{(n)} B_w \right] \\
 & + \frac{D_z \Delta t}{2 \varepsilon_S (\Delta z)^2} \left[ C_{i+1,j,k}^{(n)} A_n + C_{i-1,j,k}^{(n)} B_s \right] + \frac{A_v \Delta t}{\varepsilon_S} J_{TMP} \quad (D7)
 \end{aligned}$$

*Step 2.* For each  $i$  and  $k$ , obtain a  $C_j^{**}$  concentration vector by solving

$$\begin{aligned}
 & C_{i,j-1,k}^{**} \left[ -\frac{D_r \Delta t}{2 \varepsilon_S (\Delta r)^2} \frac{r_{j-\frac{1}{2}}}{r_j} B_b \right] + C_{i,j,k}^{**} \left[ 1 + \frac{D_r \Delta t}{2 \varepsilon_S (\Delta r)^2} \frac{1}{r_j} (B_t r_{j+\frac{1}{2}} + A_b r_{j-\frac{1}{2}}) \right] \\
 & + C_{i,j+1,k}^{**} \left[ -\frac{D_r \Delta t}{2 \varepsilon_S (\Delta r)^2} \frac{r_{j+\frac{1}{2}}}{r_j} A_t \right] = \\
 & = C_{i,j,k}^* - \frac{D_r \Delta t}{2 \varepsilon_S (\Delta r)^2} \frac{1}{r_j} \left[ C_{i,j+1,k}^{(n)} A_t r_{j+\frac{1}{2}} + C_{i,j-1,k}^{(n)} B_b r_{j-\frac{1}{2}} - C_{i,j,k}^{(n)} (B_t r_{j+\frac{1}{2}} + A_b r_{j-\frac{1}{2}}) \right] \quad (D8)
 \end{aligned}$$

*Step 3.* For each  $i$  and  $j$ , obtain a  $C_k^{(n+1)}$  concentration vector by solving

$$\begin{aligned}
& C_{i,j,k-1}^{(n+1)} \left[ -\frac{D_\theta \Delta t}{2 \varepsilon_S (r_j \Delta \theta)^2} B_w \right] + C_{i,j,k}^{(n+1)} \left[ 1 + \frac{D_\theta \Delta t}{2 \varepsilon_S (r_j \Delta \theta)^2} (A_w + B_e) \right] \\
& + C_{i,j,k+1}^{(n+1)} \left[ -\frac{D_\theta \Delta t}{2 \varepsilon_S (r_j \Delta \theta)^2} A_e \right] = \\
& = C_{i,j,k}^{**} - \frac{D_\theta \Delta t}{2 \varepsilon_S (r_j \Delta \theta)^2} \left[ C_{i,j,k+1}^{(n)} A_e + C_{i,j,k-1}^{(n)} B_w - C_{i,j,k}^{(n)} (B_e + A_w) \right]. \tag{D9}
\end{aligned}$$

The convenience of using the upwinding coefficients  $A$  and  $B$  can be particularly appreciated in the straightforward implementation of the boundary conditions. Since each of the ECS boundaries in the 3-D PMM for a closed-shell HFBR is essentially a no-flux boundary (see table 10 in section 5.2.2.2), the conditions are imposed easily by setting the appropriate coefficients to zero, i.e.,

$$\text{at } z = 0: \quad A_s = B_s = 0, \tag{D10a}$$

$$\text{at } z = L: \quad A_n = B_n = 0, \tag{D10b}$$

$$\text{at } r = 0: \quad A_b = B_b = 0, \tag{D10c}$$

$$\text{at } r = R_{HFBR}: \quad A_t = B_t = 0, \tag{D10d}$$

$$\text{at } \theta = 0: \quad A_w = B_w = 0, \tag{D10e}$$

and

$$\text{at } \theta = \pi: \quad A_e = B_e = 0. \tag{D10f}$$

At the intersections of two or three boundaries, eqs. (D10) are simply applied in an additive manner.